

Yale Cosmology Workshop

The Shapes of Galaxies and their Dark Halos



Editor

Priyamvada Natarajan

World Scientific

The Shapes of Galaxies and their Dark Halos

This page is intentionally left blank

Yale Cosmology Workshop

The Shapes of Galaxies and their Dark Halos

New Haven, Connecticut, USA

28–30 May 2001

Editor

Priyamvada Natarajan

Yale University, USA



World Scientific

New Jersey • London • Singapore • Hong Kong

Published by

World Scientific Publishing Co. Pte. Ltd.

P O Box 128, Farrer Road, Singapore 912805

USA office: Suite 1B, 1060 Main Street, River Edge, NJ 07661

UK office: 57 Shelton Street, Covent Garden, London WC2H 9HE

British Library Cataloguing-in-Publication Data

A catalogue record for this book is available from the British Library.

THE SHAPES OF GALAXIES AND THEIR DARK MATTER HALOS
Yale Cosmology Workshop

Copyright © 2002 by World Scientific Publishing Co. Pte. Ltd.

All rights reserved. This book, or parts thereof, may not be reproduced in any form or by any means, electronic or mechanical, including photocopying, recording or any information storage and retrieval system now known or to be invented, without written permission from the Publisher.

For photocopying of material in this volume, please pay a copying fee through the Copyright Clearance Center, Inc., 222 Rosewood Drive, Danvers, MA 01923, USA. In this case permission to photocopy is not required from the publisher.

ISBN 981-02-4848-2

Printed in Singapore by Uto-Print

PREFACE

‘L’essentiel est invisible pour les yeux’... says the fox in ‘The Little Prince’ by Antoine de Saint-Exupry - an apt epithet for dark matter in the Universe. Dark matter seems to be ubiquitous, on every scale - and yet, its essential nature and properties are completely unknown. While the case for the existence of dark matter no longer needs to be made - the observational evidence is convincing - it remains, nevertheless, one of the foremost and challenging problems in cosmology.

Yale University has an illustrious and long-standing tradition in Astronomy and Astrophysics research, dating back to 1714. As a pre-eminent center for stellar astrophysical research, its accomplishments, ranging from the Variable star catalog to the isochrones, have established it as one of the pioneers in the studies of galaxy formation since the 1970’s. Today the department of astronomy, while continuing to build on its traditional strengths, is expanding into previously unexplored research areas in extra-galactic astronomy and astrophysics. With this end in view, we are organizing workshops and conferences (in what we hope will be an exciting and original series) on cosmology and other areas of astrophysics.

The aim of the present conference was to bring together (during three days of focused talks and discussions) theorists, observers and numerical simulators who work on constraining the shapes of galaxies and their halos using various probes on different scales: gravitational lensing studies, globular clusters, planetary nebulae, X-ray surface brightness profiles, polar rings, Lyman- α absorbers and HI studies.

This was a memorable workshop for many reasons. Aside from the excellent quality of talks, almost everyone who wished to speak was integrated into the schedule, making it a rather strenuous affair for most participants. Attendees were always actively engaged in the discussion. Speaking of attendees, the conference was particularly notable for its demographic shift - towards the low end! Added to this, of course, was one of the most lavish conference dinners in recent memory.

There are several people whose efforts enabled the successful hosting of the workshop. Thanks to the following: the LOC; Dave Goldberg, specially for creating and maintaining the web site; the Yale conference services for their organizational help; Avi Mandell and John Yong for help with the Audio-Visual equipment and projectors; and, last but not least, the goth punkette from the local gourmet coffeeshop for lending unanticipated visual interest to the first talk by strolling across in front of the speakers with flasks of piping hot coffee

in hand! The Peabody Museum of Natural History at Yale graciously allowed us to use the imposing Hall of Dinosaurs for the conference dinner. I would also like to thank Yale for the substantial start-up funds that subsidized the cost of this workshop. Finally, I gratefully acknowledge the contributions of Dr. Daniel Cartin and Ms. Chelsea Chin of the World Scientific Publishing Company, for their assistance with producing these proceedings.

Priyamvada Natarajan
Department of Astronomy
Yale University
New Haven, CT

YALE COSMOLOGY WORKSHOP

SCIENTIFIC ORGANIZING COMMITTEE

James Binney (Oxford)

Roger Blandford (Caltech)

Claude Canizares (MIT)

Richard Ellis (Caltech)

Jeff Kenney (Yale)

Jean-Paul Kneib (Toulouse)

Jon Loveday (Sussex)

Ben Moore (Durham)

Priyamvada Natarajan (Yale)

Max Pettini (Cambridge)

Penny Sackett (Groningen)

Joseph Silk (Oxford)

Jacqueline van Gorkom (Columbia)

Simon White (Garching)

Dennis Zaritsky (Steward Obs.)

Stephen Zepf (Yale)

LOCAL ORGANIZING COMMITTEE

Susan Delong

David Goldberg

Jeff Kenney

Arunav Kundu

Priyamvada Natarajan

Stephen Zepf

This page is intentionally left blank

CONTENTS

Preface	v
INTRINSIC SHAPES OF GALAXIES	
Intrinsic galaxy shapes and their correlations <i>R. Crittenden</i>	1
Measuring the flattening of dark matter halos <i>P. Natarajan</i>	9
Power spectra for galaxy shape correlations <i>J. Mackey</i>	17
Intrinsic galaxy alignments and weak gravitational lensing <i>A. Heavens</i>	21
Shapelets: a new method to measure galaxy shapes <i>A. Refregier, T.-C. Chang and D. J. Bacon</i>	29
Bayesian galaxy shape estimation <i>S. Bridle</i>	38
A general theory of self-gravitating systems: shapes of astronomical objects <i>S. Filippi</i>	47
SHAPES FROM LENSING STUDIES	
Strong and weak lensing constraints on galaxy mass distribution <i>J.-P. Kneib</i>	50
Early-type halo masses from galaxy-galaxy lensing <i>G. Wilson</i>	58
Mass follows light <i>C. S. Kochanek</i>	62
SDSS measurements of galaxy halos properties by weak lensing <i>T. A. McKay</i>	72

Constraining halo properties from galaxy-galaxy lensing and photo-z <i>A. O. Jaunsen</i>	81
Is there a group halo? <i>O. Moller</i>	85
Constraining galaxy shapes from modeling the first probable two plane lens B2114+022 <i>K. Chae</i>	89
Detecting flattened halos with weak lensing <i>T. G. Brainerd</i>	93
Finding the arciness in arclets – exploring the octopole moments of lensed galaxies <i>D. M. Goldberg</i>	101
Determining the three-dimensional shapes of galaxy clusters <i>A. Escala and P. Natarajan</i>	105
DARK MATTER HALOS FROM N-BODY SIMULATIONS	
Shapes of dark matter halos <i>J. S. Bullock</i>	109
Substructure in CDM halos and the heating of stellar disks <i>J. F. Navarro</i>	114
On the ‘initial’ angular momentum of galaxies <i>T. Abel</i>	119
Ellipticals and bars: central masses and friction <i>J. A. Sellwood</i>	123
The morphological evolution of merger remnants <i>B. Ryden</i>	132
SHAPES MAPPED USING STELLAR TRACERS	
Properties of the outer halos of galaxies from the study of globular clusters <i>S. E. Zepf</i>	140

White Dwarfs: contributors and tracers of the galactic dark-matter halo <i>L. V. E. Koopmans</i>	150
Keck spectroscopy of dwarf elliptical galaxies in the Virgo cluster <i>M. Geha</i>	154
Halo mass dynamics of M31 using planetary nebulae velocities <i>C. Halliday</i>	158
Keck spectroscopy of red giants in M31's stellar halo <i>P. Guhathakurta</i>	162
SHAPES FROM HI STUDIES AND POLAR RINGS	
Halo tracing with atomic hydrogen <i>M. R. Merrifield</i>	170
What can polar rings tell us about the shapes of dark matter halos? <i>L. S. Sparke</i>	178
Constraints on the radial mass distribution of dark matter halos from rotation curves <i>S. S. McGaugh</i>	186
SHAPES FROM STUDIES OF SATELLITES	
Telling tails about the milky way <i>K. V. Johnston</i>	194
The shapes of galaxies and their halos as traced by stars: the milky way dark halo and the LMC disk <i>R. van der Marel</i>	202
Searching for streams of ancient galaxies in the Milky Way's halo <i>A. K. Vivas</i>	210
The extended shapes of galactic satellites <i>S. R. Majewski</i>	214
The impact of tidal interactions on satellite galaxies: a study of the M31 satellites, M32 and NGC 205 <i>P. I. Choi</i>	222

Consequences of satellite decay for galaxy halo shapes <i>E. van Kampen</i>	226
Exploring group halos using galaxy dynamics <i>A. B. Whiting</i>	230
CONSTRAINTS FROM X-RAY STUDIES	
The shapes of galaxies and clusters: an X-Ray view <i>D. A. Buote</i>	234
New features in elliptical galaxies from Chandra images <i>C. Jones</i>	242
SHAPES FROM ABSORPTION STUDIES	
The detection of Lyman- α absorption from nine nearby galaxies <i>D. V. Bowen</i>	246
CONCLUDING REMARKS <i>R. S. Ellis</i>	254

INTRINSIC GALAXY SHAPES AND THEIR CORRELATIONS

R. G. Crittenden

*Centre for Mathematical Sciences, Wilberforce Road
Cambridge CB3 0WA, England*

P. Natarajan

*Department of Astronomy, Yale University
New Haven, CT 06520-8101 USA*

U. Pen

*CITA, 60 St. George Street
Toronto, ONT M5S 1A7, Canada*

T. Theuns

*Institute of Astronomy, Maddingley Rd.
Cambridge CB3 0HA, England*

We discuss the factors leading to spatial correlations in the observed shapes of galaxies and their implications for weak lensing measurements. Focusing on a model where the intrinsic correlations arise from angular momentum correlations, we examine the predicted shape correlations and how they may be distinguished from weak lensing.

1 The Observed Shapes of Galaxies

Many factors go into determining a galaxy's observed shape. Some of these are dynamical: galaxy shapes can be tidally stretched by the local shear field, distorted by bar instabilities or they can be squashed by the galaxy's spin. Some of these are environmental: if a galaxy is closely surrounded by many other galaxies, then the mergers and collisions it experiences will greatly impact on its shape. Still other effects result from smaller scale physics, such as obscuration by dust and the detailed distribution of star forming regions within the galaxy. Finally, some factors are entirely external, such as distortions arising from gravitational lensing by intervening matter. By studying the light from galaxies on different scales and in different ways we can hope to disentangle these various effects, and thus understand each more quantitatively.

One area in which there has been considerable recent progress has been in the study of shape distortions by weak gravitational lensing. These studies have relied upon the notion that whatever internal factors determine the intrinsic galaxy shapes, they are independent from galaxy to galaxy; any shape correlations are assumed to arise from lensing alone. This is probably a reason-

able assumption if the galaxies are far apart, but that will not necessarily be the case. Here we re-examine this assumption, and look at whether there may be intrinsic shape correlations and what they could be telling us. While the intrinsic correlation signal will be small, it still could potentially be important given the weakness of the lensing effect.

1.1 Quantifying galaxy shapes

A great deal of information is contained in the distribution of light from a galaxy. Here we ignore its overall brightness and focus on the lowest order moments of the galaxy's shape, which are quantified by the ellipticity of the light distribution. This has the advantage that it is simple and can be collected for a great many galaxies. More recently, attention has also turned to higher order moments and what they might tell us (for example, see the contribution by David Goldberg in this volume.)

To quantify the projected shapes, we approximate them by ellipses with semi-axes of lengths a and b ($a > b$). The orientation of a given ellipse is measured by the angle ψ between its major axis and the chosen coordinate system, while its magnitude is given by $|\epsilon| = (a^2 - b^2)/(a^2 + b^2)$. Both the magnitude of the ellipticity and its orientation can be concisely described by the complex quantity

$$\epsilon = |\epsilon|e^{2i\psi} = \epsilon_+ + i\epsilon_x. \quad (1)$$

The ellipticity is a spin-2 field, since rotations by 180° leave it unchanged. In this sense it is identical to a map of a polarization field, and many of the tools developed for the study of microwave background polarization apply equally well here.

1.2 Galaxy models

The simplest observable we can consider is the one point distribution of the ellipticity. If the distribution of galaxy orientations is isotropic, then the one point distribution is described entirely by the distribution of the magnitude of the ellipticity, $\mathcal{P}(|\epsilon|)$.

The distribution of the ellipticity can be used to infer information about the underlying galaxy shapes. Consider a simple model where the isocontours of the light emission from a galaxy are assumed to lie on triaxial ellipsoids. If there is no absorption by dust, then the projected light distributions will be elliptical (Stark, 1976). Assuming that the galaxies are randomly oriented with respect to our line of sight, then the distribution of ellipticities may be inverted to find the distribution of the three dimensional axis ratios.

Lambas, Maddox and Loveday (1992) did just such an inversion for a local population ($z \sim 0.1$) of elliptical, spiral and S0 galaxies. They found that spiral galaxies appeared to be nearly oblate and axisymmetric, but that some triaxiality was required to fit the observed distribution. The ellipticals and S0's were also found to be triaxial, but as one might expect, they were generally more spherical and so had a lower mean ellipticity than the spirals.

2 Correlations of Galaxy Shapes

One can also consider the two point correlations functions of galaxy shapes. If the distributions are Gaussian, these statistics contain all of the information in the ellipticity field. They can be characterized by three correlation functions, $\langle \epsilon_+ \epsilon_+ \rangle$, $\langle \epsilon_x \epsilon_x \rangle$, and $\langle \epsilon_+ \epsilon_x \rangle$, where the coordinate system has been defined relative to the vector between the points. If the field is invariant under parity transformations, then the ensemble averaged correlation, $\langle \epsilon_+ \epsilon_x \rangle$, must be zero.

In determining the ellipticity correlations, it is correlations in galaxy orientations, rather than the magnitudes of their ellipticities ($|\epsilon|$), which are the most important. To see this, assume that the magnitudes of the ellipticities are independent of their orientations, from which it follows that

$$\langle \epsilon \epsilon'^* \rangle \simeq \langle |\epsilon| |\epsilon'| \rangle \langle e^{2i(\psi - \psi')} \rangle = [|\bar{\epsilon}|^2 + \langle \delta\epsilon \delta\epsilon' \rangle] \langle e^{2i(\psi - \psi')} \rangle, \quad (2)$$

where $\delta\epsilon \equiv |\epsilon| - |\bar{\epsilon}|$ and the mean ellipticity is $|\bar{\epsilon}| \simeq 0.42$. Were the orientations uncorrelated, there would be no resulting ellipticity correlations. (The angle $\psi - \psi'$ would be random, so the expectation of $e^{2i(\psi - \psi')}$ is zero.) However, if the ellipticity magnitudes were uncorrelated there would still be quite significant correlations because of the large mean ellipticity. The variance of the one point distribution is significantly smaller than the square of its mean, $\langle \delta\epsilon^2 \rangle = 0.055 \simeq 0.3|\bar{\epsilon}|^2$, so that even perfect correlations between the magnitudes would only result in a small modulation of the overall correlation.

This relation also demonstrates that given the *same* underlying mechanism for aligning galaxy orientations, the observed correlation will be larger if $|\bar{\epsilon}|$ is larger. Thus, since elliptical galaxies tend to be more spherical than spiral galaxies, we might expect their ellipticity correlation to be lower.

Which of the various intrinsic factors affecting galaxy shapes – i.e. tidal stretching, angular momentum, or galaxy collisions – has the greatest effect on the observed galaxy orientation? The answer is likely to depend on whether the galaxy has had sufficient time to virialize and begin to rotate.

The shape of an object as it initially collapses primarily depends on where the collapsing matter originated and what tidal stretching forces it experiences (e.g. Catelan et al., 2001). These factors could easily dominate yet today on

large enough scales, such as clusters. However, once a galaxy has had time to collapse and begins to rotate about its angular momentum axis, these initial distortions will be largely forgotten. What remains is a general flattening of the object along the spin axis. This will certainly be the case for spiral galaxies and is likely to be true for elliptical galaxies, which still have sufficient spin to have undergone a number of rotations.

A galaxy collision or merger can disrupt the galaxy shape significantly, lasting until the material has had time to revitalize and again reflects the direction of the total angular momentum of the original pair of galaxies. Whether this is important depends on the frequency of galaxy collisions. If the collisions occur on time scales small compared to the time it takes the galaxy to recover and revitalize, then this could be the dominant effect. It seems likely however, that the galaxy spin will be more important except in very dense regions such as clusters.

The observed correlations might be suppressed if a local process acts to misalign the observed galaxy shape. For example, we can only observe the angular momentum of the baryons, not the dark matter. If some nonlinear mechanism causes the angular momentum in baryons to not reflect that of the underlying dark matter, then we may not be able to observe any correlation. (See Tom Abel's contribution in this volume.)

3 Angular Momentum Correlations

Here we assume that angular momentum is the dominant factor determining the orientation of a galaxy's shape. To make quantitative predictions, we need to understand both how a galaxy's spin is related to its observed ellipticity and how the spins of neighboring galaxies may be correlated.

To see how a galaxy's spin relates to its ellipticity, consider a flat disk-like galaxy which rotates with angular momentum perpendicular to the plane of the galaxy. Its observed ellipticity will depend on the angle the angular momentum vector makes with respect to the line of sight, appearing perfectly round when viewed face on, but having its maximum ellipticity when viewed from its edge ($|\epsilon| = 1$.) Its orientation will depend on the direction of the angular momentum perpendicular to the line of sight, giving a complex ellipticity

$$\epsilon = (L_x^2 - L_y^2 + 2iL_xL_y)/(L^2 + L_z^2), \quad (3)$$

where the line of sight is taken to be parallel to \hat{z} . Thus the ellipticity is expected to be *quadratic* in the perpendicular angular momentum and correlations in the ellipticities are expected to be *quartic* in the angular momenta direction.

These conclusions should not change when we consider more varied galaxy shapes. If we consider models where the disks have a finite thickness (oblate), then these will not be as elliptical when viewed from edge on, leading to a suppression factor, $\alpha < 1$ in front of the above expression. If the models are also somewhat tri-axial, then the observed orientation will not exactly correspond to the direction of the perpendicular angular momentum. However, this relation will still hold statistically.

We next consider a model for how the galaxy spins might be correlated. We base this on tidal torque theory which describes how angular momentum is formed as a protogalaxy collapses (Hoyle, 1949; Doroshkevich, 1970; White, 1984; Catelan & Theuns, 1996). The angular momentum can be shown to grow linearly until the fluctuation begins to turnaround and collapse, and is proportional both to the tidal shear field it experiences and the moment of inertia of the collapsing galaxy, $L_i \propto \epsilon_{ijk} T_{jl} I_{lk}$. Most of the angular momentum is imparted early, before the protogalaxy collapses and while its inertia tensor is largest. Thus this linear approximation should be reasonable until galaxy collisions begin to occur.

As shown above, finding the ellipticity correlations requires four point moments of the angular momentum direction. To make this calculation manageable, some simplifying assumptions are needed. We assume the inertia tensors are Gaussian distributed and uncorrelated with the shear field. Even with this, neighboring galaxies spins will be aligned because they collapse in the presence of the same shear field.

The tidal torque theory works well when the perturbations initially collapse, but it can begin to fail at late times when non-linearities, such as collisions, begin to affect the spins of galaxies (Porciani et al. 2001). These effects will randomize the spins of galaxies and suppress their correlations. We will quantify this effect by the parameter $a < 0.6$ introduced by Lee and Pen (2000), which describes how correlated a galaxy's spin is with the predictions of tidal torque theory. This has been measured in various simulations and found to be approximately 0.1 – 0.2.

Here, however, we are interested in how correlations of galaxy spins are suppressed by non-linear effects in comparison to how they would be correlated in tidal torque theory. Assuming that non-linear effects act independently at different points, i.e. by assuming the correlation is simply suppressed by a factor a^2 , will probably underestimate the correlation. It is very possible that collisions will change the spins of galaxies without changing the extent to which they are correlated with each other, since the merger product will have angular momentum determined by the orbital angular momentum, which also arises through tidal torquing. Thus, we need a measure of how correlations

are changed by non-linear effects, which come from numerical studies such as Heavens et al. (2000) and Croft and Metzler (2000). We use these to estimate an effective value of the suppression, \bar{a} , relevant for the two point correlations, which is significantly higher than that found above, $\bar{a} \sim 0.25 - 0.5$.

These assumptions allow us to estimate the three dimensional correlations, which scale as

$$\langle \epsilon \epsilon' \rangle \simeq \frac{\alpha^2 \bar{a}^2}{84} \xi^2(r) / \xi^2(0), \quad (4)$$

where $\xi(r)$ is the density correlation function (Crittenden et al, 2001). The radial dependence is not surprising since the density is just the trace of the shear tensor and the ellipticity is quadratic in the shear. The prefactors just reflect the suppression due to the galaxies' thickness and the suppression from non-linear effects. This correlation must be projected into two dimensions by the Limber equation which incorporates the distribution in redshift of the galaxies.

Recently Mackey et al. (2001) suggested a related *Ansatz* for how the ellipticity depends on a galaxy's angular momentum. (See Jonathan Mackey's contribution to this volume.) We have implicitly been assuming that the galaxy shape is independent of the magnitude of its angular momentum. However, they propose that a galaxy's ellipticity is proportional to its angular momentum, motivated by the idea that a galaxy with high angular momentum will have a thinner disk. They find correlations of a similar form to those presented here, not surprisingly perhaps because, as shown above, the correlations are dominated by the momentum direction, which is the same in the two models.

However, Mackey et al. do find some significant differences related to the $E - B$ decomposition described below. This is also to be expected, because the $E - B$ decomposition is quite sensitive to the amplitude of the ellipticity and any non-linear transformation of the amplitudes will mix these. This may be a worry for the predictions of their model, as it results in some ellipticities being unphysically larger than one, and some amount of non-linear rescaling will be required to correct this.

4 Distinguishing Shape Correlations

4.1 Implications for lensing studies

In some ways, intrinsic correlations are fundamentally different from those resulting from weak lensing. The most marked difference results from the fact that intrinsic correlations are local in nature, so they should be significant only when the galaxies are physically close to one another. They are thus largest

when the survey is not very deep, or when the galaxies are restricted to lie in a narrow redshift range.

Weak lensing effects, on the other hand, introduce correlations between any galaxies which are close on the sky, independent of whether they are physically proximate. In addition, lensing effects increase as the redshift of the lensed galaxies rises and the amount of intervening matter grows. This is precisely the opposite of the behavior of intrinsic correlations.

In Alan Heavens' contribution, he shows the most recent data of shear correlations observed in surveys with a depth of $z = 1$. For such a deep survey, typical galaxies are very far apart, so the level of contamination from intrinsic correlations is expected to be small (about 10% of the lensing signal.) For lower redshift surveys, however, the lensing signal falls while the projected intrinsic correlation grows, meaning that it can no longer be ignored for surveys with mean redshifts less than $z \simeq 0.3$, such as the Sloan Digital Sky survey.

4.2 $E - B$ decomposition

A potentially very useful tool for distinguishing the different contributions to the shape correlations is the so-called " $E - B$ " decomposition (Kaiser 1992, Stebbins, 1996). In it, the galaxy ellipticity field is broken up into two components: E -modes which are associated with tangential and radial patterns, and B -modes which are associated with 'right-handed' or 'left-handed' patterns.

This decomposition is particularly useful because some mechanisms, such as weak lensing (and possibly tidal stretching), create only E -modes. Others, particularly if the mechanism is non-linear, produce both E and B modes of similar amplitude. This is true of angular momentum coupling and most sources of noise (Crittenden et al., 2000). This effect might be used to untangle intrinsic correlations from those of lensing. If the intrinsic mechanism is well understood, then given its B contribution, its E contribution may be inferred and subtracted from the observed E signal, leaving just the lensing contribution.

5 Conclusions

While the discussion here has been purely theoretical, there is growing observational evidence that intrinsic correlations are real and measurable. Brown et al. (2000) recently have applied weak lensing techniques to the low redshift SuperCOSMOS survey and observed correlations far in excess of what is expected from gravitational lensing. The amplitude of these is comparable to what is predicted by numerical and analytic models for intrinsic correlations, though their detailed structure still needs to be explained.

In addition, Lee and Pen (2001) have found evidence in the Tully catalog for spin correlations which seem consistent with the results from numerical simulations. Finally, Pen, van Wearbeke and Mellier (2001) have recently shown evidence of B modes in the VIRMOS data. (It is still unclear, however, whether this is due to intrinsic correlations or contamination from systematic errors.)

It seems likely then that we will soon be in a position to study intrinsic correlations in detail. The question is no longer whether intrinsic correlations exist, but how do they arise, and what are they telling us about our universe?

References

1. Abel, T., 2001, these proceedings.
2. Brown M.L., Taylor, A.N., Hambly, N.C., Dye, S., 2000, preprint, astro-ph/0009499
3. Catelan, P., Kamionkowski, M., & Blandford, R. D., 2001, MNRAS, 320, L7
4. Catelan, P., & Theuns, T., 1996, MNRAS, 282, 436
5. Crittenden, R., Natarajan, P., Pen, U. & Theuns, T., 2001, ApJ, 559, 552
6. Crittenden, R., Natarajan, P., Pen, U. & Theuns, T., 2000, submitted ApJ, astro-ph/0012336
7. Croft, R. A. C., & Metzler, C., 2000, ApJ, 545, 561
8. Doroshkevich, A. G., 1970, Astrofizika, 6, 581
9. Goldberg, D., 2001, these proceedings.
10. Heavens, A., 2001, these proceedings.
11. Heavens, A., Refregier, A., & Heymans, C., 2000, MNRAS, 319, 649
12. Hoyle, F., 1949, in *Problems of Cosmical Aerodynamics* (Dayton, Ohio; Central Documents Office), p. 195
13. Kaiser, N., 1992, ApJ, 388, 272
14. Lambas, D. G, Maddox, S. J., & Loveday, J., 1992, MNRAS, 258, 404
15. Lee, J., & Pen, U., 2000, ApJ, 532, L5
16. Lee, J., & Pen, U., astro-ph/0111186
17. Mackey, J., 2001, these proceedings.
18. Mackey, J., White, M. & Kamionkowski, M., 2001, astro-ph/0106364
19. Porciani, C., Dekel, A. & Hoffman, Y., 2001, astro-ph/0105123
20. Stark, A. A., 1977, ApJ, 213, 368
21. Stebbins, A., 1996 astro-ph/9609149
22. White, S. D. M., 1984, ApJ, 286, 38

MEASURING THE FLATTENING OF DARK MATTER HALOS

Priyamvada Natarajan

Yale University Astronomy Dept., New Haven, CT 06520-8101

A new technique is proposed to measure the flattening of dark matter halos using weak gravitational lensing. The shape parameters of the mass distribution of foreground galaxies can be measured from the two-dimensional shear field derived from background galaxies using an extension of the standard galaxy-galaxy lensing scheme. Modeling galaxies using an elliptical, isothermal profile, it is demonstrated that measuring the flatness is feasible with data from the on-going Sloan Digital Sky Survey (SDSS).

1 Introduction

The fundamental parameters such as the total mass and spatial extent of dark matter galaxy halos required by observations are not well constrained. Galaxy masses are primarily probed via dynamical tracers of the galactic potential: stars in the inner-most regions, HI gas in regions outside the optical radius, and orbital motions of bound satellites in the outer-most regions (e.g. Zaritsky & White 1994). However, the implications of these studies for the precise nature and composition of halos remains unclear. Probes of halo structure at radii devoid of any luminous tracers are therefore needed – weak gravitational lensing offers precisely that.

Galaxy-galaxy lensing, the tangential alignment of the images of background galaxies around bright foreground ones, is statistically detected by stacking the contribution from many individual galaxies. This technique has been used to place constraints on halo masses and sizes. By construction the method is an effective measure of the mass at large radii, since the detected polarization signal is well outside the light distribution of the lenses. The first observational attempt to look for weak tangential alignment of faint galaxies around bright galaxies was made by Tyson et al. (1984). The inability to measure galaxy shapes with the required accuracy from photographic data precluded detection. Recent studies have, however, been more successful, and detection of a signal at the 95% confidence level was first reported by Brainerd, Blandford & Smail (1996) using deep ground-based CCD data. Several subsequent studies using Hubble Space Telescope images as well as ground-based data (Griffiths et al. 1996; Dell’Antonio & Tyson 1996; Hudson et al. 1998; Fischer et al. 2000; McKay et al. 2001: see contribution by McKay et al. these proceedings for the latest SDSS results) report unambiguous detection of a galaxy-galaxy lensing signal in field survey images.

In the method proposed here, additional information that is available but not exploited currently in galaxy-galaxy lensing studies is utilized. Using the general results derived by Schneider & Bartelmann (1997), the shear field can be related to the mass multipole moments enabling an estimate of the flatness for the mass distribution.

These parameters offer an important clue to the galaxy formation process, since they provide a quantitative measure of the importance of dissipation in the assembly of galaxies. Any variation of the flattening of the total mass (predominantly the dark matter component) with radius is a probe of the efficiency of angular momentum transfer to the dark halo and might provide insights into the structure and composition of galaxy halos.

2 Extracting shape parameters for the mass distribution

The mass distribution of a lensing galaxy is described by the convergence field $\kappa(\mathbf{x})$, defined to be the surface mass-density $\Sigma(\mathbf{x})$ expressed in units of the critical surface mass density Σ_{crit} . The critical surface mass density depends on the precise lensing configuration, i.e. on the angular diameter distances from the lens to the source D_{ls} , observer to source D_{os} and observer to lens D_{ol} . It is given by, $\Sigma_{\text{crit}} = \frac{c^2}{4\pi G} \frac{D_{\text{os}}}{D_{\text{ls}} D_{\text{ol}}}$. Standard galaxy-galaxy lensing provides a measure of the mass M within an aperture, which is given by

$$M = \int d^2x w(x)\kappa(\mathbf{x}), \quad (1)$$

where $w(x)$ is a weight function normalized so that $\int d^2x w(x) = 1$. It is chosen to be, continuous, differentiable and is required to fall-off rapidly to zero outside the aperture scale β .

The shape parameters of the mass distribution are characterized by the quadrupole moments of the convergence $\kappa(\mathbf{x})$ within the aperture (Schneider & Bartelmann 1997), which are defined as

$$Q_{ij} \equiv \int d^2x x_i x_j w(x) \kappa(\mathbf{x}), \quad (2)$$

This tensor can be decomposed into a trace-free piece Q and a trace T defined as:

$$Q = Q_{11} - Q_{22} + 2i Q_{12}, \quad T = Q_{11} + Q_{22}. \quad (3)$$

The ellipticity of the mass ϵ_κ is then simply,

$$\epsilon_\kappa = \frac{Q}{T} = \frac{(a_\kappa^2 - b_\kappa^2)}{(a_\kappa^2 + b_\kappa^2)} e^{i\varphi_\kappa}, \quad (4)$$

where a_κ and b_κ are, respectively, the major and minor axes of the mass distribution, and φ_κ is its position angle relative to the positive x -axis.

Schneider & Bartelmann (1997) have shown that the multipole moments of $\kappa(\mathbf{x})$ can be derived from the observed quantity, namely the shear $\gamma(\mathbf{x})$ field. In particular, the quadrupole moments (Eq. [3]) can be expressed as

$$Q = \int d^2x e^{2i\varphi} [g_t(x) \gamma_t(\mathbf{x}) + i g_\times(x) \gamma_\times(\mathbf{x})], \quad (5)$$

where the rotated shear components γ_t and γ_\times correspond, respectively, to a tangential and curl-type shear pattern about the center of mass of the lens (see Rhodes, Refregier & Groth 2000 for an illustration). They are related to the unrotated components by,

$$\begin{aligned} \gamma_t &= -[\cos(2\varphi)\gamma_1 + \sin(2\varphi)\gamma_2] \\ \gamma_\times &= -[-\sin(2\varphi)\gamma_1 + \cos(2\varphi)\gamma_2] \end{aligned} \quad (6)$$

where φ is the polar angle from the x -axis. The associated aperture functions $g_t(x)$ and $g_\times(x)$ are given by

$$g_t(x) = 2V_2(x) - x^2 w(x), \quad g_\times(x) = -2V_2(x), \quad (7)$$

where $V_n(x) = x^{-2} \int_0^x dx' x'^{n+1} w(x')$.

Similarly, the trace part T and the mass M can also be written as

$$T = \int d^2x g_t(x) \gamma_t(\mathbf{x}), \quad M = \int d^2x h_t(x) \gamma_t(\mathbf{x}), \quad (8)$$

where $h_t(x) = 2V_0(x) - w(x)$.

3 Application to the elliptical isothermal model

We consider an isothermal model with concentric elliptical equipotentials (Natarajan & Kneib 1996). The projected potential for this model is $\psi = \alpha r$, where α is the Einstein radius and r is a generalized elliptical radius. If the x -axis is aligned with the major axis of the potential, the generalized radius is given by $r^2 = \frac{x_1^2}{1+\epsilon} + \frac{x_2^2}{1-\epsilon}$, where ϵ is the ellipticity of the equipotentials. The Einstein radius is related to the velocity dispersion of the galaxy σ_v by $\alpha = 4\pi(\frac{\sigma_v}{c})^2(\frac{D_{ls}}{D_{os}})$, and is of the order of $1''$ for galaxies.

For a weakly elliptical model ($\epsilon \ll 1$), the potential has the form,

$$\psi(\mathbf{x}) \simeq \alpha x [1 - \frac{\epsilon}{2} \cos 2(\varphi - \varphi_0)]; \quad (9)$$

where φ_0 is the position angle of the potential, and reduces to that of a singular isothermal sphere in the circular limit ($\epsilon = 0$). We restrict our analysis to the weak regime, which is the appropriate approximation for galaxy-galaxy lensing. The associated convergence $\kappa = \nabla^2\psi/2$ is given by

$$\kappa(\mathbf{x}) = \frac{\alpha}{2x} \left[1 + \frac{3\epsilon}{2} \cos 2(\varphi - \varphi_0) \right], \quad (10)$$

and the complex shear $\gamma = \gamma_1 + i\gamma_2 = [\partial_1^2 - \partial_2^2 + 2i\partial_1\partial_2]\psi/2$ is

$$\gamma = -\frac{\alpha}{2x} \left[1 + \frac{3\epsilon}{2} \cos 2(\varphi - \varphi_0) \right] e^{2i\varphi}, \quad (11)$$

The rotated shear components are thus

$$\gamma_t = \frac{\alpha}{2x} \left[1 + \frac{3\epsilon}{2} \cos 2(\varphi - \varphi_0) \right], \quad \gamma_x = 0, \quad (12)$$

yielding a tangential shear modulated by an elliptical pattern.

We then need to relate the ellipticity of the underlying mass distribution $\kappa(\mathbf{x})$ to that of the projected (2-d) potential $\phi(\mathbf{x})$. Using a normalized gaussian as the weight function $w(x) = e^{-x^2/2\beta^2}/(2\pi\beta^2)$, we evaluate the integral for the quadrupole (Eq. [3]) and monopole (Eq. [1]) moments of $\kappa(\mathbf{x})$,

$$M = \sqrt{\frac{\pi}{8}} \frac{\alpha}{\beta}, \quad |Q| = \frac{3}{8} \sqrt{\frac{\pi}{2}} \alpha\beta\epsilon, \quad T = \sqrt{\frac{\pi}{8}} \alpha\beta \quad (13)$$

The ellipticity of the mass (Eq. [4]) is thus $\epsilon_\kappa = \frac{3\epsilon}{4}$.

4 Measuring the flattening of the mass distribution

We now show how these results can be used to measure the flattening of the mass distribution. As in ordinary galaxy-galaxy lensing, the galaxy catalog is first separated into a foreground and a background subsample, using magnitude, colors or photometric redshifts. The ellipticity of the galaxies in both subsamples is then measured in the usual fashion as is done for the sheared faint background galaxies by taking second moments of the light distribution. We align the foreground galaxies along their major axes before stacking (see Fig. 1, bottom panel for a schematic). We then measure the average ellipticity of the mass ϵ_κ as described above, by replacing the integrals in equations (5) and (8) by sums over the sheared background galaxies. This yields a measurement of the component of the average ellipticity of the mass, $\epsilon_{\kappa\parallel}$ parallel to the that of the light, i.e.

$$\epsilon_{\kappa\parallel} = \text{Re}\langle\epsilon_\kappa^*\hat{\epsilon}_l\rangle, \quad (14)$$

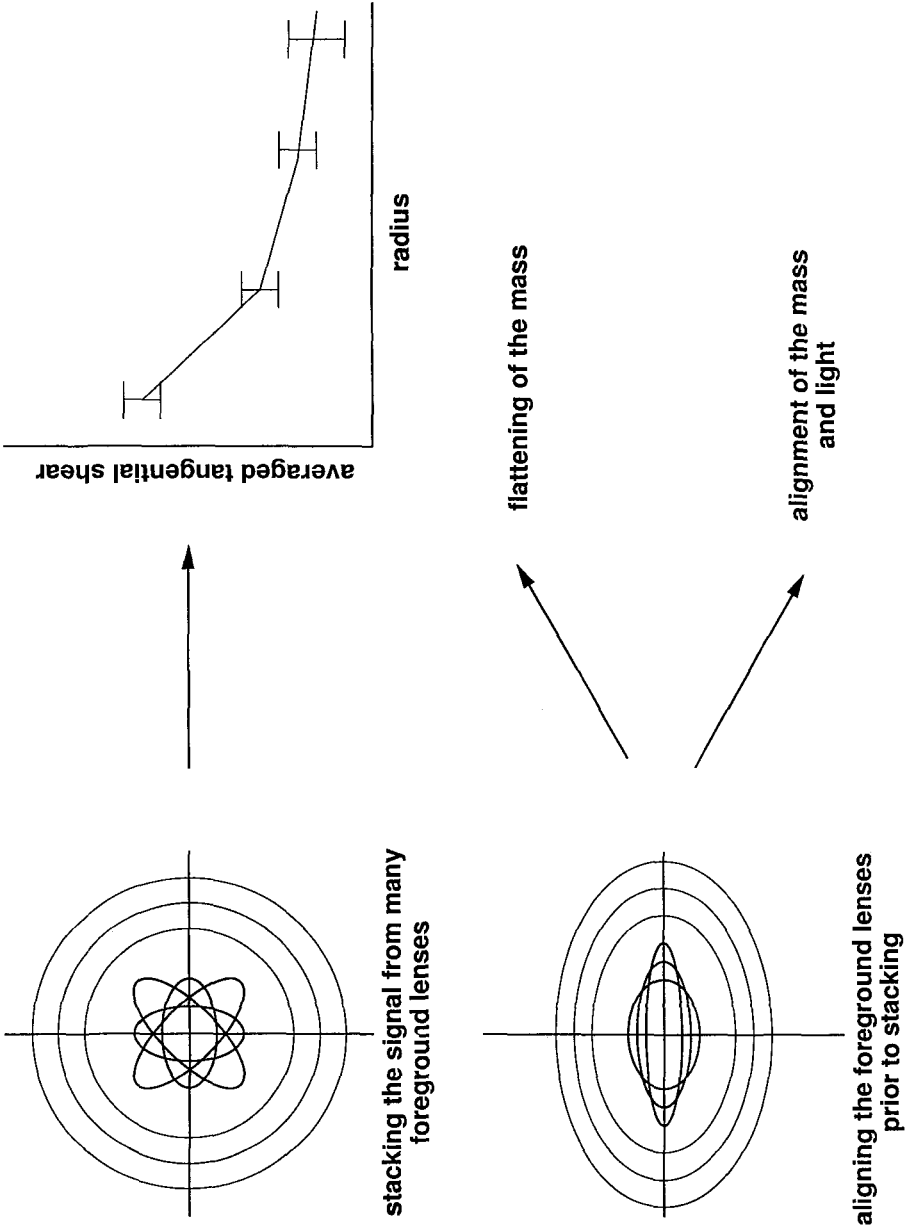


Figure 1: Schematic for determining the flattening and alignment of mass and light in galaxies statistically.

where the ellipticities are taken to be complex numbers with $\epsilon = \epsilon_1 + i\epsilon_2$, $*$ denotes complex conjugation, and $\hat{\epsilon}_l = \epsilon_l/|\epsilon_l|$ is the unit ellipticity of the light.

We then compute the uncertainty in measuring $\epsilon_{\kappa\parallel}$, by taking the square of the mean of the discrete estimators for M , T and $Q_{\parallel} = \text{Re}(Q)$, and converting back into integrals (Schneider & Bartelmann 1997). In the absence of lensing, we find

$$\begin{aligned}\sigma^2[M] &= \frac{\sigma_\epsilon^2}{n_b n_f A} \int d^2x h_r^2(x), \\ \sigma^2[T] &= \frac{\sigma_\epsilon^2}{n_b n_f A} \int d^2x g_r^2(x), \\ \sigma^2[Q_{\parallel}] &= \frac{\sigma_\epsilon^2}{2n_b n_f A} \int d^2x [g_r^2(x) + g_x^2(x)],\end{aligned}\quad (15)$$

where $\sigma_\epsilon^2 = \langle \epsilon_r^2 \rangle = \langle \epsilon_x^2 \rangle$ is the variance of the intrinsic ellipticity distribution of galaxies ($\sim 0.3^2$), n_b and n_f are respectively the number density of background and foreground galaxies, and A is the area covered by the survey.

For the elliptical isothermal model with the gaussian weight function, we can evaluate these integrals and find,

$$\begin{aligned}\sigma^2[M] &= \frac{\sigma_\epsilon^2}{4\pi n_b n_f A \beta^2}, & \sigma^2[T] &= \frac{\sigma_\epsilon^2 \beta^2}{2\pi n_b n_f A}, \\ \sigma^2[Q_{\parallel}] &= \frac{3\sigma_\epsilon^2 \beta^2}{4\pi n_b n_f A}\end{aligned}\quad (16)$$

By propagating these errors in the definition of the ellipticity of the mass (Eq. [4]), we can compute the signal to noise ratio $(S/N)_{\epsilon_\kappa} = \epsilon_{\kappa\parallel}/\sigma[\epsilon_{\kappa\parallel}]$ for measuring $\epsilon_{\kappa\parallel}$, and find, to first order in ϵ ,

$$\begin{aligned}\left(\frac{S}{N}\right)_{\epsilon_\kappa} &\simeq 4.6 \left(\frac{\epsilon_\kappa}{0.3}\right) \left(\frac{\alpha}{0.5''}\right) \left(\frac{n_b}{1.5 \text{ arcmin}^{-2}}\right)^{\frac{1}{2}} \\ &\left(\frac{n_f}{0.035 \text{ arcmin}^{-2}}\right)^{\frac{1}{2}} \left(\frac{0.3}{\sigma_\epsilon}\right) \left(\frac{A}{1000 \text{ deg}^2}\right)^{\frac{1}{2}}.\end{aligned}\quad (17)$$

In these scalings, we have used the survey specifications (ellipticity dispersion, number of foreground lenses and number of background galaxies, and approximate observed Einstein radius) quoted for the SDSS commissioning run provided in a recent preprint by McKay et al. (2001), with a modestly expanded area (1000 deg^2) from the current area of 225 deg^2 . Note that these numbers are conservative since the commissioning data suffered from very poor

seeing. The shape parameters of the mass will therefore be easily detectable with SDSS in the very near future. For the total SDSS area of 10^4 deg^2 , the significance rises to 15σ . This in fact implies that potentially, even the radial dependence of the flattening can be studied by considering annuli-shaped weight functions (for instance, the difference of two gaussians). Moreover, we will be able to study the degree of flattening as a function the morphological type of galaxies.

5 Discussion

The shapes of dark matter halos (see Sackett (1995) for a more comprehensive review) have been probed via many techniques and the consensus from these studies is that the precise shapes offer important clues to both the galaxy formation process and perhaps, even to the nature of dark matter.

Acknowledgements

My collaborator Alexandre Refregier is thanked for permission to present joint work.

References

1. Brainerd, T., Blandford, R., & Smail, I., 1996, *ApJ*, 466, 623
2. Dell' Antonio, I., & Tyson, J. A., 1996, *ApJ*, 473, L17
3. Dubinski, J., 1994, *ApJ*, 431, 617
4. Fischer, P. et al., 2000, *AJ*, 120, 1198
5. Griffiths, R. E., Casertano, S., Om, M., & Ratnatunga, K. U., 1996, *MNRAS*, 282, 1159
6. Hudson, M. J., Gwyn, S. D. J., Dahle, H., & Kaiser, N., 1998, *ApJ*, 503, 531
7. Katz, N., & Gunn, J. E., 1991, *ApJ*, 377, 365
8. Keeton, C., Kochanek, C., & Seljak, U., 1997, *ApJ*, 482, 604
9. McKay, T., et al. & the SDSS collaboration, 2001, submitted to *ApJ*, preprint astro-ph/0108013
10. Natarajan, P., & Kneib, J-P., 1996, *Proceedings of IAU 173, Astrophysical applications of Gravitational Lensing*, Melbourne, eds. Kochanek & Hewitt, p.155
11. Natarajan, P., & Refregier, A., 2000, *ApJ*, 538, L113
12. Rhodes, J., Refregier, A., & Groth, E., 2000, *ApJ*, 536, 79
13. Sackett, P., 1996, *Proc. of IAU Symp. 173, Proceedings of IAU 173, Astrophysical applications of gravitational lensing*, eds. Kochanek &

Hewitt, p.165

14. Schneider, P. & Bartelmann, M., 1997, MNRAS, 286, 696
15. Schneider, P., & Rix, H-W., 1997, ApJ, 474, 5
16. Tyson, J. A., Kochanski, G., & De'll Antonio, I. P., 1998, ApJ, 498, L107
17. Tyson, J. A., Valdes, F., Jarvis, J. F., & Mills, A. P., 1984, ApJ, 281, L59
18. Zaritsky, D., & White, S. D. M., 1994, ApJ, 435, 599

POWER SPECTRA FOR GALAXY SHAPE CORRELATIONS

Jonathan Mackey

*Harvard-Smithsonian Center for Astrophysics, 60 Garden St.,
Cambridge, MA 02138, USA*

E-mail: jmackey@cfa.harvard.edu

It has recently been argued that the observed ellipticities of galaxies may be determined at least in part by the primordial tidal gravitational field in which the galaxy formed. Long-range correlations in the tidal field could thus lead to an ellipticity-ellipticity correlation for widely separated galaxies. I present results of a calculation of the angular power spectrum of intrinsic galaxy shape correlations using a new model relating ellipticity to angular momentum. I show that for low redshift galaxy surveys, the model predicts that intrinsic correlations will dominate correlations induced by weak lensing, in good agreement with previous theoretical work and observations. The model also produces ‘*E*-mode’ correlations enhanced by a factor of 3.5 over ‘*B*-modes’ on small scales, making it harder to disentangle intrinsic correlations from weak lensing.

1 Introduction

The study of galaxy alignments has a rich history, as documented by Djorgovski⁷, although with mixed results (e.g. Cabanela & Aldering²). Recently, Lee & Pen⁹ investigated a relationship between galaxy spins and the underlying gravitational potential field with a view to reconstructing this potential. It was quickly realized that spatial correlations in the gravitational potential could induce correlations in the spins of nearby galaxies. This is interesting in its own right, but is also a potential contaminant of field-surveys for weak gravitational lensing by large scale structure.

Weak lensing shear, the coherent distortion of galaxy images on the sky induced by density perturbations along the line of sight¹¹ has now been detected by several different groups¹³. Following standard practice, all of these authors assume that all of their observed correlation in the ellipticities of galaxies comes from weak lensing. Intrinsic shape correlations, if present, should be considered when interpreting results from these field-lensing surveys.

Several authors have investigated these intrinsic galaxy shape correlations recently: with analytic arguments^{9,3,4,5,10}, using numerical simulations^{8,6}, and with observations^{12,1}. The calculation and results presented below can be found in more detail in Mackey, White & Kamionkowski¹⁰. Our calculation builds on ideas contained in Catelan, Kamionkowski & Blandford³, and uses some similar physical assumptions to Crittenden *et al.*⁴.

2 Ellipticity Model and Power Spectra Calculation

Here I briefly discuss the model and calculation. Using the same formalism as in weak lensing analyses, I describe the intrinsic ellipticity of galaxies in terms of the spin-2 (complex) ellipticity: $\epsilon = |\epsilon|e^{2i\phi} = \gamma_1 + i\gamma_2$. I assume the components γ_i of the ellipticity are determined by a galaxy's angular momentum. This makes sense in that a rotating system will become flattened perpendicular to the angular momentum vector, and will be more flattened for systems with higher angular momentum. In this case, as argued by Catelan *et al.*³, the intrinsic ellipticity is given by

$$\gamma_1 = f(L, L_z)(L_x^2 - L_y^2) \quad \text{and} \quad \gamma_2 = 2f(L, L_z)L_xL_y, \quad (1)$$

where the sky is the x - y plane, and where $f(L, L_z)$ is an unknown function which determines how ellipticity scales with the angular momentum L . I take $f(L, L_z)$ to be a constant, C , whose value must be fitted empirically to the observed rms ellipticity of galaxies. This means that $|\epsilon| \propto L^2$. Galaxies acquire angular momentum during formation by tidal torques. It can be shown¹⁴ that the angular momentum acquired to first order in the gravitational potential $\Phi(\mathbf{x})$, is $L_i \propto \epsilon_{ijk} I_{kl} \partial_l \partial_j \Phi(\mathbf{x})$, where I_{ij} is the protogalaxy's inertia tensor.

The ellipticity components γ_i can thus be calculated in terms of the gravitational potential. I then decompose the spin-2 ellipticity field into scalar (electric-type E -mode) and pseudo-scalar (magnetic-type B -mode) fields in Fourier space. This enables the construction of 3D power spectra for the ellipticities, which are convolutions over the density power spectrum. Finally, the Limber approximation is used to obtain the predicted angular power spectrum for different source galaxy distributions.

3 Results and Discussion

To demonstrate the results I use a low and a high redshift source distribution (with mean source redshifts $\langle z_{\text{src}} \rangle = 0.1$ and 1.0). The ellipticity-ellipticity angular power spectra obtained are shown in Fig. 1, along with the corresponding weak lensing prediction.

The most obvious feature in Fig. 1 is that for a low redshift survey, intrinsic correlations are expected to dominate over weak lensing, while with $\langle z_{\text{src}} \rangle = 1.0$, they are a very small contaminant to weak lensing measurements. The reasons for this are twofold: the lensing signal is proportional to the projected density which increases with survey depth, while the intrinsic signal is increasingly washed out by projection effects for deeper surveys. The predicted amplitudes are in good agreement with the calculations of Crittenden *et al.*⁴, and comparable to the observational results of Brown *et al.*¹ over angular

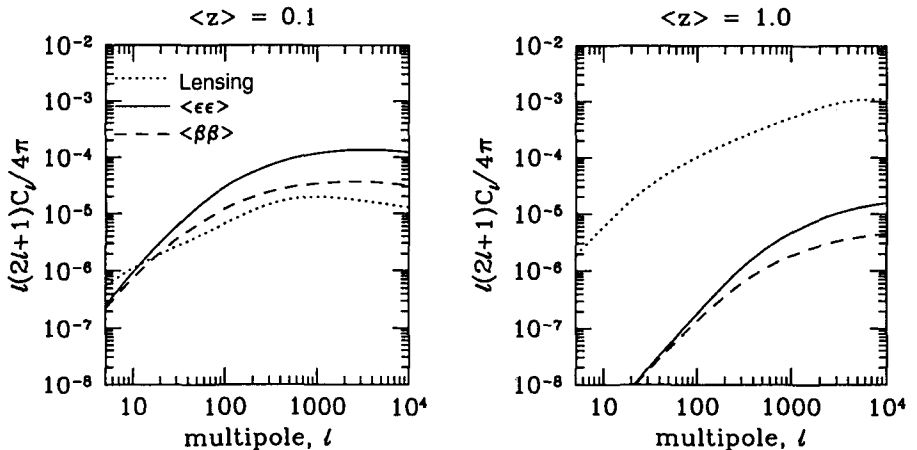


Figure 1: The angular power spectra of intrinsic shape correlations: the solid line is the EE , and the dashed line the BB intrinsic power spectrum. For comparison, the dotted line is the predicted weak lensing signal. The left panel is for a low redshift source distribution with mean $\langle z_{\text{src}} \rangle = 0.1$, and the right panel a high redshift distribution with mean $\langle z_{\text{src}} \rangle = 1.0$. For reference, $\ell \sim 200$ corresponds to an angular scale of $\theta \sim 1^\circ$.

scales from $10'$ – $100'$. They are also comparable to findings from numerical simulations^{6,8}.

The shape of the angular power spectrum reflects the shape of the underlying density power spectrum $\Delta_m^2(k)$, going roughly flat on small scales. On large scales the log-slope is 2, consistent with shot noise. The shapes of the intrinsic and lensing power spectra are quite similar, making it difficult to use this to separate the two components. A potentially better discriminant is given by the relative levels of E - and B -mode power (this was also investigated by Crittenden *et al.*⁵ in their model). Weak lensing shear has *no handedness* and can therefore produce only E -modes. Fig. 1 shows that the intrinsic power spectra have equal E - and B -mode power on large scales, but $C_l^{\epsilon\epsilon}/C_l^{\beta\beta} \simeq 3.5$ on small scales. This has two important implications for weak lensing. First, a detection of B -mode power would indicate that intrinsic correlations are present. Second, intrinsic correlations can still hide in a low signal-to-noise measurement of E -mode only power (but only up to a factor of 3.5), because of this E -mode enhancement on small scales. Thus, some caution should be used in estimating noise and contamination of weak lensing measurements solely from the level of B -mode power.

The E -mode enhancement can be understood intuitively by noting that isolated point masses can generate only E -modes. On smaller scales the density

field can be increasingly described in terms of distinct objects, giving a mostly *E*-mode signal. *B*-modes arise because the ellipticities γ_i are convolutions over the Fourier modes of the potential. It was found that large scale perturbations on the small scale potential field produce the *B*-modes.

The small scale *E*-mode enhancement is a distinctive feature of this model, and could be tested with current observational data. It is qualitatively different from that of Crittenden *et al.*⁵, who found that *E*- and *B*-modes are the same on small scales and different on large scales. The halo shapes ellipticity model of Catelan *et al.*³ is also different in that it produces only *E*-modes. Thus, the *E*-*B* decomposition is potentially a very good way to observationally distinguish between the different models of intrinsic correlations. Determining the correct model may give us new insight into galaxy formation and evolution processes, so it is important to do so.

Acknowledgments

I thank Martin White and Marc Kamionkowski for collaboration and advice on this work. Thanks especially to MW for many hours of discussion and lots of good ideas and guidance.

References

1. Brown, M. L. *et al.*, 2000, [astro-ph/0009499]
2. Cabanela J. E. & Aldering G., 1998, AJ, **116**, 1094
3. Catelan P., Kamionkowski M., Blandford R.D., 2000, MNRAS, **320**, 7
4. Crittenden, R. G. *et al.*, Natarajan, P., Pen, U., Theuns, T., 2001, ApJ, **559**, 552
5. Crittenden, R. G. *et al.*, Natarajan, P., Pen, U., Theuns, T., 2000, [astro-ph/0012336]
6. Croft R. & Metzler C., 2000, ApJ, **545**, 561.
7. Djorgovski S., 1987, in *Nearly Normal Galaxies*, (Springer, New York), p.227.
8. Heavens A., Refregier A., Heymans C., 2000, MNRAS, **319**, 649.
9. Lee J., & Pen U.-L., 2000, ApJ, **532**, L5.
10. Mackey, J., White, M., Kamionkowski, M., [astro-ph/0106364]
11. Mellier, Y., 1999, ARA&A, **37**, 127 (and references therein).
12. Pen U.-L., Lee J., Seljak U., 2000, ApJ, **543**, L107.
13. Rhodes J., Refregier A., Groth E. J., 2001, ApJ, **552**, L85 (and references therein).
14. White S. D. M., 1984, ApJ, **286**, 38.

INTRINSIC GALAXY ALIGNMENTS AND WEAK GRAVITATIONAL LENSING

A. F. Heavens

Institute for Astronomy, University of Edinburgh

Blackford Hill, Edinburgh EH9 3HJ, UK

E-mail: afh@roe.ac.uk

Gravitational lensing causes background galaxy images to become aligned, and the statistical characteristics of the image alignments can then be used to constrain the power spectrum of mass fluctuations. Analyses of gravitational lensing assume that intrinsic galaxy alignments are negligible, but if this assumption does not hold, then the interpretation of image alignments will be in error. As gravitational lensing experiments become more ambitious and seek to measure very low-level alignments arising from lensing by large-scale structure, it becomes more important to estimate the level of intrinsic alignment in the galaxy population. In this article, I review the cluster of independent theoretical studies of this issue, as well as the current observational status. Theoretically, the calculation of intrinsic alignments is by no means straightforward, but some consensus has emerged from the existing works, despite each making very different assumptions. This consensus is that

- a) intrinsic alignments are a small but non-negligible ($\lesssim 10\%$) contaminant of the lensing ellipticity correlation function, for samples with a median redshift $\bar{z} \sim 1$;
- b) intrinsic alignments dominate the signal for low-redshift samples ($\bar{z} \sim 0.1$), as expected in the SuperCOSMOS lensing survey and the Sloan Digital Sky Survey.

1 Introduction

1.1 *Lensing and galaxy shapes*

Galaxy shapes are being used increasingly as a tool in cosmology. Specifically, correlations of the orientations of galaxies on the sky, which arise as a result of gravitational lensing, can be used to measure the mass distribution in the Universe. As cosmology becomes more of a precision science, with accurate estimation of cosmological parameters possible from microwave background observations, weak lensing offers a complementary accurate method of studying the state of the cosmos. Traditional studies of large-scale structure focus on the clustering properties of galaxies, but this approach suffers from the disadvantage that galaxies may not be unbiased tracers of the mass distribution. Since it is only the mass distribution which is robustly predicted from theoretical models, it is very attractive to pursue methods which measure this distribution rather directly, without having to make assumptions about where galaxies should form in a given theoretical mass distribution.

Gravitational lensing is now established as a powerful method to measure directly the distribution of mass in the universe (e.g. Gunn 1967; Bartel-

mann & Schneider 1999 and references therein). This method is based on the measurement of the coherent distortions that lensing induces on the observed shapes of background galaxies. Recently, several groups have reported the statistical detection of weak lensing by large-scale structure (Wittman et al. 2000; van Waerbeke et al. 2000; Bacon, Refregier & Ellis 2000; Kaiser, Wilson & Luppino 2000). These detections offer remarkable prospects for precise measurements of the mass power spectrum and of cosmological parameters (e.g. Hu & Tegmark 1998).

An assumption which is made in the interpretation of alignments in galaxy images is that the directions of projected images are intrinsically uncorrelated. At first sight, this seems a reasonable assumption to make; the redshift distribution of the background galaxies is usually very broad, so most source galaxies are not physically close. However, the signal which is sought in weak lensing studies is very small, with typical ellipticity correlations of $\sim 10^{-4}$. It is by no means obvious that the intrinsic correlations will be small enough to be negligible for lensing studies.

There are sound reasons for expecting some correlations in galaxy shapes. The shapes may be determined in part by the tidal gravitational field, which will have correlations at some level, or by correlation of torques during linear evolution. Shapes may also be influenced by merger events, which may not be isotropically distributed, but influenced by filamentary or other structures.

The realization that intrinsic galaxy alignments might be important was made by a number of groups simultaneously, resulting in a number of independent studies (Heavens, Refregier & Heymans 2000, Pen, Lee & Seljak 2000, Croft & Metzler 2000, Crittenden, Natarajan, Pen & Theuns 2000, Catalan, Kamionkowski & Blandford 2001). It should be said that a calculation of intrinsic shape correlations is by no means trivial. Analytically, the problem is very difficult; numerically, it is hard to get sufficient signal-to-noise; finally, it is plausible that shapes and their correlations are at least partly determined by non-gravitational processes which are difficult to model. In summary we are far from being able to predict robustly the ellipticity distribution of galaxies.

In order to make progress, the studies have made very different simplifying assumptions in relating the density field to the ellipticities of galaxies. The remarkable outcome is, however, a level of agreement of the level of the effect which one would perhaps not have expected in advance. The conclusion of all the studies is that for a broad distribution of sources centered around $z = 1$, the alignment intrinsic in the galaxy distribution is a small but not insignificant contributor to the total expected from lensing and intrinsic effects. For a low-redshift ($z \simeq 0.1$) source population, where the intrinsic effects are larger and the lensing effect smaller, the alignment of images is dominated almost

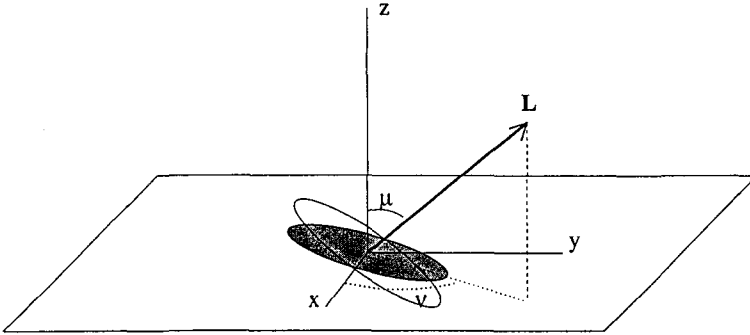


Figure 1: Simple model of a spiral galaxy. The disk of the galaxy is shown as the open ellipse, and its projection on the sky as the filled ellipse.

completely by intrinsic effects.

2 Assumptions: galaxy ellipticity

Catelan et al. (2000) assumed that the shape is determined by the linear tidal field; Mackey et al. (2001) extended this model to consider disk galaxies in more detail. Lee, Pen & Seljak (2000) and Crittenden et al. (2000) used a correlation, seen in N-body simulations between the tidal field and the moment of inertia tensor (Lee & Pen 2000). From this they determined the angular momentum vector distribution. Numerical simulations from the VIRGO consortium were analysed by Heavens et al. (2000) and Croft & Metzler (2000), with similar conclusions. Both groups investigated an ‘elliptical’ model, where the ellipticity of the visible galaxy and the halo were assumed equal. Heavens et al. also looked a ‘spiral’ model, assuming that the galaxy was a thin disk with angular momentum vector aligned with that of the halo. Given that one is seeking a very small correlation of ellipticities, it would not be very surprising if these different assumptions led to rather different answers. This turns out not to be the case.

3 Numerical simulations

I will describe here the two approaches which use numerical simulations to estimate galaxy ellipticity correlations. The articles by Rob Crittenden and Jonathan Mackey in this volume will concentrate on more analytic approaches. Both numerical papers use outputs from Virgo simulations of 17 million particles, from which halos are extracted using a friends-of-friends algorithm. El-

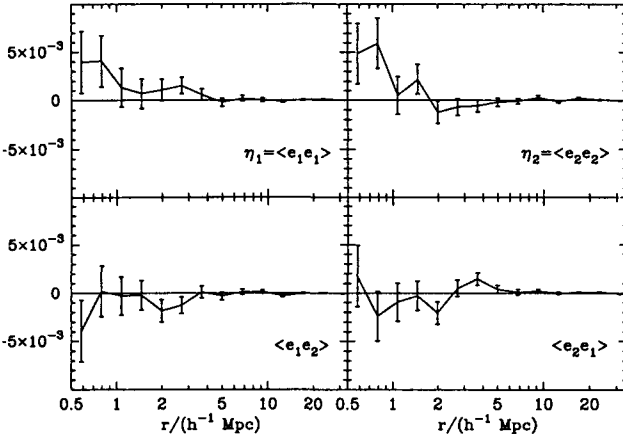


Figure 2: Three-dimensional correlation functions for ‘spirals’ in a Λ CDM model at a redshift $z = 1$.

lpticities in the spiral model are determined by the orientation of the angular momentum vector of the halo \mathbf{L} with the line of sight (see fig. 1). With the coordinate system shown in the figure, the ellipticity $e \equiv (e_1^2 + e_2^2)^{\frac{1}{2}}$ and position angle α of the projected ellipse are given by

$$e = \frac{\sin^2 \mu}{1 + \cos^2 \mu},$$

$$\alpha = \nu + \frac{\pi}{2}. \quad (1)$$

and the ellipticity is $e_i = e\{\cos 2\alpha, \sin 2\alpha\}$. Note that the observed ellipticity depends only on the orientation of \mathbf{L} , and not on its magnitude; it is also independent of the surface brightness profile, provided it depends only on radius. In some sense, e should be taken as an extreme: the average ellipticity of a randomly-oriented distribution of spirals is 0.57 - considerably larger than that observed. The ellipticity of the ‘elliptical’ models are calculated from halo quadrupole moments (Kaiser & Squires 1993). In practice, the coordinate system is rotated so that the x -axis lies along the projected separation of the galaxy pairs.

It turns out that the ellipticities based on the spiral and elliptical prescriptions are very different. The ellipticity correlation functions, however, are rather similar (fig. 3 and 2). The ellipticities themselves are typically not

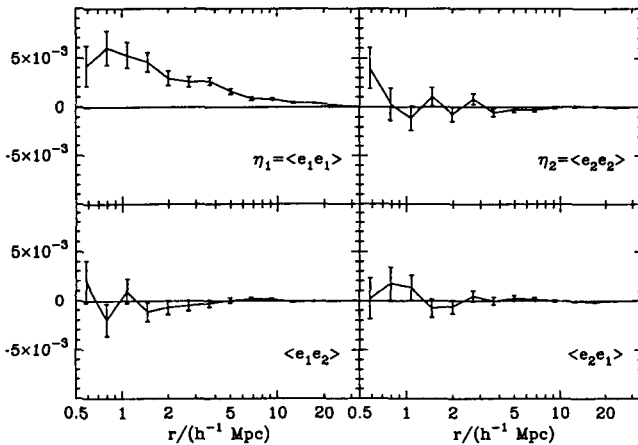


Figure 3: As fig. 2, but for ‘ellipticals’.

much less than unity, so the correlation level of $\lesssim 5 \times 10^{-3}$ is rather small; the agreement, therefore, is by no means expected.

To assess the impact on the lensing signal, the three-dimensional correlation functions are turned into two-dimensional correlations, using a modified form of Limber’s equation. Fig. 4 is typical of the results obtained for a deep survey at median redshift of unity. We see that the expected weak lensing signal (dotted) dominates, but the intrinsic signal is not entirely negligible, contributing $\sim 10\%$ of the correlation. This general conclusion has been reached by all studies.

At low redshift, the story is quite different. The lensing signal is lower as there is less mass to pass through, and the intrinsic signal is larger, because fixed angular separations translate to smaller typical physical separations. For median redshifts of order unity, as expected in SuperCOSMOS and Sloan (Gunn et al. 1995), the intrinsic effect dominates the lensing correlation by up to several orders of magnitude. This is illustrated in fig. 5, which shows the measured shear variance (which is related to the ellipticity correlation function) from the SuperCOSMOS survey, along with predictions from the various intrinsic studies (see also Pen, Lee & Seljak 2000). Although there are certainly some significant differences between the studies, all agree that on small scales the intrinsic signal should be $\sim 10^{-2}$.

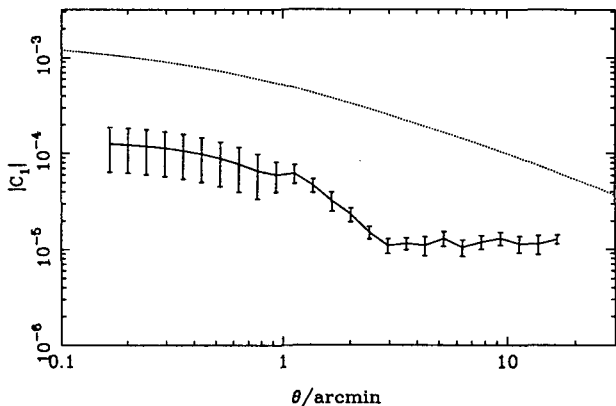


Figure 4: Intrinsic ellipticity correlation function of ‘ellipticals’, for a deep survey with median source redshift of 1, and a broad source distribution. Also shown dotted is the expected weak lensing correlation signal. We see that the lensing signal dominates for this redshift, and intrinsic effects act as a $\sim 10\%$ contaminant.

4 Discussion

I have summarized here the state of the investigations into the level of intrinsic alignment of galaxies, with a view to assessing its impact on weak gravitational lensing studies. Despite the difficulties of computing the correlation of ellipticities with confidence, several independent studies have come up with broadly similar conclusions. These are that the level of correlation is unlikely to be low enough to be ignored. For high-redshift ($z \simeq 1$) lensing samples, the intrinsic correlation, being diluted over a wide redshift range, is a small, but non-negligible ($\sim 10\%$) fraction of the correlation induced by weak lensing. At low redshifts ($z \simeq 0.1$), however, the lensing signal is smaller and the intrinsic correlation larger, to the extent that the intrinsic correlation dominates the lensing signal. This is also supported by observed correlations of galaxy shapes from the SuperCOSMOS survey (Brown et al. 2001), which shows distortions at a level far above the expected signal but broadly in line with theoretical predictions. There are some differences in the predictions for intrinsic correlations, but all agree with the above statements. It is perhaps difficult to see where the theoretical predictions could be made significantly more robust; certainly the methods based on numerical simulations would benefit by larger number of particles in each halo, and by larger volumes to improve signal-to-

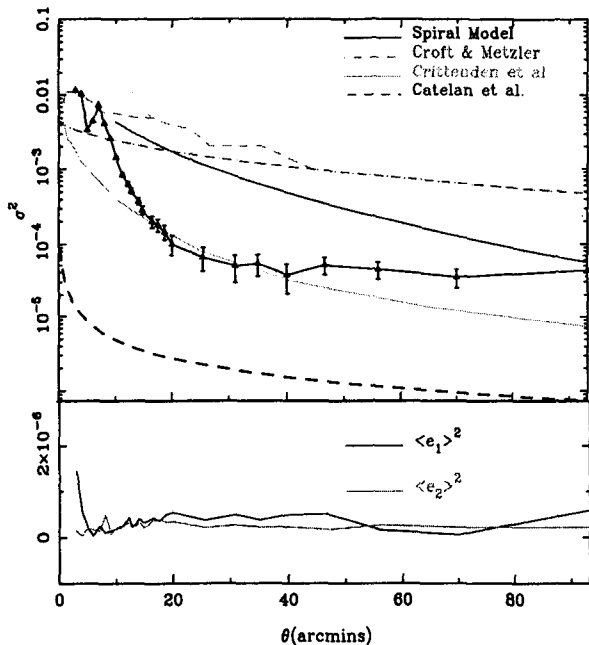


Figure 5: Shear variance estimate from the SuperCOSMOS survey (Brown et al. 2001), compared with the ‘spiral’ model of Heavens et al. (dark solid line), the elliptical model of Croft & Metzler (upper dashed), the semi-analytic model of Crittenden et al. (fainter solid), and the tidal stretch model of Catelan et al. (lower dot-dashed). The expected lensing signal is the lowest line.

noise. Analytic methods are likely to be limited by the validity or otherwise of the simplifying assumptions, and neither general method can really be expected to include non-gravitational processes reliably in the near future. Thus it is probably best to be satisfied that we know the magnitude of the effect, and therefore not attempt to do straightforward weak lensing calculations from low-redshift samples. One can try to eliminate partly the intrinsic correlation by performing a curl-gradient decomposition of the ellipticity field, since weak lensing induces only a gradient field (Crittenden et al. 2001, but see Mackey et al. 2001). Alternatively, one can sidestep the problem almost entirely; this can be done, albeit by sacrificing some signal-to-noise, by cross-correlating orientations of galaxies which are known to be distant physically, for example by using photometric redshift information.

Acknowledgments

I am grateful to my collaborators, Alexandre Refregier and Catherine Heymans, and also to Andy Taylor for the figures from the SuperCOSMOS survey. The simulations analysed in this paper were carried out using data made available by the Virgo Supercomputing Consortium (<http://star-www.dur.ac.uk/frazier/virgo/>) using computers based at the Computing Centre of the Max-Planck Society in Garching and at the Edinburgh Parallel Computing Centre. We are very grateful to Rob Smith for providing halos from the simulations.

References

1. Bacon D., Refregier A., & Ellis R. 2000, MNRAS, 318, 625
2. Bartelmann M., & Schneider P., 2001, Phys. Rep., 340, 291
3. Brown M., Taylor A.N., Hambly N., Dye S., MNRAS, in press (astro-ph/0009499)
4. Catelan P., Kamionkowski M., Blandford R.D., 2001, MNRAS, 320, 7
5. Crittenden R., Natarajan P., Pen U., & Theuns T., 2001, ApJ, 559, 552
6. Crittenden R., Natarajan P., Pen U., & Theuns T., 2001, submitted to ApJ, astro-ph/0012336
7. Croft R.A.C., Metzler C.A., 2000, ApJ, 545, 561
8. Heavens A.F., Refregier A., Heymans C.E.C., MNRAS, 319, 649
9. Gunn J.E., 1967, ApJ, 150, 737
10. Gunn J.E., Weinberg D.H., 1995, in Maddox S., Aragon-Salamanca A., eds., in Wide Field Spectroscopy and the Distant Universe, the 35th Herstmonceux Conference", p.3
11. Hu W. & Tegmark M. 1999, ApJ, 514, L65
12. Kaiser N. & Squires G. 1993, ApJ 404, 441.
13. Kaiser N., Wilson G., & Luppino G.A., 2000, submitted to ApJL, preprint astro-ph/0003338
14. Lee J., Pen U.-L., 2000, ApJ, 532, 5
15. Pen U.-L., Lee J., Seljak U., 2000, ApJ, 543, L107
16. Rhodes J., Refregier A., & Groth E., 2001, ApJ, 552, L85
17. Van Waerbeke L., et al. 2000, A&A, 358, 30
18. Wittman D.M., Tyson J.A., Kirkman D., Dell'Antonio I., & Bernstein G., 2000, Nature, 405, 143

SHAPELETS: A NEW METHOD TO MEASURE GALAXY SHAPES

A. Refregier

*Institute of Astronomy, Madingley Road, Cambridge CB3 0HA, UK;
ar@ast.cam.ac.uk*

T.-C. Chang

*Dept. of Astronomy, 550 W. 120 street, Columbia University, New York,
NY 10027, USA; tchang@astro.columbia.edu*

D. J. Bacon^a

*Institute for Astronomy, University of Edinburgh, Blackford Hill,
Edinburgh EH9 3HJ, UK; djb@roe.ac.uk*

We present a new approach to measure the shapes of galaxies, a fundamental task in observational astronomy. This approach is based on the decomposition of a galaxy image into a series of orthogonal basis functions, or ‘shapelets’. Our choice of basis functions, namely the Gauss-Hermite series, has a number of remarkable properties under distortions, convolutions and noise, which makes them particularly well suited for astrophysical applications. In particular, we describe how they can be used to measure the shear induced by weak gravitational lensing, with the precision required for upcoming surveys. We also show how shapelets can be used to reconstruct images from interferometric observations. Other application of shapelets, such as image compression, PSF deconvolution, de-projection and the study of galaxy morphology, are also briefly discussed.

1 Introduction

The measurement of galaxy shapes is a fundamental task in observational astronomy. In these proceedings, we present a new method for shape measurements described in detail in Refregier (2001). It is based on the linear decomposition of each galaxy into a series of localised basis functions with different shapes, which we call ‘Shapelets’. As a basis set, we choose the Gauss-Hermite series, whose remarkable properties make it ideal for astronomical applications. In particular, we summarise the results of Refregier & Bacon (2001) who showed how shapelets can be used to measure weak lensing, with the precision required for upcoming surveys. We also describe how shapelets can be used to reconstruct images from interferometric data, as described by Chang & Refregier (2001).

We illustrate the method using images from the Hubble Space Telescope and from the FIRST radio survey. Finally, we describe several further appli-

^aprevious address: Institute of Astronomy, Madingley Road, Cambridge CB3 0HA, UK

cations of shapelets and discuss their relevance in the context of astronomical applications requiring high precision.

2 Shapelet Method and Properties

We begin by summarising the formalism of Refregier (2001) for a description of galaxies in the Gauss-Hermite basis set. A galaxy with intensity $f(\mathbf{x})$ can be decomposed into our basis functions $B_{\mathbf{n}}(\mathbf{x}; \beta)$ as

$$f(\mathbf{x}) = \sum_{\mathbf{n}} f_{\mathbf{n}} B_{\mathbf{n}}(\mathbf{x}; \beta), \quad (1)$$

where $\mathbf{x} = (x_1, x_2)$ and $\mathbf{n} = (n_1, n_2)$. The 2-dimensional cartesian basis functions can be written as $B_{\mathbf{n}}(\mathbf{x}; \beta) = B_{n_1}(x_1; \beta) B_{n_2}(x_2; \beta)$, in terms of the 1-dimensional basis functions

$$B_n(x; \beta) \equiv \left[2^n \pi^{\frac{1}{2}} n! \beta \right]^{-\frac{1}{2}} H_n \left(\frac{x}{\beta} \right) e^{-\frac{x^2}{2\beta^2}}, \quad (2)$$

where $H_n(x)$ is a Hermite polynomial of order n . The parameter β is a characteristic scale, which is typically chosen to be close to the radius of the object. These basis functions are the eigenstates of the Quantum Harmonic Oscillator (QHO), allowing us to use the formalism developed for this problem. Similar decomposition into basis functions has been independently suggested by Bernstein & Jarvis (2001). The first few basis functions are shown in Figure 1.

Because these basis functions, or ‘shapelets’, form a complete orthonormal set, the coefficients $f_{\mathbf{n}}$ can be found using

$$f_{\mathbf{n}} = \int_{-\infty}^{\infty} d^2x f(\mathbf{x}) B_{\mathbf{n}}(\mathbf{x}; \beta). \quad (3)$$

Figure 2 shows an example of the decomposition of a galaxy in the Hubble Deep Field (Williams et al 1996). The details of the image are fully reconstructed if coefficients up to $n = 20$ are included; this decomposition thus provides an excellent and efficient description of galaxy images in practice.

The chosen basis functions have a number of remarkable properties. Firstly, they are invariant under Fourier transforms up to a scaling factor, so that

$$\tilde{B}_n(k; \beta) = i^n B_n(k; \beta^{-1}), \quad (4)$$

where tildes denote Fourier transforms. As a result, convolutions (which correspond to products in Fourier space) can be simply expressed using shapelets. Let us consider the convolution $h(x) = (f * g)(x)$ of 2 functions. Each function

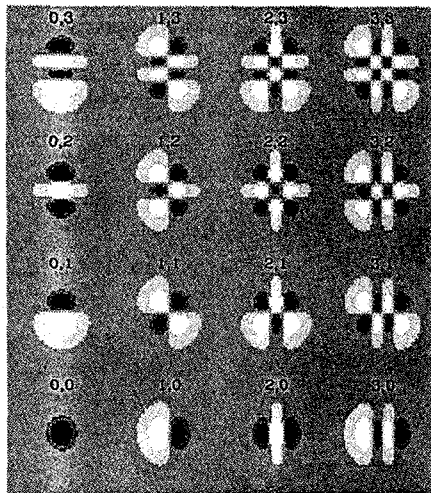


Figure 1: First few 2-dimensional Cartesian basis functions B_{n_1, n_2} . The dark and light regions correspond to positive and negative values, respectively.

can be decomposed into shapelet coefficients with scales α , β and γ , which are then related by

$$h_n = \sum_{m,l=0}^{\infty} C_{nml} f_m g_l, \quad (5)$$

where the convolution tensor $C_{nml}(\alpha, \beta, \gamma)$ can be estimated analytically using a simple recursion relation (Refregier & Bacon 2001).

Shapelets also have simple properties under coordinate transformations such as translation, dilation, rotation and shear. For instance, let us consider the distortion of an image $f(\mathbf{x})$ under the action of a weak shear γ_i , as occurs in weak gravitational lensing. To first order in the shear, the distorted image can be written as

$$f' \simeq (1 + \gamma_i \hat{S}_i) f, \quad (6)$$

where \hat{S}_i is the shear operator. It is easy to show that this operator takes a simple form in shapelet space, namely

$$\hat{S}_1 = \frac{1}{2} (\hat{a}_1^{\dagger 2} - \hat{a}_2^{\dagger 2} - \hat{a}_1^2 + \hat{a}_2^2), \quad \hat{S}_2 = \hat{a}_1^{\dagger} \hat{a}_2^{\dagger} - \hat{a}_1 \hat{a}_2, \quad (7)$$

where \hat{a}_i^{\dagger} and \hat{a}_i are the raising and lowering operators in the QHO formalism, for each dimension $i = 1, 2$. Similar operators can be constructed for the other coordinate transformations.

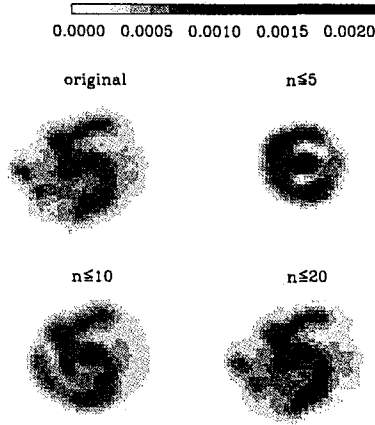


Figure 2: Decomposition of a galaxy image found in the HDF. The original 60×60 pixel HST image (upper left-hand panel) can be compared with the reconstructed images with different maximum order $n = n_1 + n_2$. The shapelet scale is chosen to be $\beta = 4$ pixels. The lower right-hand panel ($n \leq 20$) is virtually indistinguishable from the initial image.

3 Measurement of Weak Lensing

The weak distortions induced by lensing on the images of background galaxies provide a direct measure of the distribution of mass in the Universe. This weak lensing method is now routinely used to study galaxy clusters, and has recently been detected in the field (Wittman et al 2000; Bacon et al 2000; Kaiser et al 2000; Maoli et al 2001; van Waerbeke et al 2000, 2001; Rhodes et al. 2001). Because the lensing effect is only of a few percent on large scales, a precise method for measuring the shear is required. The original methods of Bonnet & Mellier (1995) and Kaiser, Squires & Broadhurst (KSB; 1995) are not sufficiently accurate and stable for the upcoming weak lensing surveys (see Bacon et al 2001, Erben et al 2001). Thus several new methods have been proposed (Kuijken 1999; Rhodes, Refregier & Groth 2000; Kaiser 2000; Bernstein & Jarvis 2001).

The remarkable properties of our basis functions make shapelets particularly well suited for providing the basis of a new method for measuring the shear (Refregier & Bacon 2001). First, the Point-Spread Function (PSF) of the instrument can be modeled by decomposing stellar images into shapelets and by interpolating the resulting coefficients across an image. Galaxy images can then themselves be decomposed into shapelet coefficients, and the analyt-

ical form of the convolution matrix (see Eq. [5]) can be used to deconvolve the Point-Spread Function. From the properties of shapelets under shears (eq. [7]), one can then construct a linear estimator for the shear from the (deconvolved) coefficients of the galaxies of the form

$$\tilde{\gamma}_{in} = \frac{f'_n - \langle f_n \rangle}{S_{inm} \langle f_m \rangle} \quad (8)$$

where f'_n are the lensed coefficients, the brackets denote an average over the unlensed galaxy population, and n is even (odd) for the γ_1 (γ_2) component of the shear. The tensor S_{inm} is the matrix representation of the shear operators of Equation (7). It is easy to show that these estimators are unbiased, i.e. that $\langle \tilde{\gamma}_{in} \rangle = \gamma_i$, if the unlensed galaxies are randomly oriented. These estimators can then be combined to construct a minimum variance global estimator for the shear over a sample of galaxies.

To test the method, we used the image simulations described in Bacon et al. (2001). These were designed to reproduce the observational conditions of ground based telescopes such as appropriate throughput, PSF and noise, along with the statistics of the galaxy population observed in HST images. An artificial shear was applied to the simulated galaxies, and the shapelet method was used on the resulting realistic images to recover the applied shear. The recovered shear values from the simulations are plotted as a function of the output shear in Figure 3. Clearly, the method is unbiased, and is found to be robust with PSF shape and size. It thus provides an improvement over the KSB method which was shown to have small but significant instabilities and biases (Bacon et al 2001; Erben et al. 2001).

4 Image reconstruction with Interferometers

Another application of shapelets is the reconstruction of images from interferometric data, as described in detail in Chang & Refregier (2001). Interferometric data are collected in the uv space, the Fourier-transform of the sky surface brightness. The observed quantity is the visibility measured for each antenna pair (i, j) at time t and at frequency ν and is given by

$$V_{ij}(\nu, t) = \int d^2l \frac{A(\mathbf{l}, \nu) f(\mathbf{l}, \nu, t)}{\sqrt{1 - |l|^2}} e^{-2\pi i[ul + vm + w(\sqrt{1 - |l|^2} - 1)]}, \quad (9)$$

where $f(\mathbf{l}, \nu, t)$ is the surface brightness of the sky at position $\mathbf{l} = (l, m)$ with respect to the phase center, and $A(\mathbf{l}, \nu)$ is the (frequency-dependent) primary beam.

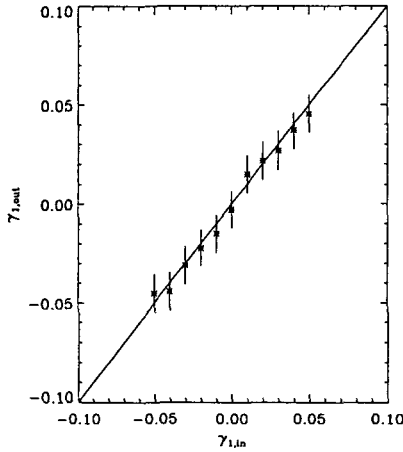


Figure 3: Input shear vs recovered shear for a set of 11 simulations. Note the linear relationship between input and recovered shear; the slope is found to be 0.97 ± 0.04 for γ_1 and 1.00 ± 0.04 for γ_2 .

In analogy with the shapelet decomposition in real space, we wish to decompose sources directly in the uv space. However, the discrete and finite sampling of the uv plane prevents a direct linear decomposition of the visibilities V_{ij} into shapelet coefficients. Instead, we simultaneously fit for the shapelet coefficients of a collection of sources on the uv plane, by using a χ^2 fit:

$$\chi^2 = (\mathbf{d} - \mathbf{M} \mathbf{f})^T \mathbf{C}^{-1} (\mathbf{d} - \mathbf{M} \mathbf{f}), \quad (10)$$

where $\mathbf{d} = \{\overline{V}_{ij}\}$ is the visibility data vector, $\mathbf{M} = \{\overline{V}_{ij}^{ns}\}$ is the theory matrix composed of visibilities corresponding to each basis function, and $\mathbf{f} = \{f_{ns}\}$ is the shapelet coefficient vector. The indices s and n stand for the source number and shapelet state, respectively. The covariance error matrix of the visibilities

$$\mathbf{C} = \text{cov}[\mathbf{d}, \mathbf{d}] = \langle (\mathbf{d} - \langle \mathbf{d} \rangle)^T (\mathbf{d} - \langle \mathbf{d} \rangle) \rangle \quad (11)$$

is provided by the interferometric hardware. The resulting χ^2 -fit is linear in its parameters and can therefore be performed by simple matrix operations. The complex effects of bandwidth smearing, time averaging and non-coplanarity of the array can be fully corrected for in the process.

As an example we consider the observing conditions of the FIRST radio survey (Becker et al. 1995; White et al. 1997). Using one of the FIRST point-

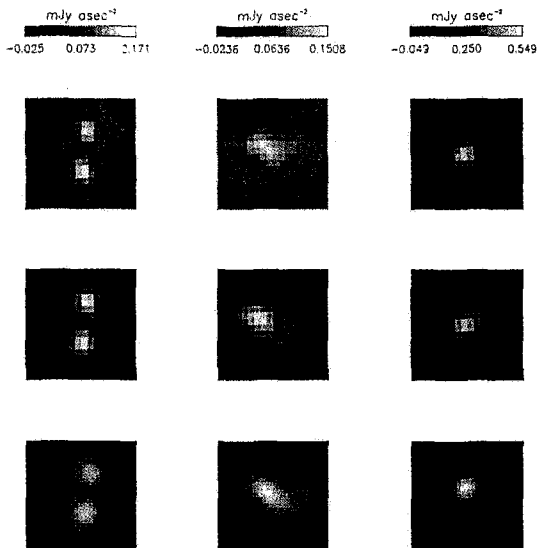


Figure 4: Reconstruction of three sources from one of the FIRST grid pointings. The 'dirty' images (which are direct inverse Fourier transformation of the data), CLEAN images, and shapelet reconstructions are shown from top to bottom, respectively. The images are $32''$ across and the resolution is about $5''.4$ (FWHM). The dirty and CLEAN images are displayed with a $1''.8$ pixel size, while the shapelet reconstruction images have $1''$ pixels. For the shapelet reconstruction, we used Wiener filtering and smoothing by a Gaussian restoring beam with a standard deviation of $2.3''$.

ings, as shown in Fig. 4, we find that our method compares well with CLEAN, the commonly used method for interferometric imaging. Our method has the advantage of being linear in the shapelet parameters, of fitting all sources simultaneously, and of providing the full covariance matrix of the coefficients, which allows us to quantify the errors and cross-talk in image shapes. It is well-suited for quantitative shape measurements which require high-precision. In particular, combining with the results from the previous section (Refregier & Bacon 2001), our results provide an accurate method for measuring weak lensing with interferometers.

5 Conclusions

Shapelets provide a new method to measure the shape of galaxies. The chosen basis functions have convenient properties under convolutions and distortions.

This makes shapelets ideally suited for the measurement of weak lensing shear, after correcting for the smearing effect of the point spread function. They can also be used to reconstruct images from interferometric data. The method is very general and is ideally suited for astrophysical applications requiring high precision. In particular, it can be used for image compression, modeling and deconvolution of the point spread function, and de-projection from 2 dimensional to 3 dimensional data. Another immediate application to explore is that of the measurement and classification galaxy morphology. Shapelets could thus help in unifying the different observational and theoretical studies of galaxy shapes presented in this volume.

Acknowledgments

We thank Richard Ellis and David Helfand for useful discussions and on-going collaboration. AR was supported by a fellowship from the EEC TMR network on gravitational lensing and by a Wolfson College Fellowship. TC was supported by NSF grant AST-98-0273. DJB was supported at the IfA by a PPARC postdoctoral fellowship.

References

1. Bacon D., Refregier A., Ellis R., 2000, MNRAS, 318, 625.
2. Bacon D., Refregier A., Clowe D., Ellis R., 2001, MNRAS, 325, 1065.
3. Becker, R.H., White, R.L., Helfand, D.J. 1995, ApJ, 450, 559
4. Bernstein G. M. & Jarvis M., 2001, accepted by AJ, astro-ph/0107431.
5. Bonnet H. & Mellier Y., 1995, A&A, 303, 331.
6. Chang T. & Refregier A., 2001, submitted to ApJ, astro-ph/0107085.
7. Erben T., van Waerbeke L., Bertin E., Mellier Y., Schnedier P., 2001, A&A, 366, 717.
8. Kaiser N., Squires G., Broadhurst T., 1995, (KSB) ApJ, 449, 460.
9. Kaiser N., 2000, ApJ, 537, 555.
10. Kaiser N., Wilson G., Luppino G. A., 2000, submitted to ApJL, preprint astro-ph/0003338.
11. Kuijken K., 1999, A&A, 352, 355.
12. Maoli R. et al, 2001, A&A, 368, 766.
13. Refregier A., 2001, submitted to MNRAS, astro-ph/0105178.
14. Refregier A. & Bacon D., 2001, submitted to MNRAS, astro-ph/0105179.
15. Rhodes J., Refregier A., Groth E. 2000, ApJ, 536, 79.
16. Rhodes J., Refregier A., Groth E. 2001, to appear in ApJL, preprint astro-ph/0101213
17. van Waerbeke L. et al, 2000, A&A, 358, 30.

18. Van Waerbeke L. et al, 2001, A&A, 374, 757.
19. White, R.L., Becker, R.H., Helfand, D.J., Gregg, M.D. 1997, ApJ, 475, 479
20. Williams R. E. et al., 1996, AJ, 112, 1335.
21. Wittman D., Tyson J. A., Kirkman D., Dell'Antonio I., Bernstein G., 2000, Nature, 405, 143.

BAYESIAN GALAXY SHAPE ESTIMATION

S. L. Bridle, J.-P. Kneib, S. Bardeau

*Laboratoire d'Astrophysique, Observatoire Midi-Pyrénées, 14 Avenue E. Belin,
31400 Toulouse, France*

S. F. Gull

*Astrophysics Group, Cavendish Laboratory, Madingley Road, Cambridge CB3 0HE,
UK*

The accurate measurement of galaxy ellipticities is vital for weak lensing studies, in particular cosmic shear. We describe a Bayesian approach to this problem in which galaxies are parameterized as sums of Gaussians, convolved with a PSF which is also a sum of Gaussians, following Kuijken (1999). We calculate the uncertainties in the output parameters using a Markov Chain Monte Carlo approach. We show that for a simple simulation, the ellipticity estimates do not give a biased result when averaged by statistical weight. It is shown that the uncertainties in the ellipticities are not increased by allowing freedom in the galaxy radial profile, or by allowing the photon shot noise level to be a free parameter. Finally we confirm the result of Kuijken (1999) that on changing the ellipticity of two point spread function Gaussian components, the reconstructed galaxy ellipticity is unbiased.

1 Introduction

The measurement of galaxy shapes from images is central to the field of weak gravitational lensing, in which the observed ellipticities of distant galaxies are used to infer properties of the intervening matter distribution. The circularizing effect of the atmosphere must be accounted for in ground based images, as well as distortions due to telescope optics, which together are called the ‘point spread function’ (PSF). In the newly developing field of ‘cosmic shear’, where the signal is extremely small and the results are being used to constrain cosmological parameters, it is particularly important to ensure that there are negligible systematic errors. The cosmic shear signal induces ellipticities of the order of 0.01, while ground based telescopes typically induce ellipticities ~ 0.05 thus accurate correction is crucial.

Galaxy shape estimation methods were first investigated by Bonnet & Mellier (1995). Today the most widely used method is that of Kaiser, Squires and Broadhurst (1995, KSB) in which the observed weighted quadrupole moments of a galaxy are modified according to the properties of stars in the image. Improvements on the KSB method have been made by Luppino & Kaiser (1997); Hoekstra et al. (1999); and Rhodes et al. (2000). Variants of the KSB method were scrutinized in the context of cosmic shear in Bacon et al. (2001) and Erben et al. (2001) who conclude that the cosmic shear results presented thus far

can be relied on, but that there are also significant limitations. For example, Bacon et al. (2001) find that the recovered shear is consistently 0.85 times the input shear and that there is a residual anti-correlation between PSF ellipticity and the corrected ellipticities of faint galaxies. Erben et al. (2001) highlight that the KSB method also breaks down for large shears ($\gamma > 0.3$).

Kaiser (2000) presented a more general approach in which more galaxies can be included in the analysis, weighted by the amount of information contained. Kuijken (1998, hereafter K98) presented a Bayesian method in which the galaxy and PSF is modeled as a sum of Gaussians and the image pixel intensities are predicted and compared to those observed. Ratnatunga, Griffiths & Ostrander (1999) have also used maximum likelihood fitting methods. Refregier and Bacon (2001) and Bernstein et al (2001) parameterize the galaxy and PSF as a sum of ‘shapelets’ which are linearly related to the gravitational shear. The approach in this paper follows that of K98, which is attractive because of its simple and intuitive galaxy parameterization. We attempt to be fully Bayesian, paying particular attention to the computation of uncertainties on the measured ellipticities, which can be used as statistical weights.

The method used to extract galaxy shape parameters from a known PSF is described in Section 2. Section 3 details the results of simulations of a single galaxy, including two tests for biases. We conclude in Section 4.

2 MCMC Gaussian parameter estimation

From the probability distribution function of the model parameter values given the data we estimate the most probable parameter values with uncertainties.

2.1 Galaxy parameterization

As in K98, galaxies are considered to be made up of sums of Gaussians. Thus the intensity as a function of position $\mathbf{x} = (x, y)$ for a galaxy is

$$B(\mathbf{x}) = \sum_i \frac{A_i}{2\pi|C_i|} e^{-(\mathbf{x}-\mathbf{x}_i)^T C_i (\mathbf{x}-\mathbf{x}_i)/2} \quad (1)$$

where the covariance matrix C can be written in terms of conventional ellipse parameters as

$$C_{1,1} = 2 \left(\frac{\cos^2(\theta)}{a^2} + \frac{\sin^2(\theta)}{b^2} \right) \quad (2)$$

$$C_{1,2} = \left(\frac{1}{b^2} - \frac{1}{a^2} \right) \sin(2\theta) \quad (3)$$

$$C_{2,2} = 2 \left(\frac{\cos^2(\theta)}{b^2} + \frac{\sin^2(\theta)}{a^2} \right) \quad (4)$$

where the covariance matrix is symmetric. In this paper we define ellipticity to be

$$e = \frac{a - b}{a + b} \quad (5)$$

and thus the elongation parallel to the x and y axes, e_+ , and the elongation along the diagonals, e_\times , are given by

$$e_+ = e \cos(2\theta) \quad (6)$$

$$e_\times = e \sin(2\theta) \quad (7)$$

Thus each Gaussian galaxy component has 6 parameters, which in this paper we consider to be the x , y position of the center; e , θ , ab and the amplitude A (see eqn. 1).

2.2 Point spread function convolution

As discussed in K98, because the galaxy is a sum of Gaussians, convolution with another sum of Gaussians is analytically simple. If the PSF is written as in eqn. 1, with m components, then the convolved galaxy may also be written as in eqn. 1 but with $n \times m$ components, the new parameters of which are

$$A_{ij} = A_i A_j \quad (8)$$

$$C_{ij} = C_j (C_j + C_i)^{-1} C_i \quad (9)$$

$$= \frac{1}{|C_j + C_i|} (|C_j| C_i + |C_i| C_j) \quad (10)$$

$$\mathbf{x}_{ij} = \mathbf{x}_i + \mathbf{x}_j. \quad (11)$$

Thus the resulting intensity as a function of position is

$$B_{\text{gal*psf}}(\mathbf{x}) = \sum_{ij} \frac{A_{ij}}{2\pi|C_{ij}|} e^{-(\mathbf{x}-\mathbf{x}_{ij})^T C_{ij} (\mathbf{x}-\mathbf{x}_{ij})/2}. \quad (12)$$

2.3 Probability estimation

Consider a small section of the image, \mathbf{D} , containing one galaxy, for example 16×16 pixels across. Assuming that the noise on each pixel is independent

and Gaussian the probability of the image given the galaxy parameters is

$$\Pr(\mathbf{D}|\mathbf{g}, \text{PSF}) = \frac{1}{\sqrt{2\pi\sigma^2}} e^{-\chi^2/2} \quad (13)$$

$$\chi^2 = \sum_{k,l} \frac{(B_{\text{gal*psf}}(\mathbf{x}_{k,l}) + b - D_{k,l})^2}{\sigma^2} \quad (14)$$

where σ is the noise level on the image and b is the background level, which are both treated as free parameters. (Note that it would be simple to switch to e.g. Poisson noise). Thus, we consider the model parameter vector \mathbf{g} to consist of $\mathbf{g} = (\sigma, b, x_1, y_1, e_1, \theta_1, ab_1, A_1, \dots, x_n, y_n, e_n, \theta_n, ab_n, A_n)$, where n is the number of Gaussian components that make up the galaxy.

Each parameter in \mathbf{g} is assigned a prior which allows the conversion to the posterior probability $\Pr(\mathbf{g}|\mathbf{D}, \text{PSF})$, where for simplicity we always assume that the PSF is known exactly. At some additional computational cost it would be possible to generalize to the case where the PSF is known with some level of uncertainty.

Some simulated data is shown in Fig. 1. The galaxy (Fig. 1a) is made up of just one Gaussian, with $e_+ = 0.2$ and $e_x = 0.1$. The PSF (Fig. 1b) is central, circular ($e = 0$), roughly the same size as the galaxy and is normalized to conserve galaxy flux. The resulting convolution is shown in Fig. 1c. A flat background level $b = 100$ and random Gaussian noise of standard deviation $\sigma = 20$ is added to produce the simulated data shown in Fig. 1d.

2.4 Markov-Chain Monte Carlo sampling

Markov-Chain Monte Carlo (MCMC) sampling is a method for estimating model parameters given a posterior probability distribution function. We use the BayeSys code of Maximum Entropy Data Consultants Ltd. (Skilling & Gull). The output of this code is a list of samples from the posterior probability distribution, \mathbf{g}_i . We do not discuss how MCMC achieves this result here, an excellent introduction to sampling methods is given in MacKay (2001). The probability distribution can be visualized by plotting points at each sample position. An example in the x, y plane is shown for a single Gaussian fit to the simulated data in Fig. 2. The number density of samples is proportional to the probability density. This figure shows that the two parameters are relatively uncorrelated, which is also found for the other parameter pairings. Perhaps not surprisingly, there is a slight degeneracy between ab and A , in which a wider, lower peaked Gaussian is degenerate with one with a narrower, higher peak.

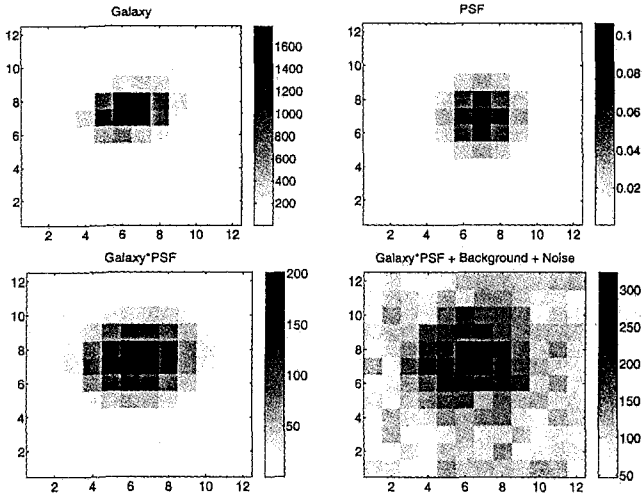


Figure 1: Simulated data.

The most probable parameter values and 68 per cent uncertainties are estimated by calculating the mean and standard deviation of the samples for each parameter. This is only strictly correct in the case that the marginal distributions are Gaussian. Otherwise this is a good indication of the uncertainty. Note that these uncertainties take into account the errors on all parameters, including the unknown x , y position of the galaxy, effectively marginalizing over them.

Note also that most probable values and uncertainties can be trivially calculated for any galaxy parameters, not just the parameterization used for the fitting. For example, e_+ for each e and θ (eqn. 7) is found by calculating e_+ for each sample, and taking the mean and standard deviation of the result, over the samples (Fig. 2 top right). Since e_+ and e_x are the quantities most closely related to the gravitational shear we focus on these two parameters in the rest of the paper.

An additional feature of this MCMC routine is that a quantity called the Evidence ($\Pr(\mathbf{D}) = \int_{\mathbf{g}} \Pr(\mathbf{D}|\mathbf{g}) \Pr(\mathbf{g})d\mathbf{g}$) is calculated during a random sampling phase of the iteration. This quantity effectively balances the goodness of fit of a model with the number of degrees of freedom, such that different parameterizations such as the number of Gaussian components may be logically decided upon.

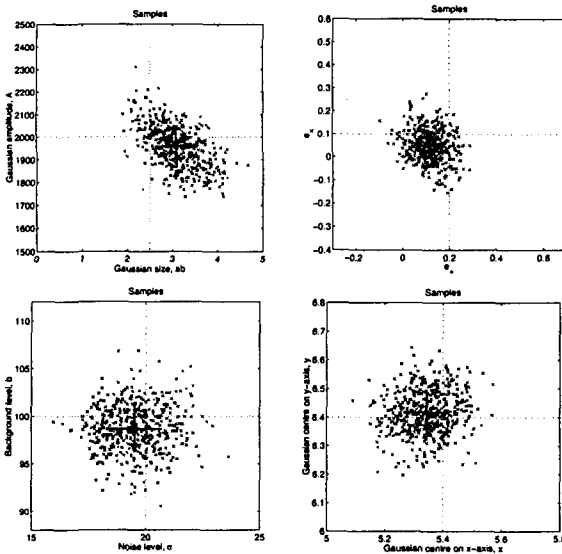


Figure 2: Samples from the posterior probability distribution.

3 Simulations

First, we consider the estimation of parameters from simulations in which the model parameters are single Gaussians for both the PSF and the galaxy.

3.1 Single Gaussian component

We use the simulation plotted in Fig. 1. The exact PSF used in the simulation is also used as an input to the galaxy parameter estimation. The parameters fitted are $\mathbf{g} = (\sigma, b, x_1, y_1, e_1, \theta_1, ab_1, A_1)$, making 8 parameters in total. For this noise realization we find $e_+ = 0.22 \pm 0.10$ and $e_x = 0.21 \pm 0.10$, compared to the true values of $e_+ = 0.20$ and $e_x = 0.10$. An important aspect of this method is that the success of the parameter estimation can be gauged by subtracting the reconstruction from the input data to make a residuals map. Statistics on this residuals map can be used to flag bad fits, e.g. in the case where two galaxies are very close, a single galaxy is not a good fit.

To assess whether these estimates with error bars are accurate approximations to the full probability distribution we perform 100 noise realizations of the same simulation, and calculate the weighted mean values of e_+ , e_x and the weighted uncertainty in the mean. After 100 noise realizations we find

$e_+ = 0.195 \pm 0.011$ and $e_x = 0.093 \pm 0.012$, there is therefore no evidence for a problem.

3.2 *Too much freedom?*

For ground based images the point spread function is adequately parameterized by one or two Gaussians (a typical Moffat profile is well approximated by the sum of two Gaussians to better than one per cent). We verify that, as discussed in K98, sums of two or three Gaussian components are adequate for exponential and de Vaucouleurs galaxy profiles, given typical galaxy sizes, CCD pixelations and PSFs. In practice we tie together the center, ellipticities and position angles of the Gaussians, although this is not required by the code. We allow complete freedom in the sizes (ab_i) and amplitudes (A_i) for each component, which has the advantage over the method of Griffiths et al. that no classification of galaxies into different types is required.

We investigate whether leaving this freedom has a significant effect on the uncertainties on the measured e_+ and e_x values. A single Gaussian was used to simulate a galaxy, and then it was reconstructed using (i) a single Gaussian and (ii) a sum of three Gaussians. Fig. 3 shows the uncertainties on e_+ and e_x as a function of galaxy luminosity for a single noise realization. The crosses are for the single Gaussian fit and the circles for the three Gaussian fit. Clearly there is very little difference. This is perhaps not surprising, given that we might expect the errors on the radial profile to be fairly uncorrelated with the errors on the ellipticity.

In contrast to K98 we keep the noise level σ as a free parameter, and estimate it from each image. The noise level is important for estimating uncertainties in e.g. e_+ and e_x , and so is not relevant in K98 where the uncertainties are not considered. The number of pixels of the image used for the fitting is likely to affect how accurately the noise level can be estimated - i.e. for a very large image we expect that the noise level can be determined much better than for a small image. Therefore we plot in Fig. 3 the results with and without the noise as a free parameter for a range of different simulated image sizes. For images greater than 8×8 , the uncertainties on e_+ and e_x are not significantly affected by allowing the noise level to be a free parameter.

3.3 *Radially varying PSF ellipticity*

In the above simulations, the PSF was circular. In this subsection we verify the results of K98, who investigate the effect of a two Gaussian component PSF in which each component has a different ellipticity. K98 find significant residuals using the KSB method and much smaller residuals using their method.

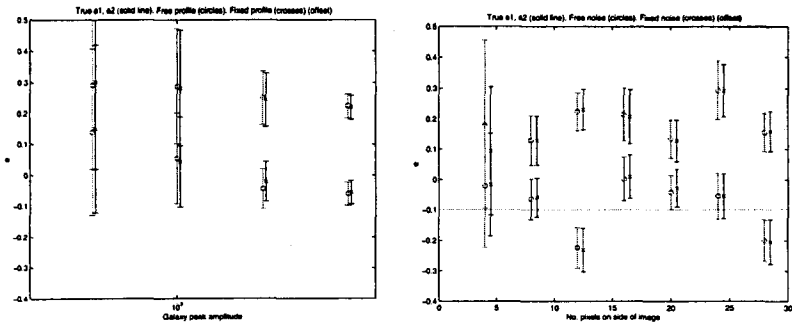


Figure 3: Left: Reconstructed ellipticity using a 3 Gaussian fit (circles), compared to the result using a 1 Gaussian fit (crosses) for a single noise realization. The simulation contains only a single Gaussian. Points are offset for clarity. The error bars are virtually unchanged on allowing more freedom in the profile. Right: Reconstructed ellipticity as a function of image size. The circles are the results when the photon noise level is a free parameter, and the crosses are obtained when the noise level is fixed at the true value (offset for clarity).

Here we simulate a circular galaxy and convolve it with a two component PSF. One component is much larger than the other, and they have opposite values of e_+ (always $e_x = 0$). The e_+ value is varied from zero to 0.5. We obtain the results shown in Fig. 4 which show that again we also have very small residuals. In fact these residuals are entirely accounted for by the errors due to the finite number of noise realizations performed. For comparison, in a very similar simulation, K98 found that KSB gave residuals of ~ 0.04 for a PSF ellipticity of ~ 0.5 .

4 Conclusions

We have presented a conceptually simple method for estimating galaxy ellipticities, with carefully calculated uncertainty estimates. This method is intrinsically designed to cope with high noise levels on the input data and naturally allows bad fits to be identified from the residuals map.

We have assumed that galaxies have an elliptical profile, which is not observed to be the case in observations of sufficient resolution. This could be addressed if the approach were extended to other parameterizations of galaxies. Most simply the galaxy could be represented by more Gaussians, each with different centers. Alternatively the parameterization of Refregier & Bacon (2001) and Bernstein et al. (2001) could be used.

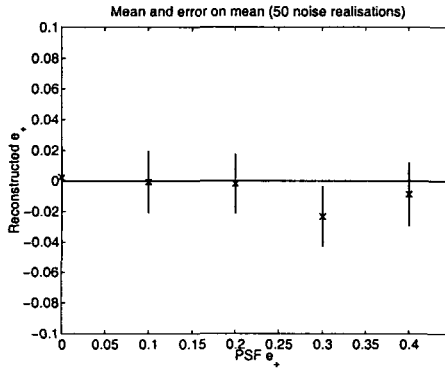


Figure 4:

Acknowledgments

SLB acknowledges financial support from the EEC TMR network ‘LENSNET’. We thank Alexandre Refregier, David Bacon, James Miskin, Oliver Czoske, Matthieu Verrani, Genyvie Soucail, and Garret Cotter for helpful discussions.

References

1. D.J. Bacon, A. Refregier, D. Clowe and R.S. Ellis, *MNRAS* **325**, 1065 (2001).
2. G.M. Bernstein and M. Jarvis, *AJ* **submitted**, (astro-ph/0107431) (2001).
3. H. Bonnet and Y. Mellier, *A&A* **303**, 331 (1995).
4. T. Erben, L. Van Waerbeke, E. Bertin, Y. Mellier and P. Schneider, *A&A* **366**, 717 (2001).
5. H. Hoekstra, M. Franx and K. Kuijken *ApJ* **532**, 88 (2000).
6. N. Kaiser, *ApJ* **537**, 555 (2001).
7. N. Kaiser, G. Squires and T. Broadhurst *ApJ* **449**, 460 (1995).
8. K. Kuijken *A&A* **352**, 355 (1999).
9. G.A. Luppino and N. Kaiser *ApJ* **475**, 20 (1997).
10. D.J.C. MacKay (2001)
<http://wol.ra.phy.cam.ac.uk/mackay/Book.html>
11. K. Ratnatunga, R. Griffiths and E. Ostrander *AJ* **118**, 86 (1999)
12. A. Refregier and D. Bacon *MNRAS* **submitted**, (astro-ph/0105179).
13. J. Rhodes, A. Refregier and E.J. Groth *ApJ* **536**, 79 (2000).

A GENERAL THEORY OF SELF GRAVITATING SYSTEMS: SHAPES OF ASTRONOMICAL OBJECTS

Simonetta Filippi

*Faculty of Engineering, University Campus Biomed., 00155 Rome, via Longoni,
83-Italy and ICRA (International Center for Relativistic Astrophysics)
E-mail: s.filippi@unicampus.it*

Alonso Sepulveda

*Department of Physics University of Antioquia, A.A. 1226, Medellin, Colombia and
ICRA
E-mail: alonso@pegasus.udea.edu.co*

Realistic self-consistent models of galaxies can be obtained by specifying the velocity field and solving the Euler equation semi-analytically. The velocity potential Ψ is introduced as the main hydrodynamic function which determines the physical quantities such as the velocity \vec{v} , the density ρ , the vorticity ζ , and the pressure p . The hydrodynamic equation is expressed in terms of the velocity potential Ψ , in order to study self gravitating equilibrium configurations parameterized by suitable velocity fields.

1 Functional method to solve Euler Equation

What is the real geometry of self-gravitating systems in equilibrium? This question is at the ground of the classical works of Chandrasekhar (1987), and of our previous papers (Filippi et al. ⁴ and references therein). Actually, starting from rotating polytropes with the polytropic index $n = 1$, new research lines for self-gravitating figures of equilibrium are determined ^{6,2,3,7}.

Here, we introduce a new analytic study of the equilibrium of self gravitating, rotating systems with a polytropic equation of state. The tools are: the Euler equation, the continuity equation, the Poisson equation, the polytropic equation of state for the rotating fluid and a non-uniform vorticity. The polytropic index is $n = 1$ and the fluid is incompressible ($\nabla \cdot \vec{v} = 0$). The reference frame rotates with a constant angular velocity $\vec{\Omega}$. Let us consider a steady state fluid with the form of limit surface $\eta(x, y, z)$ constant in time, $\eta(x, y, z) = 1$ corresponds to the boundary of the fluid in which the density $\rho|_{\eta=1} = 0$, ρ depends just on η . The surfaces $\eta(x, y, z) = \text{constant}$ are such that the Lagrangian and Eulerian derivatives vanish so that:

$$\vec{v} \cdot \nabla \eta = 0. \quad (1)$$

With $\vec{\Omega} = \Omega \hat{e}_3$ we assume

$$\hat{e}_3 \cdot \vec{v} = 0 \quad (2)$$

The eqns. (1) and (2) are simultaneously satisfied by the form of the velocity $\vec{v} = \frac{c}{2}\hat{e}_3 \times \nabla\eta$, ϕ being a functional of η .

In the incompressible case, we suppose the existence of a velocity potential \vec{h} such that $\vec{v} \equiv -\frac{c}{2}\nabla \times \vec{h}$. Using Eq. (2) we write $\vec{h} = \nabla\psi + \hat{e}_3\Psi$, where $\nabla\psi$ specifies the gauge, and the dimensionless function $\Psi = h_3 - \partial_3\psi$. The velocity field can be written as $\vec{v} = \frac{c}{2}\hat{e}_3 \times \nabla_2\Psi$ with $\nabla_2 \equiv \hat{e}_1\partial_1 + \hat{e}_2\partial_2$. The velocity profile will be determined by Ψ that contains all the relevant information including the gauges. According to Eq. (1), the surface η is a functional of Ψ and depends on an arbitrary function of z : $\eta = \eta(\Psi, g(z))$. The form of the isodensity surfaces are given by Ψ and η . The vorticity of the fluid is $\vec{\zeta} = \hat{e}_3\zeta_3 + \vec{\zeta}_2$.

2 Euler functional equations and Minimal Integrability Conditions

The Euler equation for a self-gravitating fluid in a frame rotating with a constant angular velocity $\vec{\Omega}$ and an isotropic pressure is:

$$-\frac{\nabla P}{\rho} + \nabla(\Phi + \frac{1}{2}\Omega^2(x^2 + y^2)) - \vec{v} \cdot \nabla\vec{v} - 2\vec{\Omega} \times \vec{v} = 0. \quad (3)$$

The gravitational potential Φ satisfies the Poisson equation $\nabla^2\Phi = -4\pi G\rho$. Using Ψ , we can rewrite eqn. (3) in a simpler form, convenient for further analysis. We have⁵

$$-\frac{\nabla P}{\rho} + \nabla\Phi' + \frac{C}{2}\zeta_3\nabla\Psi - \frac{C}{2}\hat{e}_3\nabla\Psi \cdot (\vec{\zeta} + 2\vec{\Omega}) = 0. \quad (4)$$

The effective potential is: $\Phi' = \Phi + \frac{1}{2}\Omega^2(x^2 + y^2) - \frac{1}{2}v^2 + C\Omega\Psi$. To establish the integrability conditions we take the curl of the eqn. (4). The Minimal Integrability Condition gives:

$$P = P(\rho), \quad \zeta_3 = \zeta_3(\Psi), \quad \nabla[\nabla\Psi \cdot (\vec{\zeta} + 2\vec{\Omega})] \times \hat{e}_3 = 0 \quad (5)$$

A barotropic pressure, the third component of the vorticity being a functional of Ψ and the third equation in (5), form the minimal integrability condition (sufficient condition). It is clear that the main hydrodynamic variables depend on Ψ : the velocity profile, the density, the pressure, the form of the surface, the third component of the vorticity. By the hydrodynamic equation (4), coupled with the integrability condition (5), the barotropic pressure $P(\rho) = \alpha\rho^k$ ($k = 1 + 1/n$) and the vorticity $\zeta_3(\Psi) = \beta\Psi^m$, the potential can be written as $\Phi' = \frac{\alpha\rho^{k-1}}{k-1} - \frac{C}{2}\frac{\beta\Psi^{m+1}}{m+1} + \text{constant}$.

By using a general and separable form for the density $\rho = \rho_0[A(\Psi) + B(\Psi)f(z) + h(z)]$, considering the polytropic index $n = 1$, we can solve the

Euler equation (4) by transforming it into a system of four differential equations for A, B, f, h . The velocity potential Ψ generates a non linear, realistic velocity field. We give an example, in polar coordinates, in the Fig. 1, generated by a velocity potential $\Psi = C_1(1 + \frac{x^2+y^2}{a^2})^p$.

By introducing a series of realistic constraints on the velocity profile of a galaxy and constraints on the integrability of the hydrodynamic equations, we demonstrate that it is possible to construct density profiles, as semi-analytical solutions of the functional Euler Equation (Ipser and Managan ², Filippi et al. ⁵).

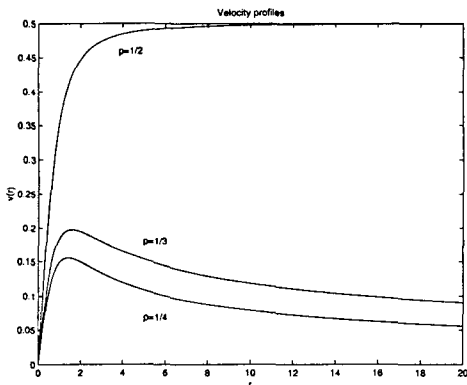


Figure 1: Velocity profiles $v(r) = \frac{C_2 p}{a^2} \frac{r}{(1+r^2/a^2)^{1-p}}$

References

1. S. Chandrasekhar in *Ellipsoidal Figures of Equilibrium*, (Dover, New York, 2d ed., 1987).
2. J. R. Ipser, and R. A. Managan, *Astroph. J.* **250**, 362 (1981).
3. K. Taniguchi, T. Nakamura, *Phys. Rev. Lett.* **84**, 581 (2000).
4. S. Filippi, R. Ruffini, A. Sepulveda, *Astroph. J.* **460**, 762 (1996).
5. S. Filippi, R. Ruffini, A. Sepulveda, *Phys. Rev. D* **in press**, 2001 (.)
6. D. Lai, F. A. Rasio, and S.L. Shapiro, *Astroph. J. Suppl.* **88**, 205 (1993).
7. P. Marronetti, and G. J. Mathews, J. R. Wilson, *Phys. Rev. D* **60**, 087301-1 (1999).

STRONG AND WEAK LENSING CONSTRAINTS ON GALAXY MASS DISTRIBUTION

Jean-Paul KNEIB

Observatoire Midi-Pyrénées, 14 Av. E.Belin, 31400 Toulouse, France

E-mail: jean-paul.kneib@ast.obs-mip.fr

Gravitational Lensing is a *unique* tool to constrain the mass distribution of collapsed structures, this is particularly true for galaxies, either on a case by case basis using multiple images of background sources (such as quasars), or statistically using the so called *galaxy-galaxy lensing* technique. First, I will present the lensing theory, and then discuss the various methods applied to current observations. Finally, I will review the bright future prospects of galaxy lensing that will benefit of the development of high resolution, large, wide and deep (lensing) surveys.

1 The Theory:

– What Do We Expect –

Although, Astrophysics is generally a question of detecting photons and making sense of them using various physical theories, Gravitational Lensing (GL) is generally a question of understanding the light paths of these photons which then allow to probe the intervening mass distribution. Thus GL must be seen as a useful tool (in a similar way as stellar dynamics) to probe the mass distribution of galaxies - objects of interest in this Conference.

1.1 Useful Gravitational Lensing Equations

A lens operates a transformation from Source plane to Image plane that is merely a simple 2D-mapping that can be describe by 3 equations relating the Source and Image properties:

1. Position:
$$\vec{\theta}_S = \vec{\theta}_I - \vec{\nabla}\varphi(\vec{\theta}_I) \quad (1)$$

this equation give the position of the source $\vec{\theta}_S$ for an image at position $\vec{\theta}_I$; φ is the lensing potential that relates to the projected Newtonian potential by: $\varphi = \frac{2}{c^2} \frac{D_{QS}}{D_{LS}} \phi^{2D}$. Furthermore, as the mapping is purely geometrical, the surface brightness of the objects are conserved through the equation: $S(\vec{\theta}_I) = S(\vec{\theta}_S)$.

2. Shape:

$$\frac{d\vec{\theta}_S}{d\vec{\theta}_I} = A^{-1} = \begin{pmatrix} 1 - \partial_{xx}\varphi(\vec{\theta}_I) & -\partial_{xy}\varphi(\vec{\theta}_I) \\ -\partial_{yx}\varphi(\vec{\theta}_I) & 1 - \partial_{yy}\varphi(\vec{\theta}_I) \end{pmatrix} \equiv \begin{pmatrix} 1 - \kappa - \gamma_1 & -\gamma_2 \\ -\gamma_2 & 1 - \kappa + \gamma_1 \end{pmatrix} \quad (2)$$

This equation defines the inverse of the amplification matrix A^{-1} at the image position $\vec{\theta}_I$. The image magnification μ is defined as: $\mu^{-1} = \det(A^{-1})$ and the reduced shear (distortion induced by the mass distribution) is $\vec{g} = \frac{\vec{\gamma}}{1-\kappa}$ where $2\kappa = \Sigma/\Sigma_{crit}$, with $\Sigma_{crit} = \frac{c^2}{4G} \frac{D_{OS}D_{OL}}{D_{LS}}$ the *critical density*. We also define the absolute shear $\bar{\gamma} = \frac{D_{OS}}{D_{LS}}\gamma$ which is independent on the redshift of the lens and the source and only depends on the mass distribution.

3. Time:
$$t_a \propto \frac{1}{2}(\vec{\theta}_S - \vec{\theta}_I)^2 - \varphi(\vec{\theta}_I) \quad (3)$$

This equation defines the arrival time of an image at position $\vec{\theta}_I$. The difference between two images gives the time-delay. Originally it was foreseen to use the time-delay to constrain the Hubble constant H_0 , but it does strongly depend on the exact mass profile and distribution. Therefore, assuming a reasonable value for H_0 , the measure of the time-delay can put strong constraints on the mass distribution, in particular in constraining the total convergence of the lens.

We will concentrate here on the determination of the mass distribution, thus assuming that we have measured the source and lens redshifts as well as determined/fixed the cosmology.

1.2 Case of a Circular Mass Distribution

All 3 equations depend on the lensing potential φ either by its gradient (position), its second derivatives (shape/amplification) or its value (time-delay). For a circular mass distribution, it is easy to show that $\partial_r\varphi = \frac{m(r)}{r}$, and that all lensing equations can be written as functions of $\frac{m(r)}{r} \propto \bar{\Sigma}(< r)$. Note that constraints are absolute in the case of multiple images but are only relative in terms of shear (galaxy-galaxy lensing) as in this case $\frac{m(r)}{r}$ can be expressed as an integral for which the limits are not always well defined [this is also true in cluster lensing and this effect is related to the *mass sheet degeneracy*].

1.3 Galaxy Mass Distributions - parametric vs. non-parametric

Parametric approaches have been favored from the beginning of lensing, as it provides simple formulae and gives analytical expressions of most or all the necessary lensing quantities. First, circular models were used like the point mass model; the singular isothermal sphere (SIS); the isothermal sphere with a core, with a truncation; the NFW model (Navarro et al 1997); and recently more general cuspy models have been proposed (Holley-Bockelmann et

al 2001). The diversity of circular models has increased to allow more freedom in the radial profile of the mass distribution, in particular following the recent developments of numerical simulations of Dark Matter halos. By changing the slope of the mass profile we can for example fix the image position but then allow a wider range of acceptable time-delay or flux-ratio between multiple images as these quantities will effectively depend on the radial profile.

Of course, circularity is not likely to be the property of galaxy mass distribution, hence the need of *elliptical mass distribution*. However only the simplest mass profiles have an analytical expression for the elliptical mass distribution. For the more complex ones (such as the NFW model or the cuspy models), either *pseudo-elliptical* models (Golse & Kneib 2001) or numerically integrated expressions have been proposed (Munoz et al 2001).

The interest of parametric expressions is their easy use, and their predictive power. Furthermore, they are usually physically motivated and thus generally dynamically stable.

The non-parametric methods have been developed in the strong lensing regime to allow more freedom in the expression of the mass distribution. In general, the mass distribution is represented as a pixelated array in the mass plane or alternatively in the potential plane; the former being generally chosen as it allows to use linear expressions (Saha & Williams 1997). Non-parametric 1D and 2D methods have been developed for cluster weak lensing, however only the 1D mass reconstruction from the weak shear profile is of interest for galaxy lensing. Although interesting, these approaches are poorly predictive and generally proposed dynamically non-stable solutions.

Both methods should be explored as their results can be complementary, however in the future we ought to develop multi-scale/multi-component modeling which will take the best of the two current competing methods.

2 Observations:

– Where Do We Fight –

Better are the observations in terms of position, shape, time-delay, better will be the constraints on the galaxy mass distribution that can be derived. However, strong and weak lensing constraints usually do not overlap, in the sense that strong lensing focus on the 1 to 10 kpc region, and the weak lensing on the 10 to 100 kpc region.

2.1 Strong Lensing: Constraints and External Shear

Because the number densities of background galaxies/quasars is small compared to the physical size of a lensing galaxies, we currently know only a small number of strong lensing systems.

For a multiple quasar system, if N is the number of multiply images observed, we thus have (as a maximum): $2(N - 1)$ constraints in position, $N - 1$ constraints in amplification, $N - 1$ constraints in time-delay. For a double system, it means a maximum of 4 constraints, but 12 for a quadruple system. Of course, external constraints are usually used, like the observed lensing galaxy center, its ellipticity and position angle (that is generally a maximum of 4). This is to compare to the description of the mass distribution of a galaxy which is represented at least by 6 or 7 parameters: $x, y, \varepsilon, \theta, \sigma_0, r_c, r_{cut}, \alpha \dots$

One can see that for double quasar the number of constraints is of the order of the number of free parameters, and that generally quadruple system are over-constrained (assuming a one clump mass model).

Of course larger number of images can arise like the 6 image B1359+154 (Rusin et al 2001) or the 10 image radio-lens B1933+503 (Cohn et al 2000), but generally they also need more complex mass distribution to be properly understood. An interesting avenue, is to detect the host galaxy of multiple quasars, indeed, the larger the number of structures identified in the host galaxy the larger the number of constraints on the mass distribution. If the host is sufficiently extended, then it will form an Einstein ring as it has been recently observed and discussed by Kochanek et al (2001). However, lensing constraints are local and thus will only shade light on the mass distribution at the location of the images. Thus ideally, we would like to observe multiple images at different radius from the galaxy center, in order to probe accurately the mass *profile*.

The current situation has enable to show that rarely a perfect fit is obtained with only one mass clump centered on the main lensing galaxy (*e.g.* Keeton, Kochanek, Seljak 1996). The simplest way to improve the fit is to introduce what is called *external shear*: a mathematical tweak of 2 parameters (the intensity γ_E and its orientation θ_E). The only, but important drawback on the use of the *external shear* is that it is not physically motivated has it has no mass. Understanding the origin of the external shear is currently an important GL question.

There is four possible origins to the external shear: 1) the main galaxy itself (by allowing the radial mass profile to change for an elliptical mass distribution) [as *e.g.* in HE2149-27, Burud et al 2001]; 2) nearby galaxies [as in most systems?]; 3) nearby group of galaxies [as *e.g.* in PG1115, in HST14176]; 4) nearby cluster of galaxies [as *e.g.* in RXJ0911, Kneib et al 2001].

The external shear contribution increases with the size of the mass perturbing the system, and decreases with its distance to the lensing system. Clearly, nearby galaxies are the most likely origin, and clusters the less likely. However because most of strong lensing galaxies are ellipticals the presence of

a nearby group or cluster is not surprising, as ellipticals are usually found in dense environments.

To gain more information on the line of sight mass contribution, deep, wide multi-color images, followed by a redshift survey of the nearby structure, or a deep X-ray observation, are needed to quantify precisely the different mass components and to explain the origin of external shear.

2.2 Galaxy-Galaxy Lensing: Scaling Laws and Recovery Methods

As massive clusters in their outskirts, foreground galaxies distort background galaxies following the weak lensing equation that reads (in the weak regime approximation): $\vec{\epsilon}_I = \vec{\epsilon}_S + \vec{g}$ where $g = \frac{\gamma}{1-\kappa} \sim \gamma$ is the reduced shear. By averaging over the (a priori) random orientation of the sources the mean ellipticity of the images equals the reduced shear: $\langle \vec{\epsilon}_I \rangle = \vec{g}$, and the dispersion of the measurements is $\sigma_g = \frac{\sigma_{\epsilon_S}}{\sqrt{N}}$. As $\sigma_{\epsilon_S} \sim 0.25$, ideally, for a 4-sigma measure the number of galaxies needed scales as $N \sim g^{-2}$. However due to the measurement errors (circularization and anisotropies of the PSF — see a number of contributions in this conference) the number of galaxies needed scales probably more as $N \sim 2 - 3 \times g^{-2}$. As we are probing regions with $g \sim 0.01$ to 0.0001 a very large amount of quality data is required.

However this simple calculations over simplify the problem, indeed galaxies have different sizes, luminosities, masses and are not at the same redshift. Using a simple approach, one can only constrain the mass of the *average galaxy* which is not exactly what we aim to learn. Therefore, it is important to use scaling laws and tune them try to understand better the mass distribution of galaxies in their diversity.

The first critical scaling is the distance. Ideally, one wants to know the redshifts of the lensing galaxies as they will allow to define their angular diameter distances, and estimate their luminosities from their broad band magnitudes. It is thus clear that any weak lensing survey with multicolor and spectroscopic informations (for the brighter galaxies) is of critical importance when we want to relate the galaxy-galaxy lensing signal to galaxy mass distribution (*e.g.* the LCRS galaxy-galaxy lensing analysis: Smith et al 2001, and the recent SDSS analysis: McKay et al 2001). Not having a spectroscopic redshift, one can alternatively used photometry redshifts or any redshift informations that can be derived from the broad-band photometry (*e.g.* the early work of Brainerd et al 1996).

The second scaling is to assume that the mass distribution can be represented by a *universal mass profile* which depends only on a very small number of parameters. The general approach first proposed by Brainerd et al.

(1996) is to scale the velocity dispersion σ and truncature radius r_{cut} of an isothermal profile with the galaxy luminosity following some general prescription like the Faber-Jackson law: $\sigma = \sigma_*(L/L_*)^{1/4}$, the Kormendy relation: $r_{cut} = r_{cut}*(L/L_*)^{0.8}$ [implying $(M/L) \propto L^{0.3}$] or assuming $(M/L) = cste$ whatever the luminosity [implying $r_{cut} = r_{cut}*(L/L_*)^{0.5}$]. Of course, this is really the simplest one can assume, the mass distribution may depend on the effective radius of the galaxy and/or its morphological type, the exponent in the scaling relations may be different that the standard ones. Furthermore, the truncated isothermal sphere may not represent the correct *universal mass profile*, hence other mass profile such as cuspy models should be investigated.

Finally, galaxy mass distribution is likely not circular. Thus, one want to relate the ellipticity of the mass to the ellipticity of the light (by reason of symmetry they should have the same orientation). Either one can assume that mass and light have the same ellipticity or one can try to understand what is the scaling law relating the 2 ellipticities.

The simplest recovering technique is what we can call the *direct averaging* where we try to estimate the mass distribution directly from the PSF corrected measured ellipticities (*e.g.* Bridle et al in this conference proceeding). Basically this means we estimate the absolute shear for a *galaxy pair* (the foreground and background galaxies separated by a distance r) at a scaled distance r/r_s (r_s is estimated from the foreground galaxy properties, such has the half-light radius, or a luminosity scaled radius) by averaging background galaxy ellipticities:

$$\bar{\gamma}(r/r_s) = \langle \frac{D_{OS}}{D_{LS}} \epsilon_I(r) \rangle$$

where the ratio of the angular distances corrects from the redshift difference from one galaxy pair to another.

Although this *direct* technique is very simple and robust, it allows only simple scaling for the mass, and the non-trivial contribution of galaxy clustering is directly included in the results, giving more an estimated of the galaxy-mass correlation function than the exact mass distribution of an average galaxy. Furthermore, 1) the mass derived from the shear γ suffers from the so-called mass sheet degeneracy hence making difficult to derive any absolute mass estimate; 2) the direct average signal is washed out by any large scale mass distribution and thus should not be applied directly in galaxy cluster fields (Natarajan & Kneib 1997).

The alternative to the *direct* approach, are *inverse* methods, such as the maximum likelihood methods presented in Schneider & Rix (1996) and Natarajan & Kneib (1997). In these methods, we consider each (background) galaxy i lensed by the nearby (foreground) galaxies. Assuming some scaling laws (see

above) one can predict the expected induced distortion on each (background) galaxy and thus compute its intrinsic ellipticity $\vec{\epsilon}_{Si}$. Then by maximizing the likelihood $L = \Pi p_S(\vec{\epsilon}_{Si})$, where p_S is the unlensed galaxy ellipticity distribution, one will be able to derive the best model that fits the observed data.

This strategy, although complex, allows to 1) probe various scaling laws, 2) test different form for the mass distribution profile, 3) use elliptical mass distribution, 4) model higher density environments like groups or clusters; thus this is the one to select specially whit good quality data which is likely to be the case for current and future surveys.

2.3 Strong and Weak Lensing: Galaxy in Clusters and Mass Evolution

It has been realized (*e.g.* Kneib et al 1996) that is is compulsory to take into account the mass distribution of galaxies in clusters to accurately model the lensing distortion. In fact as shown by Natarajan & Kneib (1997) the presence of a large scale mass distribution boost the galaxy-galaxy signal making it easier to detect if one used an adequate method. This is opening prospects to try to understand how the mass distribution is (re)distributed from small scale to large scale as a function of time and local density. Such results will be of great interest and will be important to compare to numerical simulations. Such results are just coming along (Natarajan et al 2000) and are likely to be of great interest with the development of weak lensing surveys.

3 The Future:

– How Will We Do –

To better understand the higher mass densities of galaxies, we will need to enlarge the number multiple image systems. This will come either by current facilities - for example searching for small separation multiple quasars in the new quasar surveys (SDSS, 2dF) or by future surveys (ACS/SNAP/NGST/radio). When we have increased the number of systems from the current ~ 30 to more than one thousand, we should be able to probe accurately the galaxy mass distribution *vs.* galaxy type, environment and redshift. We also need to better constrain the current multiple image systems, this is possible by probing more accurately the line-of-sight mass distribution (origin of the external shear, measure of the time-delay, accurate redshifts) and by applying strong+weak lensing techniques.

Galaxy-galaxy lensing is likely to become sort of an *industry* with the developments of high quality imaging and spectroscopic surveys and will allow to test the various scaling laws and possible *universal* mass distribution. When applied to cluster survey, galaxy-galaxy lensing will allow to test the stripping

efficiency on galaxy scale in higher densities environment. A possible interesting avenue, will also to conduct quasar-galaxy lensing survey to probe the weight of QSOs and their hosts and compare this results to *normal* galaxy mass distribution.

In short, there are good prospects to learn more on galaxy mass distribution (baryonic and dark matter) in the near future!

Acknowledgments

I thank Priya and the LOC for organizing this very useful conference. I acknowledge support from INSU-CNRS, and from EU through the research network *LENSNET* [<http://webast.ast.obs-mip.fr/lensnet>].

References

1. Brainerd, T. G., Blandford, R. D., & Smail, I. 1996, *ApJ*, 466, 623
2. Bridle et al 2001, this conference
3. Burud et al 2001, *A&A*, in press
4. Cohn, J. D., Kochanek, C. S., McLeod, B. A., & Keeton, C. R. 2001, *ApJ*, 554, 1216
5. Holley-Bockelmann, K., Mihos, J. C., Sigurdsson, S., & Hernquist, L. 2001, *ApJ*, 549, 862
6. Golse & Kneib, 2002, *A&A*, submitted
7. Kneib, J.-P., Ellis, R. S., Smail, I., Couch, W. J., & Sharples, R. M. 1996, *ApJ*, 471, 643
8. Kneib, J., Cohen, J. G., & Hjorth, J. 2000, *ApJL*, 544, L35
9. Kochanek, C. S., Keeton, C. R., & McLeod, B. A. 2001, *ApJ*, 547, 50
10. McKay et al 2001, *ApJ*, submitted, astro-ph/0108013
11. Muñoz, J. A., Kochanek, C. S., & Keeton, C. R. 2001, *ApJ*, 558, 657
12. Natarajan, P. & Kneib, J. 1997, *MNRAS*, 287, 833
13. Natarajan et al 2000, in "Gravitational Lensing: Recent Progress and Future Goals", Boston University, July 1999, ed. T.G. Brainerd and C.S. Kochanek, astro-ph/9909349
14. Rusin, D. et al. 2001, *ApJ*, 557, 594
15. Saha, P. & Williams, L. L. R. 1997, *MNRAS*, 292, 148
16. Smith, D. R., Bernstein, G. M., Fischer, P., & Jarvis, M. 2001, *ApJ*, 551, 643

EARLY-TYPE HALO MASSES FROM GALAXY-GALAXY LENSING

Gillian Wilson

Physics Department, Brown University, 182 Hope Street, Providence, RI 02912
E-mail: gillian@het.brown.edu

Nick Kaiser, Gerard A. Luppino and Lennox L. Cowie

Institute for Astronomy, University of Hawaii, 2680 Woodlawn Drive, Honolulu, HI 96822

We present measurements of the extended dark halo profiles of bright early-type galaxies at redshifts $0.1 < z < 0.9$ obtained via galaxy-galaxy lensing analysis of images taken at the CFHT using the UH8K CCD mosaic camera. Six 0.5×0.5 degree fields were observed for a total of 2 hours each in I and V , resulting in catalogs containing ~ 20000 galaxies per field. We used $V-I$ color and I magnitude to select bright early-type galaxies as the lens galaxies, yielding a sample of massive lenses with fairly well determined redshifts and absolute magnitudes $M \sim M_* \pm 1$. We paired these with faint galaxies lying at angular distances $20'' < \theta < 60''$, corresponding to physical radii of $26 < r < 77h^{-1}$ kpc ($z = 0.1$) and $105 < r < 315h^{-1}$ kpc ($z = 0.9$), and computed the mean tangential shear $\gamma_T(\theta)$ of the faint galaxies. The shear falls off with radius roughly as $\gamma_T \propto 1/\theta$ as expected for flat rotation curve halos. The shear values were weighted in proportion to the square root of the luminosity of the lens galaxy. Our results give a value for the average mean rotation velocity of an L_* galaxy halo at $r \sim 50 - 200h^{-1}$ kpc of $v_* = 238^{+27}_{-30}$ km s $^{-1}$ for a flat lambda ($\Omega_{m0} = 0.3, \Omega_{\lambda 0} = 0.7$) cosmology ($v_* = 269^{+34}_{-39}$ km s $^{-1}$ for Einstein-de Sitter), and with little evidence for evolution with redshift. We find a mass-to-light ratio of $M/L_B \simeq 121 \pm 28h(r/100h^{-1} \text{ kpc})$ (for L_* galaxies) and these halos constitute $\Omega \simeq 0.04 \pm 0.01(r/100h^{-1} \text{ kpc})$ of closure density.

1 Introduction

Galaxy-galaxy lensing (the distortion of shapes of typically faint background galaxies seen near typically brighter foreground galaxies) offers a clean probe of the dark matter halo around galaxies. Here we shall restrict attention to smaller scales where it is reasonable to interpret the results as probing relatively stable and virialized halos of individual galaxies. Clusters of galaxies have traditionally been the primary target of weak lensing studies. Individual galaxy masses are far more difficult to measure due to their being less massive and hence yielding a smaller lensing signal relative to the noise. However, by stacking pairs of galaxies it is possible to beat down the noise and measure the total average halo mass (characterized here by rotation velocity).

2 The data and galaxy samples

2.1 Data Acquisition and Reduction

The data were taken at the 3.6m CFHT telescope using the 8192×8192 pixel UH8K camera at prime focus. The field of view of this camera is $\sim 30'$ with pixel size $0.207''$. Six pointings were acquired as part of an ongoing project whose principle aim is to investigate the cosmic shear pattern caused by gravitational lensing from the large-scale structure of the Universe. This article is based on the second in a series of papers describing results from that project and focuses on properties of massive galaxy halos at radii of $20'' < \theta < 60''$ or $50 - 200h^{-1}$ kpc (Wilson, Kaiser, Luppino & Cowie² [Paper II]). Kaiser, Wilson and Luppino¹ [Paper I] presented estimates of cosmic shear variance on $2' - 30'$ scales, and Wilson, Kaiser & Luppino³ [Paper III] investigated the distribution of mass and light on galaxy group and cluster scales.

2.2 Lens and Source Galaxy Samples

Our analysis differed from other groups in that we used $V - I$ color to select a sample of bright early-type lens galaxies with reasonably well determined redshifts. As shown in § 2.2 of Paper II, with fluxes in 2 passbands and a judicious cut in red flux, one can reliably select bright early type galaxies and assign them approximate redshifts.

To investigate the evolution of halo mass with redshift, the lenses were firstly subdivided into three slices of width $dz = 0.3$ centered on redshifts 0.2, 0.5 and 0.8 (Table 1). Secondly, a wider slice of width $dz = 0.5$ centered on redshift 0.5 was analyzed.

3 Galaxy dark matter halo masses

3.1 Observed Tangential Shear Signal

For each lens, the mean tangential shear of faint ‘source’ galaxies averaged over lens-source pairs binned by angular separation is given by

$$\gamma_T(\theta) = - \frac{\sum_{\text{pairs}} W_l W_s M_{\alpha ij} \theta_i \theta_j \hat{\gamma}_\alpha / \theta^2}{\sum_{\text{pairs}} W_l W_s} \quad (1)$$

where $\hat{\gamma}_\alpha$, for $\alpha = 1, 2$, is the shear estimate for the source galaxy, θ is the projected angular separation of the lens and source, W_l , W_s are weights for

the lens and source, and the two constant matrices M_1, M_2 are

$$M_{1lm} \equiv \begin{bmatrix} 1 & 0 \\ 0 & -1 \end{bmatrix}, \quad M_{2lm} \equiv \begin{bmatrix} 0 & 1 \\ 1 & 0 \end{bmatrix}. \quad (2)$$

However, not all lens galaxies will contribute equally to the shear signal. To optimize the signal to noise, the shear contribution from each lens-source pair should be weighted by the mass of the lens. We assume here that the Faber-Jackson relation ($M \propto \sqrt{L}$) continues to larger radii and weight each lens accordingly. At each redshift, the resultant mean tangential shear signal falls off with radius roughly as $\gamma_T \propto 1/\theta$, as expected for flat rotation curve halos.

3.2 Inferred Rotation Velocity

For a mass distribution with a flat rotation curve, the shear is given by

$$\gamma_T(\theta) = \pi(v/c)^2 \langle \beta(z_l) \rangle / \theta \quad (3)$$

This equation allows one to convert between measured shear values and an equivalent rotation velocity (the dimensionless quantity $\langle \beta(z_l) \rangle$ is calculated, assuming a source galaxy redshift distribution based on spectroscopic data from Len Cowie's ongoing Hawaii Deep Fields Survey).

As a result of the magnitude cut discussed in § 2.2 the inferred rotation velocity is for some effective luminosity L_{eff} galaxy. The equivalent mean rotation velocity, v_* , for an L_* lens galaxy is computed using $v_*^2 = v^2 / (L_{\text{eff}}/L_*)^{1/2}$.

Column 2 of Table 1 shows v_* at each redshift for a flat lambda ($\Omega_{m0} = 0.3, \Omega_{\lambda0} = 0.7$) cosmology. We obtained values of $v_* = 255_{-42}^{+36} \text{ km s}^{-1}$ for $z = 0.2 \pm 0.15$, 253_{-35}^{+30} for $z = 0.5 \pm 0.15$, and 228_{-70}^{+53} for $z = 0.8 \pm 0.15$. Thus, it appears that there is little evolution in the mass of dark matter halos with redshift. We then binned the signal for lens galaxies between $z = 0.25$ and $z = 0.75$ and concluded a rotation velocity of $v_* = 238_{-30}^{+27}$ for $z = 0.5 \pm 0.25$.

For comparison, column 3 again shows v_* but for an Einstein-de Sitter cosmology. The inferred rotation velocity increases to $v_* = 275_{-50}^{+42}$, 285_{-44}^{+38} and 278_{-85}^{+65} for the same three intervals. The increase in v_* in such a universe is primarily caused by smaller $\langle \beta \rangle$ values. We would conclude an overall rotation velocity of $v_* = 269_{-39}^{+34} \text{ km s}^{-1}$ for $z = 0.5 \pm 0.25$ in this cosmology.

3.3 M/L and Contribution to Ω_0

An L_* galaxy halo with $v_* = 238 \text{ km s}^{-1}$ contains $1.31 \times 10^{12} (r/100 h^{-1} \text{ kpc}) h^{-1} M_\odot$ within a radius of r (since $M(r) = v_*^2 r / G$). An L_* galaxy has a luminosity of $1.09 \times 10^{10} h^{-2} L_B^B$, so the mass to light ratio is $M/L_B = 121 \pm$

Table 1: Rotation velocity, v_* , of an L_* galaxy as a function of redshift and cosmology.

Lens Redshift	$\Omega_{m0} = 0.3$	$\Omega_{m0} = 1.0$
	$\Omega_{\lambda 0} = 0.7$	$\Omega_{\lambda 0} = 0.0$
	v_* in km s $^{-1}$	
0.2 ± 0.15	255^{+36}_{-42}	275^{+42}_{-50}
0.5 ± 0.15	253^{+30}_{-35}	285^{+38}_{-44}
0.8 ± 0.15	228^{+53}_{-70}	278^{+65}_{-85}
0.5 ± 0.25	238^{+27}_{-30}	269^{+34}_{-39}

$28h(r/100h^{-1} \text{ kpc})$, or about $M/L_B \sim 250h$ at the outermost points we can reliably measure.

The contribution of these early-type halos to the total density of the Universe (again assuming that $M \propto \sqrt{L}$, so $M(r) = M_*(r)\sqrt{L/L_*}$) is then $\rho = M_*(r) \int dL \phi_E(L) \sqrt{L/L_*} = M_*(r) \phi_{E*} \Gamma(\alpha + 3/2)$. These early-type halos constitute $\Omega = 0.04 \pm 0.01(r/100h^{-1} \text{ kpc})$ of the closure density.

4 Conclusions

We used colors and magnitudes to cleanly select bright early-type galaxies. By measuring a weighted mean tangential shear which decreased roughly as $1/\theta$ we concluded that early-type galaxies have approximately flat rotation curve halos extending out to several hundred h^{-1} kpc. By assuming a $M \propto \sqrt{L}$ relationship we inferred a rotation velocity for an L_* galaxy of $v_* = 238^{+27}_{-30} \text{ km s}^{-1}$ for $\Omega_0 = 0.3, \lambda_0 = 0.7$ ($v_* = 269^{+34}_{-39} \text{ km s}^{-1}$ for Einstein-de Sitter). We sub-divided the galaxies and found little evidence for evolution with redshift. Finally, we determined a mass-to-light ratio for early-type halos of $M/L_B = 121 \pm 28h(r/100h^{-1} \text{ kpc})$ (for L_* galaxies) and found that these halos constitute $\Omega \simeq 0.04 \pm 0.01(r/100h^{-1} \text{ kpc})$ of the closure density.

References

1. Kaiser, N., Wilson, G., & Luppino, G. 2001, paper I, cosmic shear paper, ApJL, in press, (astro-ph/0003338)
2. Wilson, G., Kaiser, N., Luppino, G., & Cowie, L. L. 2001, paper II, galaxy-galaxy paper, ApJ, 555, 572
3. Wilson, G., Kaiser, N., & Luppino, G. 2001, paper III, mass and light paper, ApJ, 556, 601

MASS FOLLOWS LIGHT

C.S. Kochanek

Center for Astrophysics, MS-51

60 Garden St., Cambridge, MA 02138, USA

E-mail: ckochanek@cfa.harvard.edu

We use comparisons between the shapes of gravitational lens galaxies and models for their mass distributions to derive statistical constraints on the alignment of the mass distribution relative to the observed lens galaxy and on the strength of tidal shear perturbations. The mass distributions are aligned with the luminous galaxies, with a $(\Delta\theta^2)^{1/2} < 10^\circ$ upper limit on the dispersion in the angle between the major axes. Statistical constraints, such as our bound on the misalignment between mass and light, are an important new approach to reducing the uncertainties in individual lens models, particularly for lenses used to estimate the Hubble constant.

1 Introduction

The shape of the dark matter halo surrounding a luminous galaxy is a powerful means of exploring the mutual interactions of the two components. Pure dark matter halos tend to be flattened and triaxial (e.g. Bardeen et al. 1986; Frenk et al. 1988, Dubinski & Carlberg 1991, Warren et al. 1992, also Bullock, Moore, and Navarro in these proceedings), but the shape is then modified by interactions with the cooling baryons which reduce the triaxiality and the axis ratios (e.g. Evrard et al. 1994, Dubinski 1994). Many lines of observational evidence indicate that luminous galaxies are nearly oblate (see the review by Sackett 1999). While the halos of disk galaxies are rounder than the stellar distribution, Buote & Canizares (1996, 1997, 1998) typically found that the flattening of the X-ray isophotes of elliptical galaxies implied a mass distribution flatter than the luminous galaxy.

The over 60 known gravitational lenses provide a newer laboratory for comparing the mass and the light. Both the projected mass enclosed by the Einstein ring and the projected quadrupole of the gravitational field at the ring are accurately measured with little dependence on the details of the model (see Kochanek 1991, Wambsganss & Paczynski 1994, Witt & Mao 1997). The lensed images are typically 1-1.5 effective radii from the center of the lens galaxy where the quadrupole will have significant contributions from both the luminous galaxy and the dark matter halo. Even interior to the Einstein ring, there is a significant contribution of the dark matter to the enclosed mass (about half) and the matter inside and outside the Einstein ring make comparable contributions to the overall quadrupole. Thus, by comparing the gravitational field to the luminous lens galaxy we can determine whether the

mass and the light are aligned and whether they have similar shapes. Keeton et al. (1998) presented a preliminary case for alignment but found little evidence for a correlation in the axis ratios.

On a practical level, modeling uncertainties for gravitational lenses could be considerably reduced if the shape and orientation of the lens galaxy could be used to constrain the mass distribution. CMB anisotropy models have strong degeneracies between many cosmological parameters and the Hubble constant (e.g. Eisenstein, Hu & Tegmark 1998), increasing the need for precise, independent determinations of the Hubble constant. It is unlikely that the local distance ladder (e.g. Mould et al. 2000) will exceed 10% accuracy, so it is important to find new methods for measuring H_0 . The most promising new approach is to use time delay measurements in gravitational lenses. There are 9 lenses with time delay measurements (see Schechter 2000), although many still have large uncertainties in the delays. However, once the delay errors are negligible, the only important sources of uncertainty in the estimates of the Hubble constant are the systematic errors in the lens models needed to interpret the delays. These systematic errors arise from the paucity of constraints on the models of most lenses compared to the number of parameters necessary for realistic mass models which include our uncertainties about the structure of galaxies. We can obtain more constraints either by finding additional lensed structures, particularly Einstein ring images of the source's host galaxy (see Kochanek et al. 2001), by using the observed properties of the lens galaxy as constraints on the mass distribution, or by using the lens sample as a whole to derive statistical constraints on the mass distribution.

The radial distribution of the dark matter clearly differs from that of the luminous lens galaxy, as constant mass-to-light ratio (M/L) models for lenses generally work poorly (e.g. Lehar et al. 2000, Keeton et al. 2000, Cohn et al. 2001). We may, however, be able to use the shape of the luminosity distribution, the orientation of its major axis and its axis ratio, as a constraint on the shape of the mass distribution. We must, however, have clear experimental evidence for such a correlation. In §2 we examine the alignment of the mass with the light using simple statistical methods. In §3 we discuss statistical lens constraints in general, and in §4 we summarize our conclusions.

2 The Alignment of Mass and Light

We selected 20 lenses from the CfA-Arizona Space Telescope Lens Survey (CASTLES, Falco et al. 2000) based on two criteria. First, the HST data had to be of sufficient quality to determine the ellipticity and orientation of the primary lens galaxy. Second, there should be a single dominant lens galaxy.

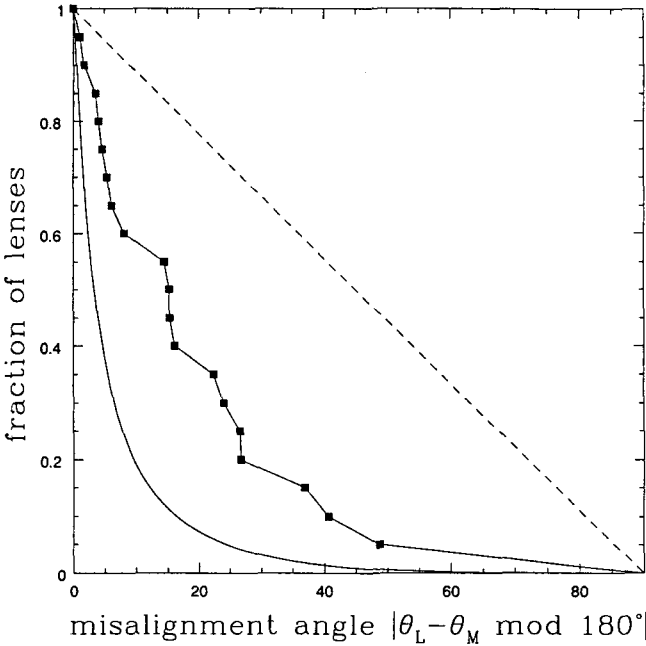


Figure 1: The misalignment angle distribution. The curve connecting the points shows the distribution for the lens sample. The solid (dashed) curve shows the expected distribution if the properties of the mass and the light are perfectly correlated (random).

The HST images were fit with photometric models including the lensed images and the lens galaxy following the procedures outlined in Lehar et al. (2000). We also modeled each lens as a singular isothermal ellipsoid (SIE) and determined the best fit model axis ratios, orientations and their uncertainties.

We can measure the misalignment between the luminous lens galaxies and the SIE models by the misalignment angle $\Delta\theta = |(\theta_L - \theta_M) \bmod 180^\circ|$ where θ_L and θ_M are the major axis position angles of the galaxy and the model with $0^\circ \leq \Delta\theta \leq 90^\circ$. If the two angles were uncorrelated, then the integral distribution would be linear, with $P(> \Delta\theta) = 1 - (\Delta\theta/90^\circ)$. If the two angles were perfectly correlated, we would still see a finite width distribution because of the uncertainties in estimating both θ_L and θ_M . If the uncertainty in measuring $\Delta\theta$ is $\sigma \ll 90^\circ$, then we would expect $P(> \Delta\theta) = \text{Erfc}(\Delta\theta/\sqrt{2}\sigma)$ where $\text{Erfc}(x)$ is the complementary error function. Fig. 1 shows that the observed distribution of misalignment angles matches neither the random nor the cor-

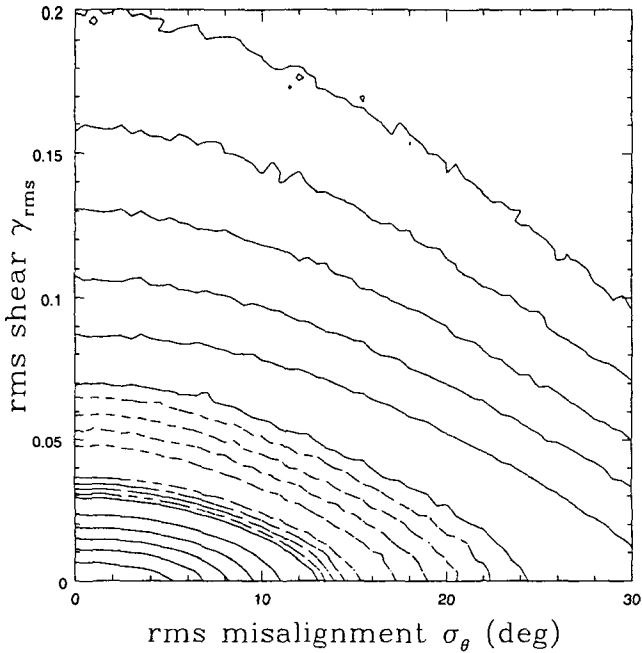


Figure 2: Logarithmic contours of the Kolmogorov-Smirnov test probabilities for matching the observed misalignment angle distribution as a function of the rms misalignment σ_θ and the tidal shear γ_{rms} . We expect tidal shears of $\gamma_{rms} \simeq 0.06$. The solid contours are logarithmically spaced by 0.5 dex and the dashed contours are spaced by 0.1 dex for log likelihoods between 0 and -0.4 . The differences between the dashed contours are not statistically significant.

related distributions. The Kolmogorov-Smirnov (K-S) test probabilities that the data are drawn from the random or perfectly correlated distributions are 4×10^{-6} and 3×10^{-4} respectively.

Before we can draw any conclusions about misalignments between the mass and the light, we must compensate for the effects of tidal shear perturbations. All lenses are modified by tidal shear perturbations due to nearby galaxies and the group or cluster halo in which the lens resides (see Keeton et al. 1997), or perturbations from large scale structure (see Barkana 1996, Keeton et al. 1997) along the ray. The lens model fits the average quadrupole of the gravitational field, which is a combination of the quadrupole from the lens galaxy and the tidal shear. We can define the shapes of the light, the mass and the model and the tidal shear by the pseudo-vectors $\vec{\epsilon} = \epsilon \{ \cos 2\theta_\epsilon, \sin 2\theta_\epsilon \}$

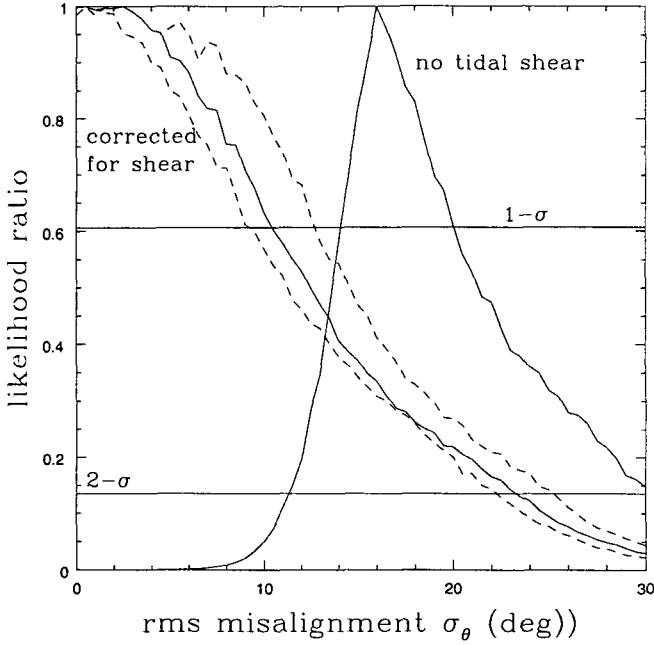


Figure 3: Likelihood ratios for the dispersion of the intrinsic misalignment distribution σ_θ . The solid curve labeled “no tidal shear” shows that a $\sigma_\theta = 16^\circ$ width is needed to explain the misalignment distribution in the absence of any tidal shear. The solid line labeled “corrected for tidal shear” shows that the theoretically expected tidal shears are large enough to explain the misalignment distribution without any intrinsic misalignment. The dashed curves show the effect of increasing and decreasing the prior estimate of γ_{rms} by 50%.

and $\vec{\gamma} = \gamma\{\cos 2\theta_\gamma, \sin 2\theta_\gamma\}$ where ϵ is the ellipticity ($\epsilon = 1 - b/a$ for axis ratio $0 \leq b/a \leq 1$), γ is the magnitude of the shear, and θ_ϵ and θ_γ are the orientations of the major axes. There are four “shapes” associated with each lens i : the shape of the luminous galaxy, $\vec{\epsilon}_{Li}$, the shape of the lens model, $\vec{\epsilon}_{Mi}$, the shape of the mass distribution of the lens galaxy, $\vec{\epsilon}_{Gi}$, and the external shear at the lens galaxy, $\vec{\gamma}_i$. A good approximation is that lens models which produce the same Einstein ring shape will be nearly indistinguishable (see Keeton et al. 1997, Kochanek et al. 2001), which corresponds to the constraint $\vec{\epsilon}_{Mi} = \vec{\epsilon}_{Gi} + 6\vec{\gamma}_i$. The factor of 6 is for SIE models, but has little effect on the conclusions.

By studying the correlations between the shapes of the models, $\vec{\epsilon}_M$, and the shapes of the luminous lens galaxies, $\vec{\epsilon}_L$, we can statistically estimate the correlations between the shapes of the mass and the light and the strength of

the external tidal shears. For our first analysis we will examine only the misalignment angle distribution. We assume that $\epsilon_G \simeq \epsilon_M$ as an estimate for the ease with which the external shear can twist the major axis of the model away from the major axis of the mass distribution. If $\theta_G - \theta_L$ is the misalignment between the mass and the light, the simplest model for its distribution is a Gaussian of width σ_θ ,

$$P(\theta_G - \theta_L) = \exp(-(\theta_G - \theta_L)^2 / 2\sigma_\theta^2) / \sqrt{2\pi}\sigma_\theta. \quad (1)$$

We wrap the tails of the Gaussian onto the 0° to 90° range of the misalignment angle. We assume the two shear components are Gaussian variables, so the probability distribution for the total shear is

$$P(\gamma) = 2\gamma \exp(-\gamma^2 / \gamma_{rms}^2) / \gamma_{rms}^2 \quad (2)$$

where γ_{rms} is the rms shear. The shape of the shear distribution is not critical because of the small sample size. We used Monte Carlo simulations to model the misalignment angle distribution including the effects measurement errors, and then used the K-S test to see if the distribution agreed with the data. Fig. 2 shows contours of the K-S test probability as a function of the rms misalignment angle, σ_θ , and the strength of the tidal shear, γ_{rms} . Although the sample is too small to determine the origin of the misalignments, we are restricted to a narrow parameter range. In the limit where there is no tidal shear, the width of the misalignment distribution must be $\sigma_\theta = 16^\circ$ ($14^\circ \lesssim \sigma_\theta \lesssim 20^\circ$), while in the limit where there are no misalignments, the rms shear must be $\gamma_{rms} = 0.04$ ($0.033 \lesssim \gamma_{rms} \lesssim 0.055$), where we have used maximum likelihood methods to convert the K-S probability distributions into uncertainties.

We can measure the dispersion σ_θ by adding a prior probability for the strength of the tidal shear based on the survey of shear in lenses by Keeton et al. (1997). The typical perturbation from large scale structure is $\gamma_{rms} \simeq 0.03$ based on standard normalizations for the non-linear power-spectrum (see Barkana 1996, Keeton et al. 1997), and the typical perturbation from objects clustered with the lens produces an effective perturbation of $\gamma_{rms} \simeq 0.05$ (see Keeton et al. 1997). The total rms shear is then $\gamma_{rms} \simeq 0.06$ after adding the two terms in quadrature. We include this estimate as a log-normal prior for γ_{rms} , assuming that its value is uncertain by a factor of two. After adding the prior to the likelihoods, the best models have $\sigma_\theta \simeq 0^\circ$ and an upper bound of $\sigma_\theta < 10^\circ$ on the rms misalignment. The results are not sensitive to the exact value we use for the prior, as raising γ_{rms} by 50% lowers the bound to 9° and lowering it by 50% raises the bound to 12° . Fig. 3 shows the likelihood ratios as a function of the rms misalignment angle.

3 Statistical Lens Constraints

Our results on the alignment of the mass and light are an example of a broader approach to improving the constraints on gravitational lenses. The problem with models of individual lenses is that they frequently have too few constraints to avoid degeneracies between physically interesting parameters. This is particularly vexing for the gravitational lenses with time delays, where there is usually a degeneracy between the value of H_0 and the radial density profile of the lens galaxy (see, e.g., Impey et al. 1998, Witt et al. 2000). Most of these problems can be eliminated using statistical constraints from the properties of the lens population.

One example of a statistical constraint method is the bounding of the central densities of lenses, most recently by Rusin & Ma (2001). Almost all lenses lack visible central (“odd”) images, which sets a lower bound on the central density of a successful model. As an example, consider a modern density model with a central density cusp $\rho \sim r^{-\beta}$ ($1 \lesssim \beta \lesssim 2$) inside break radius a , and a steeper $\rho \sim r^{-n}$ ($3 \lesssim n \lesssim 4$) profile outside. The models of most lenses will have a degeneracy between the physical parameters a and β in which the break radius decreases as the central cusp is softened so as to keep the central density high enough to make the central image invisible (see Munoz et al. 2001). The ellipticity of the lens also rises as the mass becomes more centrally concentrated in order to keep the same quadrupole moment at the Einstein ring. However, most of these permitted models for the individual lenses imply statistical properties for the lens population which are not consistent with the observed properties. Rusin & Ma (2001) used this to show that for models with break radii larger than the Einstein ring radius, only cusps steeper than $\beta \gtrsim 1.8$ were statistically consistent with the data.

Our limit on the alignment of mass and light is a second example of a statistical constraint. We know that successful models of individual lenses require contributions from both the ellipticity of the lens and external tidal perturbations but cannot determine all their parameters without degeneracies (see Keeton et al. 1997). However, by performing a joint analysis of the models for a sample of lenses, we have shown that the mass and luminosity distributions of the lens are aligned within a reasonably tight statistical limit of $\langle \Delta\theta^2 \rangle^{1/2} < 10^\circ$. We can also assign a prior on the typical strength of the tidal shear with $\gamma_{rms} \simeq 0.05$. These two restrictions can now be used to reduce the parameter degeneracies in lens models.

The next step from these two simple examples is to attack the problem of statistical constraints formally. There are two complimentary approaches. First, models of individual lenses should be weighted by the likelihood of ob-

serving them given the model parameters. This is the generalization of the limits on central densities. Second, the statistical properties of lens samples should be homogeneous. This is the generalization of our bound on the alignment of mass and light.

In our first generalization we consider models of a particular lens, where we can add the statistical constraint that models in which the observed configuration is probable should be favored over those where it is not. Consider the case of a density cusp with parameters β and a where in fitting the observed properties of the lens the fit statistic $\chi^2(\beta, a)$ has a degeneracy between the parameters. For any model (β, a) we can also calculate the probability $p_{tot}(\beta, a)$ that a lens with such physical properties will be found, and the probability $p_{obs}(\beta, a)$ that it will have the observed configuration. If two models are consistent with the observed configuration, we should statistically favor the model in which the observation is more likely by adopting the modified likelihood

$$2 \ln L(\beta, a) = -\chi^2(\beta, a) \rightarrow -\chi^2(\beta, a) + 2 \ln(p_{obs}(\beta, a)/p_{tot}(\beta, a)). \quad (3)$$

While for a particular lens this may bias the solution, for an ensemble of lenses it should be correct. The Rusin & Ma (2001) limit on the cusp exponent can be thought of as a variant of this general approach.

In our second generalization we consider (Bayesian) models for a population of lenses. For the problem of ellipticity and shear we considered in §2, the fit statistic $\chi_i^2(\vec{p}_i)$ for lens i depends on the four parameters for the angular structure, $\vec{p}_i = (\epsilon_{Gi}, \theta_{Gi}, \gamma_i, \theta_{\gamma i})$. Our calculation in §2 simplified the χ^2 by assuming it could be approximated by a degenerate constraint, $\vec{\epsilon}_M = \vec{\epsilon}_G + 6\vec{\gamma}$, on the variables. In a Bayesian formalism, the probability of the data D_i given the parameters \vec{p}_i is $P(D_i|\vec{p}_i) \propto \exp(-\chi_i^2(\vec{p}_i)/2)$, and we use Bayes theorem ($P(p|D) \propto P(D|p)P(p)$) to estimate the probability of the parameters given the data and the priors. Several of the parameters have non-uniform Bayesian priors. In particular, the major axis of the mass is constrained by that of the light by the prior $P(\theta_{Gi}|\theta_{Li}, \sigma_\theta)$ given in eqn. (1), and the shear is constrained by the rms shear by the prior $P(\gamma_i|\gamma_{rms})$ given in eqn. (2). These priors introduce new parameters, γ_{rms} and σ_θ , which require their own priors, $P(\gamma_{rms})$ and $P(\sigma_\theta)$. Thus, the Bayesian probability for a sample $i = 1 \dots N$ lenses is

$$P(\vec{p}_i, \gamma_{rms}, \sigma_\theta | D_i) \propto P(\gamma_{rms})P(\sigma_\theta) \prod_{i=1}^N P(\gamma_i|\gamma_{rms})P(\theta_{Gi}|\theta_{Li}, \sigma_\theta)P(D_i|\vec{p}_i). \quad (4)$$

While this looks formidable, we can find the probability distribution for any particular variable simply by marginalizing (integrating) over the remaining variables. For example, the Bayesian equivalent of the likelihood shown in

Fig. 2 is found by integrating over all the lens parameters,

$$P(\gamma_{rms}, \sigma_\theta | D_i) \propto P(\gamma_{rms})P(\sigma_\theta) \prod_{i=1}^N \int d\vec{p}_i P(\gamma_i | \gamma_{rms}) P(\theta_{G_i} | \theta_{Li}, \sigma_\theta) P(D_i | \vec{p}_i). \quad (5)$$

For variables constrained by the data, the final probability distribution will be significantly narrower than the prior distribution ($P(\gamma_{rms})P(\sigma_\theta)$). Our analysis in §2 is a simpler, more intuitive implementation of this approach, but it is easier to add parameters or to include terms like those from eqn. (3) in a more general Bayesian formalism.

4 Conclusions

Almost all the lens galaxies we consider are massive early-type galaxies, which have the most complex formation history of normal galaxies. First, CDM prolate-triaxial halos form in which the baryons cool into a disk and form stars. The cooling baryons compress the dark matter and the oblate shape of the baryonic potential begins to destroy the triaxiality of the dark matter. After the halo undergoes several major mergers, the disks are destroyed to leave a nearly oblate early-type galaxy with some fossil evidence for the disks. Despite this complicated formation history we can show that the final mass and luminosity distributions are aligned to within $\langle \Delta\theta^2 \rangle^{1/2} < 10^\circ$ (in projection) by examining the statistics of the misalignments between lens models and lens galaxies. The quadrupole of the mass includes similar contributions from both the luminous and the dark matter, so a small misalignment between the mass and the light should imply a small misalignment between the dark and the light.

Our approach to measuring the misalignment of mass and light is an example of a statistical lens constraint. Where models of individual lenses frequently have awkward degeneracies between physical parameters, the most famous of which is that between the Hubble constant and the radial mass distribution of the lens, samples of lenses generally should not. To lay the basis for this new approach to lens modeling, we have outlined two general and complimentary approaches to developing statistical constraints for gravitational lenses, one of which is a generalization of the methods we used to study the alignment of mass and light. Given a sample of lenses with time delay measurements (there are now 9 lenses with time delays), these statistical approaches should greatly reduce the uncertainties in estimates of the Hubble constant over that in any single system.

Acknowledgments: CSK thanks the remainder of the CASTLES collaboration for its comments. Support for the CASTLES project was provided by

NASA through grants GO-7495, GO-7887, GO-8175 and GO-8804 from STScI. CSK is also supported by the Smithsonian Institution and NASA grants NAG5-8831 and NAG5-9265.

References

1. Bardeen, J.M., et al., 1986, ApJ, 305, 15
2. Barkana, R., 1996, ApJ, 468, 17
3. Buote, D.A. & Canizares, C.R., 1996, ApJ, 457, 177
4. Buote, D.A. & Canizares, C.R., 1997, ApJ, 474, 650
5. Buote, D.A. & Canizares, C.R., 1998, MNRAS, 298, 811
6. Cohn, J.D., et al., 2001, ApJ, 554, 1216
7. Dubinski, J., & Carlberg, R.G., 1991, ApJ, 378, 496
8. Dubinski, J. 1994, ApJ, 431, 617
9. Eisenstein, D., Hu, W., & Tegmark, M., 1998, ApJL, 504, L57
10. Evrard, A.E., Summers, F.J., & Davis, M., 1994, ApJ, 422, 11
11. Falco, E.E., et al., 2000, in Gravitational Lensing: Recent Progress and Future Goals, T. Brainerd & C.S. Kochanek, eds., (ASP) astro-ph/9910025
12. Frenk, C.S., et al., 1988, ApJ, 327, 507
13. Impey, C.D., et al., 1998, ApJ, 509, 551
14. Keeton, C.R., Kochanek, C.S., & Falco, E.E., 1998, ApJ, 509, 561
15. Keeton, C.R., Kochanek, C.S., & Seljak, U., 1997, ApJ, 482, 604
16. Keeton, C.R., et al., 2000, ApJ, 542, 74
17. Kochanek, C.S., 1991, ApJ, 373, 354
18. Kochanek, C.S., Keeton, C.R., & McLeod, B.A., 2001, ApJ, 547, 50
19. Lehar, J., et al., 2000, ApJ, 536, 584
20. Mould, J.R., et al., 2000, ApJ, 529, 786
21. Munoz, J.A., Kochanek, C.S., & Keeton, C.R., 2001, ApJ, 558, 657
22. Rusin, D., & Ma, C.-P., 2001, ApJL, 549, L33
23. Sackett, P.D., 1999, in Galaxy Dynamics, eds. D. Merritt, J.A. Sellwood, & M. Valluri (PASP: San Francisco) 393, (also astro-ph/9903420)
24. Schechter, P., 2000, IAU Symposium 201, astro-ph/0009048
25. Wambsganss, J., & Paczynski, B., 1994, AJ, 108, 1156
26. Warren, M.S., et al., 1992, ApJ, 399, 405
27. Witt, H.J., & Mao, S., 1997, MNRAS, 291, 211
28. Witt, H.J., Mao, S., & Keeton, C.R., 2000, ApJ, 544, 98

SDSS MEASUREMENTS OF GALAXY HALO PROPERTIES BY WEAK LENSING

Timothy A. McKay, Erin Scott Sheldon, Judith Racusin

*University of Michigan, Department of Physics, 500 East University, Ann Arbor,
MI 48109*

Philippe Fischer

Department of Astronomy, Univ. of Toronto, Toronto, ONT, M5S, 3H8, Canada

Uros Seljak

Princeton University Observatory, Princeton, NJ 08544

Albert Stebbins, David Johnston, Joshua A. Frieman

Fermi National Accelerator Laboratory, P.O. Box 500, Batavia, IL 60510

We describe weak lensing measurements of galaxy halos. Early SDSS data are used to measure the galaxy-mass correlation function (GMCF). This GMCF is a direct measure of the massive halos which luminous galaxies occupy. To make these measurements we use a sample of $\sim 35,000$ lens galaxies and 3.6×10^6 background ‘source’ galaxies. Every lens galaxy has a spectroscopic redshift and highly accurate five color photometry. As a result our determination of the mass and size scales of the GMCF are very robust. Detailed information about all lens objects also allows us to study the relationship between the luminous properties of galaxies (luminosity, morphology, local density) and the dark matter halos which surround them. To make this comparison we define an aperture mass M_{260} , which characterizes the normalization of the GMCF. While M_{260} is essentially independent of the u' luminosity of a galaxy, we find that it is linearly dependent on luminosity in red bands. This suggests that the current rate of star formation in a galaxy (reflected by the u' light) is poorly correlated with its dark matter environment. The light in redder bands however, which reflects the integrated star formation history of the lenses, is closely coupled to the dark matter halos in which the galaxies form.

1 SDSS Data for Weak Lensing

The analyses reported in this work are based on observations obtained by the Sloan Digital Sky Survey^a. The SDSS includes both imaging and spectroscopic surveys¹ of approximately 10^4 square degrees in the North Galactic Cap. The data used in this analysis are drawn from SDSS commissioning runs. Imaging data were obtained between Fall 1997 and Spring 2000. Seeing in these early runs varied from 1.0" to 2.0". Spectroscopic targets selected from this imaging data were observed with the SDSS spectrographs over a series of nights during 2000. SDSS data are reduced and calibrated by the

^awww.sdss.org

SDSS photometric (PHOTO), astrometric (ASTROM), calibration (MT), and spectroscopic (SPECTRO) pipelines. These pipelines generate well calibrated five color imaging and spectroscopic catalogs.

To conduct our lensing mass measurements we divide the observed sample of galaxies into a foreground lens sample and a background source sample. For lens galaxies we select about 35,000 bright ($r' < 17.6$) SDSS galaxies with measured spectroscopic redshifts. For source galaxies we select 3.6×10^6 well resolved galaxies with r' magnitudes from 18.0 to 22.0.

2 Lensing measurements

The SDSS data yields measurements of the mean galaxy-mass correlation function^{2,3}. To do this we measure the mean tangential shear γ_+ around foreground lenses. This shear measurement, combined with an estimation of the source galaxy redshift distribution, yields the surface mass density contrast:

$$\Delta\Sigma_+ = \gamma_+(R)\Sigma_{crit} = \bar{\Sigma}(\leq R) - \bar{\Sigma}(R) \equiv \Delta\Sigma_+ \quad (1)$$

where Σ_{crit} is the critical density. The critical density is dependent in an important way on the geometry of the lens-source system:

$$\Sigma_{crit} = \frac{c^2}{4\pi G} \frac{D_S}{D_L D_{LS}} \quad (2)$$

where D_S and D_L are the angular diameter distances to source and lens, respectively, and D_{LS} is the distance from source to the lens. We determine this critical density using the known lens redshifts and an estimate of the mean source galaxy redshift distribution. The source galaxy redshift distribution is estimated by comparison to results from the Canada-France Redshift Survey⁴. This $\Delta\Sigma_+$ we refer to as the galaxy-mass correlation function (GMCF). Details of this analysis are presented in McKay et al. 2001⁵. The GMCF measured for the lens and source samples described in the previous section are shown in Fig. 1. Note that significant shear is detected to $1 h^{-1}$ Mpc and beyond.

3 Variations in the GMCF with lens galaxy properties

When we examine the GMCF derived for galaxies of different intrinsic luminosities, we find that the normalization can vary strongly, but that the shape is unchanged. The variation with r' luminosity in Fig. 2. Interestingly, the GMCF of various galaxies seems to be essentially independent of the u' luminosity of the galaxy. This suggests that the integrated star formation history

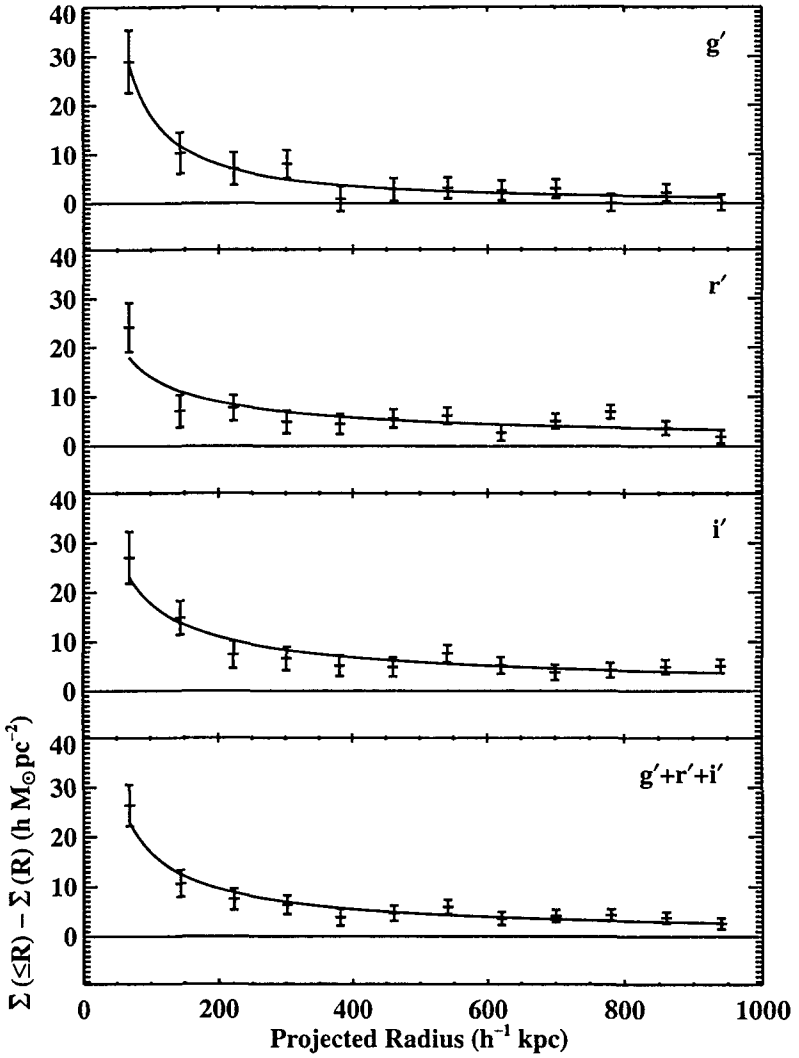


Figure 1: GMCF as a function of projected radius around $\sim 31,000$ SDSS lens galaxies. The plots are the mean density contrast in g' , r' , and i' images from the top, with the combined data on bottom. The solid lines are the best-fitting power laws. The overall best fit has the form $\Delta\Sigma_+ = (2.5_{-0.6}^{+0.7})(R/1\text{Mpc})^{-0.8\pm 0.2}hM_{\odot}\text{pc}^{-2}$.

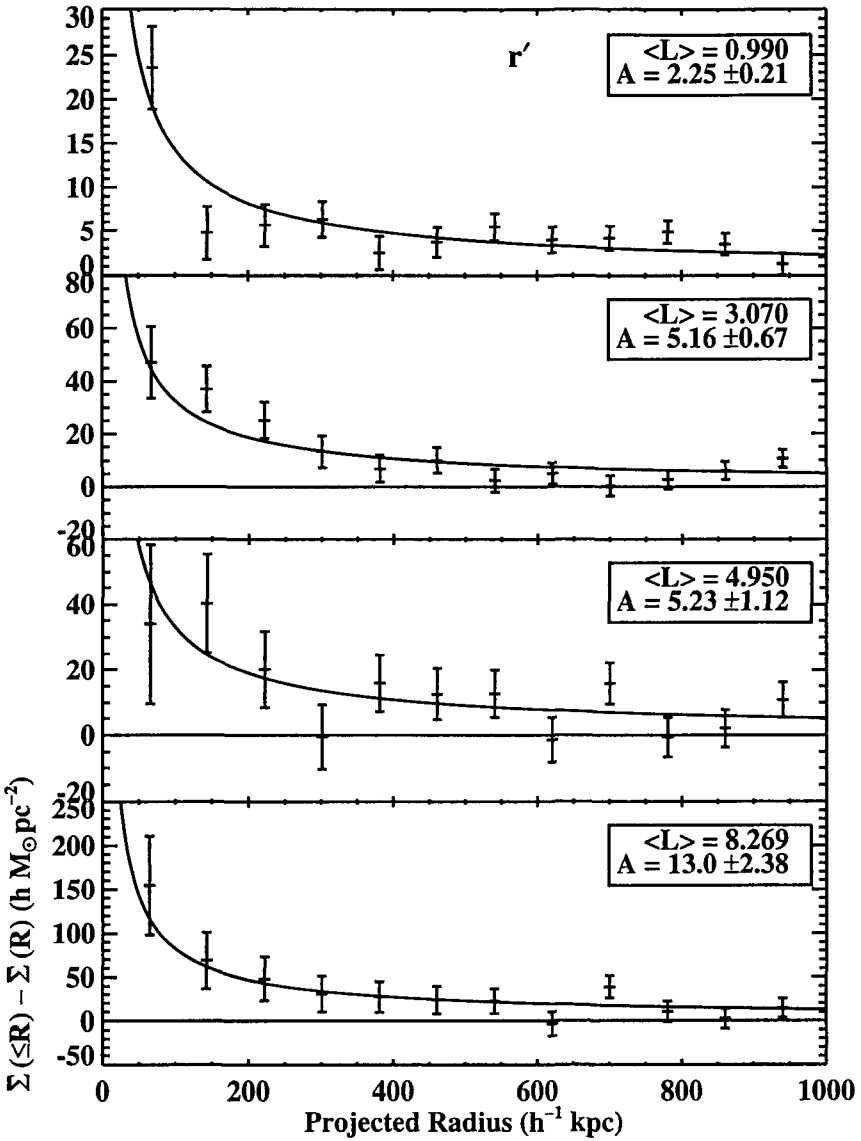


Figure 2: GMCF in bins of r^* luminosity. Lines are the best fits to $R^{-0.8}$ power law models corresponding to the noted values of the normalization A . Note that each plot has a different y-axis scale.

of the galaxy (as reflected in the r' and i' luminosity) is much more representative of the overall mass of a galaxy than is its current star formation rate (as reflected in the u' luminosity).

The GMCF measured here is not, in fact, simply the mass density contrast profile of the average galaxy. On 1 Mpc scales, which we probe the clustering of galaxies also matters. When we measure the GMCF at radii far from the central galaxy we include not only mass clearly associated with this central object, but also the mass of its neighbors. To illustrate this we compare in Fig. 3 the GMCF measured around galaxies in high and low densities regions (as determined by a Voronoi tessellation method). We observe that the central parts of the two GMCFs are very similar; this is the region dominated by mass associated with the central galaxy. The outer parts of the GMCF are, however, quite different. This illustrates that, in a general sense, the inner $250 h^{-1}$ kpc of the GMCF is associated with the central galaxy, while the outer profile is dominated by clustering effects.

4 Quantifying the mass to luminosity scaling

To quantify this variation of GMCF with luminosity, we fit the observed GMCF to a singular isothermal sphere model, and then integrate this model fit to a radius of $260 h^{-1}$ kpc. This simple approach is motivated by the results of the previous section, which suggest that the GMCF in this central region is most clearly associated with the central galaxy. We refer to this as an aperture mass M_{260} . The variation of this M_{260} with luminosity in the five SDSS passbands is summarized in Fig. 4. In this figure we see that, while the u' luminosity of a galaxy is unrelated to M_{260} , the relations between M_{260} and r' , i' , and z' luminosity are strong and linear.

5 Conclusions

Our understanding of structure formation in the universe has evolved substantially over the last thirty years. We no longer expect galaxies to form as discrete, isolated objects. Nor is the formation of a galaxy simply a series of mergers of discrete, otherwise isolated objects. Instead, luminous galaxies are roughly discrete tracers of mass, embedded in a smoothly varying dark matter environment. Over time, the very smooth matter distribution of the early universe becomes more and more inhomogeneous. Despite this, galaxies are today embedded in dark matter halos which overlap to a degree which invalidates discussion of them as discrete objects.

We have presented measurements of a galaxy-mass correlation function and its dependence on a variety of measured galaxy properties. We measured

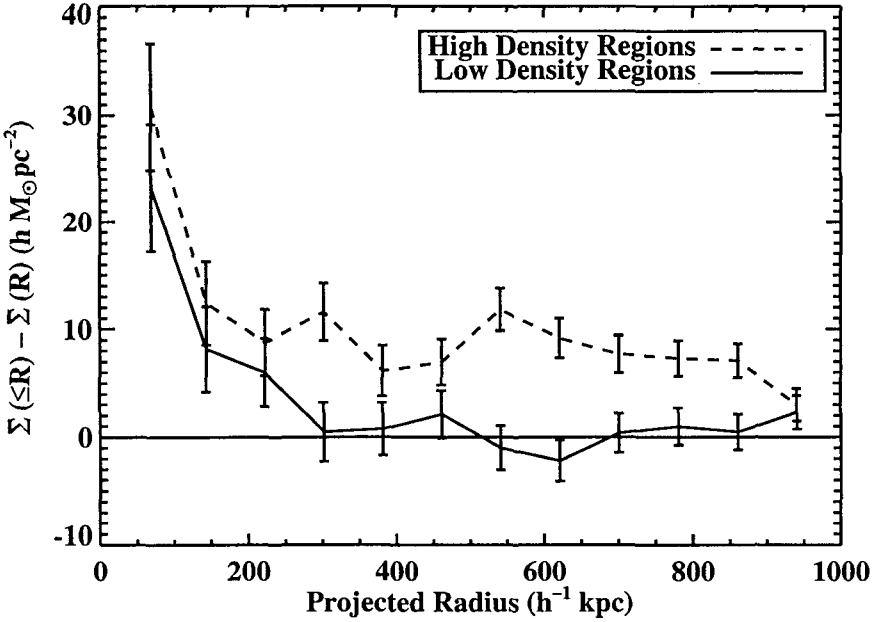


Figure 3: This figure compares the GMCF measured around galaxies in high and low density regions. The GMCFs are similar at small radii, but very different at large radii, illustrating the importance of neighbors grows with radius.

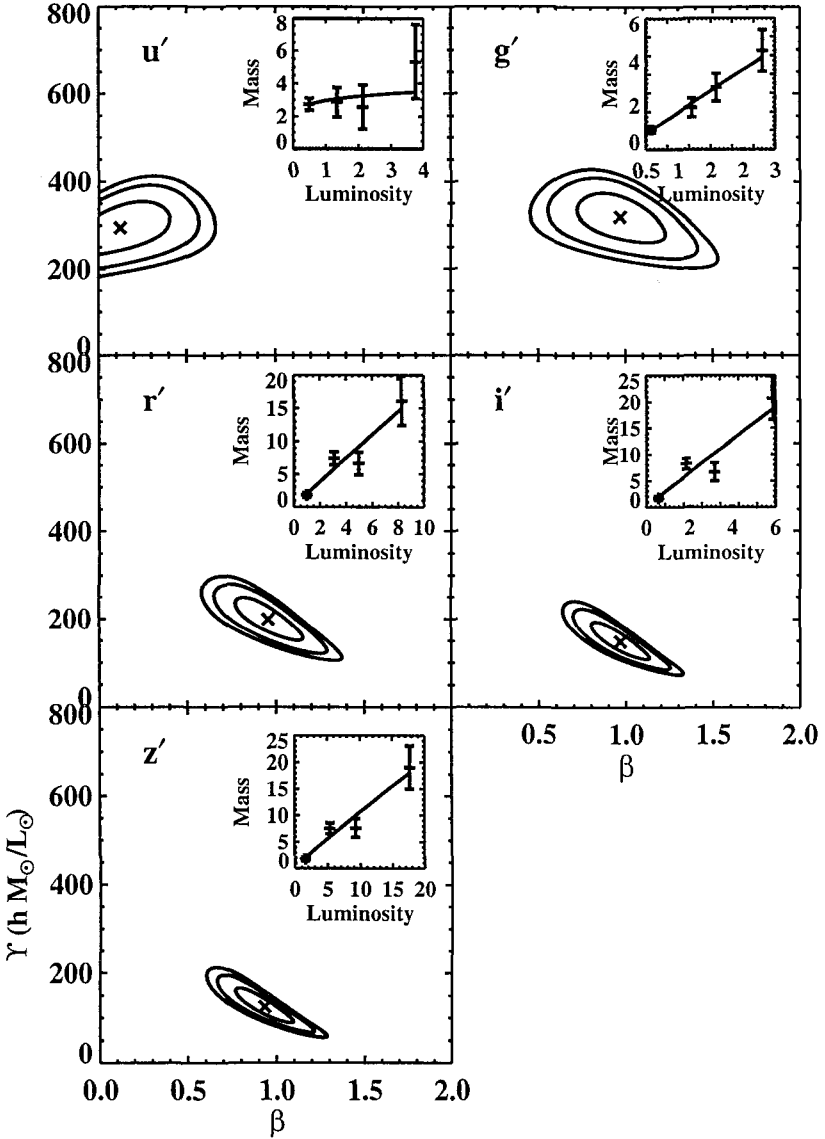


Figure 4: The five panels in this figure summarize the relation between M_{260} and luminosity in each of the five SDSS bands. For each band the small inset figure shows this directly. Points in these inset figures are the measured M_{260} and mean luminosity of galaxies in four luminosity bins. The line in these inset figures shows the best fit to a power law relation between M_{260} and luminosity of the form: $M_{260} = \Upsilon \times (L_{\text{central}}/10^{10} L_{\odot})^{\beta}$. The larger figure shows 68%, 95%, and 99% confidence contours for the fit parameters Υ and β .

the dependence of the GMCF on galaxy luminosity. While the shape of the GMCF is little affected by luminosity, the amplitude can vary strongly. The GMCF has little relation to u' luminosity, reflecting the fact that much of this luminosity is derived from localized, short lived episodes of star formation. The GMCF is strongly dependent on the luminosity of galaxies in the g' , r' , i' , and z' bands. The luminosity in these bands is dominated by low mass stars, and hence reflects the integrated star formation history of the galaxy.

We examine the variation of the GMCF with environment and find that the amplitude of the GMCF near the center is very similar for galaxies of the same luminosity drawn from overdense and underdense regions, yet the shape of the GMCF at large radii is quite different. This result confirms the notion that the GMCF in the central regions, out to perhaps $300 h^{-1}$ kpc, is dominated by mass clearly associated with the central galaxy. The GMCF at large radius, by contrast, is primarily effected by the presence of neighboring objects.

In a straightforward effort to quantify the scaling of the GMCF with central galaxy luminosity ($L_{central}$) we derived aperture masses for various classes of lenses based on fits to the inner $260 h^{-1}$ kpc of their GMCF (M_{260}). Comparison of M_{260} to the mean $L_{central}$ confirms a linear scaling in the g' , r' , i' , and z' bandpasses. These measurements of M_{260} also allowed us to probe quantitatively the $M_{260}/L_{central}$ relations for spiral and elliptical galaxies. Despite the substantial difference between the GMCF for spirals and ellipticals, there is little difference in the relationship between their GMCF and luminosities in red bands. Since spiral and elliptical galaxies occupy substantially different average local environments, the consistency of these GMCF/luminosity relations reinforces the notion that the GMCF measured within $260 h^{-1}$ kpc is primarily associated with the central object. While the studies presented here go substantially beyond previous galaxy-galaxy lensing studies, they represent only the beginning of what can be done with SDSS data. The data presented here are drawn from only about 4% of the final SDSS survey area. The full data set will allow repetition of all these measurements with more than 5 times the S/N. Extension of this approach to studies of other kinds of 'objects' is also possible. In addition to the galaxy-mass correlation function described here, we can measure the group-mass correlation function, the cluster mass correlation function, even a void-mass correlation function. All that is required is an input catalog of object locations and redshifts. A simple example demonstrating our ability to measure the cluster-mass correlation function appeared in Sheldon et al. 2001⁶.

Weak lensing within the SDSS provides a powerful new tool for probing the relationship between luminous objects and the dark matter environment

in which they reside. SDSS lensing measurements provide strong constraints on the total correlation between objects and mass, and hence provide simple, direct constraints to N-body simulation results.

Acknowledgments

Funding for the creation and distribution of the SDSS Archive has been provided by the Alfred P. Sloan Foundation, the Participating Institutions, NASA, NSF, the U.S. Department of Energy, the Japanese Monbukagakusho, and the Max Planck Society. The SDSS Web site is <http://www.sdss.org/>. The Participating Institutions are The University of Chicago, Fermilab, the Institute for Advanced Study, the Japan Participation Group, The Johns Hopkins University, the Max-Planck-Institute for Astronomy (MPIA), the Max-Planck-Institute for Astrophysics (MPA), New Mexico State University, Princeton University, the United States Naval Observatory, and the University of Washington. Tim McKay and Erin Sheldon acknowledge from NSF PECASE grant AST 9708232.

References

1. York, D. G. et al. 2000, AJ, 120, 157
2. Brainerd, T. G., Blandford, R. D. and Smail, I. 1996, ApJ, 466, 623
3. Fischer, P., et al., 2000, AJ, 120, 1198
4. Lilly, S., J., et al. 1995, ApJ, 455, 50
5. McKay, T. A. et al. 2001, submitted to ApJ
6. Sheldon, E., et al., 2001, ApJ, 554, 881

CONSTRAINING HALO PROPERTIES FROM GALAXY-GALAXY LENSING AND PHOTO-Z

Andreas O. Jaunsen

European Southern Observatory, Casillo 19001, Santiago 19, Chile

E-mail: ajaunsen@eso.org

Abstract

Here we present results from a maximum likelihood analysis of galaxy-galaxy weak lensing effects as measured in a $12.5' \times 12.5'$ field obtained at the Nordic Optical Telescope, on La Palma, Spain. The analysis incorporates photometric redshifts and gives circular velocities consistent with previous weak lensing work.

1 Data

The Canada France Redshift Survey (CFRS) 14h-field was observed in May 1998 with the Nordic Optical Telescope (NOT) and the ALFOSC instrument in UBVRI filters. The instrument field is $7'$ on each side so four pointings were made, covering in total $12.5' \times 12.5'$. The seeing conditions were good and the measured image qualities in the combined images are $1.0''$, $1.0''$, $0.8''$, $0.6''$, $0.6''$ in the UBVRI, respectively. The field contains close to 200 galaxies with z_{spec} from Lilly *et al.*¹ and Koo *et al.*². The $3\text{-}\sigma$ limiting AB magnitudes are 23.7, 25.1, 25.2, 25.5, 25.1 in the UBVRI, respectively. Objects were only considered when detected in a minimum of three bands, this gave a total of ~ 4500 objects.

2 Photometric redshifts

There are two common methods for estimating photometric redshifts. One method relies on a training sample in which the redshifts are known and then a regression is made of the observed colors with the known redshifts. The second method does not need a training sample, but instead uses template spectral energy distributions (SEDs), which are redshifted and fit to the observed colors.

We use the BPZ method as implemented by N. Benitez³. This method provides an estimate of the redshift, its uncertainty and the galaxy type. The results are shown in Fig. 1. At around $z \sim 1$ the scatter increases due to the fact that the main tracer of redshift (the 4000\AA -break) is redshifted out of the I-band.

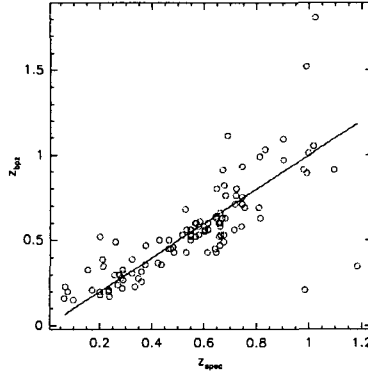


Figure 1: Plot showing the estimated photometric redshift versus the spectroscopic redshift for the sub-sample of galaxies for which this information exists

3 Weak lensing measurements

The galaxy shapes are measured using N. Kaiser's IMCAT software package based on the method described in Kaiser *et al.*⁴. Field distortion was found to be non-negligible due to flexure in the instrument and was corrected by modeling the distortion as a second order polynomial in each image with respect to a reference image taken at the USNO 1.0m telescope (thanks to A. Henden) which is known to have negligible distortion. PSF anisotropies were also identified in the individual images, which varied very smoothly from image to image. Again a second order polynomial model was applied to describe the anisotropy in each image. These models were then combined into a final model which was used to correct the combined image. The success of this correction is shown in Fig. 2. Finally, seeing effects were normalized by applying the 'pre-seeing shear polarizability' $P_\gamma = P^{sh} - \frac{P^{sh}(\star)}{P^{sm}(\star)} P^{sm}$, giving the corrected $e = e' - \gamma P^\gamma$ (Luppino & Kaiser⁵).

4 Model

We adopt the simple truncated isothermal sphere model used in Brainerd *et al.*⁶

$$\rho(r) = \frac{V^2 s^2}{4\pi G r^2 (r^2 + s^2)}$$

and the scaling relations used in Hudson *et al.*⁷

$$V = V_\star \left[\frac{L}{L_\star(z)} \right]^\eta \quad s = s_{200} \left(\frac{V}{200 \text{ km s}^{-1}} \right)^2.$$

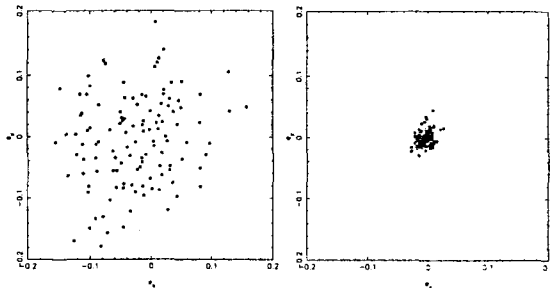


Figure 2: Plots showing the ellipticity vector components for stars before and after correction for the PSF anisotropy

This model is thus used to compute the expected shear for every source galaxy, taking into account all lens galaxies (see definition of lens galaxy in next section). The expected shear is then subtracted from the observed shape of the source galaxy giving the weak lensing corrected ellipticity, which can be compared to the true ellipticity distribution. The latter is assumed to be the best fit gaussian to the observed (raw) ellipticities. We hence maximize the corrected ellipticity distribution with respect to the assumed intrinsic (true) distribution and the likelihood function becomes

$$\log L = \sum_i \left(-\frac{|\epsilon_i - \gamma_i P_j^\gamma|}{2\sigma_e^2} \right) ,$$

where P_j^γ is the 'pre-seeing shear polarizability' and σ_e is the best fit Gaussian HWHM. A different shear, γ_i , is obtained by varying the parameters of the model (including scaling relations).

5 Results

Lenses are selected as having $z < z_s + 0.25$, a maximum $z < 0.5$ and a projected separation in the lens plane in the range $25 < r < 150$ kpc. Furthermore, in order to select secure lenses, a final criterion is imposed, namely that the photometric redshift has a probability larger than 95%. Due to the fact that the field is limited and we therefore do not know about the lenses outside the field-of-view for sources close to the edge, we only consider sources more than 150 kpc from the image borders at any given lens redshift. We apply the following cosmological parameters in the analysis: $\Omega = 0.3$, $\Lambda = 0.7$ and $h = 1$. The results are shown as confidence contours in Fig. 3.

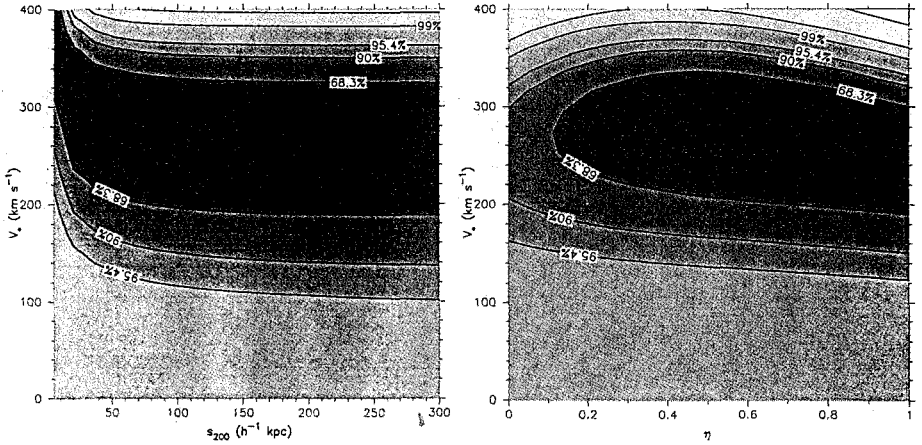


Figure 3: Two-dimensional weak lensing confidence contours on V_* , s_{200} and V_* , η

The resulting 68.3% conf. level on the circular velocity and the Tully-Fisher exponent is:

$$V_* = 280 \pm 30 \text{ km s}^{-1} \quad \eta = 0.6 \pm 0.4$$

In the near future with photo-z (optical + infrared photometry) and large fields one may explore differences in halo mass, size and scaling relations for different galaxy types and evolution effects.

References

1. S. J. Lilly, F. Hammer, Le Fèvre O., and Crampton. D. *Astrophys. J.*, 455:50–59, 1995.
2. D.C. Koo, N.P. Vogt, A.C. Phillips, et al. *Astrophys. J.*, 469:535, 1996.
3. N. Benitez. *Astrophys. J.*, 536:571, 2000.
4. N. Kaiser, G. Squires, and T. Broadhurst. *Astrophys. J.*, 449:460, 1995.
5. G. A. Luppino and N. Kaiser. *Astrophys. J.*, 475:20, 1997.
6. T. G. Brainerd, R. D. Blandford, and I. Smail. *Astrophys. J.*, 466:623–637, August 1996.
7. M. J. Hudson, S. D. J. Gwyn, H. Dahle, and N. Kaiser. *Astrophys. J.*, 503:531, 1998.

IS THERE A GROUP HALO?

Ole Möller

*Kapteyn Institute, P.O. Box 800,
9700AV Groningen, Netherlands
E-mail: ole@astro.rug.nl*

Priyamvada Natarajan

*Department of Astronomy, Yale University, 265 Whitney Avenue,
New Haven, CT 06511, USA*

Jean-Paul Kneib

*Observatoire Midi-Pyrénées, UMR5572, 14 Avenue Edouard Berlin
F-3100, Toulouse, France*

Andrew Blain

*Institute of Astronomy, Madingley Road,
Cambridge CB3 0HA, England*

We study gravitational lensing by groups of galaxies in both the strong and weak lensing regime. As the abundance of groups is high, gravitational lensing by groups is likely to be important observationally. Here, we examine the shear, magnification, image geometries and time delays produced by compact groups and discuss how these observables depend on the details of the mass distribution in the group. We find that in the weak lensing regime a tangential shear signal of order 3 per cent is to be expected and that it depends measurably on the mass distribution in the group. In the strong lensing regime we show that a group's potential may have a significant effect on the measured image geometries, magnification ratios and time delays for individual multiple-image systems. We also find that some statistical lensing properties, like the distribution of time delays, depend on the details of the groups mass distribution.

1 Introduction

Gravitational lensing by isolated galaxies and clusters of galaxies has been used successfully both as a cosmological tool and as a method to determine detailed mass distributions.⁴ In the weak lensing regime, mass profiles of clusters of galaxies have been obtained¹ and the weak lensing signal of large samples of individual galaxies has been detected and used to constrain the mass of galaxies.⁹ In the strong lensing regime, images of lensed background quasars and galaxies have been used to constrain the mass distribution of clusters and galaxies.⁷ However, lensing studies of structures on intermediate scales, between clusters and galaxies, have been rare. On those scales groups form the most common gravitationally bound entities: a large fraction of the mass of

the universe is expected to reside in groups.⁸ The weak lensing signal of groups has probably been detected by Hoekstra et al.³ but no extensive studies have been made. We investigate the weak and strong lensing properties of groups of galaxies.⁶ In particular, we examine how the mass distribution in groups may be constrained from weak lensing and/or strong lensing observations. We assume a cosmology with $\Omega_\Lambda = 0.7$, $\Omega_M = 0.3$ and $H_0 = 50 \text{ km s}^{-1}$ throughout.

2 Properties of Groups and the lensing simulations

Our groups are modeled on compact groups as cataloged by Hickson.² These groups are easily identified on the sky due to the high projected over density of galaxies. We use a model template of a typical Hickson group, consisting of 4 member galaxies. The galaxy positions are determined randomly from a modified Hubble-profile probability distribution,

$$N(\vec{r}) = \frac{N_0}{(1 + r^2/r_N^2)^{3/2}}, \quad (1)$$

where the scale length $r_N = 15 \text{ kpc}$. We model the surface mass density of the galaxies as a pseudo-isothermal mass distribution, parameterized by ellipticity ϵ , scale length r_s , and central density Σ_0 :

$$\Sigma(\vec{r}) = \Sigma_0 \frac{r_0 r_c}{r_c - r_0} \left(\frac{1}{\sqrt{r_0^2 + k^2(x, y)}} - \frac{1}{\sqrt{r_c^2 + k^2(x, y)}} \right), \quad (2)$$

where

$$k(x, y) = \sqrt{x^2 + y^2 / (1 - \epsilon)^2}. \quad (3)$$

The masses and scale lengths are determined randomly from gaussian distributions with means $\bar{M} = 10^{12} M_\odot$ and $\bar{r}_c = 0.2 \text{ kpc}$ respectively and standard deviations $\sigma_M = 5 \times 10^{11} M_\odot$ and $\sigma_r = 0.07 \text{ kpc}$ respectively. At the mass weighed geometric center of the group we also add a pseudo-isothermal group halo, with a mass of $M_h = f \times M_{\text{tot}} = 1/(1 - f) \times \sum_{i=1}^4 M_i$, where f is the fraction of the total group mass contained in the halo. The scale length is determined from a gaussian with mean $\bar{r}_h = 15 \text{ kpc}$ and standard deviation $\sigma_{rh} = 3 \text{ kpc}$.

The lensing simulations are performed using an adaptive ray-tracing method developed by Möller & Blain.⁵ With this technique, lensing simulations of a large sample of complicated lens systems are possible in a short time and the results are accurate in both the weak and strong lensing regimes.

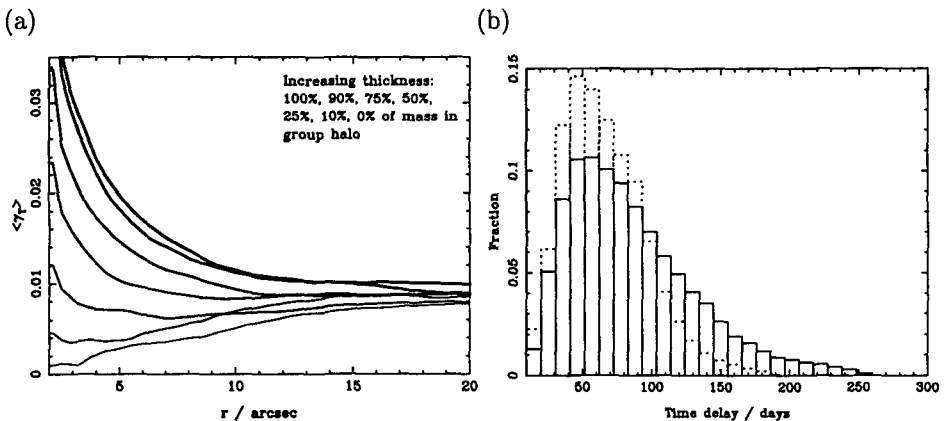


Figure 1: The left panel shows the average tangential shear around the individual group members of 100 simulated groups for different halo : galaxy mass ratios. The right panel shows the distribution of expected time delays for a sample of 100 simulated strong lens systems that are part of or near to a group. The solid histogram shows the result for 50% halo mass, the dotted line for no halo.

3 Weak and strong lensing results

In order to study weak lensing by groups we generated a sample of 100 random groups and determined the tangential shears for each group. For this purpose it is necessary to determine a center around which the shear is to be measured. Since the center of a common group halo will in general be very uncertain observationally, it is preferable to measure the tangential shear around the centers of individual galaxies, which can usually be determined with great accuracy from the light distribution. In Fig. 1 (a) we show the resulting average tangential shear profile for all 400 galaxies contained in the simulated sample for different group halo mass fractions f . The shear signal is of the order of a few percent, consistent with recent galaxy-galaxy lensing observations.⁹ The results also show that the shape of the average tangential shear profile that would be measured depends strongly on the ratio of the mass that is contained in the galaxies to that contained in a common group halo. In particular, the ratio of the tangential shear at distances of $r \sim 20$ arcsec to that at $r \sim 5$ arcsec is very sensitive to the galaxy: halo mass ratio.

In the strong lensing regime, the presence of a group near a lensing galaxy will change the effective lensing potential and is expected to affect image geometries, magnifications and time delays. We studied the strong lensing properties of individual systems as well as the statistical lensing properties of a

sample of 100 simulated groups. We found that, in individual cases, the image geometries and time delays can be affected significantly by the details of the mass distribution in the group. It is therefore crucial to take into account the groups mass distributions if accurate lens models are to be made. This is particularly important for measurements of H_0 from time delays. Statistically, we do not find that the image numbers differ significantly from that of isolated lenses. This is because the effect on the expected image geometries produced by external shear is similar to the effect produced by any intrinsic ellipticity in the lens. However, if lenses near groups are modeled as isolated lenses, a stronger angular misalignment between the light and the mass profiles is to be expected if the near groups contain massive halos. We found that the distribution of time delays expected from a sample of galaxy lenses that are part of or near to a group differs noticeably for different group mass profiles as illustrated in Fig. 1 (b). The figure shows that the time delay at large image separations is expected to be significantly larger for lenses near groups that contain a massive group halo. Note that the total group mass is the same in all cases and that this difference arises solely from variations in the mass distribution.

4 Conclusions

Our results show that the mass distribution in groups can be constrained using weak lensing observations. In particular, the relative halo: galaxy mass fraction can be estimated by measuring the ratio of the shear at radii of ~ 20 arcsec to that at 5 arcsec for a large sample of galaxies. We also found that the lensing properties of individual strong lens systems depend on the details of the mass distribution of nearby groups. We conclude that it should be possible to constrain the mass distribution in groups of galaxies very accurately from both weak and strong lensing observations.

References

1. Clowe D., Luppino G. A., Kaiser N., Gioia I. M., 2000, *ApJ*, 539, 540
2. Hickson P., 1982, *ApJ*, 255, 382
3. Hoekstra H., Franx M., Kuijken K., 2000, *ApJ*, 532, 88
4. Mellier Y., 1999, *ARA&A*, 37, 127
5. Möller O., Blain A. W., 2001, *MNRAS*, in print, astro-ph/0103093
6. Möller O. et al., 2001, *ApJ*, submitted
7. Natarajan P., Kneib J., 1996, *MNRAS*, 283, 1031
8. Ramella M., Pisani A., Geller M. J., 1997, *AJ*, 113, 483
9. Smith D. R. et al., 2001, *ApJ*, 551, 643

CONSTRAINING GALAXY SHAPES FROM MODELING THE FIRST PROBABLE TWO PLANE LENS B2114+022

K. Chae, S. Mao, I. Browne, N. Jackson, P. Wilkinson

*University of Manchester, Jodrell Bank Observatory, Macclesfield, Cheshire, SK11
9DL, UK*

P. Augusto

*Universidade da Madeira, Dep. Matemática, Caminho da Penteada, 9050 Funchal,
Portugal*

We summarize the observed properties and lens modeling results of the unique JVAS system B2114+022. We argue that the observational and modeling results are most consistent with a two-plane lensing hypothesis, particularly for the widest separated and observationally similar radio components A and D. We point out the potential power of this system for constraining galactic mass models and hence deriving the relations between the light and mass distributions.

1 Observations: Radio and Optical

The JVAS (Jodrell VLA Astrometric Survey) quadruple radio source B2114+022 is unique among ~ 15000 flat spectrum radio sources observed in the JVAS and CLASS (Cosmic Lens All Sky Survey) surveys (e.g. Browne 2001). Although optical counterparts of the radio components have not yet been established, reliable radio and optical absolute astrometry shows (cf. Fig. 1) that amid the quadruple radio components lie two early-type galaxies which are close in projection ($d \approx 1.3$ arcsec) and have different redshifts ($z = 0.316$ and $z = 0.588$). In particular, three of the radio components are within 0.6 arcsec of the foreground galaxy (G1), and the fourth component lies at the opposite side of G1. This first probable genuine two-plane lens system is a unique laboratory for studying galactic mass models owing to the unique geometric arrangements of the radio components with respect to the galaxies and “intermediate” lensing of the background galaxy by the foreground galaxy.

Radio component properties: (cf. Fig. 2 & Fig. 3; Augusto et al. 2001)

- Components A & D are similar to each other in radio surface brightness distributions and radio spectra, and appear to be different from components B & C which are in turn similar to each other.
- Components A & D have milli-arcsecond (mas)-scale compact radio cores and some more extended emission; components B & C contain no unresolved mas-scale components and extended over ~ 20 mas.

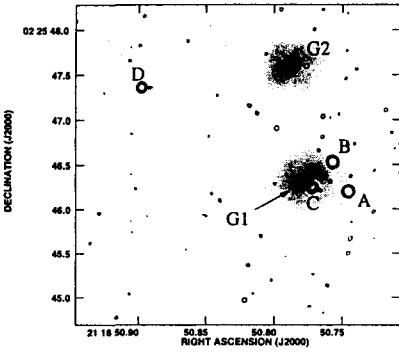


Figure 1: B2114+022: MERLIN Radio map superposed on HST NICMOS image

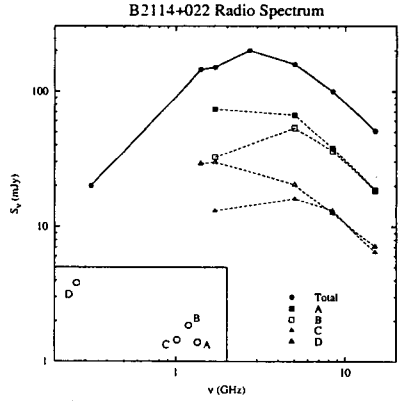


Figure 3: Radio spectra for B2114+022 and its components

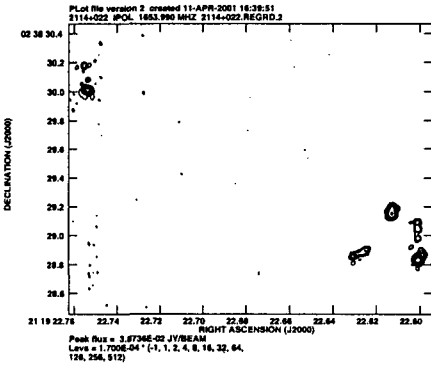


Figure 2: MERLIN+EVN 1.6 GHz Map

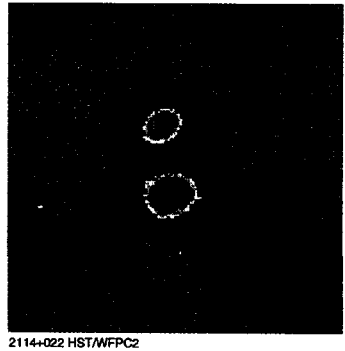


Figure 4: HST images of the two galaxies

- Components A & D have peak flux densities at $\nu \approx 2$ GHz with steeper spectra ($\alpha_{1.6}^{5.0} \approx -0.2$ to -0.1 in $S_\nu \sim \nu^\alpha$); components B & C have peak flux densities at $\nu \approx 5$ GHz with flatter spectra ($\alpha_{1.6}^{5.0} \approx 0.2$ to 0.4)
- Flux density ratio for components A and D: $f_\nu(A)/f_\nu(D) \approx 3$
- No optical or infrared emission has been detected from any of the radio sources down to $I = 25$ (*HST* WFPC2) and $H = 23$ (*HST* NICMOS).

Optical properties of the galaxies: (cf. Fig. 1 & Fig. 4; Augusto et al. 2001)

- Both galaxies are early-type galaxies with low/moderate ellipticities.
- The foreground galaxy G1's spectrum and color resemble those of a "post-starburst" galaxy; $V - H = 3.65 \pm 0.1$ and 4.65 ± 0.1 for G1 and G2 respectively.
- *Apparent* luminosity ratio of the galaxies: $L(G2)/L(G1) \sim 3$.

2 Lens Modeling

The observed properties of B2114+022, reviewed in §1, suggest that two-plane lensing is the most likely astrophysical origin, especially for components A and D cores along with their putative jets. The particular pieces of information supporting the lensing hypothesis are: (1) The positions of components A and D relative to the galaxies, (2) the small separation between G1 and component A ($d \approx 0.56$ arcsec), (3) the resemblance of components A and D to active galactic nuclei and *HST* limits on their optical/infrared brightnesses, and finally (4) the similarities of components A and D in their radio surface brightness distributions and radio spectra. All these pieces of information are consistent with a double lensing hypothesis for components A and D.

Bearing the above in mind, we are interested in answering the following two questions: (1) Can the radio components be reproduced by an astrophysically plausible lens model? (2) If yes, can this system be a robust astrophysical tool, in particular for constraining galactic mass models? Below, we attempt to answer these questions using simple power-law mass models (surface density $\kappa \sim r^{-\beta}$). Two important distinguishing features of two-plane lensing compared with single-plane two-galaxy lensing are (1) the lensing of the background galaxy by the foreground galaxy and (2) the existence of a cross term of the two potentials' 2nd derivative matrices in the inverse magnification matrix. In particular, we know *a posteriori* that isophotal shapes of G2 are modified in the sense of ellipticity change of $\Delta\epsilon \approx 0.2$ - 0.3 along east-west (Chae et al. 2001). In conjunction with the G2 image (Fig. 4), this implies that G2 is intrinsically approximately north-south oriented with low ellipticity ($\epsilon_{\text{light}} < 0.1$). In lens modeling below, we find that the data require that G2 mass distribution be approximately north-south oriented.

Double lensing scenario: We find that components A and D positions and flux density ratio can be successfully reproduced using power-law elliptical mass models for G1 and G2 whose position angles and ellipticities are broadly similar to those of the observed/inferred intrinsic light distributions. An example model using shallower-than-isothermal profiles ($\beta = 0.95$ and 0.7 for G1 and G2 respectively) is shown in Fig. 5. In this model, mass ellipticities for G1 and G2 are $\epsilon = 0.37$ and 0.29 respectively, which are higher than their respective intrinsic light ellipticities ($\epsilon_{\text{light}} \approx 0.2$ to 0.3 [G1] and 0 to 0.1 [G2]). The

mass position angles used are $PA = 120$ deg and 10 deg for G1 and G2 respectively. The ratio of the Einstein radii of the two galaxies is $R_E^{(1)}/R_E^{(2)} = 0.79$. The caustic structures for this model (cf. Fig. 5) are complicated and sensitive to model parameters. In particular, the source can easily cross the inner neighboring caustic as model parameters are varied; hence the requirement of no additional images sets limits on parameters (Chae et al. 2001).

Quadruple lensing scenario?:

Although observed radio surface brightness distributions of components B and C are apparently different from those of components A and D, it is of some interest to test a quadruple lensing hypothesis as a potential astrophysical origin for components B and C assuming that their radio surface brightness distributions were somehow modified by passage through the interstellar media of G1, since other explanations are not satisfactory anyway. It is also interesting to see how caustic structures for a quadruple lensing are changed from those of the double lensing case for this particular system. Fig. 5 shows the example of a quadruple lensing model. For this model, the power-law indices, mass ellipticities and position angles are $\beta = 0.9$ and 1 , $\epsilon = 0.07$ and 0.10 , and $PA = 89.4$ deg and 19.3 deg for G1 and G2 respectively. The ratio of the Einstein radii of the two galaxies is $R_E^{(1)}/R_E^{(2)} = 0.41$.

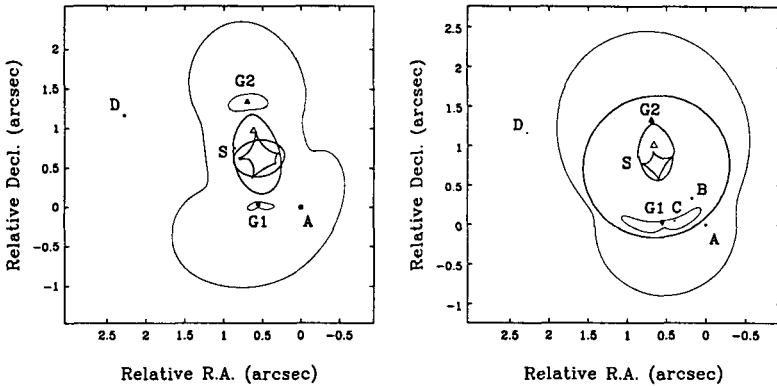


Figure 5: Caustics (thick lines) and critical curves (thin lines) for double lensing (left panel) and quadruple lensing (right panel) models for B2114+022

References

1. Augusto P., Browne I.W.A., Wilkinson P.N., Jackson N.J., et al., 2001, MNRAS, 326, 1007
2. Chae K.-H., Mao. S., Augusto P., 2001, MNRAS, 326, 101

DETECTING FLATTENED HALOS WITH WEAK LENSING

Tereasa G. Brainerd & Candace Oaxaca Wright
Boston University, Department of Astronomy
725 Commonwealth Ave., Boston, MA 02215, USA
E-mail: brainerd@bu.edu, cw@bu.edu

The systematic weak lensing of background galaxies by foreground galaxies has been detected by a number of different investigations. This effect is known as “galaxy–galaxy lensing” and it promises to provide strong constraints on the physical parameters of the dark matter halos which surround galaxies (such as their typical physical extents, total masses, and projected shapes). Here we use detailed Monte Carlo simulations to investigate galaxy–galaxy lensing by non–spherical dark matter halos and we estimate the area of a deep, ground–based imaging survey which would be required to detect the effects of flattened halos ($\langle\epsilon\rangle \sim 0.3$) on the galaxy–galaxy lensing signal.

1 Introduction

Recent attempts to detect the systematic weak lensing of background galaxies by foreground galaxies have been quite successful (see the review by Brainerd¹ and references therein). Generally good agreement has been found amongst these investigations and, in particular, observations of galaxy–galaxy lensing by the field galaxy population have yielded inferred velocity dispersions for the halos of L^* galaxies which are in good agreement with more traditional dynamical or hydrodynamical measurements ($\sigma_v \sim 140$ km/s to 190 km/s) and the inferred *maximum* radial extents of the halos of L^* galaxies are quite large ($> 100h^{-1}$ kpc to $\sim 250h^{-1}$ kpc).

To date, the published studies of galaxy–galaxy lensing by field galaxies have computed a value of the mean weak lensing shear, γ , via circular averages about the lens centers; i.e., the halos of the lenses are assumed to be spherically symmetric. However, detailed studies of a number of individual galaxies suggest that their dark matter halos are not spherically–symmetric (e.g., Keeton *et al.*², Sackett³, and Maller *et al.*⁴). In addition, high–resolution simulations of dissipationless cold dark matter models consistently result in galaxy halos with a mean projected ellipticity of $\langle\epsilon\rangle \sim 0.3$ (e.g., Dubinski & Carlberg⁵ and Warren *et al.*⁶), so from a theoretical standpoint it is not unreasonable to expect that dark matter halos are at least somewhat flattened on average.

If the halos of galaxies are flattened to the extent suggested by both current observations and theory, this should manifest itself in the galaxy–galaxy lensing signal and, so, it may be possible to use observations of galaxy–galaxy lensing to constrain the mean flattening of halos. In particular, if the halos

are elliptical in projection, an anisotropy will be induced in the galaxy–galaxy lensing signal. At a given angular distance, θ , from an elliptical lens, source galaxies which are located closer to the major axis of the mass distribution of the lens will experience greater shear than sources which are located closer to the minor axis (e.g., Schneider *et al.*⁷). Noting this, Natarajan & Refregier⁸ and Brainerd & Wright⁹ recently conducted preliminary investigations into the detectability of anisotropic galaxy–galaxy lensing. Both concluded that the signal should be detected by forthcoming wide–field surveys such as the Sloan Digital Sky Survey; however, these conclusions were based upon somewhat simplified calculations which assumed that all halos have identical ellipticities in projection on the sky, each distant source galaxy is lensed by one and only one foreground lens galaxy (i.e., “multiple deflections” were neglected), and the image shape parameters of lenses and sources were uncorrelated.

Here we report on our recent efforts to make a more realistic assessment of the detectability of anisotropic galaxy–galaxy lensing via detailed Monte Carlo simulations. A full account of our work is contained in Wright & Brainerd¹⁰ and here we present only a brief summary.

2 Monte Carlo Simulations of Galaxy–Galaxy Lensing

Our Monte Carlo simulations of galaxy–galaxy lensing due to flattened halos include the effects of multiple deflections on the final shapes of the images of the galaxies and they were designed to reproduce a number of observational constraints on the faint galaxy population: the number counts of galaxies, $\frac{d \log N}{dm}$, to a limiting magnitude of $I_{\text{lim}} = 25$ (e.g., Smail *et al.*¹¹), the shape of the redshift distribution of faint galaxies, $N(z)$, extrapolated to $I_{\text{lim}} = 25$ (e.g., LeFèvre *et al.*¹²), and the distribution of intrinsic image shapes as obtained from deep imaging with HST (e.g., Ebbels¹³). Each galaxy is assumed to reside within a dark matter halo which is represented by a truncated singular isothermal ellipsoid with a surface mass density of

$$\Sigma(\rho) = \frac{\sigma_v^2 \sqrt{f}}{2G} \left(\frac{1}{\rho} - \frac{1}{\sqrt{\rho^2 + x_t^2}} \right) \quad (1)$$

(e.g., Kormann *et al.*¹⁴). Here σ_v is the line of sight velocity dispersion, f is the axis ratio of the mass distribution as projected on the sky ($0 < f \leq 1$), x_t is a truncation radius, G is Newton’s constant, and $\rho^2 = x_1^2 + f^2 x_2^2$, where x_1 and x_2 are Cartesian coordinates.

For convenience we scale the velocity dispersion, truncation radius, and luminosity of each of the galaxies in terms of characteristic values which can

be associated with L^* galaxies:

$$\frac{\sigma_v}{\sigma_v^*} = \left(\frac{L}{L^*}\right)^{1/4} \quad \frac{x_t}{x_t^*} = \left(\frac{L}{L^*}\right)^{1/2}. \quad (2)$$

$$\frac{L}{L^*} = \left(\frac{H_0 D_d}{c}\right) (1+z)^{3+\alpha} 10^{0.4(22.9-I)}, \quad \alpha = -\frac{d \log_{10} L_\nu}{d\nu} \quad (3)$$

(e.g., Brainerd *et al.*¹⁵, hereafter BBS) and we take $\alpha = 0.42$, which is the mean slope between the R and B bands found in the Caltech Faint Galaxy Redshift Survey (Cohen *et al.*^{16, 17}). In addition, we adopt fiducial values of $\sigma_v^* = 156$ km/s and $x_t^* = 100h^{-1}$ kpc for the halos of L^* galaxies, both of which are in reasonable agreement with the current constraints based upon previous studies of galaxy–galaxy lensing by field galaxies.

At the start of the simulations, all galaxies are assigned random intrinsic position angles and it is assumed that the projected *mass* distribution of a halo is aligned with the major axis of the intrinsic *unlensed* image shape. An intrinsic ellipticity, $\epsilon \equiv 1 - b/a = 1 - f$, was assigned to each of the halos based upon a distribution function which was derived from current observational constraints on the principle moments of dark matter halos. Specifically, the values of b/a were drawn from a uniform distribution, $0.8 \leq b/a \leq 1.0$, and the values of c/a were drawn from a Gaussian distribution with a mean of 0.5 and a standard deviation of 0.2 (see, e.g., the review by Sackett³). The median and mean ellipticities of the resulting distribution are both of order 0.3.

For each galaxy in the simulation, then, we compute its final image shape due to weak lensing by foreground galaxies. Since galaxy–galaxy lensing occurs in the weak lensing regime, the net change in the shape of a distant galaxy which has been weakly lensed by more than one foreground galaxy can be computed simply as the (complex) vector sum of the shears induced by each of the individual lenses (e.g., Schneider *et al.*⁷). For each galaxy we can define an “intrinsic” shape parameter, $\vec{\gamma}_i$, which describes the image of the galaxy *prior to* being lensed:

$$\vec{\gamma}_i \equiv \frac{a-b}{a+b} e^{2i\phi}, \quad (4)$$

where a and b are the intrinsic major and minor axes of the unlensed image of the galaxy and ϕ is its intrinsic position angle. The final shape of a galaxy, $\vec{\gamma}_f$, after having been lensed by M foreground galaxies is then:

$$\vec{\gamma}_f = \vec{\gamma}_i + \sum_{j=1}^M \vec{\gamma}_j, \quad (5)$$

where $\vec{\gamma}_j$ is the weak shear due to lens j .

3 Mean Shear and Correlated Image Shapes

At a given angular distance, θ , from the center of an isolated elliptical lens, the magnitude of the shear is greatest for sources located nearest to the major axis of the lens and least for sources located nearest to the minor axis of the lens. Therefore, in a given radial annulus which is centered on the lens, the mean shear experienced by a source whose azimuthal coordinate, φ , places it within $\pm N^\circ$ of the major axis of the lens will be greater than that for a source whose azimuthal coordinate, φ , places it within $\pm N^\circ$ of the minor axis. We will denote the magnitude of the mean shear experienced by sources whose azimuthal coordinates place them within $\pm N^\circ$ of the minor axis of the lens as $\langle \gamma^- \rangle$ and, similarly, we will denote the magnitude of the mean shear experienced by sources whose azimuthal coordinates place them within $\pm N^\circ$ of the major axis of the lens as $\langle \gamma^+ \rangle$.

Using the final image shapes of the galaxies, $\vec{\gamma}_f$, we compute $\langle \gamma^- \rangle$ and $\langle \gamma^+ \rangle$ for all sources located within $N = 45^\circ$ of the projected symmetry axes of the *halos* of the lens galaxies. Here we will restrict our analysis to galaxies for which $19 < I < 23$, since a limiting magnitude of order $I = 23$ can be achieved in a reasonable amount of observing time with large ground-based telescopes. We do, however, include the effects of systematic lensing due to the galaxies with $23 \leq I \leq 25$ on the images of galaxies with $I < 23$ because the redshifts of some galaxies with $I \geq 23$ will, in fact, be smaller than the redshifts of some galaxies with $I < 23$. Results for the ratio $\langle \gamma^- \rangle / \langle \gamma^+ \rangle$ are shown in the left panel of Fig. 1 as a function of angular distance from the lens centers. As expected, the ratio is less than unity on small scales, but approaches unity on large scales (scales larger than the mean angular size of the lenses, $\langle x_t \rangle \simeq 33''$) since on large scales the truncated elliptical lenses begin to act similarly to point mass lenses.

Of course, in an observational data set one does not know the position angles of the halos *a priori* and, therefore, one must compute $\langle \gamma^- \rangle / \langle \gamma^+ \rangle$ using the observed position angles of the *images* of the foreground galaxies. In the right panel of Fig. 1 we show the results for $\langle \gamma^- \rangle / \langle \gamma^+ \rangle$, computed using the final, observed position angles of the lens galaxies and we note a quite striking trend: on angular scales larger than about $10''$, the values of $\langle \gamma^- \rangle$ actually *exceed* those of $\langle \gamma^+ \rangle$ and, hence, the ratio $\langle \gamma^- \rangle / \langle \gamma^+ \rangle$ is greater than unity!

If each source galaxy were lensed only once, and if all lens galaxies were truly isolated and not themselves lensed by foreground objects, then we would always expect $\langle \gamma^- \rangle / \langle \gamma^+ \rangle$ to be less than unity on small scales. However, since galaxies are broadly distributed in redshift and our simulations account for *all* weak lensing events for *all* galaxies, we do not have this idealized case. Instead,

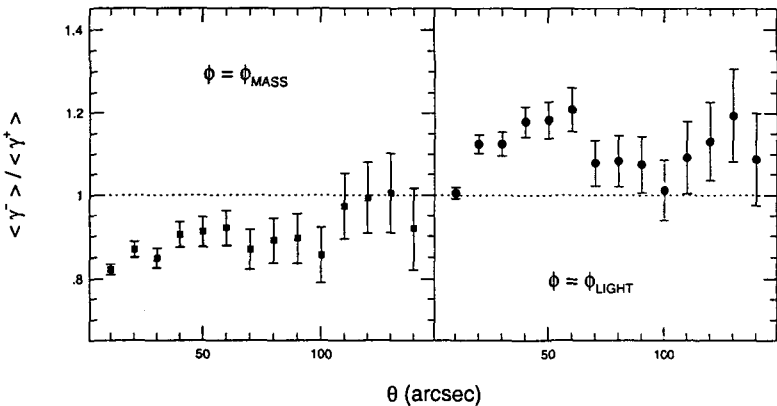


Figure 1: Left panel: $\langle \gamma^- \rangle / \langle \gamma^+ \rangle$ for all sources located within $N = \pm 45^\circ$ of the projected symmetry axes of the halos. Right panel: Same as left panel, except that here the major and minor axes of the lenses are defined by their final, post-lensing image shapes

consider the case of three galaxies with redshifts $z_1 < z_2 < z_3$. If the galaxy at z_3 is weakly lensed by both of the galaxies at z_2 and z_1 , and the galaxy at z_2 is also weakly lensed by the galaxy at z_1 , then correlated alignments of the post-lensing images of the galaxies at z_2 and z_3 will occur. This, in turn, will cause $\langle \gamma^- \rangle / \langle \gamma^+ \rangle$ as measured relative to the final image of the lens at z_2 to be greater than unity (effectively by decreasing the net ellipticity of sources at z_3 which are closest to the projected major axis of the halo of the lens at z_2 and, simultaneously, increasing the net ellipticity of sources at z_3 which are closest to the minor axis of the halo).

We quantify this effect using a correlation function of the image shapes, $C_{\gamma\gamma}(\theta) \equiv \langle \tilde{\gamma}_1 \cdot \tilde{\gamma}_2^* \rangle$, where the mean value is computed for all foreground-background pairs of galaxies separated by angles $\theta \pm \delta\theta/2$ on the sky (see, e.g., Blandford *et al.*¹⁸). Here $\tilde{\gamma}_1$ is the image shape of a galaxy with redshift z_1 and $\tilde{\gamma}_2^*$ is the complex conjugate of the image shape of a galaxy with redshift $z_2 > z_1$. This function measures the degree to which the images of galaxy 1 and galaxy 2 are aligned with one another and in the limit of no systematic alignments between images 1 and 2, $C_{\gamma\gamma}(\theta)$ is identically zero on all scales.

Shown in the left panel of Fig. 2 is $C_{\gamma\gamma}(\theta)$ computed using the *intrinsic* shape parameters, $\tilde{\gamma}_i$, of the galaxies which were used to obtain Fig. 1 above. Since the galaxies were assigned intrinsic shape parameters which were drawn at random, $C_{\gamma\gamma}(\theta)$ should be consistent with zero on all scales and this is the case in the left panel of Fig. 2. Shown in the right panel of Fig. 2 is

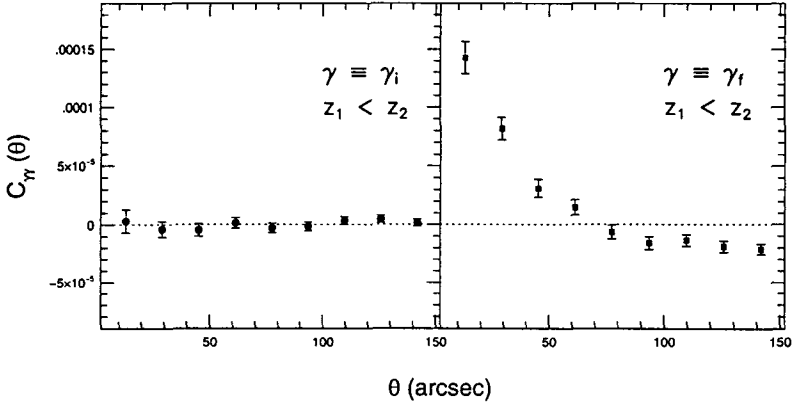


Figure 2: Left panel: Correlation function of the intrinsic (i.e., pre-lensing) images shapes. Right panel: Correlation function of the final, post-lensing image shapes.

$C_{\gamma\gamma}(\theta)$ computed using the *final* shape parameters, $\vec{\gamma}_f$, of the same galaxies and, clearly, there is a tendency for the images of foreground and background galaxies to be correlated. That is, we see that the effect of multiple weak lensing events on *pairs* of lenses and sources is to cause a slight tendency for the images of lenses and sources to be preferentially aligned with each other on scales of less than about 1 arcminute in our simulations.

This effect is strongest for foreground–background pairs in which the redshifts of the foreground and background objects are fairly similar and it should be possible to reduce the effect of correlated lens–source shape parameters by restricting our analysis to lens redshifts, z_d , which are relatively smaller than the source redshifts, z_s . There are many different ways in which one could imagine making such a cut in redshift space, but we find that simply restricting the analysis to sources with $z_s > 0.5$ and lenses with $z_d > 0.5$ is sufficient to break the correlations between the image shapes of the lenses and sources.

4 Detecting the Anisotropy

Having determined a straightforward way in which to separate the lensing–induced correlation in the images of foreground and background galaxies, we now wish to determine the size of a “realistic” observational data set which would be necessary in order to detect the effects of weak lensing by flattened halos. To do this, we define an anisotropy parameter $\mathcal{A} \equiv 1 - \frac{\langle \gamma^- \rangle}{\langle \gamma^+ \rangle}$ and ask the following simple question: If the halos of galaxies are flattened to the degree

that we have assumed, how large would an observational data set which is similar in quality to the BBS data set need to be in order to obtain a $4\text{-}\sigma$ detection of our anisotropy parameter, \mathcal{A} ?

For our estimate we will assume that multi-color photometry is available down to a limiting magnitude of $I_{\text{lim}} \sim 23$ and that it is of sufficient quality to yield photometric redshifts which are accurate to within an error of $\delta z \sim 0.1$ (this is comparable to the accuracy of the photometric redshift estimators which were investigated by Hogg *et al.*¹⁹). In addition, we account for image degradation due to seeing, sky noise, pixellation, etc. by following the procedure adopted by BBS: an error term is added to the final, post-lensing position angle of each galaxy. The error is, of course, dependent upon both the magnitude of the galaxy and its ellipticity (e.g., Table 2 of BBS). The median seeing of the BBS data was of order $0.9''$ FWHM and here we have extended their original image shape error analysis to somewhat brighter galaxies. Shown in Table 1 are the errors assigned to the post-lensing position angles of the galaxies in our simulations, based upon substacks of the BBS data.

Table 1: Errors Assigned to Post-Lensing Position Angles

ϵ	$19 < I < 20$	$20 < I < 21$	$21 < I < 22$	$22 < I < 23$
0.0–0.1	30°	30°	30°	35°
0.1–0.2	13°	16°	20°	25°
0.2–0.3	8°	11°	15°	20°
0.3–0.4	4°	6°	8°	10°
0.4–0.5	4°	6°	8°	10°
0.5–0.6	2°	3°	4°	5°
0.6–0.7	2°	3°	4°	5°

Using the redshifts and final image shapes to which errors have been assigned, we then compute \mathcal{A} and its significance as a function of the area of the survey. To reduce the correlations between foreground and background image shapes, we restrict the analysis to only those foreground galaxies with $z_{\text{phot}} < 0.5$ and background galaxies with $z_{\text{phot}} > 0.5$. We compute the average signal over angular scales of $5'' \leq \theta \leq 35''$, where the inner radius restriction insures that the isophotes of foreground and background galaxies will not overlap and the outer radius restriction is comparable to the mean angular size of the halos (i.e., a scale beyond which the anisotropy itself will decrease due to the lenses acting similarly to point masses).

Taking into account such fairly typical observational errors and accounting for the presence of correlated image ellipticities in the final data set, we find that a $4\text{-}\sigma$ detection of \mathcal{A} should be obtained with very wide field, multi-color

data sets even if the imaging quality is only modest (e.g., BBS). In particular, if the signal is averaged over angular scales of $5'' \leq \theta \leq 35''$ and all galaxies within $N = 45^\circ$ of the symmetry axes of the *images* of the lenses are used in the calculation, a survey of order 32 square degrees is necessary. The signal, of course, increases with proximity of the sources to the symmetry axes of the halos and, therefore, if we restrict the analysis to galaxies within $N = 20^\circ$ of the symmetry axes of the images of the lenses, the necessary survey area is reduced to of order 22 square degrees.

Acknowledgments

Support under NSF contracts AST-9616968 and AST-0098572, an NSF Graduate Minority Fellowship (COW), and a generous allocation of resources at Boston University's Scientific Computing and Visualization Center are gratefully acknowledged.

References

1. T. G. Brainerd, in *New Cosmological Data and the Values of the Fundamental Parameters*, proceedings of IAU Symposium 201, eds. A. Lasenby & A. Wilkinson, in press (2001)
2. C. R. Keeton, C. S. Kochanek & E. E. Falco, *ApJ* **509**, 561 (1998)
3. P. D. Sackett, in *Galaxy Dynamics*, ASP Conf. Series 182, eds. D. R. Merritt, M. Valluri & J. A. Sellwood, 393 (1999)
4. A. H. Maller, L. Simard, P. Guhathakurta, *et al.*, *ApJ* **533**, 194 (2000)
5. J. Dubinski & R. Carlberg, *ApJ* **378**, 496 (1991)
6. M. S. Warren, P. J. Quinn, J. K. Salmon, *et al.*, *ApJ* **399**, 405 (1992)
7. P. Schneider, J. Ehlers & E. E. Falco, *Gravitational Lensing*, Berlin: Springer-Verlag (1992)
8. P. Natarajan & A. Refregier, *ApJ* **538**, L113 (2000)
9. T. G. Brainerd & C. O. Wright, astro-ph/0006281
10. C. O. Wright & T. G. Brainerd, submitted to *ApJ*
11. I. Smail, D. W. Hogg, L. Yan, & J. G. Cohen, *ApJ* **449**, L105 (1995)
12. O. LeFèvre, D. Hudon, S. Lilly, *et al.*, *ApJ* **461**, 534 (1996)
13. T. Ebbels, PhD Thesis, Univ. of Cambridge (1998)
14. R. Kormann, P. Schneider & M. Bartelmann, *A & A* **284**, 285 (1994)
15. T. G. Brainerd, R. D. Blandford & I. Smail, *ApJ* **466**, 623 (1996)
16. J. Cohen, R. Blandford, D. W. Hogg, *et al.*, *ApJ* **512**, 30 (1999)
17. J. Cohen, D. W. Hogg, M. A. Pahre, *et al.*, *ApJS* **120**, 171 (1999)
18. R. D. Blandford, A. B. Saust, *et al.*, *MNRAS* **251**, 600 (1991)
19. D. W. Hogg, J. G. Cohen, R. Blandford, *et al.*, *AJ* **115**, 1418 (1998)

FINDING THE ARCINESS IN ARCLETS EXPLORING THE OCTOPOLE MOMENTS OF LENSED GALAXIES

D. M. Goldberg
*Yale University Astronomy Dept.,
New Haven, CT 06520-8101*

We introduce the octopole moment measurement of the light distribution in galaxies as a probe of the weak lensing shear field. While traditional ellipticity estimates of local shear have traditionally been limited by the width of the background intrinsic ellipticity distribution, the dispersion in the intrinsic octopole distribution is expected to be quite small, meaning that the signal is ultimately limited by measurement noise, not by intrinsic scatter. In a series of estimates, we show that current observations are at the regime where the octopole estimates will be able to contribute to the overall accuracy of the estimates of local shear fields.

1 Introduction

The analysis of weak shear fields of background galaxies lensed by clusters has proved to be a rich field of inquiry (Kaiser, Squires & Broadhurst, 1995, hereafter KSB; Mellier 1999; Bartelmann & Schneider, 2001 and references therein). It is generally taken for granted that strong lensing of galaxies, whether producing multiple images or strong arcs, should be analyzed in a fundamentally different way from weakly lensed “arclets”. It is not clear that the transition between arclet and arc is as abrupt as the current mode of analysis would suggest. Another way of thinking about strong arcs is that lensing induces large octopole moments in the light distribution. This octopole has two components: a skewness in the light distribution away from the lens, and a term which expresses itself as an arc tangential to the surface of constant shear. We explore this transition from arclet to arc.

2 The Octopole Moments

As a number of talks in this volume have discussed the KSB approach to weak lensing, we will dispense with a presentation of the standard lensing equations, and will begin by addressing the issue of analysis of higher order moments of the light distribution. Even in the weak lensing limit in which one would strictly not expect to be able to detect gravitational arcs, an arc-like signature can be found from the octopole moments of the galaxy light distribution.

We assume a radially symmetric potential throughout, and for a fiducial galaxy we further choose the coordinate system with a configuration such that

it lies along the positive x-axis. Using only linear theory, the lensed (subscript θ) and unlensed (subscript β) multipole moments of the galaxy light distribution can be related in a very straightforward way:

$$\langle x^n y^m \rangle_\theta = [A_{11}^{-1}]^n [A_{22}^{-1}]^m \langle x^n y^m \rangle_\beta = \frac{1}{(1 - \kappa - \gamma)^n} \frac{1}{(1 - \kappa + \gamma)^m} \langle x^n y^m \rangle_\beta, \quad (1)$$

where κ is the local convergence, γ is the shear, and the diagonalized amplification matrix, A_{ij} , can be defined by inspection. The second order Taylor expansion of the lensing equation can give rise to additional octopole moments:

$$\beta_i \simeq A_{ij} \theta_j + \frac{1}{2} A_{ij,k} \theta_j \theta_k. \quad (2)$$

To second order in the position, the above equations may be inverted by exploiting the properties of the derivatives of the shear and convergence:

$$\begin{aligned} x_\theta &\simeq A_{11}^{-1} x_\beta + A_{11}^{-3} \left[\gamma' + \frac{\gamma}{r} \right] x_\beta^2 + A_{11}^{-1} A_{22}^{-2} \frac{\gamma}{r} y_\beta^2 \\ y_\theta &\simeq A_{22}^{-1} y_\beta + A_{11}^{-1} A_{22}^{-2} \frac{2\gamma}{r} x_\beta y_\beta. \end{aligned} \quad (3)$$

From this coordinate transformation, we may also compute the expectation values of the observables, $\langle x^3 \rangle_\theta$ and $\langle xy^2 \rangle_\theta$:

$$\begin{aligned} \langle x^3 \rangle_\theta &= A_{11}^{-3} \langle x^3 \rangle_\beta + \left[2 \frac{g}{r(1+g)} + 5 \left(\frac{g' - g/r - g^2/r}{1-g^2} \right) \right] \langle x^4 \rangle_\theta + 3 \frac{g}{r(1-g)} \langle x^2 y^2 \rangle_\theta \\ &\quad - \left[9 \left(\frac{g' - g/r - g^2/r}{1-g^2} \right) + 6 \frac{g}{r(1+g)} \right] \langle x^2 \rangle_\theta^2 - 3 \frac{g}{r(1-g)} \langle x^2 \rangle_\theta \langle y^2 \rangle_\theta^2 \end{aligned} \quad (4)$$

$$\begin{aligned} \langle xy^2 \rangle_\theta &= A_{11}^{-1} A_{22}^{-2} \langle xy^2 \rangle_\beta + \left[3 \left(\frac{g' - g/r - g^2/r}{1-g^2} \right) + 6 \frac{g}{1+g} \right] \langle x^2 y^2 \rangle_\theta + \frac{g}{1+g} \langle y^4 \rangle_\theta \\ &\quad - \left[3 \left(\frac{g' - g/r - g^2/r}{1-g^2} \right) + 2 \frac{g}{1+g} \right] \langle x^2 \rangle_\theta \langle y^2 \rangle_\theta - \frac{g}{1-g} \langle y^2 \rangle_\theta^2 \end{aligned} \quad (5)$$

In both of these, the terms proportional to squares of the quadrupole moments arise from a second order shift in the center of light.

3 Error Analysis and Parameter Estimation

3.1 Estimation of the Errors on the Moments

We must measure both the octopole moments and the hexadecipole moments with some accuracy in order to extract the shear, and since both moments are

much more likely to be contaminated by sky noise than their quadrupole counterparts, it is possible that measuring these moments may be quite difficult.

One may approximate the uncertainty in $\langle x^n y^m \rangle$, $\sigma_{n,m}$ as:

$$\sigma_{n,m}^2 \simeq \frac{\int_0^{2\pi} d\theta \cos^{2n}(\theta) \sin^{2m}(\theta) \int_0^\infty dr w^2(r, \theta) r^{1+2n+2m} [I(r, \theta) + N]}{\left(\int_0^{2\pi} d\theta \int_0^\infty dr w(r, \theta) r I(r, \theta) \right)^2}, \quad (6)$$

where $I(r, \theta)$ is the surface brightness in counts/area of the galaxy, N is the background sky brightness in counts/area, and $w(r, \theta)$ is a mask.

3.2 Results

It now remains for us to compare errors estimated from the quadrupole moments alone to those from the octopole moments. The fiducial galaxy has a magnitude of 22 at $z = 0.5$, and has a half-light radius in the source plane of 2 kpc and a de Vaucouleurs profile. Error estimates are made for observations taken using the HST Wide Field camera using a 16.8 ks exposure. Signal and sky counts were estimated using the HST WFPC2 exposure time calculator ^a. The lens and source are separated by 100 pixels in the image, and we take a 2% mean shear.

The error ellipses from the quadrupole and octopole estimates of g and rg' , along with their combined ellipse can be found in Fig. 1, suggesting that the octopole signal may well be measurable.

4 Discussion and Future Prospects

In this talk, we have introduced a new and potentially powerful way of analyzing weak lensing shear fields – using the octopole moments of the observed light distribution as a second-order estimator of shear. In addition to estimating the shear, we also get an estimate of its radial derivative.

While we have demonstrated that within the range of reasonable physical and observational parameters the corresponding measurement uncertainties may be comparable to those found using traditional ellipticity estimates of the shear, much remains to be done, both theoretically and observationally.

The Gaussian mask used in estimating the octopole and quadrupole moments is almost certainly not optimal for this technique. One avenue of inquiry is to apply a second-order analysis to the Shapelet (Refregier, 2001; Refregier & Bacon, 2001; this volume) technique in order to get a comparable signal.

^a<http://www.stsci.edu/instruments/wfpc2/Wfpc2.etc/wfpc2-etc.html>

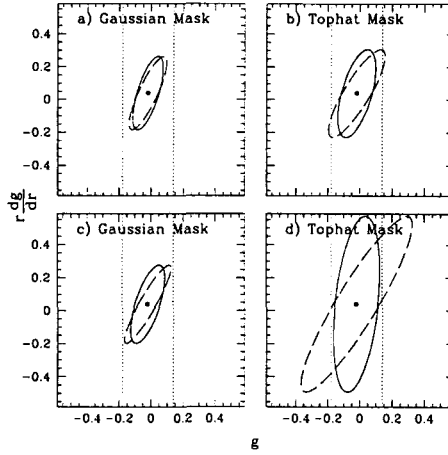


Figure 1: The calculated error ellipses using the method described in the text. The dotted lines represent the 1σ errors on g from the quadrupole technique alone. The dashed line represents the $1 - \sigma$ error ellipse on g and rg' from the octopole method. The solid ellipse is the combined error estimate. Panels a) and c) use Gaussian masks, as described in KSB, with characteristic radii set to the R_e and $2R_e$, respectively. Panels b) and d) use tophat masks, with radii equal to $2R_e$ and $4R_e$, respectively.

Future implementations of this technique will incorporate this sort of sophisticated mode of shape estimation.

Acknowledgments

The author would like to gratefully acknowledge collaboration with Priya Natarajan. We would also like to thank Ue-Li Pen and Tereasa Brainerd for helpful discussions.

References

1. Bartelmann, M. & Schneider, P., 2001, *Phys. Rep.*, 340, 291
2. Kaiser, N., Squires, G., & Broadhurst, T. 1995, *ApJ*, 449, 460
3. Mellier, Y., 1999, *ARA&A*, 37, 127
4. Refregier, A. & Bacon, D. 2001, submitted to *MNRAS*, preprint at <http://xxx.lanl.gov/abs/astro-ph/0105179>
5. Refregier, A. 2001, submitted to *MNRAS*, preprint at <http://xxx.lanl.gov/abs/astro-ph/0105178>

DETERMINING THE THREE-DIMENSIONAL SHAPES OF GALAXY CLUSTERS

Andres Escala and Priyamvada Natarajan
*Department of Astronomy,
Yale University,
New Haven, CT 06520-8101*

In this contribution, we illustrate that by combining lensing and X-ray surface brightness data the elongation of clusters along the line-of-sight can be estimated. The distribution of three dimensional shapes of the mass in clusters of galaxies could potentially place constraints on Ω and provide clues to the nature of dark matter. With the abundance of multi-wavelength data the prospects for mapping the three-dimensional shapes are promising.

1 Introduction

Clusters of galaxies have 3 constituents: dark matter (the dominant component), hot gas in the Intra-Cluster Medium (ICM hereafter), and galaxies. There are at present several independent and reliable techniques available to measure the mass of clusters of galaxies: gravitational lensing and X-ray observations are the methods that we will focus on. Gravitational lensing offers a powerful probe of the projected mass distribution in clusters and its efficacy derives from the fact that the estimates are independent of the dynamical state of the cluster. The radial mass profile of clusters is constructed using constraints from both the strong and weak lensing regimes. The multiple images and highly distorted arcs in the core regions can be used to calibrate the mass in the weak regime which is obtained using the distorted shapes of background galaxies viewed through the fore-ground cluster lens. Several sophisticated mapping techniques that yield high-resolution mass maps have been developed and applied successfully (Kaiser & Squires 1993; see Bartelmann & Schneider 2001 a for comprehensive review).

Deriving masses from the X-ray surface brightness profile, while robust, does require making several assumptions with regard to the state of the ICM gas - first, it is assumed that the gas is an efficient tracer of the dark matter potential well and secondly, that the gas is, in fact, in hydro-static equilibrium in the potential. Additionally, we assume that the cluster galaxies are also good tracers of the potential. However, with these set of assumptions, mass profiles of clusters from X-ray data have been constructed and in most cases the obtained estimates from both of these techniques are in agreement (Allen et al. 1996; Wu 2000).

2 Combining X-ray and Lensing data

Assuming that the ICM gas is in hydrostatic equilibrium with the underlying gravitational potential

$$\frac{1}{\rho_g} \nabla p = -\nabla \Phi, \quad (1)$$

where ρ_g is the gas density, p the pressure and Φ the gravitational potential. For simplicity we also assume that if there exist any non-thermal sources of pressure support, say, due to cosmic rays, magnetic fields or turbulence, these can be simply added to the pressure term on the LHS assuming that these terms don't have a radial dependence and are proportional to the thermal pressure, i.e. $p_{nt} = \alpha p_t$ with $\alpha = \text{constant}$. In the case of an ideal gas equation of State ($p = \rho_g kT / \mu m_p$), coupled with the eqn. (1) we have,

$$\frac{(1 + \alpha)kT}{\mu m_p \rho_g} \nabla \rho_g = -\nabla \Phi, \quad (2)$$

where the temperature gradient term has been neglected. Since the underlying dark matter potential dominates the dynamics of the galaxies, then we treat them as collisionless test particles and use the Jeans equation to describe them for the case of spherical symmetry,

$$\frac{1}{\rho_{gal}} \frac{d(\sigma_r^2 \rho_{gal})}{dr} + \frac{\rho_{gal}}{r} (2\sigma_r^2 - \sigma_\phi^2 - \sigma_\theta^2) = -\frac{d\Phi}{dr}, \quad (3)$$

σ_i are the three components of the velocity dispersion and ρ_{gal} is the galaxy number density profile. In the case of isotropic velocity dispersion ($\sigma_r^2 = \sigma_\phi^2 = \sigma_\theta^2$) & , eliminating the potential between the eqns. (2) & (3),

$$\frac{d \ln(\rho_g)}{dr} = \frac{\mu m_p \sigma_r^2}{(1 + \alpha)kT} \frac{d \ln(\rho_{gal})}{dr} \quad (4)$$

integrating the above, we obtain $\rho_g \propto \rho_{gal}^\beta$ with

$$\beta = \frac{\mu m_p \sigma_r^2}{(1 + \alpha)kT} \quad (5)$$

when the galaxy distribution ρ_{gal} is given by the analytic King approximation to the isothermal sphere,

$$\rho_{gal} = \rho_o (1 + r^2/r_c^2)^{-\frac{3}{2}}, \quad (6)$$

yielding the conventional isothermal β model

$$\rho_g = \rho_{g0} \left(1 + \frac{r^2}{r_c^2}\right)^{-\frac{3}{2}\beta} \quad (7)$$

The β defined in eqn. (5) can be determined from the X-ray surface brightness profile, and the measurements of the velocity dispersion and the gas temperature from X-ray spectra.

The ICM gas is modeled using an ellipsoidal β model profile (prolate):

$$\rho_g = \rho_{g0} \left(1 + \frac{R^2}{R_c^2} + \frac{z^2}{z_c^2}\right)^{-\frac{3}{2}\beta}. \quad (8)$$

Assuming that this prolate distribution has the axis along the line of sight, the total projected mass at a given radius R can be computed (Loeb & Mao 1994) which can be directly compared to mass estimate from gravitational lensing. Integrating eqn. (2) we obtain,

$$\Phi = -\frac{(1 + \alpha)kT}{\mu m_p} \ln \rho_g + C_0, \quad (9)$$

where C_0 is a constant. Using the Poisson's equation ($\nabla^2 \Phi = 4\pi G$) the total projected mass density is,

$$M(R)_{X\text{-ray}} = -\int_{\text{volume}} \frac{(1 + \alpha)kT}{4\pi G \mu m_p} \nabla^2 \ln \rho_g dV = -\frac{(1 + \alpha)kT}{4\pi G \mu m_p} \int_{\text{surface}} \nabla \ln \rho_g \cdot dS \quad (10)$$

using Gauss's theorem. Evaluating the expression for the prolate gas distribution,

$$M(R)_{X\text{-ray}} = \frac{\pi kT}{G \mu m_p} \frac{3\beta}{2} \frac{R^2}{(R^2 + R_c^2)^{1/2}} (1 + \alpha) \frac{z_c}{R_c}. \quad (11)$$

The projected mass profile from lensing is constructed by calibrating the weak lensing shear field at large radius with the tightly constrained strong lensing model in the inner regions. In the case of a circularly symmetric gravitational lens, the projected cluster mass enclosed with the Einstein radius ($r_E \sim r_{arc}$) in the strong lensing regime is:

$$M^{lens}(r = r_{arc}) = \pi r_{arc}^2 \Sigma_{crit} = \frac{c^2}{4G} \frac{d_S}{d_L d_{LS}} r_{arc}^2, \quad (12)$$

where d_S is the angular diameter distance from the observer to the source, d_L that between the observer and lens, d_{LS} between the lens and source, r_{arc} is

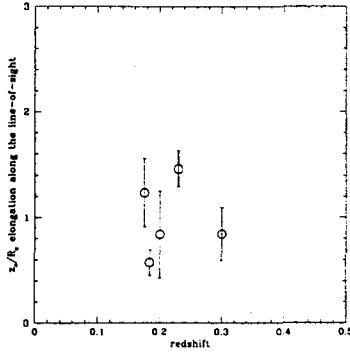


Figure 1: The elongation along the line of sight for 4 clusters estimated by combining lensing and X-ray data. The error bars plotted are $1 - \sigma$ error-bars.

the radius of the arc and Σ_{crit} the critical surface mass density. This value of $M^{lens}(r = r_{arc})$ is used to normalize the mass profile at large radius obtained from the shear field.

Since the gas traces the same gravitational potential, we require both measurements to give the same projected mass, i. e. $M^{lens}(r) = M^{X-ray}(R)$, this condition enables us to deproject the cluster,

$$\frac{z_c}{R_c} = \frac{2G}{3\sigma_r^2} \Sigma_{crit}(r_{arc}^2 + R_c^2)^{1/2} \quad (13)$$

We illustrate the above method by applying to the following cluster lenses: (i) A2218 at $z = 0.175$; (ii) A963 at $z = 0.2$; (iii) A1689 at $z = 0.18$; (iv) A2390 at $z = 0.23$.

3 Results

We present a method to estimate the elongation of clusters along the line of sight by combining X-ray and lensing data. This will enable the determination of the three-dimensional shape of clusters of galaxies.

References

1. Bartelmann, M., & Schneider, P., 2001, Phys. Rep., 340, 291
2. Allen, S. W., Fabian, A. C., & Kneib, J.-P., 1996, MNRAS, 279, 615
3. Kaiser, N., & Squires, G., 1993, ApJ, 404, 441
4. Loeb, A., & Mao, S., 1994, ApJ, 435, L109
5. Wu, Xiang-Ping, 2000, MNRAS, 316, 299

SHAPES OF DARK MATTER HALOS

J. S. Bullock

*Department of Astronomy, The Ohio State University ,
140 W. 18th Ave, Columbus, OH 43210
E-mail: james@astronomy.ohio-state.edu*

I present an analysis of the shapes of dark matter halos in Λ CDM and Λ WDM cosmologies. The main results are derived from a statistical sample of galaxy-mass halos drawn from a high resolution Λ CDM N-body simulation. Halo shapes show significant trends with mass and redshift: low-mass halos are rounder than high mass halos, and, for a fixed mass, halos are rounder at low z . Contrary to previous expectations, which were based on cluster-mass halos and non-COBE normalized simulations, Λ CDM galaxy-mass halos at $z = 0$ are not strongly flattened, with short to long axis ratios of $s = 0.70 \pm 0.17$. I go on to study how the shapes of individual halos change when going from a Λ CDM simulation to a simulation with a warm dark matter power spectrum (Λ WDM). Four halos were compared, and, on average, the WDM halos are more spherical than their CDM counterparts ($s \simeq 0.77$ compared to $s \simeq 0.71$). A larger sample of objects will be needed to test whether the trend is significant.

1 Introduction

A variety of observational indicators suggest that galaxies are embedded within massive, extended dark matter halos, lending support to the idea that a hierarchical, cold dark matter (CDM) based cosmology may provide a real description of the universe, especially on large scales (see, e.g., the review by Primack¹¹ and references therein). A useful small-scale test of CDM and variant theories may come from observations aimed at inferring the density structure of dark halos. Specifically, the quest to measure dark halo shapes has developed into a rich and complex subfield of its own.^{4,12}

Predictions for shapes of dark matter halos formed by dissipationless gravitational collapse are most reliably derived using numerical studies.^{6,5,14} These past investigations focused on galaxy-sized halos formed from power-law or pre-COBE CDM power spectra, and found that halos were typically flattened triaxial structures, with short-to-long axis ratios of $s \simeq 0.5 \pm 0.15$. Examinations based on currently favored cosmologies have been done, but they studied only cluster mass halos,^{8,13,9} and also found significantly flattened objects, $s \sim 0.4 - 0.5$. Interestingly, Thomas and collaborators¹³ saw an indication that low matter density models (with early structure formation) tended to produce more spherical clusters than high density models. This result was qualitatively consistent with indications from Warren et al.¹⁴ that high-mass halos are more flattened than (early-forming) low-mass halos. In light of these

hints that formation history plays a role in setting halo shapes, it is important to re-examine the question for a currently standard cosmological model. Specifically, this work aims at characterizing halo flattening as a function of mass and redshift for the popular flat Λ CDM cosmology. I also explore how shapes of halos are affected when going to a Λ WDM model, in which the power spectrum is damped on small scales.

2 Simulations and shape measurement

The simulations were performed using the Adaptive Refinement Tree (ART) code.⁷ The main results are derived from a Λ CDM simulation with $\Omega_m = 0.3$, $\Omega_\Lambda = 0.7$, $h = 0.7$, and $\sigma_8 = 1.0$, which followed 256³ particles of mass $1.1 \times 10^9 h^{-1} M_\odot$ within a periodic box of comoving length $60 h^{-1}$ Mpc, obtaining a formal force resolution of $1.8 h^{-1}$ kpc. A second simulation was run until $z = 1.8$ with the same particle number, half the box size, and thus eight times the mass resolution; it was used to check resolution issues. Dark halos were identified using a (spherical) bound density maxima method,² and masses were determined by counting particles within the spherical virial radius R_v , inside which the mean overdensity has dropped to a value $\Delta_v \simeq (18\pi^2 + 82p - 39p^2)/(1 + p)$, where $p \equiv \Omega_m(z) - 1$. This sample contains ~ 800 halos that span the mass range $3 \times 10^{11} - 5 \times 10^{14}$.

A second pair of simulations¹ were used to explore how shapes of halos are affected by damping the power spectrum. We compare four halos, each simulated from the same initial conditions, for a Λ CDM and Λ WDM model with the multiple-mass ART code and the same cosmological parameters and effective mass per particle discussed above. The filter mass scale for the Λ WDM run was $1.7 \times 10^{14} h^{-1} M_\odot$, and the four halos we compare have masses $(2 - 8) \times 10^{13} h^{-1} M_\odot$.^a Simulation results were kindly supplied by P. Colín.

Halo axis ratios are determined using the moments of the particle distributions within the virial radius R_v . The short-to-long axis ratio, s , and intermediate-to-long axis ratio q are calculated by iteratively diagonalizing the tensor⁵

$$M_{ij} = \Sigma \frac{x_i x_j}{a^2}, \quad a \equiv \sqrt{x^2 + \frac{y^2}{q^2} + \frac{z^2}{s^2}}, \quad (1)$$

where $q^2 \equiv M_{yy}/M_{xx}$ and $s^2 \equiv M_{zz}/M_{xx}$.

^aAlthough this filtering mass is much too large to be consistent with Ly- α forest measurements,¹⁰ the simulation provides a useful comparison to test the effect of an imposed filtering scale, since the halo masses considered are well within the affected regime. Since

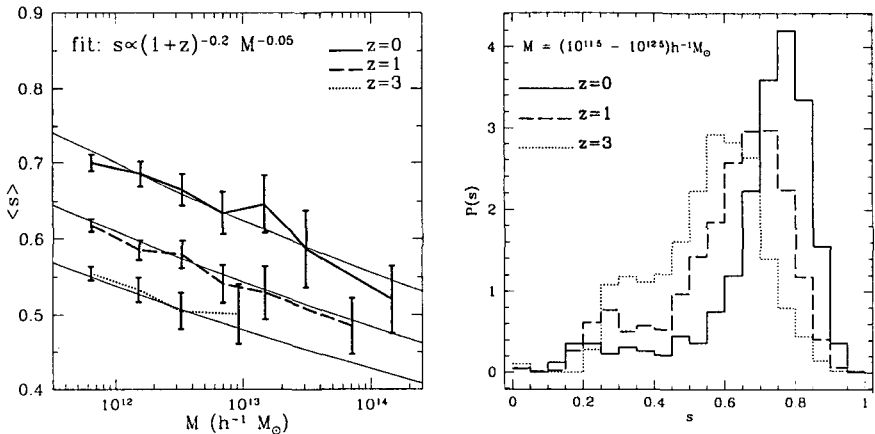


Figure 1: (Left) The average short-to-long axis ratio, s , as a function of halo mass at $z = 0$, 1, and 3. Error bars reflect the Poisson uncertainty associated with the number of halos in each mass bin and *not* the scatter about the relation. (Right) Distribution of measured s values for $\sim 10^{12} h^{-1} M_{\odot}$ halos as a function of z

3 Results

The left panel in Fig. 1 shows the average value of s as a function of halo mass for three redshifts, $z = 0$, 1, and 3. Low mass halos, on average, are rounder than high mass halos, as are halos of fixed mass at low z . The relation is well-approximated by $s \simeq 0.7(M/10^{12} h^{-1} M_{\odot})^{-0.05}(1+z)^{-0.2}$ over the mass and redshift ranges explored. The right panel of Fig. 1 shows the distribution of s parameters for galaxy-mass halos as a function of z . The average and rms dispersion in these distributions are $s = 0.70 \pm 0.17$, 0.61 ± 0.17 , and 0.55 ± 0.15 , for $z = 0$, 1, and 3, respectively. Note that the distributions are quite non-Gaussian, with a significant tail of highly flattened halos.^b

How do the shapes of halos change with radius? The axial ratios presented in Fig. 1 were obtained using particles within R_v . The left panel of Fig. 2 shows this average “virial” flattening measurement as a function of halo mass (at $z = 0$) compared with the average s measured within a sphere of radius $30 h^{-1} \text{kpc}$ for each halo. Although the difference is quite small for the low mass halos (since $30 h^{-1} \text{kpc}$ contains much of the halo mass), generally halos

the effect should simply scale with the filtering mass, similar results would be obtained for $\sim 5 \times 10^{10} h^{-1} M_{\odot}$ halos formed from $\sim 1 \text{keV}$ WDM particles.

^bIn order to check resolution effects, the $z = 3$ distribution was compared to the corresponding one obtained in the high resolution simulation and found to be statistically equivalent.

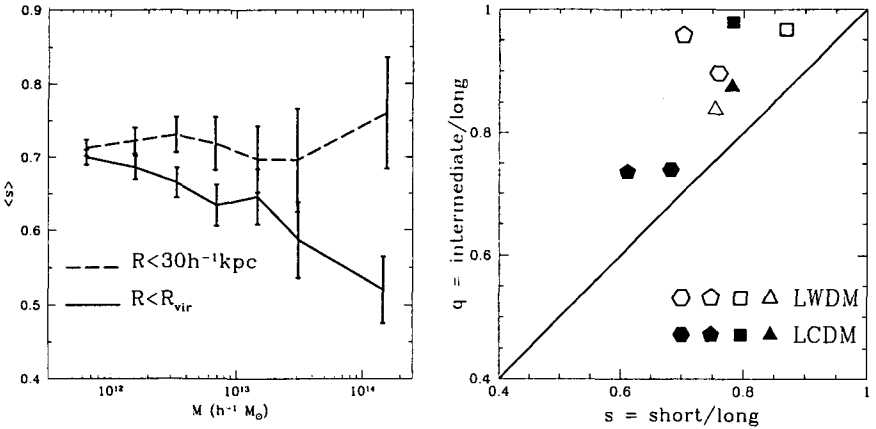


Figure 2: (Left) s as a function of mass measured within halo virial radii R_{vir} (solid) and within $30 h^{-1} \text{kpc}$ spheres from halo centers. (Right) q and s parameters for halos simulated using ΛCDM (solid symbols) and ΛWDM (open symbols) cosmologies. Individual halos, identified by mass and location between the two runs maintain the same symbol shape.

are rounder at small radii. Interestingly, within this fixed central radius, halos typically have the same flattening, $s \sim 0.7$, independent of the halo mass.

Finally in the right panel of Fig. 2, we compare the measured s and q values of four halos, simulated in ΛCDM and ΛWDM . There is a tendency for the halos to be rounder (approaching the upper right corner) in WDM, although one halo (designated by the triangles) does become slightly flatter in WDM. The average flattening shifts from $s \simeq 0.71$ for CDM to 0.77 for WDM, but it is difficult to make strong conclusions based on four halos. Indeed, Moore⁹ has simulated a single halo using CDM and WDM power spectra and finds a very similar shape for each. A larger sample of objects will be needed to test for systematic trends.

4 Conclusions

We find that ΛCDM galaxy-mass halos at $z = 0$ are more spherical than previously believed, with $s = 0.70 \pm 0.17$. High mass halos show more substantial flattening, as do halos of fixed mass at high redshift: $s \propto (1+z)^{-0.2} M^{-0.05}$. Halos are also more spherical in their centers, and tend to become more flattened near the virial radius. These trends suggest collapsed structures become more spherical with time, perhaps because they have had more time to phase mix and to obtain isotropic orbit distributions. It is also possible that the

accretion history itself plays a role. Halos formed within a Λ WDM simulation show a slight indication of being less flattened than their Λ CDM counterparts. This may be a reflection of substructure differences between the two models, but a larger number of halos will be needed to decisively test this conclusion. A more complete description of these results, and some discussion of shape correlation with other halo parameters is presented in a forthcoming paper.³

Acknowledgments

I thank my collaborators Pedro Colín, Ricardo Flores, Andrey Kravtsov, Anatoly Klypin, Ariyeh Maller, Joel Primack and Risa Wechsler for allowing me to present our results here. Thanks to Tsafrir Kolatt, Ben Moore, and David Weinberg for insightful discussions, and to Priya Natarajan for organizing this stimulating meeting. This work was supported by NASA LTSA grant NAG 5-3525 and NSF grant AST-9802568.

References

1. V. Avila-Reese et al., 2001, *ApJ*, 559, 516
2. J.S. Bullock et al. 2001, *MNRAS*, 321, 559
3. J.S. Bullock, R. Flores, A.V. Kravtsov, A.A. Klypin, J.R. Primack, A. Maller, and R.H. Wechsler, in preparation
4. D. Buote 2001; M.R. Merrifield 2001; L.S. Sparke 2001 (these proceedings)
5. J. Dubinski and R.G. Carlberg 1991, *ApJ*, 378, 496
6. C.S. Frenk et al., 1988 *ApJ*, 372, 507
7. A.V. Kravtsov et al., 1997 *ApJS*, 111, 73
8. J.J. Mohr et al., 1995 *ApJ*, 447, 8
9. B. Moore, 2001 (these proceedings)
10. V.K. Narayanan et al. 2000, *ApJ*, 543, L103; R. Barkana et al., 2001, *ApJ*, 558, 482; S.H. Hansen et al., 2001, *astro-ph/0106108*
11. J.R. Primack, ASP Conf. Ser. 201: Cosmic Flows Workshop, 2000, Eds. S. Courteau and J. Willick, 389, *astro-ph/0007187*
12. P.D. Sackett, ASP Conf. Ser. 182: Galaxy Dynamics - A Rutgers Symposium, August 1999, eds. D.R. Merritt et al., 393, *astro-ph/9903420*; K.V. Johnston et al. 1999, *ApJL*, 512, 109; Ibata et al., 2001, *ApJ*, 551, 294
13. P.A. Thomas et al. 1998, *MNRAS*, 296, 1061
14. M.S. Warren et al. 1992, *ApJ* 399, 405

SUBSTRUCTURE IN CDM HALOS AND THE HEATING OF STELLAR DISKS

Julio F. Navarro
Department of Physics and Astronomy,
University of Victoria,
Victoria, BC, V8P 1A1, Canada

Numerical simulations have revealed the presence of long-lived substructure in Cold Dark Matter (CDM) halos. These surviving cores of past merger and accretion events vastly outnumber the known satellites of the Milky Way. This finding has prompted suggestions that substructure in cold dark matter (CDM) halos may be incompatible with observation and in conflict with the presence of thin, dynamically fragile stellar disks. N-body simulations of a disk/bulge/halo model of the Milky Way that includes several hundred dark matter satellites with masses, densities and orbits derived from high-resolution cosmological CDM simulations indicate that substructure plays only a minor dynamical role in the heating of the disk. This is because the orbits of satellites seldom take them near the disk, where their tidal effects are greatest. We conclude that substructure might not preclude virialized CDM halos from being acceptable hosts of thin stellar disks like that of the Milky Way.

1 Introduction

One recent highlight of cosmological N-body simulations has been the discovery that during the merger and accretion events that characterize the assembly of dark matter halos the central regions of accreted halos may survive for several orbital times as dynamically distinct, self-bound entities in the parent halo (Klypin et al 1999, Moore et al 1999, hereafter K99 and M99, respectively). The population of surviving halo cores, or “subhalos”, typically contributes less than $\sim 10\%$ of the total mass of the system, with the bulk of the mass in a smooth monolithic structure, as envisioned in the pioneering analytical work of White & Rees (1978). Despite the small fraction of the total mass they make up, at any given time a large number of subhalos are expected within the virialized region of a cold dark matter halo. For example, M99 find that up to 500 satellites with circular velocities exceeding ~ 10 km/s may have survived within ~ 300 kpc from the center of the Galaxy. Comparing this with the dozen or so known Milky Way satellites of comparable velocity dispersion implies that most subhalos must have failed to form a significant number of stars.

Even if luminous galaxies fail to “turn on” in most subhalos a potential difficulty has been cited by M99: the fluctuating gravitational potential induced by the clumpy structure of the halo may act to heat and thicken fragile

stellar disks beyond observational constraints. I present here the results of an attempt to quantify the effects of substructure on the dynamical evolution of thin stellar disks embedded in dark matter halos.

2 Substructure in CDM halos

The mass function of substructure halos, their internal structure, and the parameters of their orbits are the main properties of the subhalo population that determine the tidal effects of substructure on stellar disks. The short-dashed curves in Fig. 1 (left panel) show the subhalo velocity function corresponding to galaxy-sized dark matter halos formed in the $\Omega = 1$ CDM and in the Λ CDM cosmogonies. Circular velocity (instead of mass) is used to characterize subhalos because of its weaker dependence on the exact way in which substructure is identified. Still, circular velocities do change as a function of radius from the center of a subhalo, and there is no unique way of defining subhalo circular velocities. Fig. 1 reports results for V_{peak} and V_{outer} , which correspond to the maximum circular speed within the subhalo, and to its value at the outermost bound radius, respectively. Scaled to the virial velocity of the halo, the substructure velocity function is roughly independent of the mass of the parent halo (M99) and of the cosmological parameters (K99). The results of K99 are shown by the dot-dashed line in Fig. 1 (left) and are in reasonable agreement with our determination.

How does the subhalo velocity function compare with the observed number of satellites in the vicinity of the Milky Way? The solid squares in Fig. 1 (joined by a solid line) illustrate the cumulative number of known Milky Way satellites as a function of the circular velocity of their halos, as plotted by M99. Here, circular velocities are derived for the halos of dwarf spheroidals assuming that stars in these systems are on isotropic orbits in isothermal potentials. This is a plausible, but nevertheless questionable, assumption. Dark halos differ significantly from simple isothermal potentials, and numerical simulations indicate that circular velocities decrease substantially near the center. If stars populate the innermost regions of subhalos their velocity dispersions may substantially underestimate the subhalo peak circular velocities. This has been discussed by White (2000), who finds, using the mass model proposed by Navarro, Frenk & White (1997, NFW), that dwarf spheroidals may plausibly inhabit potential wells with circular velocities up to a factor of 3 times larger than inferred under the isothermal assumption. Such correction may reconcile, at the high mass end, the Milky Way satellite velocity function with the subhalo function, as shown by the dotted line in Fig. 1. Thus, the possibility remains that the number of *massive* satellites expected in the CDM scenario

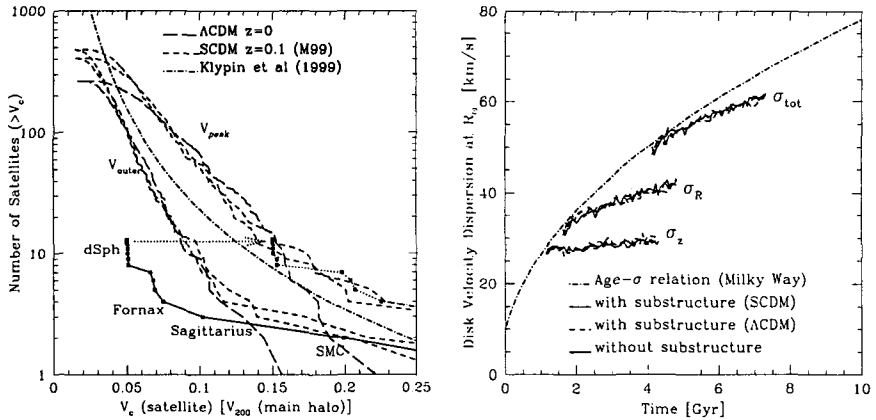


Figure 1: Left: Cumulative circular velocity function of substructure halos. Velocities are normalized to the circular velocity of the parent halo measured at the virial radius. Only subhalos within the virial radius of the main halo are included. Right: Stellar disk velocity dispersion as a function of time in our Milky Way model compared with the age-velocity dispersion relation in the solar neighborhood, as compiled recently by Fuchs et al (2000, dot-dashed curve).

might not be in gross conflict with observation.

On the other hand, this does not erase the large number of low mass “dark” satellites that should inhabit the main halo. Can thin stellar disks survive unscathed in this clumpy environment? The tidal heating rate by substructure can be shown to scale as $dE/dt \propto \int n(m_s) m_s^2 dm_s$, where m_s is the subhalo mass (White 2000). Since, according to numerical simulations, $n(m_s) \propto m_s^{-1.8}$ (Ghigna et al 2000, Springel et al 2000), tidal heating by substructure is dominated by the few most massive subhalos. One consequence of this result is that stochastic effects are expected to dominate the heating rate and a statistically significant sample of systems should be simulated in order to obtain conclusive results. The results reported here (which are based on a couple of realizations) should then be viewed as preliminary until confirmed by further studies.

3 The Evolution of Stellar Disks in a Λ CDM halo

In order to assess the dynamical influence of subhalos on stellar disks we have carried out a series of numerical simulations that follow the evolution of a disk of particles within a dark matter halo with substructure similar to that

of the halos shown in Fig. 1 (left). We choose parameters so that the model reproduces many of the observational characteristics of the Milky Way galaxy, as in Velázquez & White (1999). The galaxy model is first evolved without substructure halos in an attempt to assess the deviations from equilibrium induced by noise in the particle distribution. N-body disks are notoriously unstable, and substantial numbers of particles are needed to ensure stability over several rotation periods. The simulations we report here use 40,000 particles in the disk, 13,333 in the bulge, and 2.2×10^6 in the halo, all of equal mass, $m_p = 1.4 \times 10^6 M_\odot$. Within this system we insert substructure halos, using a procedure which ensures that the subhalos have approximately the same masses, densities and orbits as those in the CDM halos.

We evolve the disk model first for about 3.5 Gyrs without including substructure in order to quantify the heating rate due to noise in the particle distribution. The (R, z, ϕ) velocity dispersions of disk particles at the solar circle (i.e., 8.5 kpc from the center) grow from (31, 27, 26) km s^{-1} to (43, 30, 33) km s^{-1} over the same period (see solid lines in Fig. 1). Quantifying this heating rate by the usual expression $\sigma_{tot}^2 = \sigma_0^2 + Dt$, we find $D \sim 200 \text{ km}^2 \text{ s}^{-2} \text{ Gyr}^{-1}$, about a factor of two less than inferred for stars in the solar neighborhood from the age-velocity dispersion (Fuchs et al 2000).

The two-body heating rate in our equilibrium stellar disk model is thus low compared with the actual heating experienced by stars in the disk of the Galaxy. This implies that our disk model is stable enough to verify numerically whether substructure in the halo leads to heating rates inconsistent with observational constraints. This is shown by the dashed lines in Fig. 1, which show the evolution of the disk velocity dispersion when the substructure halos are added to the system. Clearly, the heating rate is approximately the same with and without substructure, a result that may be traced to the fact that there are no satellites more massive than $10^{11} M_\odot$ and that their orbits seldom take them near the disk. If substructure in the halos we consider is representative of galaxy-sized CDM halos (and we have no reason to suspect it is not), this would imply that tidal heating rates of thin stellar disks by substructure halos may be consistent with the observational evidence.

4 Discussion

These results suggest that concerns regarding excessive tidal heating of thin stellar disks by substructure in CDM halos may be less serious than previously thought. We conclude that the substructure observed in virialized CDM halos is not clearly inconsistent with the existence of thin stellar disks such as that of the Milky Way. These conclusions are subject to a number of caveats. The

most obvious one is that our study explores only two numerical realizations of a disk galaxy within clumpy dark matter halos, and it is always hazardous to extrapolate from such a small number of cases. Our study does show, however, that it is possible at least in some cases to maintain a stellar disk in spite of substructure. A second caveat is that we have explored a model motivated by the present-day structure of the Milky Way and by the $z = 0$ substructure of a CDM halo. Models that take into account the ongoing formation of the disk and a more realistic treatment of the evolution of substructure are clearly desirable in order to refine the conclusions presented here.

Finally, as discussed by Navarro & Steinmetz (2000), it is quite difficult to account simultaneously for the masses, luminosities, rotation speeds, and angular momenta of galaxy disks in cosmogonies such as CDM, where much of the mass of a virialized halo tends to be assembled through a sequence of mergers. Until these issues are fully resolved it would be premature to extend a clean bill of health to the CDM paradigm regarding the formation and evolution of spiral galaxies like our own Milky Way.

Acknowledgments

I thank my collaborators, Andreea Font, Joachim Stadel and Tom Quinn for allowing me to present the results of our collaboration. This research has been supported by CIAR, CFI, NSERC and the Alfred P. Sloan Foundation.

References

1. Fuchs, B. et al. 2000, in "Dynamics of Star Clusters and the Milky Way", ASP Conference Series, eds. Deiters et al.
2. Ghigna, S. et al. 2000, ApJ, 544, 616
3. Klypin, A. et al, 1999, ApJ, 516, 530
4. Moore, B. et al, 1999, ApJ, 524, L19 (M99)
5. Navarro, J. F., Frenk, C. S. & White, S. D. M. 1997, ApJ, 490, 493
6. Navarro, J. F. & Steinmetz, M. 2000, ApJ, 538, 477.
7. Springel, V., White, S.D.M., Tormen, G., Kauffmann, G. 2000, MNRAS, submitted (astro-ph/0012055)
8. Velázquez, H. & White, S. D. M. 1999, MNRAS, 304, 254
9. White, S. D. M. & Rees, M. J. 1978, MNRAS, 183, 341
10. White, S.D.M. 2000, "ITP Conference on Galaxy Formation and Evolution", http://online.itp.ucsb.edu/online/galaxy_c00/white/

ON THE ‘INITIAL’ ANGULAR MOMENTUM OF GALAXIES

Tom Abel, Rupert C. Croft, Lars Hernquist
Harvard Smithsonian Center for Astrophysics,
MA, US-02138 Cambridge
E-mail: Hi@TomAbel.com

Spherical density profiles and specific angular momentum profiles of Dark Matter halos found in cosmological N-body simulations have been measured extensively. The distribution of the total angular momentum of dark matter halos is also used routinely in semi-analytic modeling of the formation of disk galaxies. However, it is unclear whether the initial (i.e. at the time the halo is assembled) angular momentum distributions of baryons is related to the dark matter at all. Theoretical models for ellipticities in weak lensing studies often rely on an assumed correlation of the angular momentum vectors of dark matter and gas in galaxies. Both of these assumptions are shown to be in reasonable agreement with high resolution cosmological smoothed particle hydrodynamical simulations that follow the dark matter as long as only adiabatic gas physics is included. However, we argue that in more realistic models of galaxy formation one expects pressure forces to play a significant role at “turn-around”. Consequently the torquing force on DM and baryons will be uncorrelated and their respective angular momenta are not expected to align. An SPH simulation with ad-hoc feedback is presented that illustrates these effects. Massive low redshift elliptical galaxies may be a notable exception where “light may trace mass”.

1 Introduction

The high frequency of disk galaxies and their exponential profiles over many scale radii is perhaps one of the most striking global features of observed galaxies. Theoretical studies investigating the origin of this angular momentum in these galaxies have a long history (e.g. Weizsäcker 1951). In most modern investigations the *Ansatz* of Mestel (1963) is used where one assumes that any parcel of fluid retains its initial specific angular momentum. In hierarchical structure formation scenarios the luminous parts of galaxies form from gas that is cooling within dark matter (DM) halos that are continuously merging to build larger and more massive objects. These assumptions are also made in most recent models of disk galaxy formation (e.g. Mo, Mao and White 1998). The typical initial angular momentum of halos may be estimated from linear theory (Peebles 1969). However, its distribution is typically measured from N-body simulations that follow the formation and evolution of structure in the dark matter only. In the following we derive a rough estimate of the the magnitude of pressure forces that contribute significantly to the torquing forces.

2 Forces and Torques

The critical density and the total mass, M , in a spherical volume of comoving radius R with an over-density $\delta = \rho/\bar{\rho}_m$ of the mean matter density ($\bar{\rho}_m = \Omega_m \rho_c$) are given by,

$$\rho_c = \frac{3H_0^2}{8\pi G}, \quad M = \delta \frac{4\pi}{3} R^3 \Omega_m \rho_c, \quad (1)$$

where the symbols have their usual meaning (see e.g. Peebles 1993). Let f be the fraction of the torquing force from surrounding structures on this spherical over-density to the radial force of the sphere. The torquing force is $F_t = f G M \rho / r^2$ where r is a proper radius of the sphere. Here f is necessarily somewhat smaller than the radial force of its own gravity^a. To get a rough idea of what pressure gradient may change the torquing we simply compare

$$\frac{1}{\rho_b} \frac{\partial P}{\partial r} = f \frac{G M}{r^2} \quad (2)$$

Using difference instead of differential, substituting $r = R/(1+z)$ and using ΔR^b to denote the comoving length scale over which the pressure gradient is taken we find,

$$\Delta P \sim f \frac{3H_0^4}{16G\pi} \delta^2 \Omega_b \Omega_m (1+z)^4 R \Delta R. \quad (3)$$

Assuming constant density this translates to the very small temperature gradient of

$$\Delta T \sim f \frac{\Delta P \mu}{k_B \rho_b} = \delta \frac{H_0^2 m_P}{2k_B} \Omega_m (1+z) R \Delta R, \quad (4)$$

$$\Delta T \approx 2.6 \times 10^3 \text{ K} \delta \frac{f}{0.1} (1+z) R_{Mpc} \frac{\Delta R_{Mpc}}{0.3}. \quad (5)$$

Such small pressure gradients are expected to originate from well known processes such as ionization fronts from reionization, galactic outflows driven by black holes, and galactic feedback as required in semi-analytical models of galaxy formation (e.g. Kauffmann et al. 2000). The larger the mass of the object the larger the pressure gradient has to be to alter the angular momentum acquisition of the gas as compared to the dark matter.

^aOtherwise the fluid parcel would not collapse with the sphere.

^bThis δR is taken smaller than the total radius since for a realistic density distribution most of the mass is at large radii.

3 Simulations

To investigate the relation between angular momentum of the baryons and the DM we have performed two different cosmological smoothed particle hydrodynamics simulations using GADGET (Springel, Yoshida, and White 2000). Both simulations use 128^3 for each the DM and the gas in a periodic volume of 10 comoving Mpc side-length. Both are evolved from redshift 60 to $z = 3$ with initial conditions drawn from a realization appropriate for a spatially flat universe with $\Omega_m = 0.3$, $\Omega_b h^2 = 0.02$ and $h = 0.7$. Both simulations follow only gravity and adiabatic gas physics. In one run we have artificially increased abruptly the temperature of the gas to 4×10^6 Kelvin at redshift 7 to mimic a strong feedback case. We use HOP (Eisenstein and Hut 1998) to identify

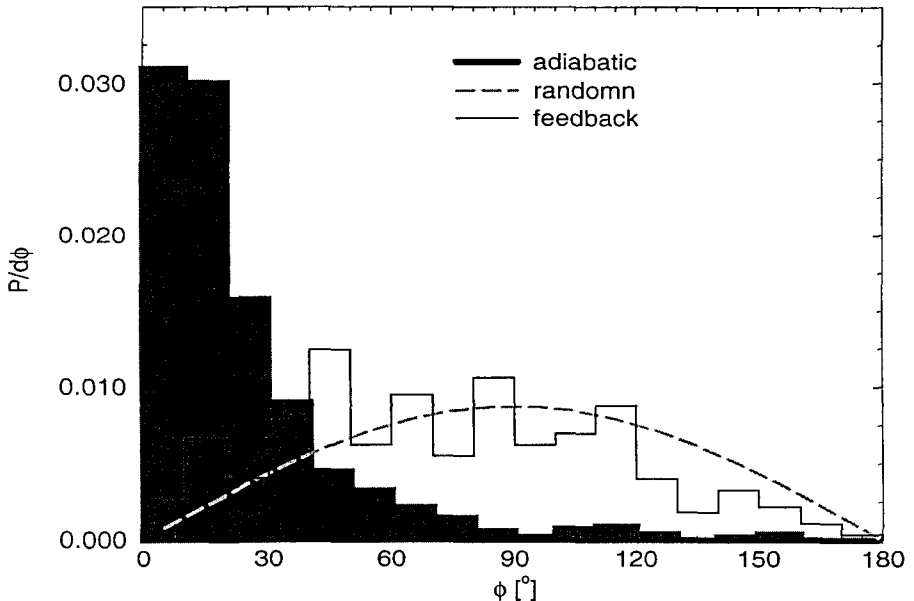


Figure 1: Alignment angle between the total specific angular momentum vectors of dark matter and gas for purely adiabatic gas physics (filled histogram) and an ad-hoc feedback model (empty histogram).

centers of halos. Then we go out radially and define a halo as all the mass within the radius where the over-density in the dark matter corresponds to 200 times the mean density. Within these halos we then measure the total and specific angular momentum vectors. In Fig. 1 we show the distributions of the alignment angles between the dark matter and the baryonic component for all halos that have no other overlapping halo. Clearly for the purely adiabatic case there is remarkable agreement between the directions of the angular momenta

with a median alignment angle of 20 degrees. However, as soon as pressure forces are introduced as in the ad-hoc feedback the respective angles become uncorrelated. The imperfect alignment between the DM and the gas in the purely adiabatic run comes most likely from non-linear angular momentum exchange at virialization. Such non-linear effects may well be aggravated in simulations which also include the cooling of the gas.

4 Discussion and Conclusions

In this short contribution we have pointed out that large scale pressure forces have significant influence on the formation of galaxies. Until the physical processes acting on the gas in the intergalactic medium are fully understood it is difficult to assess the mass scales on which such large scale non-gravitational forces may play a role. Because of space constraints we could only remark here that the collisionless and collisional components will exchange angular momentum during merging events. This will further diminish the possible correlation of the spins of DM and gas. Our results have important implications for models which associate the dark matter angular momentum vector and their correlations with observed ellipticities of galaxies (see contributions by Crittenden, Mackey and Heavens in this volume). Since the directions of the angular momentum of radial shells within halos varies as function of radius (Moore this volume) and the luminous part of galaxies may be re-oriented from the torquing up of their non-spherical parent halos (Moore and Sellwood, this volume) we are led to conclude that current models of the formation and evolution of disk galaxies are oversimplified. However, one interesting exception may be low redshift massive elliptical galaxies. If most of their stars have formed at early times in smaller higher redshift objects, the shapes and angular momentum distributions of gas and DM may be strongly correlated. This would be a natural explanation of the strong lensing observations of Kochanek (this volume) which indicate that “light traces mass” for these galaxies.

References

1. Eisenstein, D. J. & Hut, P., *ApJ* **498**, 137 (1998)
2. Kauffmann, G., Colberg, J. M., Diaferio, A., & White, S. D. M., *MNRAS* **303**, 188 (1999)
3. Mestel, L., *MNRAS* **126**, 553 (1963)
4. Mo, H. J., Mao, S., & White, S. D. M., *MNRAS* **295**, 319 (1998)
5. Peebles, P. J. E., *ApJ* **155**, 393 (1969)
6. Springel, V., Yoshida, N., White, S. D. M., 2001, *New Astr.*, **6**, 79
7. von Weizsäcker, C. F. *ApJ* **114**, 165 (1951)

ELLIPTICALS AND BARS: CENTRAL MASSES AND FRICTION

J. A. Sellwood

*Department of Physics & Astronomy, Rutgers University
136 Frelinghuysen Road, Piscataway, NJ 08854-8019, USA
E-mail: sellwood@physics.rutgers.edu*

I give a very brief review of aspects of internal dynamics that affect the global shape of a galaxy, focusing on triaxiality, bars and warps. There is general agreement that large central masses can destroy triaxial shapes, but recent simulations of this process seem to suffer from numerical difficulties. Central black holes alone are probably not massive enough to destroy global triaxiality, but when augmented by star and gas concentrations in barred galaxies, the global shape may be affected. Even though we do not understand the origin of bars in galaxies, they are very useful as probes of the dark matter density of the inner halo. Finally, I note that dynamical friction acts to reduce a misalignment between the spin axes of the disk and halo, producing a nice warp in the outer disk which has many of the properties of observed galactic warps.

1 Introduction

I was asked by the organizers to discuss the huge topic of what N -body simulations can tell us about the shapes of galaxies. As a comprehensive survey would be voluminous, I here restrict myself to a few internal evolutionary processes affecting galaxy shapes where there have been noteworthy recent developments. I also point out some areas where a lot more work is required. Other speakers describe aspects of galaxy formation, and the properties of collapsed halos.

2 Triaxiality and central masses

Soon after Schwarzschild (1979) showed that a large fraction of the stars must pursue box orbits to support a triaxial mass distribution in an elliptical galaxy, it was realized that a central mass, or just a density cusp, might destroy triaxiality. The reason, most clearly articulated by Gerhard & Binney (1985), is that a box orbit carries a star arbitrarily close the center, where a central mass will deflect it through a large angle, scattering the star into an orbit of different shape. The loss of stars on the structure-supporting box orbits must change the global shape of the galaxy, at least in the inner regions. Only tube orbits, which avoid the center, remain once the potential becomes axisymmetric and the central mass concentration will no longer drive evolution. This general expectation has been confirmed in N -body simulations, beginning with the

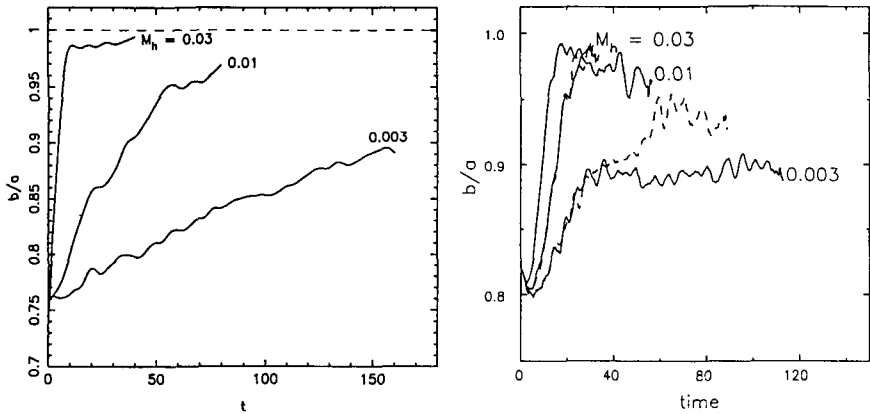


Figure 1: Comparison between my results (right) and those obtained by MQ98 (left). The plotted quantity is the ratio of the intermediate- to long-axes of the moment of inertia tensor of the 50% most bound particles as a function of time. The three solid curves show the results from models into which three different central masses were grown over the time interval 0 to 15 for MQ98 and 0 to 28 in my models. The dashed curves on the right shows results from reruns of two cases using the SCF method.

pioneering work by May, van Albada & Norman (1985) and most recently by Merritt & Quinlan (1998, hereafter MQ98).

While the simulations by MQ98 appear to have been performed with considerable care, one aspect of their results seemed highly surprising. As shown in Fig. 1 (left), the shape of their initially triaxial model responded gradually to the introduction of a small central mass, and continued to evolve for many tens of dynamical times after the central mass reached a steady value at $t = 5$ for $M_h = 0.3$ and $t = 15$ for the two lower mass cases. I suspected that this behavior was a numerical artifact, possibly caused by their use of the so-called SCF method proposed by Hernquist & Ostriker (1992): although the basis set of functions is complete, truncation to a comparatively few terms provides a severe restriction on the complexity of shapes which can be represented. Perhaps their numerical technique couples shape changes at different radii, which have greatly differing orbital time scales, rendering their simulations unable to sustain a shape which is axisymmetric near the center while remaining non-axisymmetric in the outer parts. I therefore decided to check their work by following their procedure as closely as possible but employed a different method to compute the gravitational field. The code, which closely resembles that previously described by McGlynn (1984) and requires somewhat less computer time than the SCF method (Sellwood 1997), expands the

mass distribution in surface harmonics on a 1-D grid of shells, thus avoiding any coupling between the shape of the gravitational field at different radii.

My results (Fig. 1, right) are markedly different from those reported by MQ98 (Fig. 1, left). I find that the original triaxial shape both evolves rapidly as the central mass rises and stops evolving as soon as the increase stops at $t \sim 28$. The rate of evolution in the two lower central mass models is clearly slower in the simulations by MQ98, whereas I find even more rapid evolution (not shown) when I grow the central mass as fast as did MQ98.

Reverting to an independent implementation of the SCF method with the same number of terms gives the results shown by the dashed lines in Fig. 1 (right). These lines track the solid curves as the central mass rises, but the later diverging trend, most obvious for the smallest central mass, shows that indeed the shape continues to evolve after the central mass stops growing when the SCF code is used. This behavior confirms my suspicions that the SCF method to compute the gravitational field caused the slow evolution reported by MQ98. I have made a number of other tests, varying the usual numerical parameters of time step, softening length of the central mass, *etc.*, which have made no difference to the behavior. While the slower initial evolution reported by MQ98 remains unexplained, the continuing shape changes in their models appear to result from a numerical artifact.

Black hole masses may be smaller than first believed (*e.g.* Merritt & Ferrarese 2001) and their host galaxies therefore able to remain strongly triaxial. I find that masses $\lesssim 0.1\%$ have a negligible effect on the global shape for as long as I run the calculations.

The effect of a central mass on rapidly-rotating, triaxial bar is perhaps even less well understood. The mass of a central black hole alone is unlikely to be large enough to affect the global shape, but augmented by a stellar cusp and other concentrations of stars and gas, the central masses can be enormous. There is general agreement that large central masses will destroy a bar; a mass of 5% of that of the disk is clearly plenty (Norman *et al.* 1996), but Friedli (1994) claims that as little as 1% is sufficient, while Sellwood & Moore (1999) were able to grow a bar in a disk with a central mass larger than this! The criterion seems to be more complicated than just a simple mass fraction and the central density required to destroy a bar is not yet known.

3 The Origin of Bars

It is now clear that we do not understand the origin of bars in galaxies. The original prejudice (*e.g.* Sellwood & Wilkinson 1993) that they were probably created by the well-known global instability (Miller *et al.* 1970; Hohl 1971;

Kalnajs 1972) now seems untenable for two reasons.

First, most bright galaxies should be stable because they have dense bulges. My own recent work (Sellwood 1985, 1999; Sellwood & Evans 2001) has established beyond doubt the correctness of Toomre's (1981) idea that an entire disk can be stable if it has a dense center. A disk with a rotation curve that stays high close into the center, even if fully-self-gravitating, has no tendency to form a bar; early simulations simply lacked the dynamic range in density and time-scales to show this. However, a problem now arises for barred galaxies because they too have inner mass distributions which ensure a strong inner Lindblad resonance (ILR) that should have prevented the bar from forming. Indications of strong ILRs in nearby barred galaxies include nuclear rings (Buta & Crocker 1993; Benedict *et al.* 1999), ring-like concentrations of molecular gas (*e.g.* Sakamoto *et al.* 1999; Jogee & Kenney 2000) and offset dust lanes (Athanasoula 1992). Binney *et al.* (1991), Weiner & Sellwood (1999) and others also find evidence for an ILR in the bar of the Milky Way, which seems inevitable given the central density distribution (Becklin & Neugebauer 1968). This abundance of evidence is strongly suggestive, but indirect. Definitive verification requires detailed modeling of the mass distribution and velocity field within the galaxy, together with a determination of the pattern speed in each case (Lindblad, Lindblad & Athanasoula 1996; Regan, Vogel & Teuben 1997; Weiner *et al.* 2001) – all three cases reveal clear ILRs. The question raised by these observations is that if the bars have strong ILRs, which we now know should have inhibited the bar instability, how did the bars form in the first place? It is possible the central density rose after the bar formed, but the mass inflow required to produce such strong ILRs may well have destroyed the bar.

Second, bars seem to have formed long after their host disks came into existence. There appears to be deficiency of bars in galaxies at $z > 0.5$ (van den Bergh *et al.* 1996; Abraham *et al.* 1999), suggesting that bars form late in the evolution of a disk galaxy. While some bars could be missed because of bandshifting (*e.g.* Bunker *et al.* 2000), a marked deficiency remains (van den Bergh *et al.* 2000, 2001). Thus most bars appear to form long after their host disks were assembled, which requires a slow, secular process quite different from the rapid dynamical instability.

I have observed an alternative mode of bar formation in number of simulations which remains consistent with both these properties and might conceivably be the way bars form in nature. It is well known that spiral patterns remove angular momentum from stars near the inner Lindblad resonance. The damping of the wave in second order perturbation theory (Kalnajs 1971; Lynden-Bell & Kalnajs 1972; Mark 1974) depends on the assumption that the

perturbation is too weak to trap the stars, but larger amplitude patterns can cause stars to be trapped. Simulations (Sellwood 1981; Sellwood & Moore 1999) show that trapping in this way leads to bar which grows in length and strength in an episodic manner with each favorable pattern. It should be noted that this process differs from that proposed by Lynden-Bell (1979) because it relies on rapid changes in the angular momenta (or actions) of stars.

Is this the way real bars are formed? Further work is in hand to test whether the mechanism can account for the observed fraction of bars, the distribution of bar strengths and whether the resulting bars have properties consistent with those observed.

4 Dynamical friction on bars

Even though we do not understand their origin, bars allow us to impose powerful constraints on the dark matter (DM) content of the inner regions of galaxies. Weiner *et al.* (2001) show how the non-axisymmetric flow pattern driven by a bar can be used to determine the M/L of the bar and disk; they find, for the case of NGC 4123, that the stars must contribute essentially all the central attraction to account for the orbital speeds in the inner parts of that galaxy, and that the central density of DM must be low. Their powerful argument, however, does not belong in this review because it involves no N -body simulations.

Debattista & Sellwood (1998, 2000) use N -body simulations to obtain a similar constraint on the inner DM content of barred galaxies. Tremaine & Weinberg (1984a) argued that a bar rotating in a dense DM halo would lose angular momentum to the halo through dynamical friction, and Weinberg (1985), using perturbation theory, showed that the time scale for bar slow-down could be short (a few bar rotations).

There is strong, but not overwhelming, evidence to indicate that bars in real galaxies are fast – *i.e.* corotation lies only just beyond the end of the bar. Merrifield & Kuijken (1995), Gerssen *et al.* (1999) and Debattista & Williams (2001) apply the method of Tremaine & Weinberg (1984b) to three barred galaxies, finding in all cases that the bar is fast. Modeling the gas flow yields the pattern speed less directly; our work on NGC 4123 (above), and that of Lindblad *et al.* (1996) and Regan *et al.* (1997), again indicates that bars in real galaxies rotate rapidly. The position of dust lanes in bars suggests that fast rotation is generic (van Albada & Sanders 1982; Prendergast 1983; Athanassoula 1992). Thus it appears that bars in real galaxies have not suffered much friction.

Our simulations confirmed Weinberg's prediction of rapid bar slow down

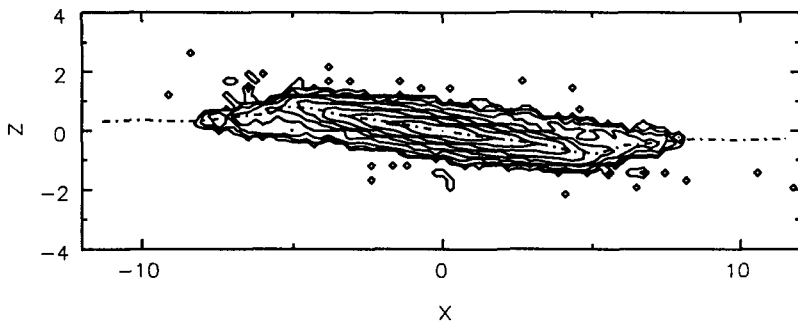


Figure 2: Contours of projected disk density after about 3 orbits at $R = 5$ disk scales. By this time, the inner disk has tilted $\sim 10^\circ$ away from its original plane, which was horizontal. The dot-dash line indicates the cross-section of a layer of test particles, which should trace the expected locus of the HI layer.

when the halo has a moderate central density, unless the halo has large angular momentum in the same sense as the disk. Friction decreases the bar pattern speed, driving the corotation point out to unacceptable distances. The halo angular momentum required to avoid strong braking is unrealistically large, even when the halo is flattened to $b/a \simeq 0.5$ and rotation is confined to the inner halo only. Bars are therefore able to maintain their observed high pattern speeds only if the halo has a central density low enough for the disk to provide most of the central attraction in the inner galaxy.

5 Friction-induced warps

Debattista & Sellwood (1999) found a quite different use for dynamical friction between the disk and halo: If the spin axes of the disk and of the DM halo are misaligned, dynamical friction will cause the angular momentum vectors to move closer towards alignment. This occurs even when the halo is not significantly flattened by rotation.

Their simulations of this process showed that the inner disk tips more rapidly than the outer disk, because its higher density induces a stronger frictional response. The outer disk therefore lags as the inner disk tips, creating a warp as shown in Fig. 2. The inner tilt is straight while the warp has a leading twist, just as observed (*e.g.* Briggs 1990).

Note that the weak coupling between the inner and outer disk is an *advantage* in this mechanism, since it creates the warp, whereas it is the principal obstacle for would-be warp mode theories which founder because coupling is

too weak to persuade the edge to precess at uniform rate (*e.g.* Toomre 1983).

The warp shown in Fig. 2 does not last indefinitely; it is a transient response when the two spin vectors find themselves out of alignment. Fortunately, a duration of several galaxy rotations is plenty long enough to be consistent with the observed prevalence of warps, as it is likely the spin vector of the halo changes from time to time as a result of late minor mergers (*e.g.* Quinn & Binney 1992), the natural consequence of any hierarchical theory of structure formation. (See also the contributions by Moore and by Bullock to these proceedings.)

It should be noted that random motions of stars in the plane provide a significant additional source of stiffness for a disk, one which is ignored in the usual treatment of the disk as a collection of wire rings coupled only by gravity. Random motion is important because adjacent mass elements of the disk share the same stars, and therefore cannot tip relative to each other as much as if gravity were the only restoring force. Debattista & Sellwood (1999) present the only calculations so far to include this effect, and show that the stiffness of the disk rises markedly with the level of random motion of the disk stars.

Acknowledgments

I would like to thank V. Debattista for comments on a draft version. This work was supported by NASA LTSA grant NAG 5-6037 and by NSF grant AST-0098282.

References

1. Abraham, R. G., Merrifield, M. R., Ellis, R. S., Tanvir, N. & Brinchman, J. 1999, *MNRAS*, **308**, 596
2. Athanassoula, E. 1992, *MNRAS*, **259**, 345
3. Becklin, E. E. & Neugebauer, G. 1968, *Ap. J.*, **151**, 145
4. Benedict, G. F., Howell, A., Jorgensen, I., Chapell, D., Kenney, J. & Smith, B. J. 1998, STSCI Press Release C98
5. Binney, J. J., Gerhard, O. E., Stark, A. A., Bally, J. & Uchida, K. I. 1991, *MNRAS*, **252**, 210
6. Briggs, F. H. 1990, *Ap. J.*, **352**, 15
7. Bunker, A., *et al.* 2000, astro-ph/0004348
8. Buta, R. & Crocker, D. A. 1993, *Astron. J.*, **105**, 1344
9. Debattista, V. P. & Sellwood, J. A. 1998, *Ap. J.*, **493**, L5
10. Debattista, V. P. & Sellwood, J. A. 1999, *Ap. J.*, **513**, L107
11. Debattista, V. P. & Sellwood, J. A. 2000, *Ap. J.*, **544**, 704

12. Debattista, V. P. & Williams, T. B. 2001, in *Galaxy Disks and Disk Galaxies*, eds. J. G. Funes SJ & E. M. Corsini, ASP Conference Series **230**, (San Francisco: Astronomical Society of the Pacific) p 553
13. Friedli, D. 1994, in *Mass-Transfer Induced Activity in Galaxies*, ed. I. Shlosman (Cambridge: Cambridge University Press) p 268
14. Gerhard, O. E. & Binney, J. 1985, MNRAS, **216**, 467
15. Gerssen, J., Kuijken, K. & Merrifield, M. R. 1999, MNRAS, **306**, 926
16. Hernquist, L. & Ostriker, J. P. 1992, Ap. J., **386**, 375
17. Hohl, F. 1971, Ap. J., **168**, 343
18. Jogee, S. & Kenney, J. 2000, in *Dynamics of Galaxies From the Early Universe to the Present*, eds. F. Combes, G. A. Mamon & V. Charmandaris, ASP Conference Series **197**, (San Francisco: Astronomical Society of the Pacific) p 193
19. Kalnajs, A. J. 1971, Ap. J., **166**, 275
20. Kalnajs, A. J. 1972, Ap. J., **175**, 63
21. Lindblad, P. A. B., Lindblad, P. O. & Athanassoula, E. 1996, A. & A., **313**, 65
22. Lynden-Bell, D. 1979, MNRAS, **187**, 101
23. Lynden-Bell, D. & Kalnajs, A. J. 1972, MNRAS, **157**, 1
24. Mark, J. W-K. 1974, Ap. J., **193**, 539
25. May, A., van Albada, T. S. & Norman, C. A. 1985, MNRAS, **214**, 131
26. McGlynn, T. A. 1984, Ap. J., **281**, 13
27. Merrifield, M. R. & Kuijken, K. 1995, MNRAS, **274**, 933
28. Merritt, D. & Quinlan, G. 1998, Ap. J., **498**, 625 (MQ98)
29. Merritt, D. & Ferrarase L. 2001, astro-ph/0107134
30. Miller, R. H., Prendergast, K. H. & Quirk, W. J. 1970, Ap. J., **161**, 903
31. Norman, C. A., Sellwood, J. A. & Hasan, H. 1996, Ap. J., **462**, 114
32. Prendergast, K. H. 1983, in *Internal Kinematics and Dynamics of Galaxies*, IAU Symp. **100**, ed E. Athanassoula (Dordrecht: Reidel) p 215
33. Quinn, T. & Binney, J. 1992, MNRAS, **255**, 729
34. Regan, M. W., Vogel, S. N. & Teuben, P. J. 1997, Ap. J., **482**, L143
35. Sakamoto, K., Okamura, S. K., Ishizuki, S. & Scoville, N. Z. 1999, Ap. J., **525**, 691
36. Schwarzschild, M. 1979, Ap. J., **232**, 236
37. Sellwood, J. A. 1981, A. & A., **99**, 362
38. Sellwood, J. A. 1985, MNRAS, **217**, 127
39. Sellwood, J. A. 1997, in *Computational Astrophysics*, eds. D. A. Clarke & M. J. West (San Francisco: ASP Conference Series **123**), 215
40. Sellwood, J. A. 1999, in *Galaxy Dynamics - A Rutgers Symposium*, eds. D. Merritt, J. A. Sellwood & M. Valluri (San Francisco: ASP) **182**, p 351

41. Sellwood, J. A. & Evans, N. W. 2001, *Ap. J.*, **546**, 176
42. Sellwood, J. A. & Moore, E. M. 1999, *Ap. J.*, **510**, 125
43. Sellwood, J. A. & Wilkinson, A. 1993, *Rep. Prog. Phys.*, **56**, 173
44. Toomre, A. 1981, in *The Structure and Evolution of Normal Galaxies*, ed. S. M. Fall & D. Lynden-Bell (Cambridge: Cambridge University Press), p. 111
45. Toomre, A. 1983, in *Internal Kinematics and Dynamics of Galaxies*, IAU Symposium **100**, ed E. Athanassoula (Dordrecht: Reidel) p 177
46. Tremaine, S. & Weinberg, M. D. 1984a, *MNRAS*, **209**, 729
47. Tremaine, S. & Weinberg, M. D. 1984b, *Ap. J.*, **282**, L5-L7
48. van Albada, T. S. & Sanders, R. H. 1982, *MNRAS*, **201**, 303
49. van den Bergh, S. *et al.* 1996, *Astron. J.*, **112**, 359
50. van den Bergh, S. *et al.* 2000, *Astron. J.*, **120**, 2190
51. van den Bergh, S., Cohen, J. G. & Crabbe, C. 2001, *astro-ph/0104458*
52. Weinberg, M. D. 1985, *MNRAS*, **213**, 451
53. Weiner, B. J. & Sellwood, J. A. 1999, *Ap. J.*, **524**, 112
54. Weiner, B. J., Sellwood, J. A. & Williams, T. B. 2001, *Ap. J.*, **546**, 931

THE MORPHOLOGICAL EVOLUTION OF MERGER REMNANTS

Barbara Ryden & Jeremy Tinker

The Ohio State University, Dept. of Astronomy,

140 W. 18th Avenue, Columbus OH 43210

E-mail: ryden, tinker@astronomy.ohio-state.edu

Elliptical galaxies formed in a major merger have a tendency to become more nearly spherical with time, thanks to the gravitational effect of their central black hole (or black holes). Observational results indicate that elliptical galaxies with older stellar populations ($t > 7.5$ Gyr) have rounder central isophotes than ellipticals with younger stellar populations. In addition, the older ellipticals tend to have core profiles, while the younger ellipticals have power-law profiles. Numerical simulations of galaxy mergers indicate that if one or both of the progenitors have a central black hole with mass $\sim 0.2\%$ of the stellar mass, then the effect of the black hole(s) is to make the central regions of the remnant rounder, with a characteristic time scale of a few gigayears.

1 Analytic

In a hierarchical clustering scenario, elliptical galaxies form by the merger of smaller stellar systems. Mergers of equal-mass progenitors tend to form fairly flattened systems; after violent relaxation, the ratio of the shortest to longest axis of the merger remnant is typically $c/a \sim 0.5^{1,9}$. However, once an elliptical merger remnant has completed violent relaxation, its shape does not remain constant. In the central regions of the galaxy – well inside the effective radius – the morphological evolution is driven by two-body relaxation, the result of close gravitational encounters between the point masses of which the galaxy is made. The net effect of two-body relaxation is to make a galaxy more nearly spherical with time.

Consider an idealized case of two-body relaxation in which a mass M is plunked down in an isothermal stellar system with velocity dispersion σ . The introduced mass will disrupt the orbits of stars which come within a critical distance $b \sim GM/\sigma^2$. If the mass M is just another star, with mass $M \sim 1 M_\odot$, then stars will have to come within a distance $b \sim 5 R_\odot (\sigma/200 \text{ km s}^{-1})^{-2}$ before their orbits are randomized. Thus, for a typical elliptical galaxy, stars must come within a few stellar radii of each other for two-body relaxation to occur, and the star/star relaxation time is much longer than a Hubble time. If stars were the only point masses which elliptical galaxies contained, we would thus conclude that the effects of two-body relaxation on the structure of ellipticals are negligibly small so far. However, there's more to a galaxy than stars. Most,

if not all, elliptical galaxies contain central black holes, with a mass given by the relation⁴ $M_{\text{BH}} \approx 10^8 M_{\odot} (\sigma/200 \text{ km s}^{-1})^{4.8}$. With this black hole mass, a star coming within a distance $b \sim 10 \text{ pc} (\sigma/200 \text{ km s}^{-1})^{2.8}$ will have its orbit disrupted. Thus, relaxation due to star/black-hole encounters will be vastly more effective than relaxation due to star/star encounters. The net effect of the central black hole will be to increase the entropy of the stellar system and to make it more nearly spherical with time.

It should also be noted that if an elliptical forms by the merger of two progenitors, each with a central black hole, a binary black hole may exist for many Gyrs before dynamical friction, gas dynamical effects, and gravitational radiation will cause the two black holes to coalesce. Three-body interactions between a star and a bound black hole binary will generally increase the star's kinetic energy. Thus, binary black holes have been proposed as a mechanism for lowering the stellar density in the central regions of an elliptical and creating a 'core' profile^{2,3}.

2 Observational

Given the brevity of human life, we cannot sit and watch for a few billion years while a post-merger elliptical becomes rounder with time; nor can we take the time to circumnavigate a galaxy and discover its true three-dimensional shape at a given time. The best we can do, to test our belief that merger remnants become rounder with time, is to examine a sample of elliptical galaxies and see whether the apparent shape of a galaxy is correlated with the time elapsed since it last underwent a major merger.

Estimating the time that has passed since an elliptical galaxy's last major merger is not a simple or straightforward task. However, if the merger in question involved a pair of reasonably gas-rich galaxies, then the merger will be accompanied by a burst of star formation that will leave its spectroscopic mark on the galaxy. Terlevich and Forbes have recently compiled a catalog¹ of spectroscopic galaxy ages, based on a homogeneous data set of galaxies with high-quality $H\beta$ and $[\text{MgFe}]$ absorption line indices. The stellar population model of Worthey¹² is used to assign an age to the stellar population of each galaxy in the catalog. For the 74 elliptical galaxies in the Terlevich & Forbes catalog, we searched the published literature for isophotal fits, and found the apparent axis ratio $q \equiv b/a$ at six reference radii: $R \equiv (ab)^{1/2} = R_e/16, R_e/8, R_e/4, R_e/2, R_e,$ and $2R_e$. Details of the analysis, for those who love details, are given by Ryden, Forbes, & Terlevich⁸.

Figure 1 is a plot of q versus the spectroscopic age t at the six reference radii. Particularly at the innermost radius, $R = R_e/16$, there is a correlation

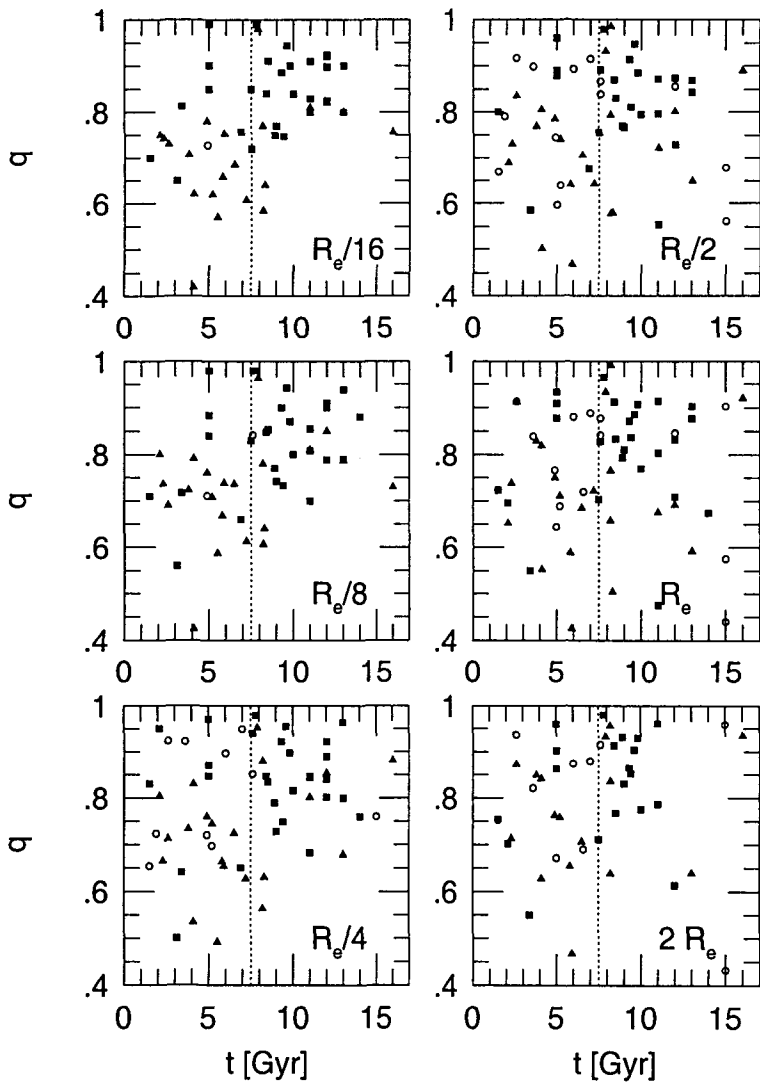


Figure 1: Isophotal axis ratio q versus estimated age t of the central stellar population. Axis ratios are measured at $R = R_e/16$, $R_e/8$, $R_e/4$, $R_e/2$, R_e , and $2R_e$. Galaxies with core profiles are indicated by squares, galaxies with power-law profiles are indicated by triangles, and galaxies with unknown profile type are indicated by open circles.

between q and t , with ‘old’ ellipticals tending to be rounder than ‘young’ ellipticals. A Kolmogorov-Smirnov test, comparing the distribution of $q(R_e/6)$ for galaxies with $t \leq 7.5$ Gyr to the distribution for galaxies with $t > 7.5$ Gyr, reveals that the distributions differ significantly, with $P_{KS} = 0.00034$.

The question ‘Why are there so many round old ellipticals?’ is similar to the question ‘Why are there so many little old ladies?’ It is tempting to interpret the prevalence of little old ladies as being due purely to the evolution of individuals, with ladies tending to become littler as they grow older. However, there are other effects at work as well. For instance, extremely large ladies tend to die prematurely; in addition, today’s population of old ladies grew up when nutritional standards were lower, thus resulting in reduced adult stature. Both these effects, neither of which involves the morphological evolution of individual ladies, contribute to the predominance of little old ladies over large old ladies. Similarly, the predominance over round old ellipticals over flattened old ellipticals is not necessarily due to the morphological evolution of individual galaxies.

The difference in apparent shape between galaxies with young stellar populations and those with old stellar populations is tied, in a most intriguing manner, to the core/power-law distinction. Elliptical galaxies with power-law profiles have luminosity densities which are well fit by a pure power law all the way to the limit of resolution; ellipticals with core profiles, by contrast, have densities which show a break to a shallower inner slope^{5,6,7}. In Figure 1, core ellipticals are designated by squares, power-law ellipticals are designated by triangles, and ellipticals of unknown profile type are designated by empty circles. *Note that the ‘old’ ellipticals tend to have core profiles and round central isophotes, while the ‘young’ ellipticals tend to have power-law profiles and flattened central isophotes.* The 29 known core galaxies in our sample have a mean and standard deviation for their estimated stellar ages of $t = 8.6 \pm 3.3$ Gyr; the 22 known power-law galaxies have $t = 6.9 \pm 3.5$ Gyr.

3 Numerical

The observational results are consistent with a scenario in which elliptical galaxies are formed in a major merger, then evolve to become more nearly spherical with time. However, they do not compel such a scenario – remember the cautionary tale of the little old ladies! Fortunately, numerical simulations of galaxy mergers, and of the evolution of merger remnants, can be run on timescales much shorter than a Gyr (and, more to the point, shorter than than the lifetime of a graduate student.)

We ran n-body simulations (with no attempt to include gas dynamical

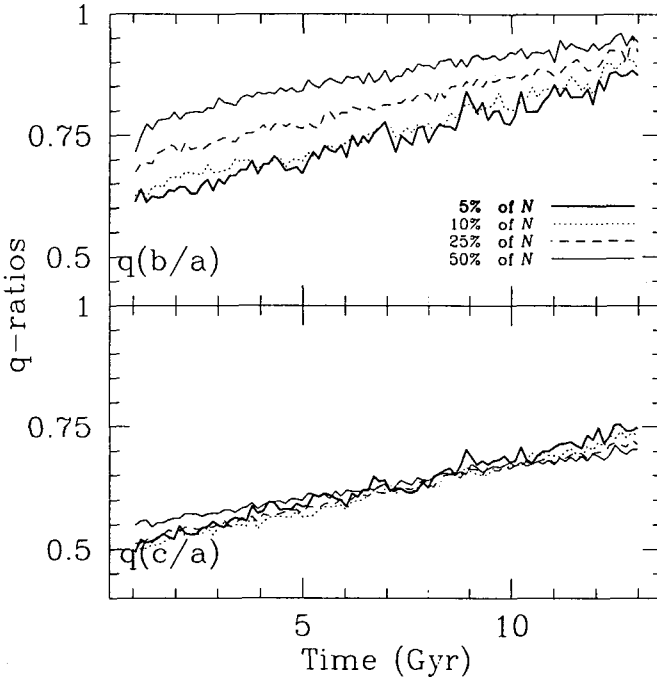


Figure 2: The top panel shows the evolution of the intermediate-to-long axis ratio (b/a) of a numerical merger remnant. The bottom panel shows the evolution of the short-to-long axis ratio (c/a) for the same remnant. In each panel, the heavy solid line indicates the 5% of the particles which are most tightly bound. In this simulation, the merging progenitors did NOT contain central black holes.

effects) of the merger of a pair of disk/bulge/halo galaxies. In our merger simulations, each progenitor has a disk:bulge:halo mass ratio of 1:1:5.8. (The progenitors can be thought of as a pair of 50 galaxies, with big bulges and no gas). The disk, the bulge, and the halo each contain 16K particles. We ran three different merger simulations, differing only in the mass of the central black hole assigned to each progenitor galaxy. One simulation contained no central black hole in either progenitor. In the next simulation, one of the progenitor galaxies contained a central black hole equal in mass to 0.2% of its total stellar mass (disk + bulge). In the final simulation, one progenitor contained a black holes equal in mass to 2% of its total stellar mass.

We used the n-body code GADGET¹⁰ for all integrations. GADGET is a tree code designed to run on distributed memory, multi-processor comput-

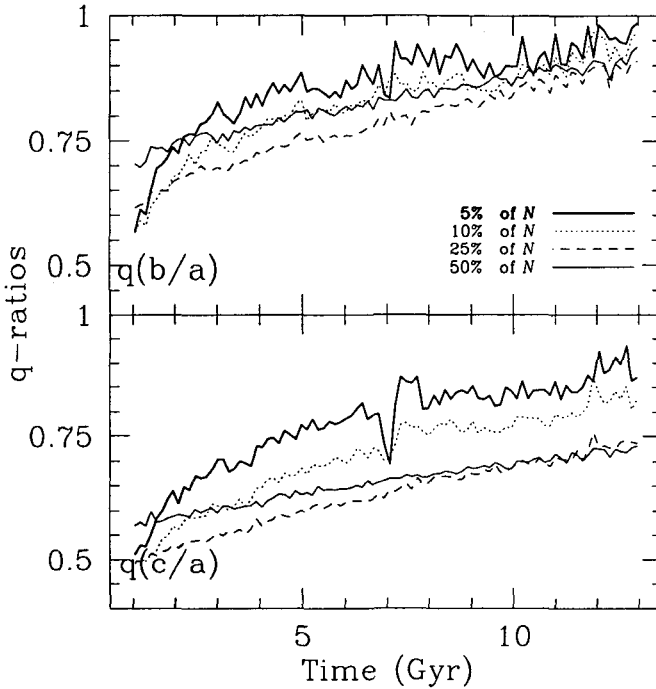


Figure 3: As in Figure 2, but for a simulation in which one progenitor has a moderately massive central black hole (equal in mass to 0.2% of its stellar mass).

ers. It employs continuously variable timesteps which are individual to each particle. The timesteps are computed with an accuracy parameter, η , set to 0.02. The gravitational smoothing lengths for the disk, bulge, and halo particles were 0.08, 0.08, and 0.4 respectively. For force calculations between any particle and a black hole, a smoothing length of 0.001 was used. (For reference, the disk scale length of the progenitor galaxies was 1.0.)

In the first simulation, whose results are presented in Figure 2, the merging galaxies contained no central black holes. Note that both the intermediate-to-long axis ratio (illustrated in the upper panel of Figure 2) and the short-to-long axis ratio (illustrated in the lower panel) evolve steadily toward unity in this simulation, despite the absence of a central black hole. This is a spurious two-body relaxation effect, resulting from the coarseness of our simulation; instead of being made of tens of billions of stars, the ‘luminous’ portions of our simulated galaxies contain only tens of thousands of mass points.

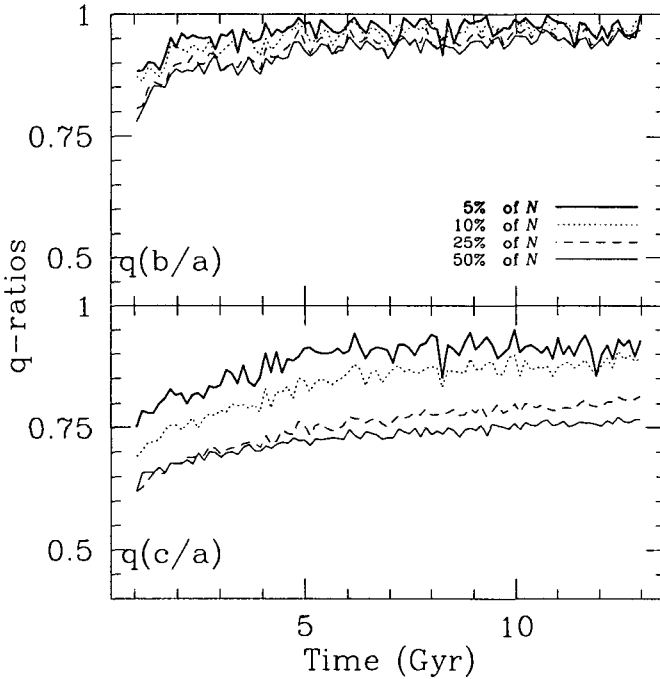


Figure 4: As in Figure 2, but for a simulation in which one progenitor has an extremely massive central black hole (equal in mass to 2% of its stellar mass).

In Figure 3, showing the evolution in shape of a merger remnant with moderate mass black holes (0.2% of the total stellar mass of the progenitors), we see that the evolution toward a spherical shape is more rapid than in the absence of black holes. Moreover, the drive toward a spherical shape is most rapid for the 5% most tightly bound particles (the heavy solid line in Figure 3) than for the 50% most tightly bound (the light solid line). In short, the added black holes drive the central, most tightly bound, regions of the merger remnant toward a spherical shape on Gyr timescales.

Adding black holes an order of magnitude more massive, as shown in Figure 4, dramatically shortens the time for making the merger remnant spherical. With big black holes, equal to 2% of the total stellar mass, the merger remnant rapidly becomes very nearly oblate (that is, the ratio b/a , shown in the upper panel of Figure 4, rapidly approaches one.) The ratio c/a , shown in the lower panel, approaches unity more gradually. However, we can conclude that if

merging galaxies contained extremely massive black holes, equal to one or two percent of their total stellar mass, then merger remnants would become nearly oblate on timescales shorter than a Gyr. The relative scarcity of nearly circular isophotes ($q > 0.95$) in the central regions of elliptical galaxies – see the upper left panel of Figure 1 – argues that elliptical galaxies are probably not oblate in their central regions. However, given the relatively small size of the Terlevich-Forbes sample, this is not a chiseled-in-stone conclusion.

More data are needed (unsurprisingly). A larger sample size of observational data will help to pin down the relationship among galaxy age, isophote shape, and luminosity profile type. Much work remains to be done (also unsurprisingly). Higher-resolution numerical simulations will reduce the ugly effects of spurious two-body relaxation and will enable us to focus on the physically real effects of massive black holes.

Acknowledgments

Thanks are due to A. Terlevich and D. Forbes for the use of their age catalog. The numerical work was supported by a grant from the Ohio Supercomputer Center.

References

1. Barnes, J. 1992, *ApJ*, 393, 484
2. Ebisuzaki, T., Makino, J., & Okumura, A. K. 1991, *Nature*, 354, 212
3. Faber, S. M., et al. 1997, *AJ*, 114, 1771
4. Ferrarese, L., & Merritt, D. 2000, *ApJ*, 539, L9
5. Ferrarese, L., van den Bosch, F. C., Ford, H. C., Jaffe, W., & O'Connell, R. W. 1994, *AJ*, 108, 1598
6. Forbes, D. A., Franx, M., & Illingworth, G. D. 1995, *AJ*, 109, 1988
7. Lauer, T. R., et al. 1995, *AJ*, 110, 2622
8. Ryden, B. S., Forbes, D. A., & Terlevich, A. I. 2001, *MNRAS*, in press
9. Springel, V. 2000, *MNRAS*, 312, 859
10. Springel, V., Yoshida, N., & White, S.D.M, 2001, *New Astron.*, 6, 79
11. Terlevich, A. I., & Forbes, D. A. 2001, *MNRAS*, submitted
12. Worthey, G. 1994, *ApJS*, 95, 107

PROPERTIES OF THE OUTER HALOS OF GALAXIES FROM THE STUDY OF GLOBULAR CLUSTERS

Stephen E. Zepf

*Dept. of Physics and Astronomy, Michigan State University
and Department of Astronomy, Yale University, zepf@pa.msu.edu*

This paper reviews some recent work on the properties of the outer halos of galaxies. I particularly focus on recent and upcoming advances made with the study of globular clusters. Globular clusters can be observed out to ~ 100 kpc from the centers of galaxies, allowing the study of galactic halos well beyond the regions probed by many other techniques such as observations of the integrated light of galaxies. In the few well-studied cases to date, the study of globular cluster systems has provided dynamical evidence for dark matter halos around elliptical galaxies, and demonstrated kinematic differences between different globular cluster populations that shed light on the formation history of their host galaxies.

1 Why Outer Halos?

One of the primary motivations for studying the outer halos of galaxies is to study the nature of dark matter. The reason the outer halos of galaxies are important for addressing the nature of dark matter is that most galaxies are only dark matter dominated at large distances from their centers. In the inner regions of galaxies ($r \lesssim R_e$), the observed stars and gas typically make a significant contribution to the mass budget. Exactly what that contribution is for different galaxies remains a subject of active research and vigorous debate. This vigorous debate is symptomatic of the problem of determining the dark matter content of the inner parts of galaxies accurately. Specifically, because the observed baryons make up a non-negligible fraction of the mass in the inner regions of most galaxies, an accurate determination of the dark matter properties in these regions requires a very accurate accounting of the mass contribution of these baryons. Since it is a severe challenge to achieve such an accurate accounting of the baryonic mass in the inner regions of galaxies, the dark matter properties of the inner regions of galaxies remain somewhat uncertain. Moreover, in regions in which baryons are a significant fraction of the mass, the dissipation, star formation, and feedback that can happen in the baryons may affect the distribution of the dark matter. Although it is possible to study special classes of objects (e.g. low surface brightness galaxies) for which the observed baryons appear to be negligible in the mass budget at all radii, this approach still leaves open the question of the dark matter properties of galaxies in general. An obvious path to take is to study the outer halos of galaxies in which the baryonic contribution is much smaller, and one can obtain

a “clearer” view of the dark matter around galaxies.

A second motivation for studying the outer halos of galaxies is that the outskirts of galaxies have long dynamical times, and therefore these regions may retain more of a memory of their initial conditions than central regions for which the crossing times are much smaller than the Hubble time. Specifically referring to the shapes of galaxies and their halos, it is possible that the outer regions might more closely reflect the initial conditions, while various dissipative processes may re-arrange the matter in the central regions.

A third reason for studying the outer halos of galaxies is that they are still uncharted territory. Why this is the case, and some possibilities for making advances in this area are the subject of the following sections.

2 Why Globular Clusters?

The most significant challenge to studying galaxies at large distances from their centers is that there is very little light in the regions to observe. For galaxies rich in neutral hydrogen, HI disks can be traced to large radii, and these provide valuable constraints on the dark matter profile at large radii. These constraints on the dark matter profiles provided by extended HI rotation curves are some of the strongest available. However, even in these cases, one would ideally like to constrain the shape of the dark matter halo in a galaxy and not just its profile. This has proven to be a very challenging task (see review by Sackett 1999).

Early-type galaxies do not have an easily observed tracer such as HI, so one needs to look for other ways to constrain the mass profile of these galaxies. One approach is to determine the velocity dispersion of the integrated light. However, as shown in Fig. 1, the integrated light of these galaxies drops rather rapidly with increasing radius, and falls well below the sky brightness at very modest radii. As a result, even the most dedicated attempts with large telescopes have not been able to constrain the velocity dispersion of the stars beyond about $2R_e$, and radial limits of about half of that are more typical. Data adequate to characterize the higher order moments useful for constraining the orbital anisotropy are at least as limited in radial extent. Moreover, one would also like to study the stellar populations of galaxies at large radii, and the rapid decline of the surface brightness of the integrated light of all galaxies makes this a daunting challenge.

Globular clusters provide a valuable tracer of both the kinematics and the stellar populations of galaxies out to large radii. Firstly, as individual dense collections of stars, there is no problem observing globulars that are present at large radii. Secondly, as shown in Fig. 1, globular clusters have

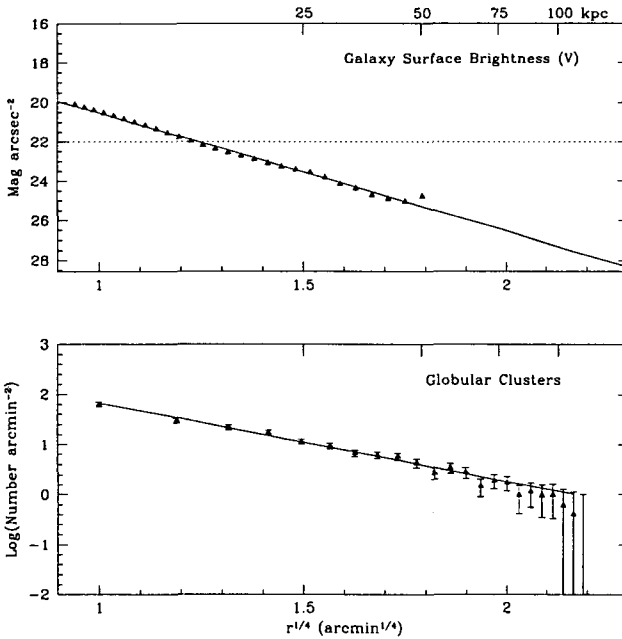


Figure 1: A plot of the surface density against radius of the starlight (upper panel) and globular clusters (lower panel) for the Virgo elliptical NGC 4472 (data from Rhode & Zepf 2001). The light dashed line represents the surface brightness of a dark sky. This plot demonstrates the great difficulty extending studies of the integrated light to large radii. The greater spatial extent of the globular cluster system relative to the integrated light is also clearly seen.

extended spatial distributions, so they can be found in useful numbers at large radii, particularly around luminous ellipticals which typically have populous globular cluster systems. Thirdly, globular cluster systems provide information both about the dynamics of the outer halos of galaxies through their radial velocities, and about the chemical enrichment and possibly even age through their photometric and spectroscopic properties.

Planetary nebulae are also valuable probes of the outer halos of galaxies. Like globular clusters, each planetary nebulae can be observed equally well no matter how far away it is from the center of its host galaxy. They also have the advantage that much of their light is emitted in a single line, so obtaining an accurate radial velocity for a planetary nebula can be straightforward. However, the surface density of planetary nebulae does not have the large spatial

extent of the globular cluster systems, and they have not yet provided as much information about the formation history of galaxies at large radii as globulars. A final approach, reviewed at this meeting by David Buote, is to use the properties of the hot gas emitting in X-rays found around luminous early-type galaxies. With sufficiently accurate X-ray imaging spectroscopy, it is feasible to determine the dark matter distribution and metal abundances in hot gas, as well as testing for asymmetries that might indicate objects for which the assumption of hydrostatic equilibrium in the gas at large radii is questionable. An obvious goal is to combine as many approaches as possible, as they each have different sets of assumptions and possible systematic errors, which might be revealed through careful inter-comparison.

3 Two Dimensional Shapes and Inferences about Three-Dimensional Distributions

The two dimensional distribution of light in galaxies has been fairly well characterized within about $1R_e$. One of the uses of these data is to try to constrain the three-dimensional shapes of galaxies. An unconstrained inversion of two-dimensional data to the intrinsic three-dimensional shape is problematic (Rybicki 1987), but either through constrained inversion techniques (e.g. Ryden 1992, Lambas, Maddox, & Loveday 1992) or through the addition of kinematic data (e.g. Franx, Illingworth, & de Zeeuw 1991, Bak & Statler 2000), some progress can be made. Overall, the evidence suggests that at least a small amount of triaxiality is common, with most galaxies being nearly oblate and a modest fraction nearly prolate.

It would be of clear interest to extend these studies to the outer regions of galaxies which might be less influenced by evolution and more closely reflect the conditions when they formed. CCD Mosaics covering larger areas are beginning to make this feasible, although the large surveys of galaxies used in the statistical studies given above are a long way away. Both the integrated light and the globular clusters can be studied this way, with the integrated light offering much more signal, and the clusters potentially reaching to larger radii, but being limited by defining the two-dimensional shape with a modest number of points.

As an example of how this work might develop in the future, we present in Fig. 2 our new results for the position angle and ellipticity of the integrated light and globular clusters around NGC 4472. The position angle of the globular cluster system is consistent with that of the integrated light over the same radial range. The latter qualification matters, since our data confirm that there is a position angle twist in this galaxy, which can be taken as evidence

for some level of triaxiality. The ellipticity of the globular cluster system is marginally smaller (rounder) than that of the galaxy light, but this requires confirmation by additional data.

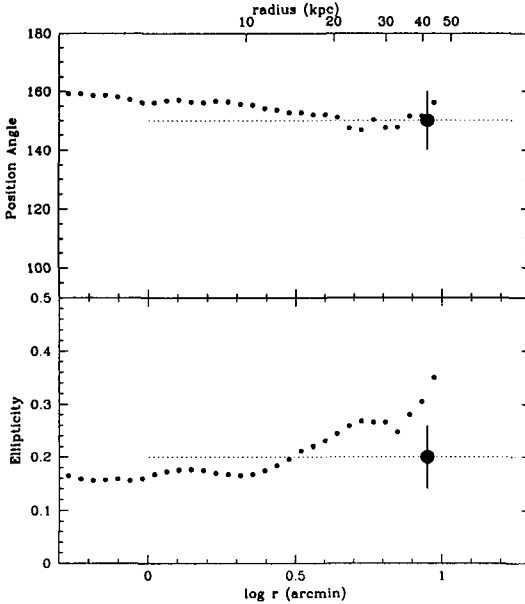


Figure 2: The position and ellipticity as a function of radius for the starlight (plotted as small dots) and the globular clusters (plotted as a large dot) in NGC 4472. The globular cluster point is a radial average over the range indicated by the light dashed line, with the radial location of the dot as the approximate median radius of the globular cluster sample. The uncertainty in the position angle and ellipticity of the NGC 4472 globular clusters system is given by the vertical line about the globular cluster point. This analysis is based on the Mosaic images presented in Rhode & Zepf (2001). This plot shows that the position angle of the globular cluster system is consistent with that of the integrated light over the same radial range. The ellipticity shows marginal evidence that the globular cluster system is slightly rounder than the galaxy, but this requires confirmation by additional data.

4 Radial Velocities

4.1 Kinematics of Individual Populations

One of the valuable applications of radial velocities of substantial numbers of globular clusters around elliptical galaxies is to compare the kinematics of the metal-rich and metal-poor globular clusters previously identified in photometric studies. The kinematics of these systems can shed light on their formation

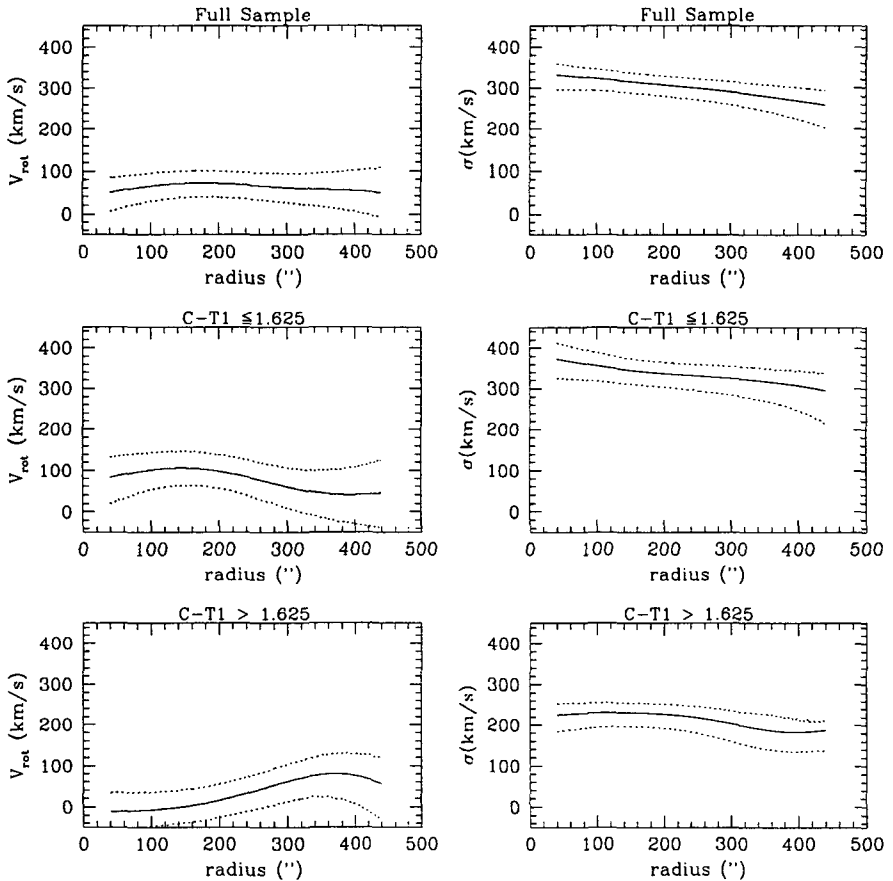


Figure 3: Plots of the rotation and velocity dispersion fields for the globular clusters of NGC 4472 from Zepf et al. (2000). The top panels are for the full data set, the middle panels for the metal-poor (blue) clusters and the bottom panels for metal-rich (red) clusters. A Gaussian kernel with $\sigma = 100''$ was used for the radial smoothing for all of the datasets. The dotted lines show the 1σ uncertainties, as determined from bootstrapping. The curves are highly correlated in the radial direction with the smoothing used. The plots show modest rotation in the full sample and the metal-poor cluster population which is essentially constant with radius. The red sample has essentially zero rotation at small radius and a tentative (1σ) rise to modest rotation at larger radii. The velocity dispersion is significantly larger than the rotation at all radii.

history. As an example, results from our recent study of the NGC 4472 cluster system are shown in Fig. 3. These data confirm our earlier result (Sharples et al. 1998) that the metal-poor globulars have a larger velocity dispersion than the metal-rich globulars. Perhaps most importantly, the results shown in Fig. 3 indicate that the metal-rich globular cluster system has little or no rotation, with an upper limit of $(v/\sigma)_{proj} < 0.34$ (99% confidence level). The absence of rotation in the metal-rich population in this elliptical strongly distinguishes NGC 4472 from spirals like those in the Local Group, which have metal-rich cluster populations with significant rotation. This result argues against models in which all metal-rich systems formed more or less similarly with the only difference being the mass of the central forming “bulge”. Instead, the comparison of the significant rotation in the metal-rich Galactic clusters with the insignificance of rotation in the metal-rich clusters of NGC 4472 suggests a model in which elliptical galaxies like NGC 4472 form in major mergers which create the metal-rich globular cluster population and transfer angular momentum outwards, while disk galaxies like the Milky Way have only had more minor mergers, which may lead to modest amounts of globular cluster formation but which are not as efficient at angular momentum transfer.

It is of interest to compare the results for NGC 4472 to those of other ellipticals. There are two other galaxies for which published data are sufficient to make reliable statements about the kinematics of their globular cluster systems. One of these is M87, the central galaxy in the Virgo cluster. Here Côté et al. (2001) used data from Cohen (2000), Cohen & Ryzhov (1987) and their own observations to find $(v/\sigma)_{proj} \sim 0.4$, although with large error bars because of large uncertainties in the rotation. There is evidence that much of the rotation signal comes from the outer regions (see also Kissler-Patig & Gebhardt 1998), so modest rotation and significant angular momentum transport is also suggested for the metal-rich system of this giant elliptical. The third system with significant data is the recent merger, NGC 5128 (Cen A). The kinematics here appear to be different, in that the metal-rich system appears to be rotating significantly, while the metal-poor system shows little rotation (Hui et al. 1995 and references therein). Possible differences between this system and that of NGC 4472 and M87 are that the NGC 5128 system has not yet come to equilibrium and transported angular momentum outwards, or that NGC 5128 is a lower luminosity elliptical which tend to be more rotationally supported.

4.2 Mass Profiles

Measurements of the radial velocities of globular clusters also provide information about the mass distribution of the host galaxy and the orbits of the

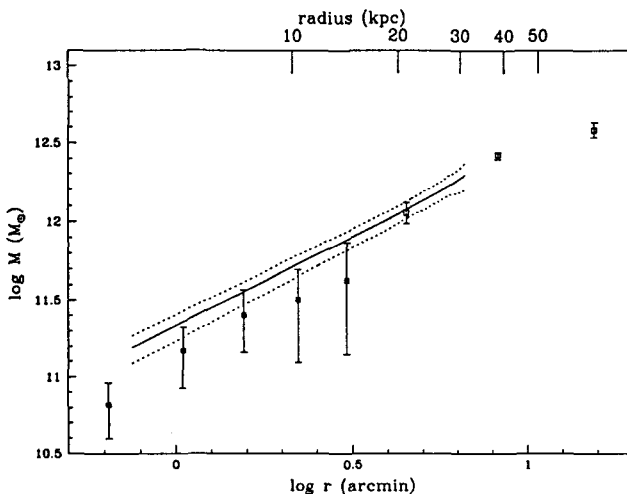


Figure 4: A plot of the mass of NGC 4472 as a function of radius from Zepf et al. (2000). The lines are masses inferred from the radial velocities of the globular clusters. The central solid line is the best fit to the 144 radial velocities discussed in this paper. The dotted lines are the 1σ lower and upper limits determined via bootstrapping. All of these are based on the assumption of isotropic orbits for the globular clusters. The points are masses inferred from ROSAT observations of the hot gas around NGC 4472 (Irwin & Sarazin 1996). The open squares represent points for which the assumption of hydrostatic equilibrium on which the X-ray masses are based may be uncertain because the X-ray isophotes are irregular at these radii. The overall agreement between the masses inferred from the two techniques is good, suggesting that the assumptions underlying each approach are probably roughly correct. The conclusion that then follows is that NGC 4472 has a substantial dark halo, with a mass-to-light ratio at several tens of kpc that is at least a factor of five greater than in the inner regions of the galaxy.

clusters. Globular clusters are particularly useful probes of the dynamics of the outer halos of elliptical galaxies because they can be observed out to much larger radii than it is possible to obtain spectroscopy of the integrated light. A very large number of velocities are required to independently determine the mass distribution and the orbits of the tracer particles in a completely non-parametric way (e.g. Merritt & Tremblay 1994). However, if the mass distribution inferred from X-ray observations and the assumption of hydrostatic equilibrium in the hot gas is adopted, the orbits of the globular clusters can be constrained. Conversely, if assumptions are made about the cluster orbits (e.g. that they are isotropic), then the mass distribution can be estimated. In practice, a sensible approach is to check for consistency of the mass distribution determined via the X-ray observations of the hot gas with dynamical

measurements (possibly both from globulars and planetary nebulae) given simplifying assumptions about the orbits, as each technique has its own systematic concerns which are mitigated if the independent approaches agree.

In Fig. 4, we present the mass profile of NGC 4472, estimated from the velocity dispersion profile given in Fig. 3 and the density profile of the clusters given in Fig. 1. We also show for comparison the mass profile estimate based on X-ray observations of the hot gas around this galaxy. The general agreement in these two mass estimates suggests both techniques are probably not beset by terrible systematic errors, and thus provides further evidence for the existence of massive dark halos around elliptical galaxies. The agreement between the two independent mass estimates also suggests that the assumption of isotropic orbits used to obtain the mass estimate from the globular cluster velocities is unlikely to be dramatically off. Similar results are found for M87 (e.g. Côté et al. 2001, Romanowsky & Kochanek 2001, Cohen & Ryzhov 1997). In detail, anisotropy is required at some level for the NGC 4472 globular cluster system because the flattening of system can not be supported by the negligible rotation observed. This is not necessarily true of the M87 system. One of the potential advantages of the study of individual tracers (either globular clusters or planetary nebulae) is that both shape and kinematic information covering the full two-dimensional projected distribution on the sky are obtained (unlike single slices from standard long-slit spectroscopy), which may be useful for future larger studies that attempt to constrain the three-dimensional shape of galactic halos.

Acknowledgments

The research described here would not have been carried out successfully without the contributions of many collaborators. The photometric studies are primarily the thesis work of Katherine Rhode, and were made feasible by the CCD Mosaic imagers at NOAO. The dynamical study of NGC 4472 is based on data obtained at the CFHT and WHT and came to fruition through the hard work of my many colleagues on that project, including Mike Beasley, Ray Sharples, Terry Bridges, and Dave Hanes. Support for various aspects of the work presented here has been provided by NASA Long-Term Space Astrophysics grant NAG5-9651, by a NASA GSRP Fellowship for K. Rhode, and by HST NASA grants AR-07981 and AR-08755, from the Space Telescope Science Institute, operated by AURA, Inc. under NASA contract NAS-5-26555.

References

1. J. Bak and T.S. Statler, *AJ*, **120**, 110 (2000).

2. J.C. Cohen, *AJ*, **119**, 162 (2000).
3. J.C. Cohen, and A. Ryzhov, A., *ApJ*, 486, 230 (1997).
4. P. Côté, *et al.*, *ApJ*, 2001, 559, 828
5. M. Franx, G.D., Illingworth and P.T. de Zeeuw, *ApJ*, **383**, 112 (1991).
6. M. Kissler-Patig and Gebhardt, K., *AJ*, **116**, 2237, (1998)
7. X. Hui, H.C. Ford, K.C. Freeman and M.A. Dopita, *ApJ*, **449**, 592 (1995).
8. J.A. Irwin and C.L. Sarazin, *ApJ*, **471**, 683 (1996).
9. D.G. Lambas, S.J. Maddox and J. Loveday, *MNRAS*, **258**, 404 (1992).
10. D. Merritt, *PASP*, **111**, 129 (1999).
11. D. Merritt and B. Tremblay *AJ*, **108**, 514 (1994).
12. K.L. Rhode and S.E. Zepf, *AJ*, **121**, 210 (2001).
13. A.J. Romanowsky and C.S. Kochanek, *ApJ*, **552**, 722 (2001).
14. G.B. Rybicki in *Structure and Dynamics of Elliptical Galaxies*, ed. P.T. de Zeeuw, 397 (Kluwer, Dordrecht, 1986).
15. B.S. Ryden, *ApJ*, **386**, 42 (1992).
16. P. Sackett, in *Galaxy Dynamics*, ed. D. Merrit, J. Sellwood and M. Valuri, 393, (ASP, San Francisco, 1999).
17. R. Sharples, *et al.*, *AJ*, **115**, 2337 (1998).
18. S.E. Zepf, *et al.*, *AJ*, **120**, 2928 (2000).

WHITE DWARFS: CONTRIBUTORS AND TRACERS OF THE GALACTIC DARK-MATTER HALO

L.V.E. Koopmans & R.D. Blandford

Caltech, mailcode 130-33, Pasadena CA 91101, USA

We examine the claim by Oppenheimer et al. (2001) that the local halo density of white dwarfs is an order of magnitude higher than previously thought. As it stands, the observational data support the presence of a kinematically distinct population of halo white dwarfs at the >99% confidence level. A maximum-likelihood analysis gives a radial velocity dispersion^a of $\sigma_U^h = 150_{-40}^{+80}$ km s⁻¹ and an asymmetric drift of $v_a^h = 176_{-80}^{+102}$ km s⁻¹, for a Schwarzschild velocity distribution function with $\sigma_U : \sigma_V : \sigma_W = 1:2/3:1/2$. Halo white dwarfs have a local number density of $1.1_{-0.7}^{+2.1} \times 10^{-4}$ pc⁻³, which amounts to $0.8_{-0.5}^{+1.6}$ per cent of the nominal local dark-matter halo density and is $5.0_{-3.2}^{+9.5}$ times (90% C.L.) higher and thus only marginally in agreement with previous estimates. We discuss several direct consequences of this white-dwarf population (e.g. microlensing) and postulate a potential mechanism to eject young white dwarfs from the disc to the halo, through the orbital instabilities in triple or multiple stellar systems.

1 Introduction

Recently, Oppenheimer et al. (2001; O01 hereafter) found 38 white dwarfs (WD) in a sample of 99 high proper motion WDs, which were claimed to have kinematics inconsistent with that of both the old stellar disc *and* the thick disc, and therefore form a newly discovered halo population with an inferred density at least an order of magnitude higher than previously thought (e.g. Gould et al. 1998). Reid et al. (2001) have challenged this result and conclude that these WDs form the high-velocity tail of the thick disc, based on a comparison of their $U-V$ velocity distribution with that of M-dwarf stars. Unfortunately, neither conclusion is statistically supported.

We discuss a maximum-likelihood analysis of the complete sample of 99 WDs and derive the local phase-space density of thick-disc *and* halo WDs. This then allows us to draw more robust conclusions. For a discussion of the selection of the sample, we refer to O01. Details of the likelihood analysis and phase-space density estimate can be found in Koopmans & Blandford (2001; KB01 hereafter). For clarity, throughout the proceeding the low- and high-velocity dispersion components are referred to as the thick-disc and halo population, respectively. This does not imply that all WDs could not have originated from the thin or thick disc (e.g. Hansen 2001; KB01).

^aHereafter, if not otherwise indicated, errors give the 90% statistical confidence level.

2 The White-Dwarf Velocity Distribution Function

We model the local (\vec{x}_0) velocity distribution function (VDF) as a superposition of two Schwarzschild (i.e. Maxwellian) VDFs, i.e. $f_B(\vec{x}_0, \vec{v})$. We assume a constant space density of WDs throughout the surveyed volume. Each component has two free parameters, the radial velocity dispersion (σ_U) and the asymmetric drift (v_a). In addition, the parameter r_n is the ratio of the thick-disc to halo WD number densities (n). We assume that the vertex deviations are zero and that the ratios of the radial (U), azimuthal (V) and vertical (W) velocity dispersions of the ellipsoidal VDFs are $\sigma_U:\sigma_V:\sigma_W=1:2/3:1/2$, in agreement with observations (see KB01 for references). The probability that an observed WD with a velocity vector on the sky, $\vec{p} = (v_l, v_b)$, is drawn from this VDF becomes $P = \int_{-\infty}^{\infty} (v_l^2 + v_b^2)^{3/2} f_B(\vec{v} = \vec{p} + v_r \hat{r}) dv_r / \int_{\mathcal{V}} (v_l^2 + v_b^2)^{3/2} f_B(\vec{v} = \vec{p} + v_r \hat{r}) d^3v$, where v_r is the radial velocity along the line-of-sight and v_l and v_b are the velocities projected on the sky in Galactic coordinates. This assumes that the WDs are all proper-motion limited ($\sim 90\%$ are). \mathcal{V} is then the velocity space in which the WDs could have been found, given the restriction that $v_l^2 + v_b^2 > (\mu_0 r)^2$, where r is the distance to the WD and μ_0 is the survey's lower limit on the proper motion ($\mu_0 \sim 0.33'' \text{ yr}^{-1}$). For the $\sim 10\%$ magnitude limited WDs, we find that their maximum detection volumes (V_{max}) are nearly identical. For these, we modify the likelihood function, although the differences in parameter estimates are within the quoted errors. Varying the five free parameters and optimizing the log-likelihood, $\mathcal{L} = \sum_i \log(P_i)$, of the sample, we solve for their most likely values and their error range. The results (excluding 3 thin-disc WDs) are: (a) $\sigma_{U,d} = 62_{-10}^{+8} \text{ km s}^{-1}$, (b) $\sigma_{U,h} = 150_{-40}^{+80} \text{ km s}^{-1}$, (c) $v_{a,d} = 50_{-11}^{+10} \text{ km s}^{-1}$, (d) $v_{a,h} = 176_{-80}^{+102} \text{ km s}^{-1}$ and (e) $r_n = 16_{-11}^{+30}$ (KB01).

3 The Local Halo White-Dwarf Density

To normalize the local phase-space density of halo plus thick-disc WDs, i.e. $n_{0,\text{WD}}^{\text{td+h}} \cdot f_B(\vec{x}_0, \vec{v})$, it remains to estimate their local density, $n_{0,\text{WD}}^{\text{td+h}}$. We do this in the conventional way, by summing the $1/V_{\text{max}}$ values of the halo plus thick-disc WDs, where V_{max} is the smallest of the two volumes in which a WD could have been detected, when limited either by its proper motion or by its magnitude (e.g. O01; KB01). We find that $\sim 90\%$ of the WDs are proper-motion limited and three WDs are very likely associated with the thin disc. The latter WDs are removed from the sample, as we are only interested in the halo plus thick-disc density, for which we determined the VDF. We find $n_{0,\text{WD}}^{\text{td+h}} = (1.9 \pm 0.5) \times 10^{-3} \text{ pc}^{-3}$, of which $n_{0,\text{WD}}^h = 1.1_{-0.7}^{+2.1} \times 10^{-4} \text{ pc}^{-3}$ belongs to the halo, given r_n found from the maximum-likelihood analysis of the sample. The local halo plus thick-disc density estimate agrees within $\sim 1 \sigma$ with the estimate from Reid et al. (2001). The halo density is $5.0_{-3.2}^{+9.5}$ times

higher than the best previous estimate of $\bar{n}_{0,\text{WD}}^{\text{h}} = 2.2 \times 10^{-5} \text{ pc}^{-3}$ from Gould et al. (1998), inferred from the mass function of halo stars. Locally, our density estimate amounts to $0.8_{-0.5}^{+1.6}\%$ of the nominal local dark-matter halo density of $8 \times 10^{-3} M_{\odot} \text{ pc}^{-3}$ (Gates et al. 1995).

4 The Global Halo White-Dwarf Density

Given the *local* phase-space density of halo plus thick-disc WDs and a potential model for the Galaxy, we can estimate the *global* white-dwarf density in a large part of the Galactic halo, using Jean's theorem (e.g. May & Binney 1986). For simplicity, we assume a spherical logarithmic potential, $\Phi(r) = v_c^2 \ln(r/r_c)$, with rotation velocity $v_c = 220 \text{ km s}^{-1}$ and a solar radius of $r_c = 8 \text{ kpc}$. For the halo WDs, which are less affected by the disc/bulge potentials this is probably a reasonable assumption, although this does not hold for the lower-velocity thick-disc WDs. A analytic expression for the phase-space density of halo WDs can then be derived for any point in halo that is in dynamic contact with the Solar neighborhood (KB01). From this phase-space density model, we find an oblate ($q = (c/a)_{\rho} \sim 0.9$) distribution of halo WDs with a total mass inside 50 kpc of $\sim 2.6 \times 10^9 M_{\odot}$ and a radial mass profile $n(r) \propto r^{-3.0}$. We expect q to decrease further if a proper flattened Galactic potential is used. This halo WD mass amounts to $\sim 0.4\%$ of the total Galactic mass inside 50 kpc , $\sim 4\%$ of the Galactic stellar mass, or $\Omega_{\text{WD}} \sim 10^{-4}$. Including disc WDs, the total mass of WDs in the Galaxy is $\sim 9\%$ of the stellar mass, in agreement with standard population synthesis models (Hansen 2001; KB01).

5 The LMC Microlensing Optical Depth

Given our analytic expression of the halo WD phase-space density, we can integrate over the line-of-sight towards the Large Magellanic Cloud (LMC) to estimate the microlensing optical depth of this population. We find $\tau_{\text{WD}}^{\text{h}} \sim 1.3 \times 10^{-9}$, which is $\sim 10^2$ times lower than observed (Alcock et al. 2000). The thick-disc WDs have a ~ 3 times higher optical depth. The integrated halo plus thick-disc WD optical depth is therefore still 1–2 orders of magnitude too small.

6 Conclusions, Discussion & Future

Modeling of the local phase-space density of halo plus thick-disc WDs indicates that there is a population of pressure-supported halo WDs with a *local* density $5.0_{-3.2}^{+9.5}$ times higher than previously estimated, although globally ($r \lesssim 50 \text{ kpc}$) the mass contribution is negligible ($\sim 0.4\%$). Both the low- and high-velocity populations have similar color, magnitude and ages distributions (Hansen 2001;

KB01). Two particularly interesting surveys to search for more high proper motion WDs are: (i) a wide survey with the Advanced Camera for Surveys (ACS) on the Hubble Space Telescope, which we estimate should find ~ 5 WDs (KB01) and (ii) a similar survey as that by O01 towards the Galactic anti-center to constrain the WD velocities perpendicular to the Galactic plane.

The white-dwarf data set from O01 and results derived from it (i.e. our most likely model) have met a number of internal and external consistency checks (KB01) and agree with all observational constraints (e.g. direct observations, metal pollution of the ISM, microlensing, etc.) known to us. The color-color relation of the WDs shows them to be quite young (Hansen 2001) and have a birth rate roughly that expected from Galactic population synthesis models (KB01). Why then do a large fraction of these WDs have such high spatial velocities? *To explain this we postulate the following; the majority of high-velocity WDs in the Galactic halo originate from multiple (i.e. $N \geq 3$) stellar systems in the Galactic disc. In case of a triple stellar system, stellar evolution (i.e. mass loss and/or transfer) of the (probably more massive) inner binary stars changes the ratios of orbital periods and eventually destabilizes the system. At that point, the lightest star, a WD in the inner binary, is ejected from the system into the halo – possibly through a slingshot of the outer star – leaving behind a recoiled compact binary (KB01).* This postulate implies a direct relation between the radial surface density of the stellar disc, the star-formation rate and population synthesis models, which all seem to be in agreement (KB01), but still need considerable study.

Acknowledgments

We thank Ben Oppenheimer for valuable discussions, David Graff and Andy Gould for pointing out an error in the normalization of our likelihood function. This research has been supported by NSF AST-9900866 and STScI GO-06543.03-95A.

References

1. Alcock, C. et al. 2000, ApJ 542, 281
2. Gates, E.I., Gyuk, G., & Turner, M.S. 1995, ApJL 449, L123
3. Gould, A., Flynn, C., & Bahcall, J.N. 1998, ApJ 503, 798
4. Hansen, B.M.S., 2001, ApJ, 558, L39
5. Koopmans, L.V.E. & Blandford, R.D., 2001, MNRAS submitted (KB01)
6. May, A. & Binney, J. 1986, MNRAS 221, 857
7. Oppenheimer, B.R., Hambly, N.C., Digby, A.P., Hodgkin, S.T., & Saumon, D., Science, Vol. 292, 698 (O01)
8. Reid, I.N., Sahu, K.C. & Hawley, S.L., 2001, ApJ, 559, L942

KECK SPECTROSCOPY OF DWARF ELLIPTICAL GALAXIES IN THE VIRGO CLUSTER

M. Geha, P. Guhathakurta
UCO/Lick Observatory, Santa Cruz, CA 95064, USA
E-mail: mgeha, raja@ucolick.org

R. van der Marel
STScI, 3700 San Martin Drive, Baltimore, MD 21218, USA
E-mail: marel@stsci.edu

Keck spectroscopy is presented for four dwarf elliptical galaxies in the Virgo Cluster. At this distance, the mean velocity and velocity dispersion are well resolved as a function of radius between 100 to 1000 pc, allowing a clear separation between nuclear and surrounding galaxy light. We find a variety of dispersion profiles for the inner regions of these objects, and show that none of these galaxies is rotationally flattened.

1 Introduction

Dwarf elliptical galaxies (dEs) are among the poorest studied galaxies due to their faint luminosities, $M_V \gtrsim -17$, and characteristic low effective surface brightness $\mu_e(V) > 22$ mag arcsec⁻² (Ferguson & Binggeli 1994). The defining characteristic of dEs is an exponential surface brightness profile. The majority of dEs brighter than $M_V = -16$ have compact nuclei typically containing 5 to 20% of the total galaxy light; most dEs fainter than $M_V = -12$ show no sign of a nucleus (Sandage *et al.* 1985). Although the sample of dEs with measured internal kinematics is small (Bender & Nieto 1990; Peterson & Caldwell 1993), these observations have provided strong evidence that dwarf and classical ellipticals evolve via very different physical processes.

Here we present Keck spectroscopy for four Virgo dEs. Velocity and velocity dispersion profiles are measured out to ~ 1 kpc, assuming a Virgo Cluster distance of 16.1 Mpc (Kelson *et al.* 2000). These are the initial results of a larger project to study the dynamics of dwarf elliptical galaxies.

2 Keck Observations

Four Virgo dEs were observed with the Echelle Spectrograph and Imager (ESI) on the Keck II telescope in March 2001. The spectra were obtained through a $0.75'' \times 20''$ slit placed along the major axis of each galaxy with wavelength coverage $\lambda\lambda 3900\text{--}9500\text{\AA}$ and resolution of 23 km s^{-1} (Gaussian sigma). As shown in Table 1, the observed galaxies cover a range of ellipticities and three of the

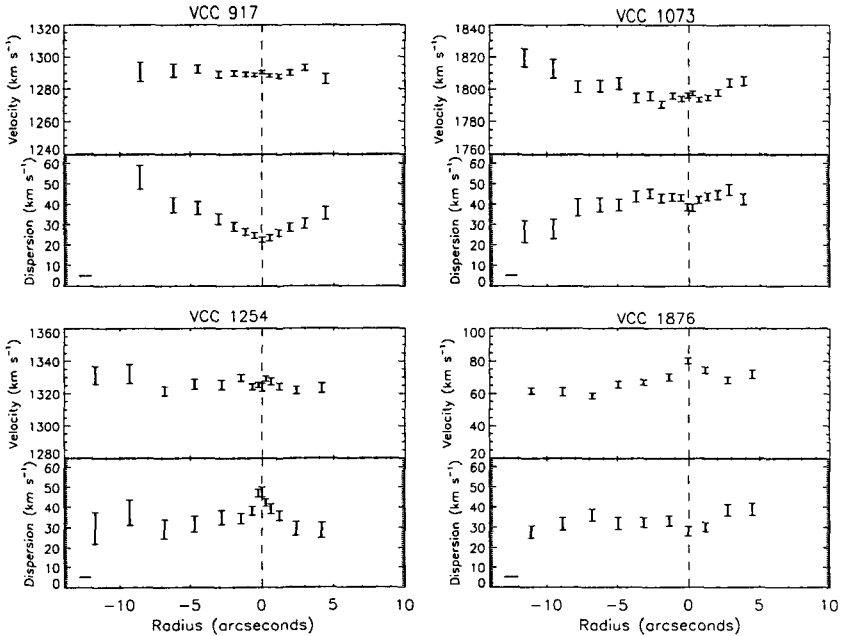


Figure 1: Mean velocity and velocity dispersion profiles for four Virgo dEs. The bar at the lower left of each panel indicates the seeing FWHM during each observation. At the distance of the Virgo Cluster, $1'' \sim 100$ pc.

four are nucleated dwarfs (dE,N). These objects lie near the bright end of the dE luminosity function and were selected to have archival WFPC2 imaging. Mean radial velocities and velocity dispersions were determined using a pixel space χ^2 minimization scheme described in van der Marel (1994). The data were spatially rebinned to achieve a $S/N > 5$ at all radii. Velocities are measured relative to a KOIII template star using the Mg b region, $\lambda\lambda 5000 - 5400 \text{ \AA}$; an analysis of the full wavelength region will be presented in a forthcoming paper. Tests show that the galaxies' internal velocity dispersions are recovered accurately down to the instrumental resolution of 23 km s^{-1} .

3 Discussion

3.1 Anisotropic Dispersion Versus Rotational Flattening

The observed shapes and kinematics of elliptical galaxies between $-20 < M_B < -18$ are consistent with rotational flattening. This trend does not appear to extend to lower luminosity classical ellipticals and the three Local Group dwarf

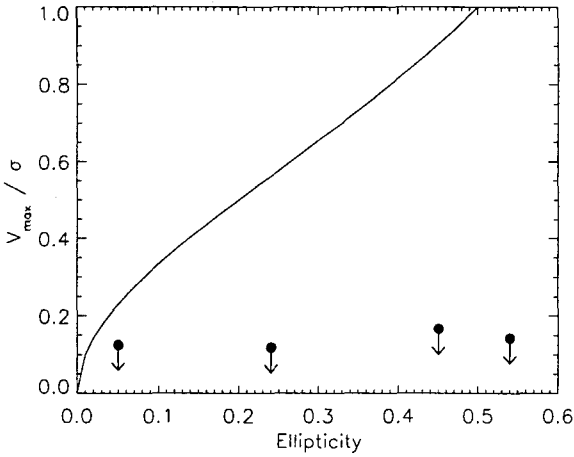


Figure 2: The ratio of the upper limit on the rotation velocity v_{\max} to observed velocity dispersion σ plotted versus mean ellipticity for four Virgo dwarf ellipticals. The solid line is the expected relation for an oblate, isotropic galaxy flattened by rotation.

ellipticals (Davies *et al.* 1983; Bender & Nieto 1990). The four Virgo dEs presented here are also not rotationally flattened. For each galaxy, an average ellipticity ϵ was determined by standard ellipse fitting of archival WFPC2 V -band images between radii of $1'' - 20''$ (see Table 1). From the velocity profiles shown in Fig. 1, we estimate an upper limit to the maximum rotation velocity, v_{\max} . An average velocity dispersion σ is determined for each galaxy beyond $r > 1''$ to avoid nuclear contamination.

The ratio v_{\max}/σ is plotted against ellipticity in Fig. 2 and is compared to the ratio expected from an isotropic, rotationally flattened body (Binney & Tremaine 1987). The upper limits on v_{\max}/σ determined for these galaxies are 2 to 8 times smaller than expected if the observed flattenings were due to rotation. Thus, we conclude that these dEs are primarily flattened by anisotropic velocity dispersions.

3.2 Velocity Dispersion Profiles and dE Nuclei

Although the mean velocity profiles presented in Fig. 1 are qualitatively similar, the velocity dispersion profiles are more heterogeneous. The velocity dispersion of the non-nucleated dE VCC 917 decreases smoothly towards the galaxy center in contrast to the three nucleated dwarfs, which vary more abruptly

Table 1: Observed Virgo Cluster Dwarf Elliptical Galaxies

Galaxy Name	M_B	Type	ϵ
VCC 917	-16.4	dE6	0.54
VCC 1073	-17.3	dE3,N	0.24
VCC 1254	-16.4	dE0,N	0.05
VCC 1876	-16.8	dE5,N	0.45

in the central few arcseconds. The nuclear velocity dispersions of two dE,Ns, VCC 1073 and VCC 1876, are lower than the surrounding galaxy, whereas the nuclear velocity dispersion of VCC 1254 is higher. The origin of nuclei in dEs is largely unknown, but their presence has been correlated to global galaxy parameters such as shape and specific globular cluster frequency (Ryden & Terndrup 1994; Miller *et al.* 1998). A favored hypothesis is that the nuclei are dense star clusters, possibly remnants of larger stripped or harassed objects (Moore *et al.* 1998). More work is needed to determine whether the kinematic profiles presented here are consistent with these scenarios.

Dynamical mass modeling of classical ellipticals has placed strong constraints on their origin and evolution. We are in the process of modeling these dE kinematic data using techniques similar to those described in van der Marel (1994). We will investigate the variation of M/L ratio across our sample of galaxies and as a function of galactic radius within each galaxy. In addition, we plan to study the position of these dEs in the Fundamental Plane. These results will be presented in an forthcoming paper.

References

1. R. Bender & J. Nieto, *A&A* **239**, 97 (1990).
2. J. Binney & S. Tremaine, *Galactic Dynamics*, Princeton Univ. Press, 1987.
3. R. Davies *et al.*, *ApJ* **266**, 41 (1983).
4. H. Ferguson & B. Bingelli, *A&A Rev* **6**, 67 (1994).
5. D. Kelson *et al.*, *ApJ* **529**, 768 (2000).
6. B. Miller *et al.*, *ApJ* **508**, L133 (1998).
7. B. Moore *et al.*, *ApJ* **495**, 139 (1998).
8. R. Peterson & N. Caldwell, *AJ* **105**, 1411 (1993).
9. B. Ryden & D. Terndrup, *ApJ* **425**, 43 (1994).
10. A. Sandage *et al.*, *AJ* **90**, 1759 (1985).
11. R. van der Marel, *MNRAS* **271**, 270 (1994).

HALO MASS DYNAMICS OF M31 USING PLANETARY NEBULAE VELOCITIES

C. Halliday, D. Carter, Z.C. Jackson

*Astrophysics Research Institute, Liverpool John Moores University,
Egerton Wharf, Birkenhead, CH41 1LD, U.K.*

E-mail: ch@astro.livjm.ac.uk

T. Bridges

Anglo-Australian Observatory, Sydney, Australia

N.W. Evans; M. Wilkinson

Theoretical Physics, Oxford; IoA, Cambridge, U.K.

N. Tanvir; G.K.T. Hau

University of Hertfordshire, U.K.; Universidad Catolica, Chile

We present an investigation of the halo dynamics of M31 using planetary nebulae (PNe) velocities. We describe our current velocity data, and imaging to enable spectroscopy to be performed deeper into the galaxy halo (~ 20 kpc). In the future we will measure the total mass, mass distribution and velocity anisotropy as a function of radius. We plan to compare kinematics of the globular cluster and PNe populations to test if both trace similar stellar populations.

1 Introduction

The Andromeda Galaxy M31 is our closest giant spiral galaxy and we are capable of conducting a robust analysis of its halo dynamics. The rotation of M31, first detected by Baade in the early 1900s, has been measured using HI 21cm data^{1,2} and HII emission line regions³ and these different measurements were found to be in close agreement⁴. In spite of considerable model degeneracies, spiral galaxies are widely believed to be dark-matter dominated in their outer parts, although strong alternative interpretations have been presented⁵. In cosmological simulations galaxies form within dark matter halos - observational tests of such results are important. Measuring the mass density profile of M31's halo is also critical to the interpretation of ongoing microlensing experiments.

Traditionally the dynamics of hot stellar components (galaxy bulges and ellipticals) have been studied using the integrated light. Due to steep radially declining surface brightness profiles, observations have been limited to the galaxy center and are impractical for study of the halo dynamics. Alternative techniques have been developed which use tracers of the halo potential

such as globular clusters and planetary nebulae (PNe) with^{6,7} and without^{8,9} assumptions about the velocity anisotropy.

An accurate measurement of the total mass of M31 has important consequences for studies of the dynamics of the Local Group. Evans & Wilkinson (2000) have recently found M31 to be *less* massive than the Milky Way in contradiction to previous studies. Their measurement is uncertain by a factor of ~ 2 , the chief source of uncertainty being the small number of available tracer velocities particularly at large radii.

We present our survey to constrain the mass distribution of the halo of M31 with PNe velocities. PNe are found to have bright [OIII] emission lines and PNe have been detected using [OIII] narrow band and continuum imaging^{10, 11, 12}. Here we present our existing PNe velocity data and imaging survey.

2 Observations, Data and Astrometry

2.1 Spectroscopic data

Multi-object spectra were obtained for 294 PNe using WYFFOS at the WHT 4.2m telescope, La Palma, Canary Islands. Astrometry was completed based on the published positions of Ciardullo et al. (1989) (C89): primary and secondary coordinate systems were defined using Digital Sky Survey^a and INT WFC archive images for both the epoch of our observations (J2000) and that of C89 (1975) - for further details see Halliday et al. (2001). Calibration exposures were obtained during each night as required.

Data reduction was completed using the **wyfred** task of the **rgo** and **wyffos** packages in IRAF^b. Typical examples of our planetary nebula (PNe) spectra are given in figure 1. PNe velocities were obtained by measuring the wavelength of both [OIII] lines where available and correcting for the heliocentric redshift for M31 and the motion of the Earth relative to the Sun during observations.

2.2 Imaging and Astrometry

[OIII] and Stromgren Y continuum images were obtained using the Wide Field Camera of the INT 2.5m telescope, La Palma for 12 WFC fields centered on the nucleus of M31. The total area covered was ~ 2.5 square degrees corresponding to an area of radius ~ 20 kpc. In the future we propose to extend the coverage of our survey to ~ 30 kpc to provide a yet stronger constraint of the halo mass.

^aThe Digitized Sky Survey was produced at the Space Telescope Science Institute under U.S. Government grant NAG W-2166.

^bImage Reduction and Analysis Facility of the National Optical Astronomy Observatories, Tucson, Arizona, U.S.A..

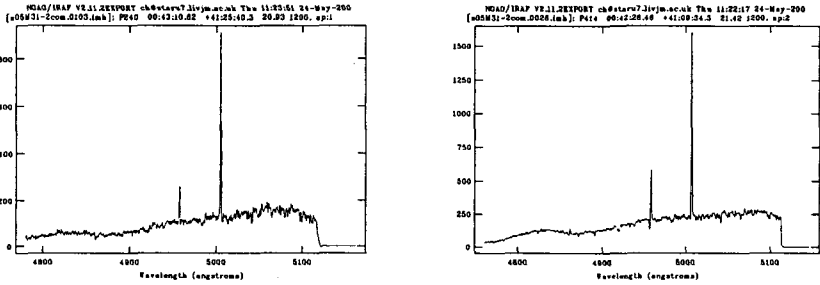


Figure 1: Examples of our WYFFOS PNe spectra. Our spectral resolution is 1\AA and our wavelength range of $\sim 350\text{\AA}$ is centered on the $[\text{OIII}]\lambda 4959\text{\AA}$ and $[\text{OIII}]\lambda 5007\text{\AA}$ emission lines.

Astrometry is being completed using ARK algorithms developed by Tim Naylor in preparation for follow-up spectroscopy to be performed in October 2001. Using positions for fiducial stars from USNO-A2 catalog¹⁴ PNe candidates are selected by comparing photometric $[\text{OIII}]$ and continuum magnitudes for detected stellar objects.

3 Preliminary results and future work

We are involved in an investigation of the M31 halo using globular cluster velocities¹⁵. In the future we plan to compare the kinematics of the PNe and GC populations and where good agreement is found the mass distribution will be constrained using both velocity samples. In figure 2 we show our velocity data together with the GC velocities of Perrett et al..

Acknowledgments

CH acknowledges support of PPARC Grant no. PPA/G/S/1998/00114 and thanks Priya Natarajan for organising such an interesting conference.

References

1. Kent, S.M., *AJ* **93**, 816 (1987).
2. Roberts, M.S., Whitehurst, R.N., *ApJ* **201**, 327 (1975).
3. Rubin, V.C., Ford, W.K., *ApJ* **159**, 379 (1970).
4. Kent, S.M., *PASP* **101**, 489 (1989).
5. Evans, N.W., in *IDM 2000: Third International Workshop on the Identification of Dark Matter*, ed. N. Spooner (World Scientific).

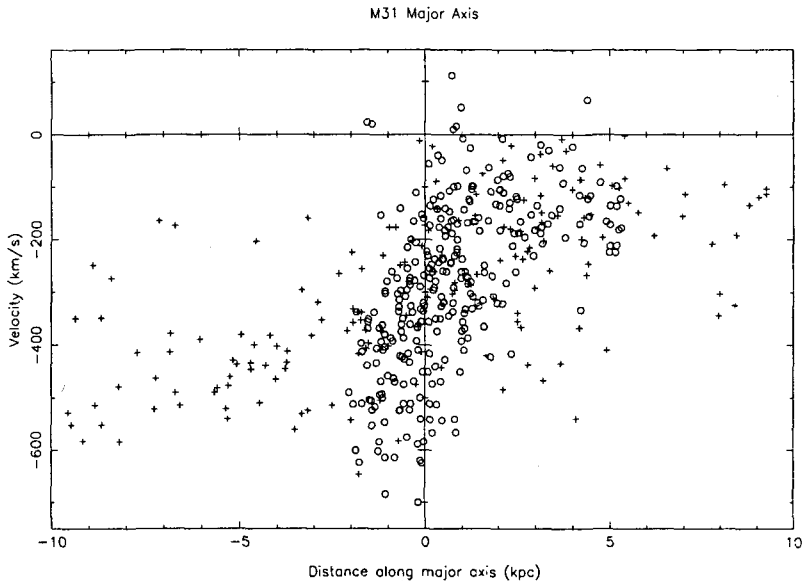


Figure 2: Velocity data for M31 for our PNE data (open circle symbols) and the GC data of Perrett et al. (crosses). Velocities were obtained by projecting the measured radial velocities along the major axis of M31 (i.e. position angle 41° taken from RC3).

6. Hui, X., Ford, H.C., Freeman, K.C., Dopita, M.A., *ApJ* **449**, 592 (1995).
7. Zepf, S.E., Beasley, M.A., Bridges, T.J., Hanes, D.A., Sharples, R.M., Ashman, K.M. and Geisler, D., *AJ* **120**, 2928 (2000).
8. Merritt, D., Saha, P. *ApJ* **409**, 75 (1993).
9. Evans, N.W., Wilkinson, M. *MNRAS* **316**, 929 (2000).
10. Arnaboldi, M., Mendez, R. H., Capaccioli, M., Ciardullo, R., Ford, H. C., Gerhard, O., Hui, X., Jacoby, G. H., Kudritzki, R. P., Quinn, P. J. *ApJ* **472**, 145 (1996).
11. Arnaboldi, M., Freeman, K.C., Gerhard, O., Matthias, M., Kudritzki, R. P., Mendez, R.H., Capaccioli, M., Ford, H. C. *ApJ* **507**, 759 (1998).
12. Ciardullo, R., Jacoby, G. H., Ford, H. C., Neill, J. D. *ApJ* **339**, 53 (1989).
13. Halliday, C., Carter, D., Jackson, Z.C., Bridges, T.J., in preparation.
14. Monet, D., Bird, A., Canzian, B., Dahn, C., Guetter, H., Harris, H., Henden, A., Levine, S., Luginbuhl, C., Monet, A. K. B., Rhodes, A., Riepe, B., Sell, S., Stone, R., Vrba, F., Walker, R. *A Catalog of Astrometric Standards*, U.S. Naval Observatory, Washington DC.
15. Perrett, K., Hanes, D., Bridges, T.J. and others, in preparation.

KECK SPECTROSCOPY OF RED GIANTS IN M31's STELLAR HALO

P. Guhathakurta

UCO/Lick Observatory, University of California, Santa Cruz, CA 95064

E-mail: raja@ucolick.org

I present results from an ongoing Keck spectroscopic survey of red giant stars in the halo of the Andromeda spiral galaxy (M31) and its dwarf spheroidal satellites. The observed shape of M31's stellar halo, roughly 2:1 in projection, is consistent with rotational flattening: its rotation speed and line-of-sight velocity dispersion are measured to be $v_{\text{rot}} \approx \sigma_v \approx 150 \text{ km s}^{-1}$. The M31 stellar halo appears to be denser and/or larger than our Galaxy's halo. Yet, the best estimate of the mass of M31's dark halo, using the most extensive set of dynamical tracers available, suggests that the galaxy is likely to be less massive than our own. A small group of metal-rich stars is seen at a common velocity indicative of substructure in M31's halo or a disk that is very extended and/or warped. The unusual properties of the M31 satellite LGS3, classified as a transition type object between dwarf spheroidals and dwarf irregulars, may be related to its being on a highly eccentric orbit around the parent galaxy. The brightest of the M31 dwarf spheroidal satellites, Cas dSph (or And VII), has an internal velocity dispersion of about 9 km s^{-1} , which is indicative of a dark matter content consistent with the extrapolation of the properties of other Local Group dwarf spheroidal satellites.

1 Overview

A spectroscopic survey of M31 with the Keck 10-meter telescope is presented in this paper.^{4, 5, 8, 9} The survey can be divided into two broad categories: (1) study of field halo red giants, and (2) study of dwarf spheroidal satellites.

To date, the field halo red giant spectroscopy part of our program has been carried out with the LRIS spectrograph working in the near infrared Ca II triplet region. Multislit observations of 35–40 red giant candidates per mask have been obtained in four fields in the M31 halo. Three of these fields are on the minor axis and one is on the major axis (Fig. 1). The current sample size is about 250 stars, of which only about half are secure members of the M31 halo. In the next few years, halo observations will be carried out more efficiently using the soon-to-be-commissioned DEIMOS spectrograph with its larger slitmask area which should enable more extended spatial coverage. Other planned improvements for future observations are better photometric pre-screening of red giant candidates through the use of the DDO51 filter and wider wavelength coverage including the Mg b region.

The dwarf satellite part of the program also relied on LRIS multislit observations in the Ca II triplet region in the initial phase; it has subsequently been

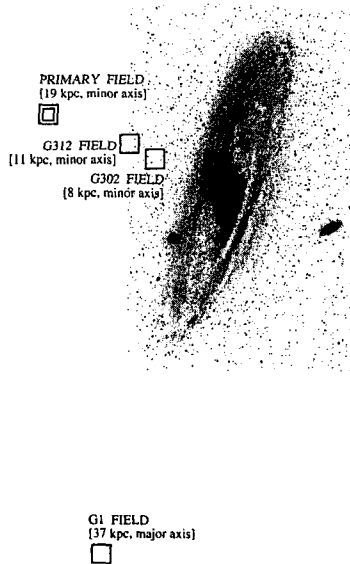


Figure 1: Grayscale image of M31, covering $\sim 2.5^\circ \times 1.5^\circ$, showing the approximate location of four fields in which Keck/LRIS spectra of field halo red giant stars have been obtained. North is left and east is down. Photometric and spectroscopic studies of the primary field are complete^{8,9} and data analysis of the other three fields is in progress.

carried out with the echelle spectrographs HIRES and ESI in order to achieve finer spectroscopic resolution and broader wavelength coverage, though at the cost of reduced multiplexing capability.

2 M31's Halo: Dynamics, Structure, and Metallicity

Our primary M31 halo field is at a projected distance of about 19 kpc on the minor axis (Fig. 1). Fig. 2 shows the distribution of radial velocities of candidate red giants in this field: the distribution is much broader than that expected for foreground Galactic dwarf stars, showing a tail towards large negative velocities. This negative velocity tail is well fit by a Gaussian centered on M31's systemic velocity of -297 km s^{-1} . The line-of-sight velocity dispersion (1σ) of M31's stellar halo is inferred to be about 150 km s^{-1} .

The other three halo fields are centered on the M31 globular clusters G1, G302, and G312 (Fig. 1). These fields were targeted for spectroscopy because they had already been imaged with the Hubble Space Telescope^{6,10} for photometric determination of the halo metallicity distribution. The photometric studies assumed a negligible degree of foreground contamination. However, our spectroscopy shows clear concentrations of stars with velocities near zero

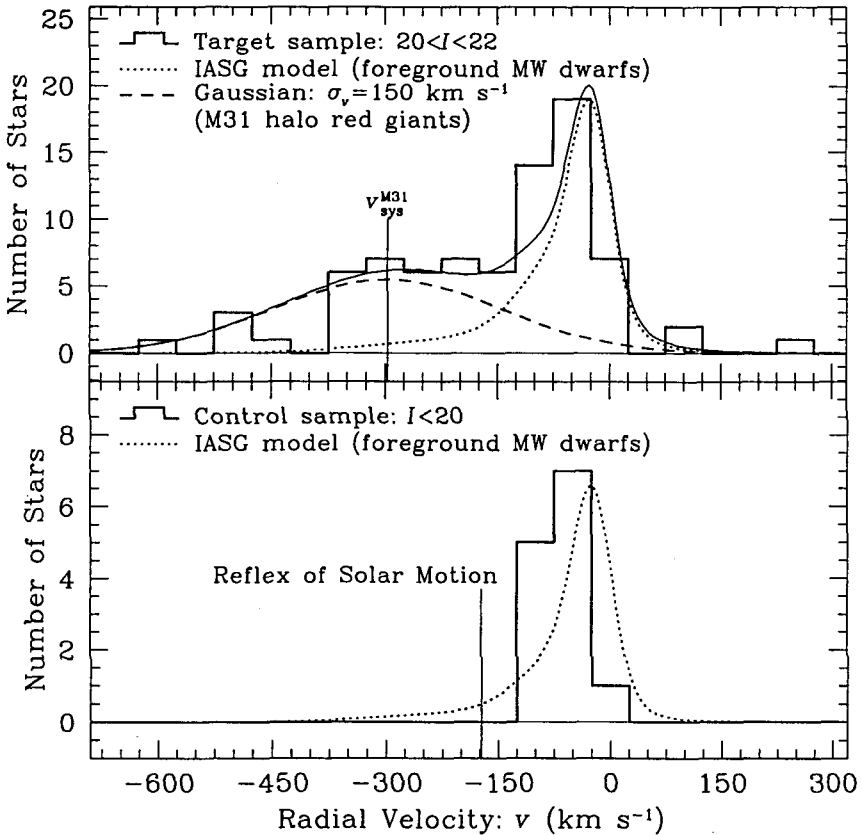


Figure 2: Distribution of heliocentric radial velocities for the primary 19 kpc minor axis field sample (upper histogram) and for a control sample (lower histogram). The velocity distribution in the primary field is well fit by the combination of a Gaussian with $\sigma = 150 \text{ km s}^{-1}$ centered on M31's systemic velocity of $v_{\text{sys}}^{\text{M31}} = -297 \text{ km s}^{-1}$ (dashed line) and the prediction of the IASG Galactic star count model (dotted line); the solid curve in the upper panel is the sum of these two components. The control sample consists of stars brighter than the tip of M31's red giant branch. These stars have radial velocities close to zero as expected; in detail, the peak of the observed distribution of foreground stars is slightly offset towards more negative values than the prediction of the IASG model (dotted line in both panels). In any event, the foreground star velocity distribution is well separated from M31's systemic velocity. The reflex (inverse) of the projection of the solar rotation velocity vector in the direction of M31 is shown in the lower panel.

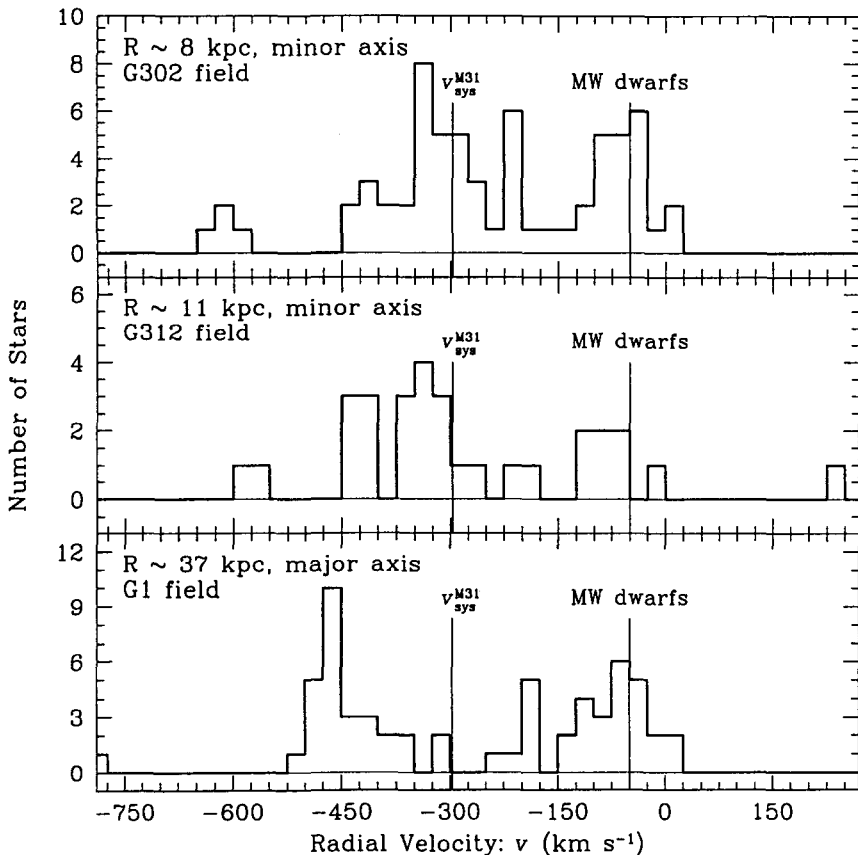


Figure 3: Distribution of radial velocities for the other three Keck/LRIS spectroscopy fields, whose spatial locations within the M31 halo are shown in Fig. 1. Though each field is centered on an M31 globular cluster, the area covered by the LRIS multislit spectroscopic mask is several times the cluster tidal radius so there should be negligible contamination from cluster red giants. There appears to be a significant number of foreground Galactic dwarf stars in the G1 and G302 fields, and possibly even in the G312 field, judging from the observed concentration at the peak position predicted by the IASG Galactic star count model. Excluding this probable foreground concentration, the *rest* of the stars are roughly centered on M31's systemic velocity in the minor axis G302 and G312 fields, but offset by about -150 km s^{-1} in the major axis G1 field, implying rotation of the stellar halo.

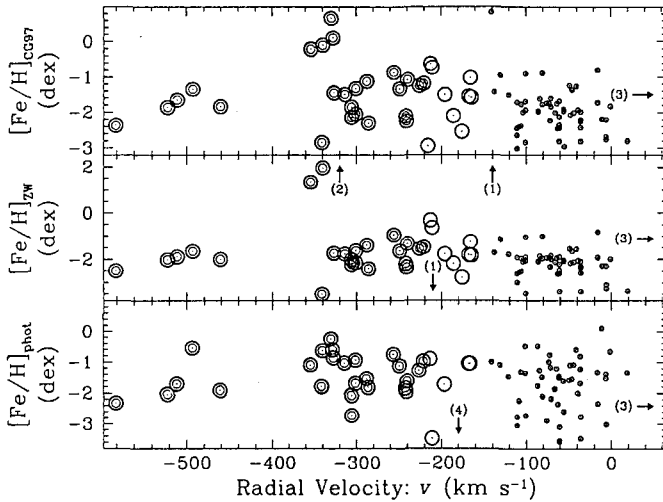


Figure 4: Metallicity of stars in the primary M31 halo field on the spectroscopic Carretta-Gratton¹ (top) and Zinn-West¹¹ (middle) scales, derived from the Ca II triplet line strength, and photometric scale (bottom) plotted versus radial velocity. Stars with large negative radial velocities are mostly red giants in M31's halo (double circles), those with velocities near zero are mostly foreground Milky Way dwarf stars (small circles), and those in the intermediate velocity range are a mix of the two (large circles). The number of objects located beyond the limits of the plot is indicated with an arrow. There are four high metallicity stars with $v \approx -340$ km/s⁻¹, close to $v_{\text{sys}}^{\text{M31}} = -297$ km/s⁻¹. Their properties are consistent with what might be expected for red giants in M31's disk, albeit a very extended/warped disk.³ Alternatively, these stars might mark a metal-rich debris trail in M31's halo.

indicating that foreground contamination can be as high as 30%–40% (Fig. 3).

The major axis G1 field shows an M31 population that is offset from the systemic velocity by about -150 km/s⁻¹ (Fig. 3). This suggests that the stellar halo of M31 has a rotation velocity of about this magnitude; its sense of rotation is the same as that of M31's disk. It should be noted though that the G1 sample may be contaminated by stars in the outer disk of M31 and this may bias the measurement of the halo rotation speed. The metallicity information that we are currently extracting for these stars may help us distinguish between M31 disk and halo red giants. Taken at face value, the rotation speed and line-of-sight velocity dispersion are comparable. This would then imply that the observed 2:1 flattening of the projected isophotes of M31's halo⁷ can be explained in terms of rotational flattening with $v_{\text{rot}}/\sigma_v \approx 1$.

Four stars stand out in the primary halo field in terms of their combination of high metallicity (near solar abundances based on Ca II line strength) and common velocity, close to the M31 systemic velocity (Fig. 4). Such properties

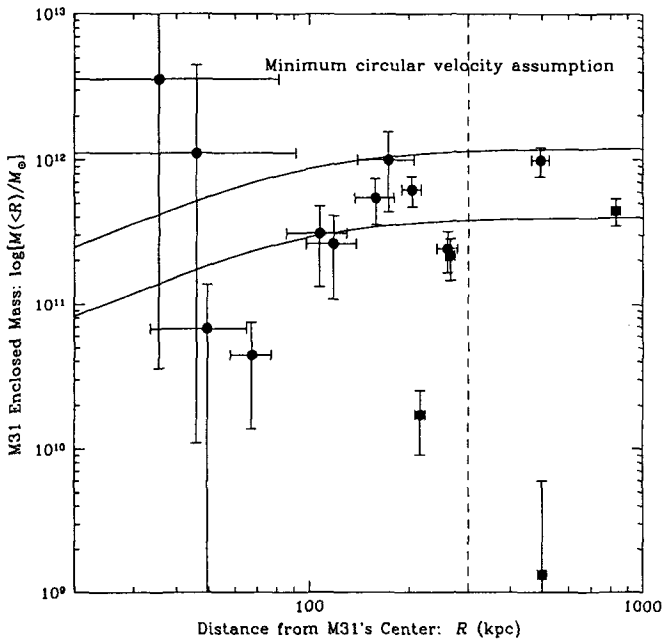


Figure 5: Enclosed mass of the M31 subgroup vs deprojected radius, derived using dwarf satellites as dynamical tracers (each shown as a data point). The mass calculation assumes that each satellite has the *minimum* circular velocity consistent with the observations: thus, the true mass of M31 is likely to be near the upper envelope of the data points. The solid lines show bounds on M31's mass from a rigorous dynamical analysis using these and other tracers of the halo.² Error bars (1σ) are based on uncertainties in the velocity and distance estimates. Satellites beyond $R = 300$ kpc (dashed line) may not be bound to the parent.

might be expected for the M31 disk if it were to be very extended (in-plane disk radius of few tens of kpc) and/or severely warped.³ Alternatively, these stars might represent a metal-rich debris trail in the halo.⁷

3 Dwarf Satellites: Intrinsic Properties and Dynamical Tracers

Dwarf satellites serve as useful tracers of the parent galaxy gravitational potential. Fig. 5 shows the enclosed mass of M31 calculated from the measured radial velocities and deprojected distances of all of its known dwarf satellites. The calculation assumes that: (1) M31's halo has a spherically-symmetric mass distribution; (2) satellites are bound and on circular orbits (may not be true for those beyond $R > 300$ kpc); and (3) our view of all satellite orbits is edge-on. This last assumption implies that the calculation will tend to underestimate

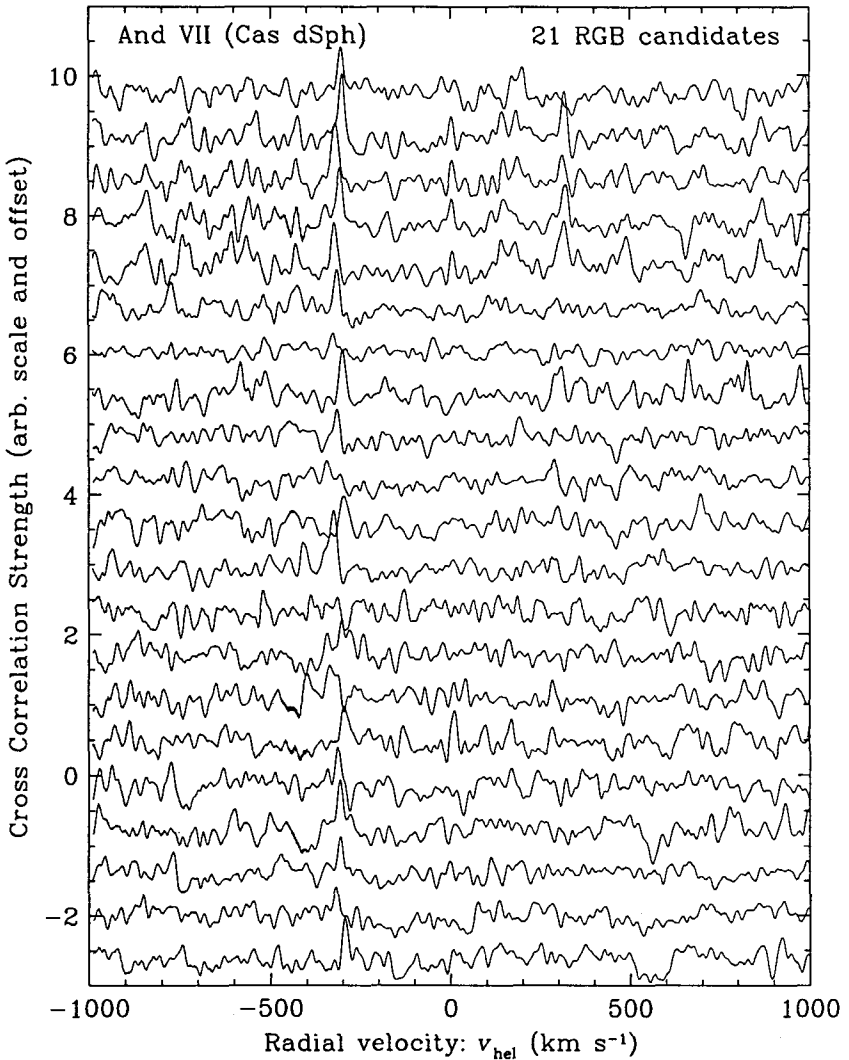


Figure 6: Cross-correlation functions (CCFs) for 21 red giant candidates in the outer M31 dSph satellite, Cas dSph (And VII) derived from Keck/HIRES multislit echelle observations. Four multislit masks, each containing 5–6 short slitlets ($1''$ – $2''$), were used. The CCF peaks are concentrated near $v \approx -300 \text{ km s}^{-1}$, marking Cas dSph's systemic velocity in its orbit around M31. Radial velocity variations from star to star are due to internal motions within the satellite; the 1σ line-of-sight velocity dispersion is $\sim 9 \text{ km s}^{-1}$.

the mass of the parent. This is consistent with a more careful mass estimation which suggests that M31 is probably less massive than the Milky Way,² even though its stellar halo is much denser and/or larger.⁹

One satellite, LGS3, yields a remarkably small enclosed mass: $\approx 10^5 M_{\odot}$ (off the bottom of the plot in Fig. 5). It is interesting to note that LGS3 has unusual stellar population characteristics and is classified as a transition type (dwarf spheroidal \rightarrow dwarf irregular). Could it be on a highly plunging orbit? If so, could ram pressure stripping by a hot gaseous halo in M31 have something to do with LGS3's atypical star-formation history?

The intrinsic properties of even the simplest dwarf satellites, the dwarf spheroidals, are surprisingly complex, and their formation and evolution remain poorly understood. We are carrying out high-resolution spectroscopy of the M31 dwarf spheroidal satellites to better constrain their dark matter content. Preliminary results on the internal velocity dispersion of Cas dSph (And VII) from HIRES multislit observations are shown in Fig. 6.

Acknowledgements

The results presented here are drawn from various projects and I am grateful to my collaborators David Reitzel, Linda Pittroff, Drew Phillips, Eva Grebel, and Steve Vogt. Many thanks to Priya Natarajan for organizing an excellent workshop and displaying infinite patience in editing these proceedings.

References

1. E. Carretta and R.G. Gratton, *A&AS* **121**, 95 (1997).
2. N.W. Evans, M.I. Wilkinson, P. Guhathakurta, E.K. Grebel and S.S. Vogt, *ApJL* **540**, L9 (2000).
3. P. Guhathakurta, P.I. Choi and D.B. Reitzel, *BAAS* **197**, #37.02 (2000).
4. P. Guhathakurta *et al.*, *AJ* in preparation (2002).
5. P. Guhathakurta, D.B. Reitzel and E.K. Grebel, in *Discoveries and Research Prospects from 8- to 10-Meter-Class Telescopes*, ed. J. Bergeron, *Proc. SPIE* **4005**, 168 (2000).
6. S. Holland, G.G. Fahlman and H.B. Richer, *AJ* **112**, 1035 (1996).
7. R. Ibata, M. Irwin, G. Lewis, A.M.N. Ferguson and N. Tanvir, *Nature* **412**, 49 (2001).
8. D.B. Reitzel and P. Guhathakurta, *AJ* submitted (2002).
9. D.B. Reitzel, P. Guhathakurta and A. Gould, *AJ* **116**, 707 (1998).
10. R.M. Rich, K.J. Mighell, W.L. Freedman and J.D. Neill, *AJ* **111**, 768 (1996).
11. R. Zinn and M.J. West, *ApJS* **55**, 45 (1984).

HALO TRACING WITH ATOMIC HYDROGEN

Micheal R. Merrifield

*School of Physics & Astronomy, University of Nottingham
Nottingham NG7 2RD*

UK

E-mail: michael.merrifield@nottingham.ac.uk

This paper reviews the constraints that can be placed on the shapes of disk galaxies' dark halos using the distribution and kinematics of atomic hydrogen. These data indicate that dark halos are close to axisymmetric, with their axes of symmetry co-aligned with their disk axes. They also appear to be oblate, with shortest-to-longest axis ratios displaying quite a broad range of values from ~ 0.2 to ~ 0.8 . These results are consistent with the predicted shapes of halos in cold dark matter scenarios, but rule out some of the more exotic dark matter candidates. However, the total number of measurements is still depressingly small, and more data are required if halo shape is to become a powerful diagnostic for theories of galaxy formation and evolution.

1 Introduction

Atomic hydrogen (HI) is ubiquitous in the Universe, and the convenient 21cm line means that its kinematics are readily determined, making it an ideal tracer for dynamical studies of the mass distributions of galaxies. The simplest application lies in determining the radial mass profiles in galaxies using their HI rotation curves – indeed, it was through such studies that the existence of dark matter in these systems was first credibly demonstrated.¹ Taking such analyses a stage further, one can start to study the shape of the mass distribution, and hence infer something about the shape of the dark halo. Clearly, this further step requires one to relax the assumption of spherical symmetry in the analysis, and such a step always complicates the analysis. Further, the hydrodynamical nature of the gas can be conveniently ignored when one treats it as a thin axisymmetric disk of material on circular orbits. If one relaxes the imposed symmetry, the orbits of the material in what may now be a triaxial potential become much more complex, making it likely that hydrodynamically-dictated collisions between different components will occur. In addition, since one is now interested in the full three-dimensional structure of the galaxy, one cannot just consider the distribution in the direction in which the gas disk is primarily centrifugally supported; the hydrodynamical processes that support the gas distribution in other directions must also be included in the analysis.

Despite these complexities, we can still obtain at least crude measures of the full three-dimensional shapes of disk galaxies' halos from HI studies. In

Section 2, we look at the constraints that such analyses place on the shapes of halos in the planes of disk galaxies, while Section 3 looks at the corresponding data perpendicular to their disk planes.

2 Halo Shapes in the Planes of Galaxies

As mentioned above, the key to studying galaxies' mass distributions is that the orbits of material are dictated by the gravitational potential. If the mass distribution is not spherically symmetric, one would expect this to show up as a corresponding absence of symmetry in the orbits. One problem in studying disk galaxies is that it is not entirely straightforward to establish their symmetry: a disk that appears elliptical may do so because it is intrinsically non-symmetric, but it could equally be an axisymmetric disk that is not viewed face on. Thus, the simplest use of HI in this context is to establish a disk's orientation, by using the fact that the width of the 21cm emission integrated from the entire galaxy depends on how close the galaxy is to face on. Fig. 1 shows a simple implementation of this approach, where I have plotted apparent optical ellipticity versus HI line width for a sample of nearby galaxies. Those galaxies with very small line widths, which must lie close to face-on, all have very low ellipticities, implying that disk galaxies are close to round in shape, and hence that the potential in the disk plane is nearly axisymmetric. Fitting this data distribution with an elliptical disk model places a constraint on the mean ellipticity in the gravitational potential of $\epsilon < 0.1$.

In fact, localized star formation, spiral arms, etc, may render a face-on globally-circular disk somewhat elliptical in appearance, so this plot can really only provide an upper limit on the true ellipticities of disks; a better analysis² using near infrared data to avoid most of this problem places an even tighter constraint on the ellipticity of the potential in the plane, yielding a value of $0.045^{+0.03}_{-0.02}$.

A related constraint can be derived by noting the tightness of the Tully-Fisher relation. Using infrared photometry, the relationship between the inclination-corrected HI line widths and absolute magnitudes of disk galaxies shows a scatter of only ~ 0.25 magnitudes.³ If disk galaxies were intrinsically elliptical, then there would be two new contributions to the scatter: first, if the apparent ellipticity were used to estimate a galaxy's inclination, then non-circular disks would lead to erroneous inclination corrections in the HI line width; and second, the non-circular motions of the HI gas would mean that the relationship between observed line width and average circular speed would vary depending on the orientation of the disk's major axis, again blurring the relation. A study of these effects⁴ placed a limit on the average ellipticity of the potential in the

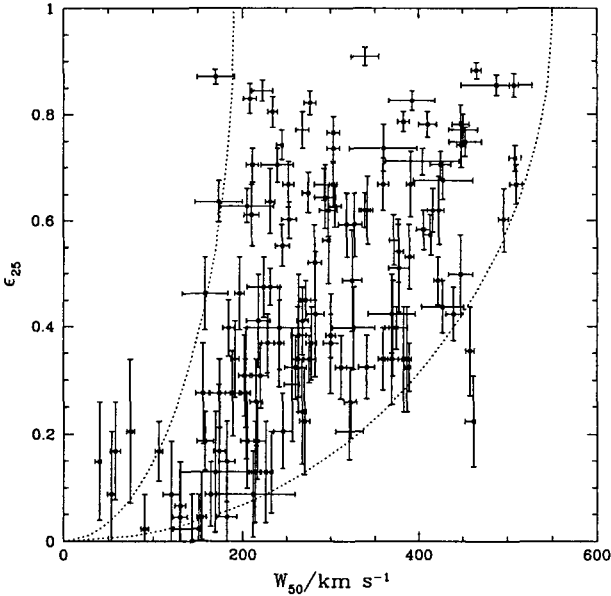


Figure 1: The ellipticities of disk galaxies as determined at the 25 mag arcsec⁻² isophote, plotted against the full width half maximum of their HI line widths. The data were drawn from the LEDA database, and consist of all galaxies of types Sa – Sc that are bright in HI ($M_{21} < 13$), and that have their axis ratios determined to better than 10%. Since ellipticity is defined to be positive, there will be a bias in this plot that increases the mean ellipticity where it is close to zero. The lines show where thin axisymmetric disks with two different rotation speeds should lie on this plot.

planes of disk galaxies of $\epsilon < 0.1$. Such an analysis complements what we learn from the optical disk shape analysis, since the HI disks generally lie at larger radii: we thus have some indication that the shape of the mass distribution does not vary significantly over a range in radii.

In addition to these global techniques for modeling the average properties of the gravitational potentials of an ensemble of galaxies, one can also study the kinematics of HI in individual galaxies in order to measure their halo shapes. In particular, the HI rings found around some galaxies make exceptional probes of these systems' shapes. For example, a study⁵ of the HI gas ring around the early-type galaxy IC 2006 showed that the line-of-sight velocity as a function of azimuth around the ring could be accurately modeled if the ring were intrinsically circular. Formally, this analysis measures the el-

lipticity of the potential at the radius of the ring as $\epsilon = 0.012 \pm 0.026$. These techniques can be extended to studies of complete disks of HI or H α emission, essentially by fitting the gas intensity and line-of-sight velocity at each point using a series of tilted rings. Such studies^{6,7} also indicate that the potential is close to axisymmetric in the disk plane of normal spiral galaxies, with typical values of $\epsilon \sim 0.05$, although there seem to be a few galaxies with ellipticities as large as $\epsilon \sim 0.2$.⁷

3 Halo Shapes Perpendicular to the Planes of Galaxies

Perpendicular to the planes of disk galaxies, constraints on the shapes of halos are rather harder to come by. One obvious approach is to look at polar ring galaxies, in which a ring of material, usually containing HI, orbits around the pole of a disk galaxy. In such a fortuitous arrangement, one can use the type of analysis described above to model the kinematics of the ring, and hence assess the shape of the potential in this direction. Although such analyses provide some of the most reliable information on the shapes of halos,⁸ there is one important caveat associated with these studies: polar ring systems are not normal galaxies. The ring probably formed in a significant merger, and it is quite likely that such a cataclysmic event will also alter the structure of the halo in the resulting composite system. It is therefore not obvious that the shapes of halos in these systems are representative of the general population.

A more generally applicable technique involves looking at the distribution of gas in a disk galaxy perpendicular to its plane.⁹ The thickness of the gas layer is dictated by the hydrostatic balance between the internal turbulent motions of the gas, and the pull of gravity towards the plane: the more mass there is close to the plane, the thinner the distribution into which the gas is gravitationally squeezed. Thus, if one uses the rotation curve to derive the radial distribution of mass, one can then determine how closely this mass is concentrated toward the galactic plane by the observed thickness of the gas layer. Since the density of the dark halo drops with radius, the force confining the gas layer decreases, and so one characteristically sees a “flaring” in the HI layer at large radii; it is exactly how the layer thickness increases with radius that provides the constraint on halo flattening.

In the mid-1990s, this technique was successfully applied to a few galaxies,^{9,10} but there were a number of initial doubts over its validity. In particular, the hydrodynamical behavior of the gas means that the physics is nowhere near as clear cut as for a pure gravitational problem: other forces such as cosmic ray and magnetic field pressures could well be significant, and it is not even obvious quite what velocity dispersion should be associated with the turbulent

motions of gas clouds in the hydrostatic equilibrium equation. These concerns were compounded when both of the initial applications (to NGC 891 and NGC 4244) implied highly flattened dark halos with shortest-to-longest ratios in the density distribution of ~ 0.3 . These results were only marginally consistent with those derived using other observational techniques (such as the study of polar ring systems), and were not at all what most theories suggested.

In order to test the validity of the method, we decided to apply it to the Milky Way's HI layer, as in our own galaxy there are other techniques that one can use to determine the halo shape. The first requirement for such an analysis is a reliable measure of the Galaxy's rotation curve. In the inner Galaxy, this is readily determined from HI data by the tangent point method, but at Galactic radii larger than the Sun's (where the crucial flaring in the gas layer occurs), this method is not available. Fortunately, an alternative technique has been developed,¹¹ which assumes only that the thickness of the Galactic gas layer does not vary with azimuth around the Galaxy, and that the material is moving around circular orbits. With these assumptions, one can solve simultaneously for both the rotation curve and the thickness of the layer as a function of radius – both the ingredients required for determining the shape of the dark halo. Applying the gas layer technique to these data resulted in a measurement of the Milky Way's halo shortest-to-longest ratio of ~ 0.7 .¹² This result showed that the gas layer flaring method does not always result in the systematically highly-flattened halos that the first two applications had, apparently by chance, returned. Further, we were able to show that the result was consistent with the constraint on halo flattening that one can derive from an analysis of stellar kinematics perpendicular to the Galactic plane in the Solar neighborhood: in that case, one uses a similar hydrostatic balance between the stellar velocity dispersion and the pull of gravity toward the plane to derive the total mass near the plane in the Solar neighborhood; after subtracting the contribution from stars and gas in this region, one obtains the amount of dark matter, and hence can derive the flattening of the halo.

Returning for a moment to the shape of the halo in the planes of disk galaxies (Section 2), it is worth noting that the technique described above for determining the Milky Way's rotation curve depends on the assumption of axisymmetry. If this assumption turns out to be invalid, one makes a different error in the derived rotation curve than one would make using more conventional standard candle methods for estimating the rotation curve. Interestingly, there is a small difference between the rotation curves derived by these two methods, which has been used¹³ to estimate that the potential in the plane of the Milky Way has an ellipticity of $\epsilon \sim 0.07$.

Further confirmation that the gas layer flaring method does not return

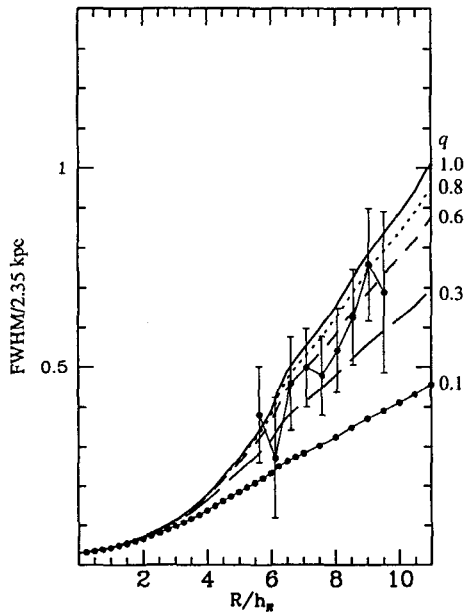


Figure 2: The thickness of the HI layer in NGC 3198. Observed values⁴ have been fitted by dark halo models with a variety of longest-to-shortest axis ratios, q .

systematically highly flattened halos has come from recent work that we have undertaken on NGC 3198. As the preliminary results presented in Fig. 2 show, the variation in the thickness of the HI layer with radius in this galaxy is not consistent with a highly flattened halo, but favors a shortest-to-longest axis ratio of ~ 0.6 .

4 Summary

Studying different aspects of the kinematics of HI gas in disk galaxies provides us with a range of tools for probing the overall distribution of mass in these systems. Since the gas extends to large radii where the mass is dominated by dark matter, these tools are well suited to studying the shapes of galaxies' dark halos. In the planes of disk galaxies, the distribution seems to be very close to axisymmetric, with some indications of an ellipticity in the potential of ~ 0.05 . Perpendicular to the plane, a broader range of flattenings is apparent: as Fig. 3 summarizes, shortest-to-longest axis ratios ranging from ~ 0.2 to

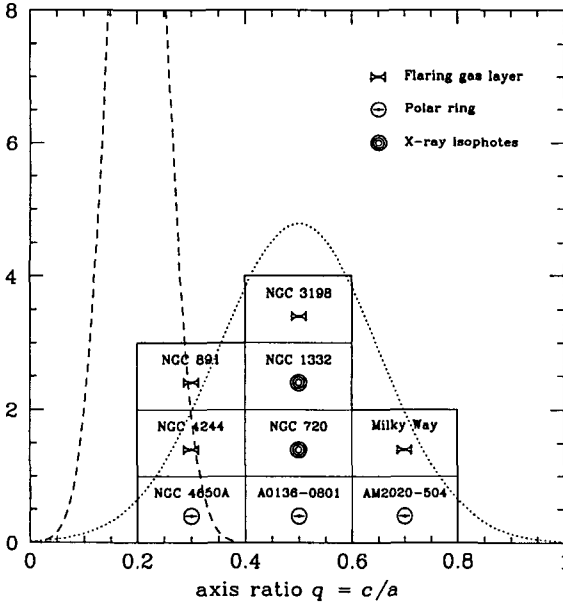


Figure 3: Distribution of measured shortest-to-longest axis ratios of galaxies' dark halos using the available credible techniques. The name and method for each galaxy is indicated. The dotted line shows the distribution predicted by cold dark matter simulations, while the dashed line shows the distribution expected if cold molecular gas were to make up the dark matter.

~ 0.6 are all found. Further, the results from HI seem to be consistent both with those obtained from studies of polar ring galaxies (so the fears expressed in Section 3 seem to be unfounded) and those derived from the X-ray isophotes of elliptical galaxies.¹⁵

Using the data in Fig. 3, one can begin to make quantitative comparisons with theory. As the figure shows, the observations are quite compatible with the predicted halo flattenings that should occur when galaxies form in standard cold dark matter cosmologies,¹⁶ but are inconsistent with the highly-flattened mass distribution that one would predict if all the dark matter were made up from cold molecular material.¹⁷ However, perhaps the most notable fact apparent from Fig. 3 is quite how few reliable measurements of halo shape have actually been made. The challenge for the next few years is to populate this histogram with sufficient new data for it to become a powerful diagnostic for testing theories of galaxy formation and evolution.

Acknowledgements

It is a pleasure to acknowledge Rob Olling's driving contribution to much of the original research described in this review.

References

1. S. Kent, *AJ* **93**, 816 (1987)
2. H.-W. Rix & D. Zaritsky, *ApJ* **447**, 82 (1995)
3. R. Giovanelli et al., *AJ* **113**, 53 (1997)
4. M. Franx & T. de Zeeuw, *ApJ* **392**, L47 (1992)
5. M. Franx, J.H. van Gorkom & P.T. de Zeeuw, *ApJ* **436**, 642 (1994)
6. R.H. Schoenmakers, M. Franx & P.T. de Zeeuw, *MNRAS* **292**, 349 (1997)
7. D.R. Andersen, et al., *ApJ* **551**, L131 (2001)
8. L. Sparke, this volume.
9. R.P. Olling, *AJ* **110**, 591 (1995)
10. R.P. Olling, *AJ* **112**, 481 (1996)
11. M.R. Merrifield, *AJ* **103**, 1552 (1992)
12. R.P. Olling & M.R. Merrifield, *MNRAS* **311**, 361 (2000)
13. K. Kuijken & S. Tremaine, *ApJ* **421**, 178 (1994)
14. F.J. Sicking, PhD Thesis, University of Groningen, 1997.
15. D. Buote, this volume.
16. J. Dubinski, *ApJ* **431**, 617 (1994)
17. D. Pfenniger, F. Combes & L. Martinet, *A&A* **285**, 79 (1994)

WHAT CAN POLAR RINGS TELL US ABOUT THE SHAPES OF DARK MATTER HALOS?

L. S. Sparke

*Department of Astronomy, University of Wisconsin-Madison
475 N. Charter Street, Madison WI 53706, USA*

A polar ring galaxy has a ring or disk of dust, gas and stars orbiting almost over the pole of a central early-type galaxy. Measuring orbital speeds in the ring and the central object thus probes two roughly perpendicular planes. This can give a sensitive indication of how flattened the galactic mass distribution, which includes the unseen halo, must be. If the dark halos of polar ring systems are typical, the dark halos of galaxies range from nearly round, to being so flat that they approach the boundary of dynamical stability.

1 Introduction

Polar ring systems are ‘multi-spin galaxies’ (Rubin 1994); they represent galaxy mergers that have not been completed, or examples of late galaxy formation through delayed infall. The outer gas-rich material appears to be a recent acquisition; it shares neither the rotation nor the symmetry axis of the inner galaxy. This is generally an S0 or an elliptical, that contains little gas, and consists largely of old stars. Whitmore *et al.* (1990; PRC) used photographic survey plates to compile a Polar Ring Catalog listing over 100 polar ring galaxies and related objects. Polar rings are not common; the PRC estimates their frequency as $\lesssim 0.5\%$ of all S0 galaxies.

Fig. 1 shows the polar ring around UGC 7576. Typically for objects in the PRC, it is seen edge-on; a polar ring is essentially an ‘upended’ low-surface-brightness disk, so face-on examples would easily be missed in surveys. The stellar ring is very flat, and extends less far in radius than the HI gas. That gas lies entirely in the polar structure, and continues beyond 10 scale lengths of the inner disk, with the rotation speed remaining almost constant. This indicates that the galaxy has an extended dark halo. This is typical of polar ring galaxies (Schweizer *et al.* 1983, van Gorkom *et al.* 1987). Since these systems include material orbiting in two very different planes, they allow us to probe the three-dimensional shape of the mass distribution.

The best information on how the dark halos of galaxies deviate from axisymmetry in the equatorial or disk plane comes from looking at orbits in that plane: see Sackett (1999), and papers here by Merrifield and van der Marel. The dynamics of polar rings are comparatively insensitive to such distortions, unless they are locked into a resonance (*e.g.* Arnaboldi & Sparke 1994). We

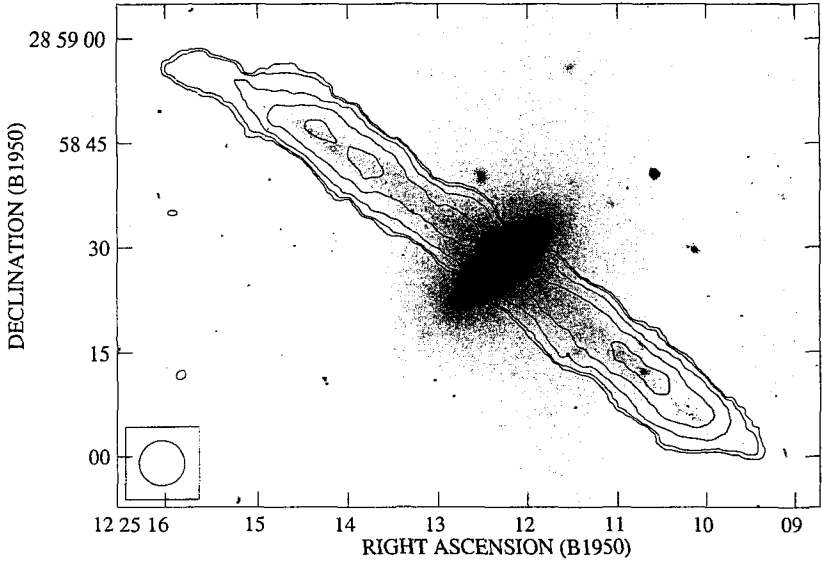


Figure 1: V-band image of UGC 7576 (PRC A-4); the inner S0 galaxy is encircled by a thin polar ring of dust, gas and stars. Contours show 21 cm emission of HI mapped at the VLA; the circle at left shows the beam (Cox 1996; Cox *et al.*, in preparation).

can more effectively use them to estimate the flattening in the perpendicular plane. If we describe the dark halo as a ‘pseudo-isothermal’ distribution of mass, flattened towards the central galaxy’s equatorial plane at $z = 0$, then

$$\rho(R, z) = \frac{\rho_0 r_H^2}{r_H^2 + R^2 + z^2 a^2 / c^2}; \quad (1)$$

the density $\rho(R, z)$ is roughly constant within the core radius r_H , while the equal-density contours are ellipsoids with axis ratio c/a . The surfaces of equal gravitational potential Φ are generally less flattened than the equidensity surfaces; the ellipticity $\epsilon_\rho \equiv 1 - c/a \approx \epsilon_\Phi/3$. The gravitational potential of the galaxy is the sum of the halo potential and that of the visible matter, in stars and gas; we can use the orbits in the polar plane to estimate how far from round the entire mass distribution could be.

2 Comparing Equatorial and Polar Rotation Curves

If the potential of a galaxy is spherical, then the orbital speed at a given radius is the same for orbits in all orientations. The equatorial rotation curve of the central body, measured using stellar absorption lines, should match that in the polar ring. But when the mass distribution is flattened towards the equator of the central stellar body, then the polar gas will follow oval orbits. When the non-axisymmetric part of the gravitational potential falls off more slowly with radius than r^{-2} , epicyclic analysis (*e.g.* eqn. 3-120 of Binney & Tremaine 1987 — thanks to Agris Kalnajs for pointing out this general condition) shows that the orbits are elongated perpendicular to the inner galaxy, and gas moves most slowly when highest above the equator. The polar rotation curve then falls below that in the disk. The first tests, by Schweizer *et al.* (1983) and Whitmore *et al.* (1987), indicated near-spherical dark halos, but with substantial uncertainty.

Sackett *et al.* (1994; S94) made a careful study of the ‘prototypical’ polar ring in NGC 4650A (PRC A-5), obtaining new absorption-line spectroscopy of the inner S0 galaxy. Correcting for asymmetric drift in the stellar disk, they derived circular speeds significantly higher than at the same galactocentric radius in the polar ring. They fitted both polar and equatorial rotation curves by a model combining a ‘maximum disk’ assumption for the visible stars of the S0 (yielding $\mathcal{M}/L_B \approx 2$), a reasonable guess at the ring mass, and a halo described by eqn. 1. This required $c/a \approx 0.3 - 0.4$; the dark halo has the flattening of an E6 or E7 galaxy, which is close to the limit of stability for a gravitating system (*e.g.* Merritt & Sellwood 1994).

However, the mass in the ring itself can change the polar rotation curve substantially. Sackett & Sparke (1990) pointed out that a model placing almost four times as much mass in the ring as in the central galaxy could fit the observed rotation; no dark halo was needed. Pfenniger *et al.* (1994) and Gerhard & Silk (1996) have suggested that the dark matter in galaxies is molecular gas, broadly following the distribution of the HI gas. Combes & Arnaboldi (1996), using the new HI maps of Arnaboldi *et al.* (1997), investigated a ‘heavy ring’ model for NGC 4650A, that had $\Sigma(\text{dark}) \propto \Sigma(\text{HI})$, together with a spherical halo of large core radius ($r_H = 8 \text{ kpc}$). This model could indeed explain the observed velocities, although they were forced to take $\mathcal{M}/L_B \sim 4$ for stars in the S0 galaxy and $\mathcal{M}/L_B \sim 5$ for the ring, which is high for such a blue and presumably fairly youthful system (Gallagher *et al.* 2001).

3 Using the two-dimensional velocity field in the ring

If the ring is far enough from edge-on, we can map the two-dimensional velocity field of gas within it. The velocity field carries far more information than the polar rotation curve alone, and can constrain the galaxy's flattening independently of the equatorial rotation curve. Just as in the disks of spiral galaxies showing an oval distortion, the velocity contours are distorted. The kinematic major axis (along which the rotation is maximal) no longer lies perpendicular to the kinematic minor axis, where the velocity is zero: see Sancisi *et al.* (1979), and Fig. 2 of Sackett (1991).

Sackett & Pogge (1995) performed such a test, using an H α velocity field for the polar ring A0136-0801, measured with a Fabry-Perot system. They showed that a wide variety of halo shapes could yield velocity fields in agreement with the observations. But simultaneously fitting the distribution of emission required the gas to follow oval orbits, corresponding to a dark halo with $c/a \approx 0.5$. Any dark matter residing in the polar ring itself would tend to make the gas orbits more circular, so this is a lower limit on the halo's flattening.

In the HI maps of NGC 5122, the zero-velocity contour is visibly skewed, suggesting a flattening $c/a \sim 0.7$ for the overall potential (Cox & Sparke 1996). Unfortunately, HI velocity fields generally have too little spatial resolution to be suitable for this analysis. Using a Fabry-Perot system to measure optical emission lines yields better resolution. However, the patchier distribution of emitting gas means that parts of the velocity field may be missing, and these data have the reputation of being fiendishly difficult to reduce.

4 Flattening inferred from precessing rings

The ring in Fig. 1 is misaligned by about 15° with the apparent minor axis of the central body. This is typical of objects in the PRC; most lie within 20° of the apparent minor axis of the central galaxy (Whitmore 1984, 1991). The inclined orbits of the ring material will tend to precess in the galaxy's gravitational field. Orbital times are longer at larger radii, so precession will be fastest at the inner edge of the ring, and a twist should develop. Hence the untwisted ring of UGC 7576 is either very young, or has been stabilized in some way. Self-gravity in the ring can counter the twisting (Sparke 1986). Sparke (1991) presents a model showing that this ring has enough mass to hold itself together if the dark halo is spherical, or nearly so. The radial distribution of polar material strongly influences its gravitational stability; unfortunately, this is difficult to measure in a near-edge-on ring. So these models provide little information on the halo flattening.

Models of twisted polar rings, where self-gravity has been insufficient

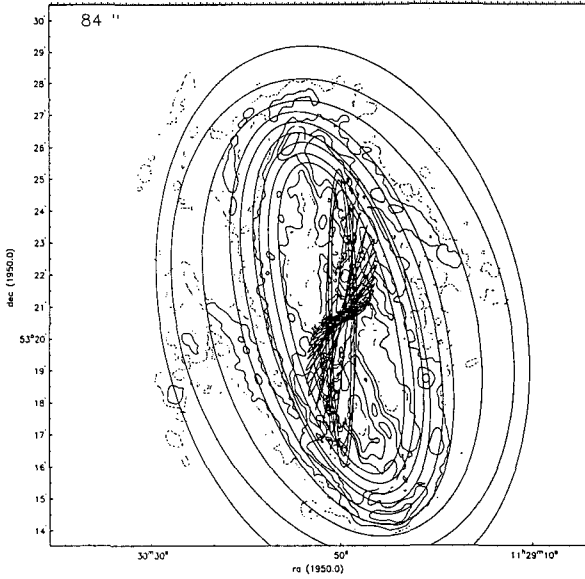


Figure 2: NGC 3718 (PRC D-18): twisted-ring fit by U.J. Schwarz to the HI velocity field, superposed on contours of total HI emission (VLA C-array; G. van Moorsel).

to prevent precession, give better constraints on the halo shape. Steiman-Cameron *et al.* (1992) showed that the complex dust lanes in the S0 galaxy NGC 4753 (PRC D-23) could be well reproduced by starting with an initially inclined, planar, disk, and allowing it to twist in a mass distribution given by eqn. 1 with $r_H \approx 0$. The timescale is set by requiring that the smoothly-distributed material at the outer edge of the disk has completed one or two orbits while the twisting took place; this implies $c/a \gtrsim 0.85$ for the galaxy as a whole. The total gravitational potential, and hence the dark halo, must be significantly rounder than the stellar distribution.

The galaxy NGC 3718, classified Sa, has a warped and twisted disk of gas and stars, highly inclined to the inner stellar body. A peculiar symmetric dust lane running across the main stellar disk indicates where the gas disk turns nearly edge-on to our line of sight; concentrations of gas, dust and stars in the ‘spiral arms’ show the pattern of twisting. The HI kinematics indicate a complex bisymmetric structure, with multiple velocity peaks where our line of sight passes more than once through the twisted disk (Schwarz 1985; van Moorsel, Schwarz & Sparke 2002, in preparation). Fig. 2 shows a tilted-ring fit to the HI data cube of van Moorsel *et al.*. The gas is assumed to follow

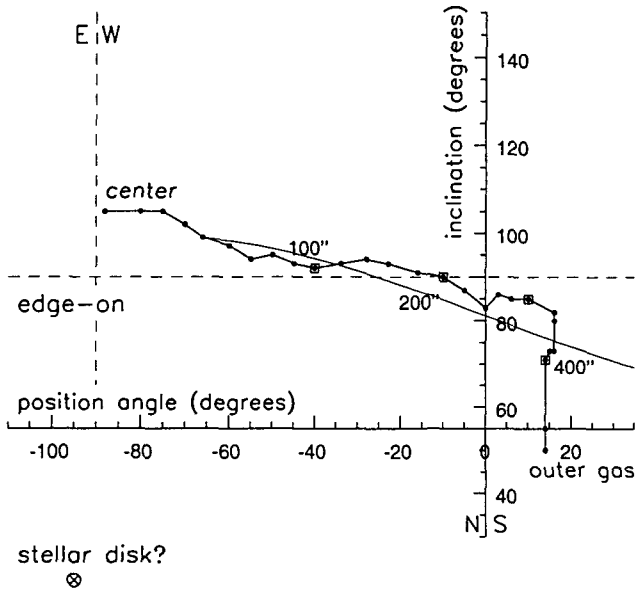


Figure 3: Position angle and inclination for the tilted rings of Fig. 2; curve shows the locus of material inclined at 80° to a disk with $i = 20^\circ$, $PA = -95^\circ$.

circular orbits, that twist roughly 120° in position angle between radii of $30''$ and $500''$, warping through edge-on to our line of sight. As in other polar rings, the gas in the twisted disk maintains roughly a constant orbital speed, about 250 km s^{-1} at all radii.

Because dust in the polar structure partially obscures it, we cannot determine the orientation of the underlying stellar disk from its isophotes. But if we assume that it is close to $i = 20^\circ$, $PA = -95^\circ$, then the orbits of Fig. 2 are inclined by $\sim 80^\circ$: see Fig. 3. The observed twisting can then be interpreted as precession in a gravitational potential flattened towards the stellar disk.

We can make a crude mass model for this galaxy by using Peletier & Willner's (1993) near-infrared photometry. In the H band, roughly 60% of the light comes from an exponential disk of scale length $h_R = 27''$; the remainder is in a central bulge. Fig. 4 shows the rotation curve used in the tilted-ring fit, compared to that for the model disk and bulge, plus a spherical halo with core $r_H = 150''$ and rotation speed $V_H = 300 \text{ km s}^{-1}$ at large radii. This model was chosen to place the maximum mass in the visible components; these have $\mathcal{M}/L_B \sim 5$. The lower panel shows how much a planar disk of gas, initially tilted 80° to the galaxy pole, would precess in the time required for one orbit

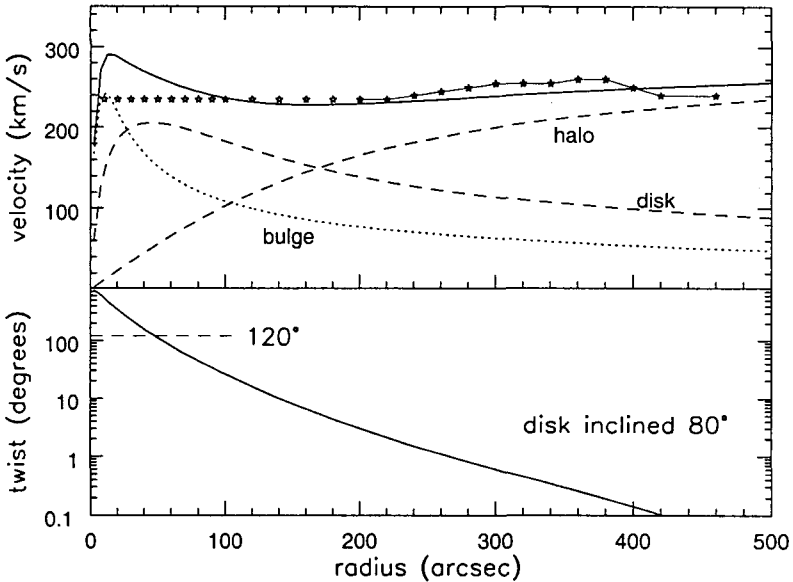


Figure 4: Top, points show rotation curve of the tilted-ring fit in Fig. 2; at $r < 200''$, this was set at 250 km s^{-1} . Model curves correspond to $\mathcal{M}_{\text{disk}} = 7 \times 10^{10} \mathcal{M}_{\odot}$, and a Plummer bulge with $a_P = 10''$ and $\mathcal{M}_{\text{bulge}} = 2 \times 10^{10} \mathcal{M}_{\odot}$. The bulge is given less than 40% of the mass, to minimize the inner peak in rotation. Below, expected precessional twisting between radius r and gas at $500''$, during one orbital period of this outermost gas.

of the gas at radius $500''$. Even with a spherical halo, the model disk reaches 120° twist at $r \approx 50''$. A substantially flattened dark halo would cause even stronger differential precession.

Thus it appears that some galaxies have strongly oblate dark halos, as in NGC 4650A and A0136-0801, while in NGC 3718 and NGC 4753, the halo is quite round. To some extent, this follows from observational selection: in a system with a flattened halo, a gas disk like those in NGC 3718 and NGC 4753 would rapidly be twisted beyond recognition. However, the dark halos of galaxies seem to be more diverse than many theorists would prefer.

References

1. Arnaboldi, M., Oosterloo, T., Combes, F., Freeman, K.C. & Koribalski, B. 1997 AJ 113, 585
2. Binney, J. & Tremaine, S. 1987 'Galactic Dynamics' (Princeton University Press)

3. Combes, F. & Arnaboldi, M. 1996 AAp 305, 763
4. Cox, A.L. & Sparke, L.S. 1996 in 'Minnesota lectures on extragalactic neutral hydrogen', *ed.* E.D. Skillman, ASP Conf. Ser. 106, 168
5. Cox, A.L. 1996 PhD thesis, University of Wisconsin-Madison, USA
6. Gallagher, J.S., Sparke, L.S., Matthews, L.D., Kinney, A.L., Frattare, L., English, J., Iodice, E. & Arnaboldi, M. 2001 ApJ, submitted
7. Gerhard, O.E. & Silk, J. 1996 ApJ 472, 34
8. van Gorkom, J.H., Schechter, P.L. & Kristian, J. 1987 ApJ 314, 457
9. Iodice, E., Arnaboldi, M., de Lucia, G., Freeman, K.C., Gallagher, J.S. & Sparke, L.S. 2001 AJ, submitted.
10. Merritt, D. & Sellwood, J.A. 1994 ApJ 425, 551
11. Peletier, R.F. & Willner, S.P. 1993 ApJ 418, 626
12. Pfenniger, D., Combes, F. & Martinet, L. 1994 AAp 285, 79
13. Rubin, V.C. 1994 AJ 108, 456
14. Sackett, P.D. & Sparke, L.S. 1990 ApJ 361, 408
15. Sackett, P.D. 1991 in 'Warped Disks and Inclined Rings Around Galaxies', *eds.* S. Casertano, P. Sackett & F. Briggs (Cambridge Univ. Press)
16. Sackett, P.D., Rix, H.-W., Jarvis, B.J. & Freeman, K.C. 1994 ApJ 436, 629
17. Sackett, P.D. & Pogge, R.W. 1995 in 'Dark Matter', AIP Conf. Ser. 36, 141
18. Sackett, P.D. 1999, in 'Galaxy Dynamics', *eds.* D.R. Merritt, M. Valluri & J.A. Sellwood, ASP Conf. Ser. 182, 393
19. Sancisi, R., Allen, R.J. & Sullivan, W.J. 1979 AAp 78, 217
20. Schwarz, U.J. 1985 AAp 142, 273
21. Schweizer, F., Whitmore, B.C. & Rubin, V.C. 1983 AJ 88, 909
22. Sparke, L.S. 1986 MNRAS 219, 657
23. Sparke, L.S. 1990 in 'Dynamics and Interactions of Galaxies', *ed.* R. Wielen (Springer: Berlin)
24. Sparke, L.S. 1991 in 'Warped Disks and Inclined Rings Around Galaxies', *eds.* S. Casertano, P. Sackett & F. Briggs (Cambridge University Press)
25. Steiman-Cameron, T.Y., Kormendy, J. & Durisen, R.H. 1992 AJ 104, 1339
26. Whitmore, B.C., McElroy, D.B. & Schweizer, F. 1987 ApJ 314, 439
27. Whitmore, B.C. 1984 AJ 89, 618
28. Whitmore, B.C. 1991 in 'Warped Disks and Inclined Rings Around Galaxies', *eds.* S. Casertano *et al.*, (Cambridge University Press)
29. Whitmore, B.C., Lucas, R.A., McElroy, D.B., Steiman-Cameron, T.Y., Sackett, P.D. & Olling, R.P. 1990 AJ 314, 439 (PRC)

CONSTRAINTS ON THE RADIAL MASS DISTRIBUTION OF DARK MATTER HALOS FROM ROTATION CURVES

Stacy S. Mcgaugh

Department of Astronomy, University of Maryland, College Park, MD

E-mail: ssm@astro.umd.edu

Rotation curves place important constraints on the radial mass distribution of dark matter halos, $\rho(r)$. At large radii, rotation curves tend to become asymptotically flat. For $\rho(r) \propto r^\alpha$, this implies $\alpha \approx -2$, which persists as far out as can be measured. At small radii, the data strongly prefer dark matter halos with constant density cores ($\alpha \approx 0$) over the cuspy halos ($\alpha \leq -1$) predicted by cosmological simulations. As better data have been obtained, this cusp-core problem has become more severe.

1 Introduction

Rotation curves played an essential role in establishing the need for dark matter halos (Rubin, Thonnard, & Ford 1978; Bosma 1978). Assuming Newtonian gravity holds, dark matter is required in all spirals to explain the asymptotically flat rotation curves observed at large radii. The need for dark matter is less obvious at small radii.

Rotation curves provide strong constraints on the radial shape of the gravitational potential of galaxies. This translates to a constraint on the distribution the various mass components, both luminous and dark. Though the constraint on the potential is strong, there can be degeneracies between the contributions of the various mass components. In particular, the mass of the stellar disk can often be traded off against the mass in dark matter, leaving considerable room for differences of opinion about disk masses and halo distributions.

This disk-halo degeneracy has plagued the field for a good while now. Consequently, there is at present a wide diversity of opinion as to how important the luminous and dark mass are at small radii. These range between two easily identifiable extremes: maximal disks and cuspy halos. In between these is a range occupied by models with stellar mass-to-light ratios which are plausible for the composite stellar populations of spiral galaxies. Which of these various options one prefers is largely a matter of how one weighs the evidence. Dynamicists find much to recommend maximal disks. Cosmologists expect cuspy dark matter halos, for which the disk mass must be minimal. Those who study stellar populations prefer intermediate disk masses.

Ideally, data should dictate some resolution to this difference of opinion. Low surface brightness (LSB) galaxies can play an important role in this. The

properties of these objects differ from those of high surface brightness (HSB) galaxies in the sense that the mass discrepancy is more pronounced at all radii. This goes a long way towards breaking the long standing disk-halo degeneracy.

2 Halo Models

The subject of this conference is halo shapes. Ideally, we would like a complete map of the dark matter distribution in galaxies, $\rho(r, \theta, \phi)$. Unlike many of the other contributions in these proceedings, the data discussed here provide little handle on the distribution in θ and ϕ . I therefore restrict my comments to the azimuthally averaged $\rho(r)$. I will focus on the limits of small and large radii, where the density distribution may be approximated as a power law: $\rho(r) \propto r^\alpha$.

There are two basic halo models which are widely considered: those with constant density cores ($\alpha \approx 0$) at small radii, and those with cusps ($\alpha \leq -1$). The pseudo-isothermal halo, with a constant density core rolling over to $\alpha = -2$ at large radii has traditionally been used in fitting rotation curves. Cuspy halos are motivated by cosmological simulations in which dark matter halos are found to take a form with a steep central cusp ($\alpha = -1$: Navarro, Frenk, & White 1997 or $\alpha = -1.5$: Moore et al. 1999), rolling over to $\alpha = -3$ at large radii. These models are different in both limits, and data can distinguish between them.

3 Large Radii

It is well established (e.g., Sofue & Rubin 2001) that at large radii, rotation curves tend to become flat. That is, $V \rightarrow \text{constant}$. This implies $\alpha \approx 2$.

This is a remarkable fact, best illustrated by some historical cases where the rotation can be traced to very large radii by 21 cm emission. For example, Fig. 1 shows the case of NGC 2403 (Begeman, Broeils, & Sanders 1991), where the rotation curve is observed to remain flat out to 10 scale lengths. By this point, the luminous mass is totally encompassed, and its contribution to the rotation has fallen far below the observations.

This basic observation remains poorly understood. While a flat rotation curve is generally presumed to be the signature of the dark matter halo, it could well be an indication of new physics (e.g., Milgrom 1983). Even setting this possibility aside, models for dark matter halos do a remarkably poor job of explaining the flatness of rotation curves which motivated them.

The trick is in understanding why rotation curves remain flat for as far as they do. The pseudo-isothermal model was designed to do this, but in practice the disk contribution in HSB galaxies is large enough that the halo contribution

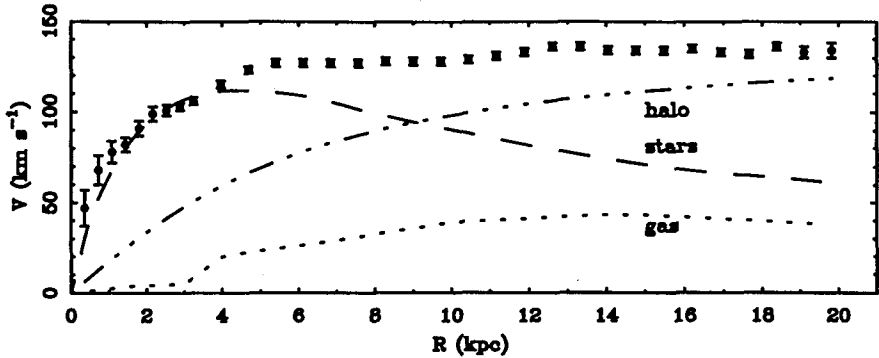


Figure 1: The rotation curve of NGC 2403 (points), measured out to ~ 10 scale lengths. The contributions of visible stars (for $\Upsilon_*^B = 1.5 M_\odot/L_\odot$) and gas are shown as dashed and dotted lines, respectively. The rotation curve becomes approximately flat at large radii, and stays that way indefinitely. Note that there is little room for dark matter at small radii, and that the halo contribution (dot-dashed line: Begeman et al. 1991) is still rising at the last measured point.

is often still rising to the last measured point (Fig. 1). The observed flatness is a fine-tuned combination of falling disk and rising halo. This is even more true for cuspy halos, which do not themselves produce flat rotation curves, as $\alpha \neq -2$.

There are enough parameters available to any halo model that it is usually possible to obtain a fit to data. However, the inverse is not true. If one tries to build *ab initio* disk+halo models, the resulting rotation curves have more curvature than do real galaxies (McGaugh & de Blok 1998). Flat rotation curves do not arise naturally.

4 Small Radii

While the strongest constraints at large radii are most commonly obtained from extended 21 cm measurements, those at small radii are provided by data of high spatial resolution. For HSB galaxies, some excellent CO data exist (Sofue & Rubin 2001), while for LSB galaxies (which are notoriously difficult to detect in CO) the best constraints are provided by $H\alpha$ data (Swaters, Madore, & Trewhella 2000; McGaugh, Rubin, & de Blok 2001; de Blok & Bosma 2002). These latter have seeing limited ($\sim 1''$) resolution, an order of magnitude improvement over early studies of these objects in HI (van der Hulst et al. 1993; de Blok, McGaugh, & van der Hulst 1996).

High resolution observations of the shapes of rotation curves are useful for mapping out the shape of the potential at small radii. There are two issues to which the initial rate of rise of the rotation curve is particularly important: maximal disks and cuspy halos. I will discuss first the issue of disk mass, then the test for halo models (core or cusp).

4.1 Disk Masses

The mass of the stars in the disk is of interest in itself, and must be constrained in order to estimate the remaining dark mass. The luminosity and distribution of the stars themselves are well observed; the parameter of merit is the stellar mass-to-light ratio Υ_* . This can vary over a wide range, from the pathological limit of zero (minimum disk) up to a maximum allowed by the data (maximum disk).

In general, maximum disk works well to explain the shape of the inner rotation curve, especially in HSB galaxies (e.g., Palunas & Williams 2000). A natural inference is that the disk does in fact dominate where its rotation curve matches the observed one well. There is considerable ancillary evidence to support the supposition that disk masses are nearly maximal for HSB galaxies (e.g., Sellwood 1998), including our own Milky Way (Gerhard 2000). Many aspects of the observed dynamics appear to require that the disk contain significant mass, a conservative lower limit being half of the total mass at two scale lengths.

Though maximum disk works well in HSB galaxies, it makes less sense in LSB galaxies. Fig. 2 illustrates several possible disk masses for the LSB galaxy F583-1, ranging from $\Upsilon_* = 0$ up to 12 in the R -band. A reasonable stellar population value of $\Upsilon_*^R = 1.5 M_\odot/L_\odot$ makes a small contribution to the total rotation everywhere. If such a stellar population model is anywhere close to the right number, as it appears it must be for consistency with the baryonic Tully-Fisher relation (McGaugh et al. 2000; Bell & de Jong 2001), then the halo dominates this galaxy down to well within 1 kpc.

Considering the dynamical evidence alone, one can certainly contemplate a much higher disk mass. The maximum disk $\Upsilon_* = 6.5$ in this case (de Blok, McGaugh, & Rubin 2001) if one does not allow the disk contribution to exceed the smooth envelope of the data. If one allows a little bit of overshoot and tries to ‘fit’ as much of the data with the disk as possible (e.g., Palunas & Williams 2000), then $\Upsilon_* \approx 12$. Maximum disk is not as well defined a concept in LSB as in HSB galaxies. The required mass-to-light ratios are unreasonably high for stellar populations: this just transfers some of the mass discrepancy from halo to disk. Even with high disk Υ_* , the halo dominates down to small radii.

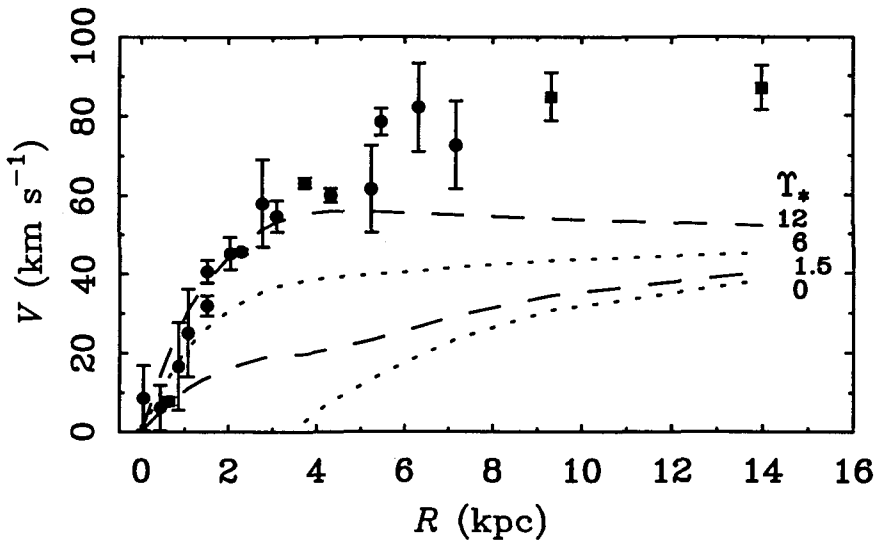


Figure 2: The rotation curve of the LSB galaxy F583-1. Circles are the H α data of McGaugh, Rubin, & de Blok (2001); squares are the HI data from de Blok, McGaugh, & van der Hulst (1996). Lines show the baryonic disk contribution for various assumed mass-to-light ratios. These range from zero (no stellar mass: the lowest line is gas only) up to $\Upsilon_*^R = 12$ (topmost line). For reasonable stellar population mass-to-light ratios ($\Upsilon_*^R \approx 1.5$), LSB galaxies are halo dominated down to small radii (< 1 kpc in this case). A substantially larger (maximal) disk mass is consistent with the data, but requires an absurdly large mass-to-light ratio. This just shifts some of the dark matter from halo to disk, and a dominant halo is still required.

4.2 Cuspy Halos

Simulations of structure formation in the CDM cosmogony (e.g., Navarro, Frenk, & White 1997; Moore et al. 1999) now resolve the structure of individual dark matter halos. Though there remains some debate over details, there does now appear to be widespread agreement that at small radii CDM halos should have a cuspy distribution ($\alpha \leq -1$). This is markedly different from the constant density cores of pseudo-isothermal halos traditionally (and successfully) used in rotation curve fits. A cusp has more dark mass at small radii, which reduces the disk mass which can be simultaneously accommodated. Cuspy halos and maximal disks are mutually incompatible.

The maximum allowance one can make for the cusp is in the limit of zero disk mass. This is obviously an unrealistic extreme: stars do have mass. So does gas, which can be significant in LSB galaxies (Fig. 2). However, allowing

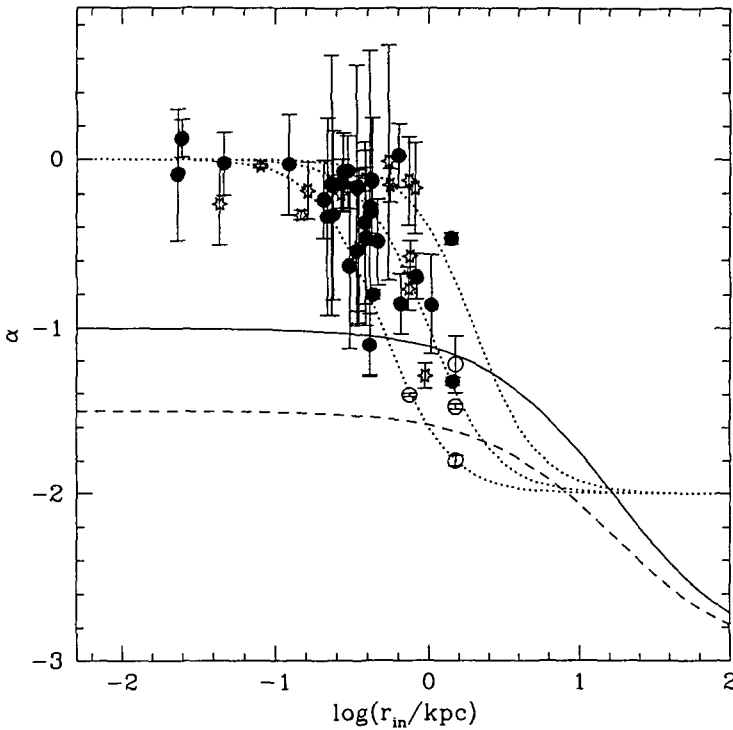


Figure 3: The cusp slope α plotted against the radius of the innermost measured point. The best resolved data strongly prefer cores (dotted lines) over cusps (solid and dashed lines).

for a reasonable amount of baryonic mass limits the room available for a cusp, so as a conservative limit let us explore the case of zero disk.

Using the most recent high resolution $H\alpha$ data, we have interrogated the rotation curves of a large sample of LSB galaxies for the cusp slope they prefer (de Blok et al. 2001). The median $\alpha = -0.2$: much closer to a constant density core than to a cusp. This is in the limit of zero disk mass. As one begins to make allowance for the stars, then the amount of rotation attributable to the dark matter is reduced, further reducing the allowed cusp slope.

There has been considerable controversy over this issue, with much discussion of how beam smearing in 21 cm data might hide a cusp (e.g., van den Bosch & Swaters 2000). The new high resolution $H\alpha$ data address this issue

directly (de Blok et al. 2001; see also Blais-Oullette et al. 2001; Salucci 2001; Borriello & Salucci 2001; Côté et al. 2000). Fig. 3 shows the cusp slopes derived from $H\alpha$ data as a function of physical resolution. Resolution has the opposite effect from what is implied by van den Bosch & Swaters (2000). It is only the data which are poorly resolved which are consistent with a cusp. Such data are also consistent with a constant density core with a modest (~ 1 kpc) core radius. On the other hand, those objects which are well resolved strongly prefer $\alpha = 0$ over $\alpha \leq -1$. *All* the data are consistent with $\alpha = 0$, while *none* of the best resolved data tolerate a significant cusp.

The inner slope α shown in Fig. 3 has been derived in the limit of zero disk mass. Once allowance is made for the stars, the situation for cusps becomes even worse. While there may be very good theoretical reasons to expect cuspy halos, there is no guarantee that reality will be cooperative. The cusp-core problem is genuine.

5 Conclusions

Rotation curves provide strong constraints on the radial potential in disk galaxies. This in turn constrains the mass and distribution of the luminous and dark components of these galaxies. Disk masses consistent with those expected for stellar populations are consistent with the dynamical data, provided halos have constant density cores rather than cusps. Cuspy halos require abnormally low stellar mass-to-light ratios, and are strongly at odds with much of the data even in the extreme limit $\Upsilon_* \rightarrow 0$.

Acknowledgments

I am most grateful to my collaborators, Vera Rubin and Erwin de Blok, for their long, concerted, and ultimately fruitful efforts. I thank Albert Bosma and Jerry Sellwood for their attempts to inject some sanity into the debate over disk masses and cuspy halos. All of us who attended this most entertaining workshop owe a great debt of gratitude to its organizers, especially Priya Natarajan. The work of SSM is supported in part by NSF grant AST9901663.

References

1. Bell, E.F., & de Jong, R.S. 2001, ApJ, 550, 212
2. Begeman, K., Broeils, A., & Sanders, R.H. 1991, MNRAS, 249, 523
3. Blais-Ouellette, S., Amram, P., & Carignan, C. 2001, AJ, 121, 1952
4. Borriello, A., & Salucci, P. 2001, MNRAS, 323, 285
5. Bosma, A. 1978, Ph.D. Thesis, University of Groningen
6. Côté, S., Carignan, C. & Freeman, K.C. 2000, AJ, 120, 3027
7. de Blok, W.J.G., & Bosma, A., 2002, A&A, submitted
8. de Blok, W.J.G., McGaugh, S.S., Bosma, A., & Rubin, V.C. 2001, ApJ, 552, L23
9. de Blok, W.J.G., McGaugh, S.S., & Rubin, V.C. 2001, AJ, in press (astro-ph/0107366)
10. de Blok, W.J.G., McGaugh, S.S., & van der Hulst 1996, MNRAS, 283, 18
11. Gerhard, O. 2000, in *Galaxy Disks and Disk Galaxies*, eds. J.G. Funes, & E.M. Corsini (astro-ph/0010539)
12. McGaugh, S.S., & de Blok, W.J.G., 1998, ApJ, 499, 41
13. McGaugh, S.S., Rubin, V.C., & de Blok, W.J.G. 2001, AJ, in press (astro-ph/0107326)
14. McGaugh, S.S., Schombert, J.M., Bothun, G.D., & de Blok, W.J.G. 2000, ApJ, 533, L99
15. Milgrom, M. 1983, ApJ, 270, 365
16. Moore, B., Quinn, T., Governato, F., Stadel, J., & Lake, G. 1999, MNRAS, 310, 1147
17. Navarro, J.F., Frenk, C.S., & White, S.D.M. 1997, ApJ, 490, 493
18. Palunas, P., & Williams, T.B. 2000, AJ, 120, 2884
19. Rubin, V.C., Thonnard, N., & Ford, W.K. 1978, ApJ, 225, L107
20. Salucci, P. 2001, MNRAS, 320, L1
21. Sellwood, J. 1999, in *Galaxy Dynamics*, eds. D. Merritt, J. Sellwood & M. Valluri (astro-ph/9903184)
22. Sofue, Y. & Rubin, V.C. 2001, ARA&A, 39, 137
23. Swaters, R.A., Madore, B.F., & Trewhella, M., 2000, ApJ, 531, L107
24. van den Bosch, F.C., & Swaters, R. 2000, preprint (astro-ph/0006048)
25. van der Hulst J.M., Skillman E.D., Smith T.R., Bothun G.D., McGaugh S.S., de Blok W.J.G., 1993, AJ, 106, 548

TELLING TAILS ABOUT THE MILKY WAY

Kathryn V. Johnston

Van Vleck Observatory, Wesleyan University, Middletown, CT 06457

email: kvj@astro.wesleyan.edu

If a satellite in orbit around the Milky Way is losing mass due to tidal forces the debris will spread in leading/trailing streamers along its orbit. These streamers are dynamically cold and (if in an orbit at sufficient distance from the Galaxy) can maintain coherence for a Hubble time. Such unique properties make them particularly sensitive probes of the mass distribution in the Milky Way. In this contribution I will briefly outline the properties of tidal debris and evidence for its existence around the Milky Way. I will then review methods for recovering the global mass distribution in the Milky Way using such stellar distributions. Finally, I will describe an approach to using tidal debris as a constraint on the degree of dark matter substructure around the Milky Way.

1 Introduction

The most compelling evidence to date for streams of debris from satellite destruction around the Milky Way comes from stars associated with the Sagittarius dwarf galaxy. The main body of this galaxy is itself highly elongated in the direction of its proper motion^{8,9}. Moreover, there have been numerous reports of over-densities in star counts^{23,20,3,21} and RR Lyrae variables^{22,1,2,10,30} that plausibly align with its orbit up to 60 degrees away from its center. More recently, an over-density has been revealed in the angular distribution of faint-high-latitude carbon stars along the Great Circle along Sgr's proper motion vector: 47 out of a sample of 100 lie within 10 degrees of this plane⁷.

All of the above observations are reminiscent of simulations of satellite destruction which show distortions of tidally stripped satellites and streams of associated debris aligned along its orbit^{14,12} — as illustrated in Fig. 1. The dynamics of the debris is simple to describe in terms of test particle orbits around the parent galaxy. The streaming is caused by the small spread in orbital properties in the debris which leads to a corresponding spread in orbital times^{29,11,5}.

Given this expectation that tidal streams consist of cold stellar phase-space distributions whose evolution is easy to understand and describe it is interesting to ask to what extent these structures can be exploited to learn something about the parent galaxy around which they orbit. This idea is analogous to using the coldness of the Galactic disk to constrain both the potential of the Galaxy (i.e. assuming the stars are all on near-circular orbits) and the presence of possible substructures within it such as $10^6 M_\odot$ black holes

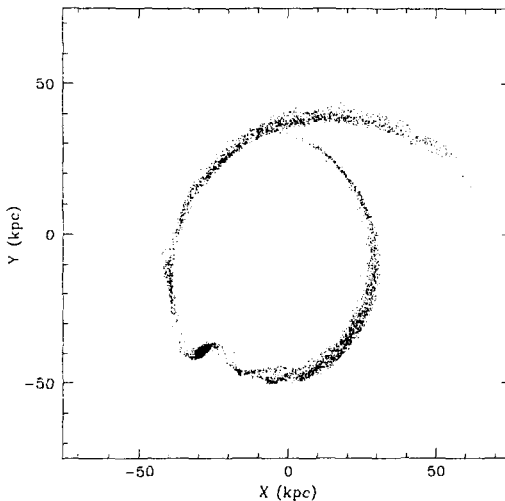


Figure 1: Final positions of particles from a simulation following 4.5 Gyrs evolution of a $10^8 M_{\odot}$ satellite in orbit, 30-55 kpc from the center of the Milky Way.

¹⁷ or dark matter satellites ⁴. We discuss the utility of tidal streams for both these purposes in the following sections.

2 Measuring the Potential of the Milky Way Using Tidal Debris

2.1 Approach 1: Exploiting the Expectation that Stellar Debris is on Nearly the same Orbit as the Satellite

One approach to measuring the potential with tidal debris is to integrate the satellite's orbit backwards and forwards and try to fit any available observations of debris stars to the orbit, with the "best" potential corresponding to the closest fit ²⁵. This algorithm can be applied with limited observations (e.g., just angular positions and line-of-sight velocities) of any accuracy. The clearest example of a practical application of this idea is the interpretation of the Carbon star stream associated with Sgr ⁷. The authors argue that the alignment of the stream with a single Great Circle suggests that the potential of the Milky Way must be close to spherical. If the potential was far from spherical the orbits of stars in the stream would precess and the stream's width would increase beyond that observed.

2.2 Approach 2: Exploiting the Expectation that Stellar Debris was Once Part of the Satellite

In reality debris in trailing/leading streamers are *not* on exactly the same orbit as their parent satellite, but rather in orbits offset in energy from the satellite’s orbit by $\sim \pm \epsilon$ where

$$\epsilon = r_{\text{tide}} \frac{\partial \Phi}{\partial r} \approx s v_{\text{circ}}^2. \quad (1)$$

Here, $r_{\text{tide}} = rs$ is the tidal radius of the satellite, $\Phi(\mathbf{r})$ is the Galactic potential, v_{circ} is the circular velocity of the Milky Way and s is the *tidal scale*

$$s = \left(\frac{m_{\text{sat}}}{M_{\text{Gal}}} \right)^{1/3}, \quad (2)$$

where m_{sat} is the satellite’s mass and M_{Gal} is the mass of the Galaxy enclosed within the satellite’s orbit. Once the observational errors are small enough to detect the offset of the particles from the satellite’s orbit Approach 1 will be biased by this systematic offset, rather than limited by the observational errors themselves. An alternative is to integrate the satellite and the debris stars backwards in time in a variety of potentials, and identify the “best” potential as the one in which most stars recombine with the satellite. This approach was first applied to find constrain the Milky Way’s potential by requiring that the Magellanic stream recombine with the Large Magellanic Cloud¹⁸ — although it is unclear whether the approach is strictly valid in this case because the neglect of possible drag terms on the gas. In the future, with the advent of upcoming astrometric satellite missions such as NASA’s Space Interferometry Mission (SIM) or ESA’s Global Astrometric Imager for Astrophysics (GAIA) that can measure proper motions with an equivalent accuracy of better than 10 km/s to distances of 100 kpc, this method should be able to recover the shape and radial profile of the Milky Way’s mass distribution to within a few percent accuracy¹⁵.

3 Constraints on Dark Matter Substructure in the Milky Way’s Halo from Tidal Debris

As cosmological N-body simulations have reached higher and higher resolutions, it has become apparent that CDM cosmologies naturally produce far more dark matter satellites around galaxies than the number actually observed around the Milky Way^{24,16}. This naturally leads to the question of what will happen to cold tidal streamers in a potential that includes many dark matter lumps on top of the global, smooth background. The expectation is that the

lumps will scatter stars in the stream and distort it. Hence, the existence of (for example) the cold stream of Carbon stars associated with Sgr might be used to constrain the degree to which the Milky Way does in fact contain dark matter satellites.

We¹³ have tackled this question using N-body simulations of the evolution of test-particle streams as they orbit in a Galactic halo containing dark matter lumps. The halo is represented by 10^7 equal mass particles, whose mutual interactions are calculated using a basis-function-expansion technique⁶. The masses of the lumps are drawn from the CDM circular-velocity distribution of dark matter satellites²⁴. Each is represented by a fixed NFW potential^{26,27} (which does not evolve during the simulation) with concentrations chosen to match the cosmology. Hence, the stream particles are scattered both by direct encounters with the lumps themselves and by the wake that they excite in the self-consistent halo (which is expected to produce an order-unity enhancement³¹) — resolving the latter effect adequately requires 10^7 particles.

Fig. 2 compares the results from the evolution of an Sgr-like stream distribution over 4 Gyrs in a perfectly smooth halo potential (top panels), with one in which 256 lumps (chosen from the top end of the dark matter satellite mass spectrum) are also orbiting (bottom panels). The left hand panels show the final positions in coordinate space and the right hand panels show the final positions in “observables” relative to the Sun where v is the (Galactic standard of rest) line-of-sight velocity, Ψ is the angle along the original orbit of the satellite and $\Delta\theta$ is the angle away from the original satellite orbit. Although there are marked differences between these two simulations it is hard to visually assess the degree of scatter in the lower panels compared with the upper. Note that although the lower plot of $\Delta\theta$ against Ψ does suggest that the plane of the orbit has precessed in the lumpy potential, this will not be generally observable as we only know the orbit of the satellite today.

To quantify the degree of scatter we defined the quantity B to be sensitive to the small-scale structure in the observables:

$$\begin{aligned}
 B_m^\Psi &= [\Sigma\Delta\theta_i \cos(m\Psi_i)]^2 + [\Sigma\Delta\theta_i \sin(m\Psi_i)]^2 \\
 B_m^v &= [\Sigma\Delta\theta_i \cos(mv_i/v_{\max})]^2 + [\Sigma\Delta\theta_i \sin(mv_i/v_{\max})]^2 \\
 B_m &= \sqrt{B_m^\Psi + B_m^v}/N \\
 B &= \sqrt{\Sigma_{m=5,10} B_m^2}
 \end{aligned} \tag{3}$$

where the sum is over all N particles in the stream and v_{\max} is the maximum line-of-sight velocity. Note that we define Ψ and $\Delta\theta$ by first finding the best-fit Great Circle to the stream stars using the method of Great Circle Cell Counts¹². Fig. 3 illustrates the results of calculating B using all 500 particles in our

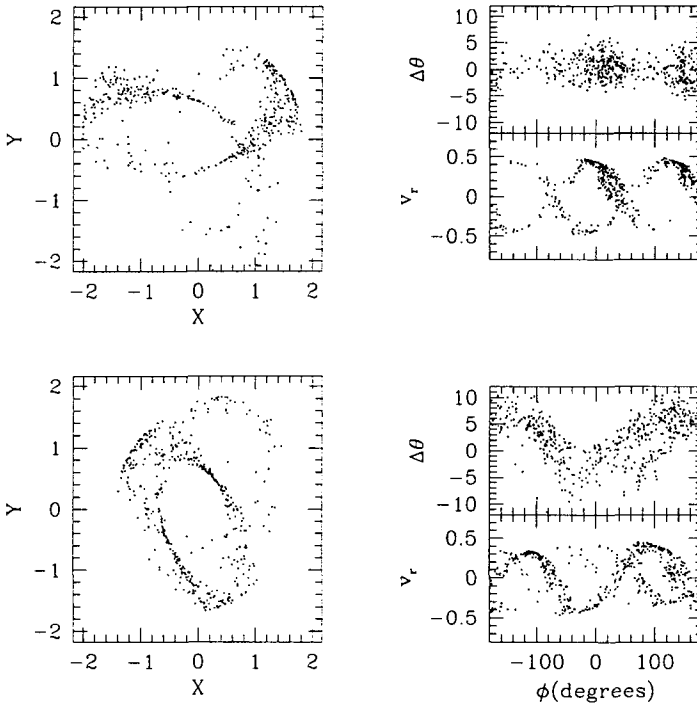


Figure 2: Final position of Sgr-like stream particles after 4 Gyrs evolution in a smooth potential (upper panels) and one containing 256 lumps (lower panels). Left hand panels are coordinate-space projections and right-hand panels are observable space projections.

stream from all 36 of our simulations — 6 sets of 6 simulations, containing the top 1,4,16,64,128 or 256 most massive lumps. The 6 simulations within each set had the same mass lumps, but different random orbits for each lump. The bold dashed line in the figure shows the results for a stream evolved in a smooth potential. The figure demonstrates that although B serves as a good general discriminant between smooth and lumpy potentials, the results are very sensitive to the exact orbits of the lumps. It also suggests that the top few most massive lumps have the most influence on the scattering.

We now apply our results to the Carbon star stream associated with Sgr. We calculate B for the 47 Carbon stars lying within 10 degrees of Sgr's orbital path. We then repeat our analysis of our simulations, this time drawing just 47

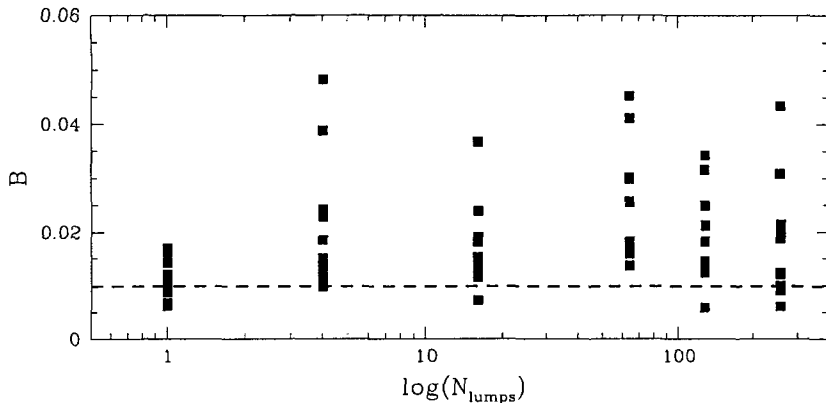


Figure 3: Scattering index, B , calculated for 500 stream particles as a function of number of lumps included in each simulation for all 36 simulations containing lumps (solid squares) and simulation in smooth potential (bold dashed line).

particles, restricted to lie at Galactic latitudes $|b| > 30$ degrees and within 10 degrees of the best-fit Great Circle to the stream. Fig. 4 compares the results of the real data (bold dotted line) with the simulations in lumpy potentials (solid squares). The results for a set of ten different samples drawn from the simulations in the smooth potential are indicated by the lower shaded region. Clearly the signal from Sgr's stream lies above that of the stream evolved in the smooth potential. Nevertheless, we are hesitant to see this as evidence that the halo is filled with dark matter lumps since we have not assessed the degree of contaminants in the Sgr data set. Moreover, we do know of one very massive, visible lump in our own halo: the Large Magellanic Cloud. The upper shaded region indicates the degree of structure induced when a simulation is performed containing an LMC-like lump in an appropriate orbit relative to our Sgr stream.

We conclude that, although the current data set for Sgr does not provide a strong constraint on the degree of dark matter substructure around the Milky Way, the future prospects are brighter. As large scale halo surveys such as the Sloan Digital Sky Survey^{10,32} and other giant-star surveys^{19,28} are completed we can hope to both refine the Sgr debris data set and find debris associated with other satellites. These streams could be used in combination to search for signatures of dark matter lumps.

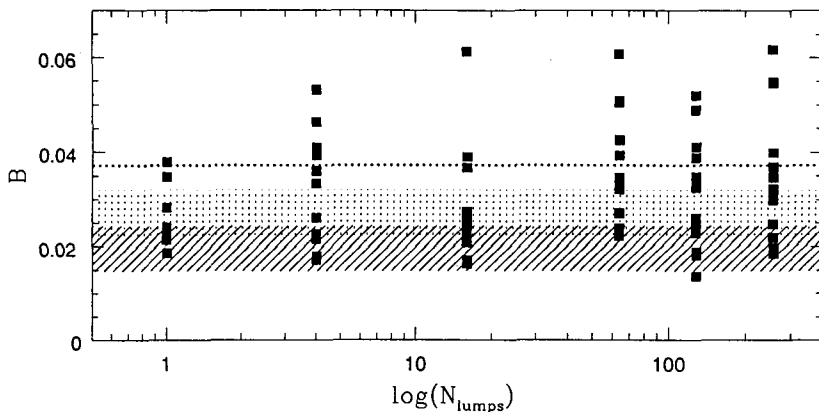


Figure 4: Scattering index for Sgr carbon star stream (bold dotted line), compared to 47 particles from simulations with lumps (squares), smooth potential simulation (lower shaded region) and simulation with LMC-like lump (upper shaded region).

Acknowledgements

This work was supported in part by NASA LTSA grant NAG5-9064.

References

1. Alard, C. 1996, *ApJ*, 458, L17
2. Alcock, C. et al. 1997, *ApJ*, 474, 217
3. Dohm-Palmer, R. C. et al. 2001, *ApJ*, 555, L37
4. Font, A. S. and Navarro, J. F., 2001, *astro-ph/0106268*
5. Helmi, A. and White, S. D. M., 1999, *MNRAS*, 307:495–517.
6. Hernquist, L. and Ostriker, J. P., 1992, *ApJ*, 386:375–397.
7. Ibata, R., Lewis, G. F., Irwin, M., Totten, E., and Quinn, T., 2001, *ApJ*, 551:294–311.
8. Ibata, R. A., Gilmore, G. & Irwin, M. J. 1994, *Nature*, 370, 194
9. Ibata, R. A., Wyse, R. F. G., Gilmore, G., Irwin, M. J. & Suntzeff, N. B. 1997, *AJ*, 113, 634
10. Ivezić et al., 2000, *AJ*, 120:963–977.
11. Johnston, K. V., 1998, *ApJ*, 495:297+.
12. Johnston, K. V., Hernquist, L., and Bolte, M., 1996, *ApJ*, 465:278+.
13. Johnston, K. V., Spergel, D. N., 2001, *in preparation*.
14. Johnston, K. V., Spergel, D. N., and Hernquist, L., 1995, *ApJ*, 451:598+.

15. Johnston, K. V., Zhao, H., Spergel, D. N., and Hernquist, L., 1999, *ApJ*, 512:L109–L112.
16. Klypin, A., Kravtsov, A. V., Valenzuela, O., and Prada, F., 1999, *ApJ*, 522:82–92.
17. Lacey, C. G. & Ostriker, J. P. 1985, *ApJ*, 299, 633
18. Lin, D. N. C., Jones, B. F. & Klemola, A. R. 1995, *ApJ*, 439, 652
19. Majewski, S. R., Ostheimer, J. C., Kunkel, W. E., and Patterson, R. J., 2000a, *AJ*, 120:2550–2568.
20. Majewski, S. R., Siegel, M. H., Kunkel, W. E., Reid, I. N., Johnston, K. V., Thompson, I. B., Landolt, A. U., and Palma, C., 1999, *AJ*, 118:1709–1718.
21. Martínez-Delgado, D., Aparicio, A., Gómez-Flechoso, M. Ángeles, & Carrera, R. 2001, *ApJ*, 549, L199
22. Mateo, M., Mirabal, N., Udalski, A., Szymanski, M., Kaluzny, J., Kubiak, M., Krzeminski, W., & Stanek, K. Z. 1996, *ApJ*, 458, L13
23. Mateo, M., Olszewski, E. W. & Morrison, H. L. 1998, *ApJ*, 508, L55
24. Moore, B., Ghigna, S., Governato, F., Lake, G., Quinn, T., Stadel, J., and Tozzi, P., 1999, *ApJ*, 524:L19–L22.
25. Murali, C. and Dubinski, J., 1999, *AJ*, 118:911–919.
26. Navarro, J. F., Frenk, C. S., and White, S. D. M., 1996, *ApJ*, 462:563+.
27. Navarro, J. F., Frenk, C. S., and White, S. D. M., 1997, *ApJ*, 490:493+.
28. Morrison, H. L., Mateo, M., Olszewski, E. W., Harding, P., Dohm-Palmer, R. C., Freeman, K. C., Norris, J. E., and Morita, M. (2000). *AJ*, 119:2254–2273.
29. Tremaine, S. (1993). In *AIP Conf. Proc. 278: Back to the Galaxy*, pages 599+.
30. Vivas, A. K. et al., 2001, *ApJ*, 554, L33
31. Weinberg, M. D., 1998, *MNRAS*, 299, 499
32. Yanny et al., 2000, *ApJ*, 540:825–841.

THE SHAPES OF GALAXIES AND THEIR HALOS AS TRACED BY STARS: The Milky Way Dark Halo and The LMC Disk

Roeland P. van der Marel

STScI, 3700 San Martin Drive, Baltimore, MD 21218, USA

Email: marel@stsci.edu

Stars and their kinematics provide one of the tools available for studies of the shapes of galaxies and their halos. In this review I focus on two specific applications: the shape of the Milky Way dark halo and the shape of the LMC disk. The former is constrained by a variety of observations, but an accurate determination of the axial ratio q_{DH} remains elusive. A very flattened Milky Way dark halo with $q_{\text{DH}} \leq 0.4$ is ruled out, and values $q_{\text{DH}} \geq 0.7$ appear most consistent with the data. Near-IR surveys have revealed that the LMC disk is not approximately circular, as long believed, but instead has an axial ratio of 0.7 in the disk plane. The elongation is perpendicular to the Magellanic Stream, indicating that it is most likely due to the tidal force of the Milky Way. Equilibrium dynamical modeling of galaxies is important for many applications. At the same time, detailed studies of tidal effects and tidal streams have the potential to improve our understanding of both the Milky Way dark halo and the structure of satellite galaxies such as the LMC.

1 Introduction

A large variety of tracers can be used to study the three-dimensional shapes of galaxies and their dark halos. Other contributions to this volume discuss the use of cold gas (e.g., HI), hot gas (X-rays), globular clusters, planetary nebulae, satellite galaxies, and gravitational lensing (both weak and strong) to study this important topic. By contrast, the present review focuses on the constraints that can be obtained from studies of stars and their kinematics. It is not possible in the context of this relatively short paper to review this topic fully for all possible classes of galaxies. So instead I focus here on two subjects for which studies of stars and their kinematics are particularly relevant: the three-dimensional shape of the Milky Way dark halo, and the intrinsic shape of the Large Magellanic Cloud.

2 The Shape of the Milky Way Dark Halo

The Milky Way consists of various separate components, including the thin disk, thick disk, central bulge, central black hole, metal-poor halo and dark halo. The general structure of the Milky Way and its various components have been reviewed by many previous authors, including, e.g., Freeman (1987), Gilmore, Wyse & Kuijken (1989), Gilmore, King & van der Kruit (1990),

Majewski (1993) and Binney & Merrifield (1998). Here I focus on the shape of the Galactic Dark Halo, a subject previously reviewed by Sackett (1998).

2.1 Constraints from Metal-Poor Halo Star Kinematics

The density distribution of the metal-poor halo has been studied using blue horizontal branch stars, RR Lyrae stars, stars counts and globular clusters. These studies have shown that the metal-poor halo is approximately a spheroidal system with an axial ratio q_{MWH} and a mass density profile that falls radially as a power-law, $\rho \propto r^{-n}$. An unweighted average of the many determinations available in the literature (as cited in, e.g., Chen et al. 2001) yields $q_{\text{MWH}} = 0.73 \pm 0.11$ and $n = 2.95 \pm 0.37$ (where the quoted errors are the RMS variations between different studies). In the solar neighborhood one can determine the three-dimensional stellar velocity ellipsoid of the metal-poor halo stars, because both line-of-sight velocities and proper motions can be measured. An unweighted average of determinations in the literature (as cited in, e.g., Martin & Morrison 1998) yields $(\sigma_R, \sigma_\phi, \sigma_z) = (155 \pm 16, 105 \pm 7, 97 \pm 7) \text{ km s}^{-1}$. One can show that these observations yield a lower limit on the axial ratio q_{DH} of the Milky Way dark halo. Hydrostatic equilibrium in an oblate collisionless system requires that there is more pressure parallel to the equatorial plane than perpendicular to it, i.e., $\mathcal{R} \equiv (\sigma_R^2 + \sigma_\phi^2) / 2\sigma_z^2 > 1$. The flatter the Milky Way dark halo, the smaller the ratio \mathcal{R} for the metal-poor halo stars must be to sustain a system of axial ratio q_{MWH} . An analysis based on the Jeans equations as in van der Marel (1991) yields the strict limit that $q_{\text{DH}} > 0.4$, with all larger values allowed (depending on the unknown details of the stellar phase-space distribution function). This rules out certain models for galactic dark halos, such as those in which all the dark matter resides in the disk (e.g., Pfenniger, Combes & Martinet 1994).

2.2 Constraints from Disk Star Kinematics

Observations of the kinematics of stars in the Milky Way disk have been used to estimate that the total surface mass density of material within 1.1 kpc from the equatorial plane is $\Sigma_{\text{tot}} = 71 \pm 6 M_\odot / \text{pc}^2$ (Kuijken & Gilmore 1991). Approximately half of this mass can be accounted for by the known luminous components of the Milky Way. From star count analyses Kuijken & Gilmore (1989) find that $\Sigma_{\text{lum}} = 35 \pm 5 M_\odot / \text{pc}^2$, while Gould, Bahcall & Flynn find $\Sigma_{\text{lum}} = 26 \pm 4 M_\odot / \text{pc}^2$. For any family of dark halo models that reproduce the Milky Way rotation curve, the amount of dark matter Σ_{dark} within 1.1 kpc from the equatorial plane increases as q_{DH} is decreased. Given that $\Sigma_{\text{tot}} = \Sigma_{\text{lum}} + \Sigma_{\text{dark}}$, this yields a constraint on q_{DH} (Olling & Merrifield 2000). However,

this constraint is not much more stringent than $q_{\text{DH}} = 0.7 \pm 0.3$, given the uncertainties in Σ_{lum} and the Galactic constants R_0 (the solar distance to the Galactic center) and V_0 (the circular velocity at the solar radius).

Other kinematical properties of disk stars provide the only useful constraints on the in-plane ellipticity $(b/a)_{\text{DH}}$ of the Milky Way dark halo. Evidence for non-circularity derives primarily from the local value of σ_ϕ/σ_R for thin disk stars, and from discrepancies between the Galactic rotation curve at $R > R_0$ when estimated using stellar and gaseous tracers respectively. Kuijken & Tremaine (1994) conclude tentatively from this evidence that the gravitational potential has an ellipticity of ~ 0.08 , with the sun positioned roughly along the minor axis. The gravitational potential of a mass distribution is always rounder than the density distribution, and the in-plane ellipticity of the dark halo density must therefore be $(b/a)_{\text{DH}} \approx 0.2$. This would be somewhat surprising, given that studies of other disk galaxies have found that their ellipticities do not typically exceed ~ 0.1 (Franx & de Zeeuw 1992; Rix & Zaritsky 1995; Schoenmakers, Franx & de Zeeuw 1997).

2.3 Constraints from Tidal Streams of Stars in the Halo

When an infalling satellite is tidally disrupted by a galaxy, the tidally stripped material will phase-mix along the satellite orbit. This gives rise to tidal streamers (Johnston, Hernquist & Bolte 1996). It has been suggested that much of the metal-poor halo was built up in this way (Searle & Zinn 1978), and evidence for this is now accumulating (Helmi et al. 1999). In a circular potential the tidal stream will move in a planar orbit, and will appear to an observer approximately as a great circle on the sky. By contrast, in an axisymmetric potential the orbit will precess, and the projected distribution on the sky will be considerably more spread out. Using a study of carbon stars, Ibata et al. (2001) recently found a stream that is associated with the Sagittarius dwarf galaxy. They argue that the stream has only a small width on the sky, and from numerical simulations it is inferred that this implies $q_{\text{DH}} > 0.7$ for the Milky Way dark halo. However, the stream has so far been delineated by only 38 carbon stars. So while this is a promising new method for studying the Milky Way dark halo shape, the resulting constraint on q_{DH} should be considered somewhat tentative at present, given the limited statistics.

2.4 Constraints from Other Tracers

Although this review focuses on stars and their kinematics, it is useful in the present context to discuss what other tracers and methods can be used to constrain the shape of the Milky Way dark halo.

[HI flaring] The thickness of the HI layer of the Milky Way increases with galactocentric distance. The exact amount of disk flaring is directly related to the axial ratio of the dark halo through the equations of vertical hydrostatic equilibrium, as modeled in detail by Olling & Merrifield (2000). Unfortunately, the results of this analysis depend sensitively on the poorly known Galactic constants R_0 and V_0 . When acceptable margins on these constants are taken into account, the observed HI flaring can be fit with models in which q_{DH} is anywhere between 0.5 and prolate values > 1 . This degeneracy can be lessened when the models are required to also fit the constraints from the stellar kinematics of the thin disk, as described in Section 2.2 (because the latter have a different functional dependence on the Galactic constants). Olling & Merrifield (2000) advocate $q_{\text{DH}} \sim 0.8$ as their best-fit value, but this is obtained for values $R_0 \approx 7.6$ kpc and $V_0 \approx 190$ km s $^{-1}$ that differ considerably from the commonly accepted values. In the absence of accurate independent determinations of R_0 and V_0 these results therefore remain tentative.

[Microlensing] In a dark halo composed of massive compact halo objects (MACHOs) the optical depth for microlensing in different directions will depend on the axial ratio q_{DH} of the dark halo. Sackett & Gould (1993) argued that the ratio of the optical depths towards the LMC and the SMC can thus be used to estimate q_{DH} . Although surveys towards the LMC and the SMC have indeed detected microlensing, the prospects for a determination of q_{DH} are not promising. The latest results from the MACHO collaboration indicate that only $\sim 20\%$ of the dark halo is composed of MACHOs (Alcock et al. 2000). Hence, microlensing can only yield constraints on q_{DH} if the MACHOs trace the rest of dark halo material, and this is unclear as long as the nature of the MACHOs remains unknown. In addition, there remains controversy concerning the contribution of LMC and SMC self-lensing to the observed optical depths (e.g., Sahu 1994; Afonso et al. 2000), which complicates any interpretation of the data.

3 The Intrinsic Shape of the LMC

The LMC is our nearest significant neighbor galaxy. While for the Milky Way the shape of the dark halo continues to be one of the outstanding questions, for the LMC it is still an important question what the shape of the stellar component itself is. This is of fundamental importance for several issues, including the study of the Milky Way dark halo through modeling of the Magellanic

Stream and the tidal disruption of the Magellanic Clouds (e.g., Moore & Davis 1994; Lin, Jones & Klemola 1995; Gardiner & Noguchi 1996) and the study of compact objects in the dark halo through microlensing studies (e.g., Sahu 1994; Alcock et al. 2000).

3.1 *The Vertical Structure of the LMC*

The LMC is believed to be approximately planar. This is supported by: (a) the small vertical scale height (< 0.5 kpc) indicated by the line-of-sight velocity dispersion of Long Period Variables (Bessell, Freeman & Wood 1986), star clusters (Freeman, Illingworth & Oemler 1983; Schommer et al. 1992), planetary nebulae (Meatheringham et al. 1988) and carbon-rich AGB stars (Alves & Nelson 2000); and (b) the relatively small scatter in the period-luminosity-color relationships for Cepheids (Caldwell & Coulson 1986) and Miras (Feast et al. 1989). There is some evidence for an increasing scale height at large radii (Alves & Nelson 2000). There is no evidence for a halo component in the LMC comparable to that of our own Galaxy (Freeman et al. 1983), although it has been a topic of debate whether the LMC contains secondary populations that do not reside in the main disk plane (e.g., Luks & Rohlfs 1992; Zaritsky & Lin 1997; Zaritsky et al. 1999; Weinberg & Nikolaev 2000; Zhao & Evans 2000).

3.2 *The Viewing Angles of the LMC Disk Plane*

It has only very recently been possible to accurately determine the viewing angles of the LMC disk plane: the inclination angle i and the line-of-nodes position angle Θ . The method relies on the fact that one side of the LMC disk plane is closer to us than the other, which causes stars on one side of the LMC to be brighter than those on the opposite side. Van der Marel & Cioni (2001) detected this effect using an analysis of spatial variations in the apparent magnitude of features in the color-magnitude diagrams extracted from the near-IR surveys DENIS (e.g., Cioni et al. 2000a) and 2MASS (e.g., Nikolaev & Weinberg 2000). Sinusoidal brightness variations with a peak-to-peak amplitude of ~ 0.25 mag were detected as function of position angle. The same variations are detected for asymptotic giant branch (AGB) stars (using the mode of their luminosity function) and for red giant branch (RGB) stars (using the tip of their luminosity function), and these variations are seen consistently in all of the near-IR DENIS and 2MASS photometric bands. The best fitting geometric model of an inclined plane yields an inclination angle $i = 34.7^\circ \pm 6.2^\circ$ and line-of-nodes position angle $\Theta = 122.5^\circ \pm 8.3^\circ$.

3.3 *The Shape of the LMC Disk*

The LMC morphology has been studied with many different tracers (reviewed by Westerland 1997), including e.g. stellar clusters, HII regions, supergiants, planetary nebulae, HI emission and non-thermal radio emission. However, near-IR surveys provide the most accurate view because of the large statistics and insensitivity to dust absorption. van der Marel (2001) used the 2MASS and DENIS data to construct a star count map of RGB and AGB stars. The resulting LMC image shows the well-known bar, but indicates that the intermediate-age/old stellar component is otherwise quite smooth (see also Nikolaev & Weinberg 2000, Cioni et al. 2000b). This contrasts with the younger populations that dominate the light in optical images. Ellipse fitting shows that the position angle and ellipticity profile have large radial variations at small radii, but converge to $PA_{\text{maj}} = 189.3^\circ \pm 1.4^\circ$ and $\epsilon = 0.199 \pm 0.008$ for $r > 5^\circ$.

Van der Marel (2001) stressed the importance of the fact that Θ differs from PA_{maj} . This indicates that the LMC disk is not circular. Deprojection of the near-IR starcount map yields an intrinsic ellipticity 0.31 in the outer parts of the LMC. This elongation had not been previously recognized, because traditionally the line of nodes position angle Θ had generally been determined under the (incorrect) assumption that the LMC is circular (as discussed and reviewed in van der Marel & Cioni 2001).

3.4 *The Tidal Effect of the Milky Way*

The elongation of the LMC is considerably larger than typical for disk galaxies (see the discussion in Section 2.2). Weinberg (2000) recently stressed the importance of the Galactic tidal field for the structure of the LMC. To lowest order one would expect the main body of the LMC to become elongated in the direction of the tidal force, i.e., towards the Galactic Center. By contrast, material that is tidally stripped will phase mix along the orbit (see Section 2.3). For an orbit that is not too far from being circular, one thus expects the elongation of the main body to be perpendicular to any tidal streams that emanate from it (a generic feature of satellite disruption that is often seen in numerical simulations and observations, e.g., Johnston 1998; Odenkirchen et al. 2001). The results of van der Marel (2001) show indeed that LMC is elongated in the general direction of the Galactic center, and is elongated perpendicular to the Magellanic Stream and the velocity vector of the LMC center of mass. This suggests that the elongation of the LMC has been induced by the tidal force of the Milky Way.

4 Conclusions

Stars and their kinematics provide an important tool for the study of the shapes of galaxies and their dark halos. The discussions in this review show that while for the nearest galaxies some important lessons have been learned, other issues continue to be poorly understood. The Milky Way dark halo cannot be very flattened, but otherwise its axial ratio is not well constrained. For the LMC we have only recently learned that its disk is quite elongated, and that the tidal effect of the Milky Way on LMC structure may be larger than previously believed. It appears that detailed studies of tidal effects and tidal streams have the potential to improve our understanding of both the Milky Way dark halo and the structure of satellite galaxies such as the LMC.

References

1. Afonso, C., et al. 2000, *ApJ*, 532, 340
2. Alcock, C., et al. 2000, *ApJ*, 542, 281
3. Alves, D. R., & Nelson, C. A. 2000, *ApJ*, 542, 789
4. Bessell, M. S., Freeman, K. C., & Wood, P. R. 1986, *ApJ*, 310, 710
5. Binney, J. J., & Merrifield, M. 1998, *Galactic Astronomy* (Princeton: Princeton University Press)
6. Caldwell, J. A. R., & Coulson, I. M. 1986, *MNRAS*, 218, 223
7. Chen, B., et al. 2001, *ApJ*, 553, 184
8. Cioni, M. R., et al. 2000a, *A&AS*, 144, 235
9. Cioni, M. R., Habing, H. J., & Israel, F. P. 2000b, *A&A*, 358, L9
10. Feast, M. W., Glass, I. S., Whitelock, P. A., & Catchpole, R. M. 1989, *MNRAS*, 241, 375
11. Franx, M., & de Zeeuw, P. T. 1992, *ApJ*, 392, L47
12. Freeman, K. C., Illingworth, G., & Oemler, A. 1983, *ApJ*, 272, 488
13. Freeman, K. C. 1987, *ARA&A*, 25, 603
14. Gardiner, L. T., & Noguchi, 1996, *MNRAS*, 278, 191
15. Gilmore, G., Wyse, R. F. G., & Kuijken, K. 1989, 27, 555
16. Gilmore, G., King, I. R., & van der Kruit, P. C. 1990, *The Milky Way as a Galaxy* (Mill Valley: University Science Books)
17. Gould A., Bahcall J. N., & Flynn C. 1997, *ApJ*, 482, 913
18. Helmi, A., White, S. D. M., de Zeeuw, P. T., & Zhao, H. 1999, *Nature*, 402, 53
19. Ibata, R., Lewis, G. F., Irwin, M., Totten, E., & Quinn, T. 2001, *ApJ*, 551, 294
20. Johnston, K. V., Hernquist, L., & Bolte, M. 1996, *ApJ*, 465, 278
21. Johnston, K. V., 1998, *ApJ*, 495, 297

22. Kuijken K., & Gilmore G. 1989, MNRAS, 239, 605
23. Kuijken K., & Gilmore G. 1991, ApJ, 367, L9
24. Kuijken K., & Tremaine, S. D. 1994, ApJ, 421, 178
25. Lin, D. C. N., Jones, B. F., & Klemola, A. R. 1995, ApJ, 439, 652
26. Luks, Th., & Rohlfs, K. 1992, A&A, 263, 41
27. Majewski, S. R. 1993, ARA&A, 31, 575
28. Martin, J. C., & Morrison, H. L. 1998, AJ, 116, 1724
29. Meatheringham, S. J., Dopita, M. A., Ford, H. C., & Webster, B. L. 1988, ApJ, 327, 651
30. Moore, B., & Davis, M. 1994, MNRAS, 270, 209
31. Nikolaev, S., & Weinberg, M. D. 2000, ApJ, 542, 804
32. Odenkirchen, M., et al. 2001, ApJ, 548, L165
33. Olling, R.P., & Merrifield, M. R. 2000, MNRAS, 311, 361
34. Pfenniger, D., Combes, F., & Martinet, L. 1994, A&A, 285, 79
35. Rix, H.-W., & Zaritsky, D. 1995, ApJ, 447, 82
36. Sackett, P. D., Gould, A. 1993, ApJ, 419, 648
37. Sackett, P. D. 1998, in *Galaxy Dynamics*, ASP Conf. Series 182, Merritt, D. R. Valluri, M., & Sellwood, J. A., eds., p. 393 (San Francisco: ASP)
38. Sahu, K. C. 1994, Nature, 370, 275
39. Schoenmakers, R. H. M., Franx, M., & de Zeeuw, P. T. 1997, MNRAS, 292, 349
40. Schommer, R. A., Suntzeff, N. B., Olszewski, E. W., & Harris, H. C. 1992, AJ, 103, 447
41. Searle, L., & Zinn, R. 1978, ApJ, 225, 357
42. van der Marel, R. P. 1991, MNRAS, 248, 515
43. van der Marel, R. P. 2001, AJ, in press [astro-ph/0105340]
44. van der Marel, R. P., & Cioni, M. R. 2001, AJ, in press [astro-ph/0105339]
45. Weinberg, M. D. 2000, ApJ, 532, 922
46. Weinberg, M. D., & Nikolaev, S. 2000, ApJ, 548, 712
47. Westerland, B. E. 1997, *The Magellanic Clouds* (Cambridge: Cambridge University Press)
48. Zaritsky, D., & Lin, D. N. C. 1997, AJ, 114, 2545
49. Zaritsky, D., Shectman, S. A., Thompson, I., Harris, J., & Lin, D. N. C. 1999, AJ, 117, 2268
50. Zhao, H. S., & Evans, N. W. 2000, ApJ, 545, L35

SEARCHING FOR STREAMS OF ANCIENT GALAXIES IN THE MILKY WAY'S HALO

A. Katherina Vivas & Robert Zinn

Yale University. Astronomy Department. PO Box 208101. New Haven, CT 06511

E-mail: vivas@astro.yale.edu; zinn@astro.yale.edu

We present results from our survey of RR Lyrae stars in the halo of the Milky Way. Since these stars are standard candles, the survey is capable of finding spatial structures in the halo, such as streams of debris left by the destruction of small satellites by the tidal forces of the Milky Way. We have found a large clump of stars at 50 kpc from the galactic center which is likely related to a tidal tail of the Sagittarius dwarf spheroidal galaxy. Several other over-densities were found in different regions. The halo of the Milky Way does not seem to have a uniform distribution of stars far from the galactic center.

1 Introduction

Although the Milky Way's halo has been studied in far greater detail than any other galaxy's, several of its properties such as its extent, shape, density profile, and most importantly, its substructure, remain poorly known, particularly in its outer regions. Traditionally, the halo has been pictured as a region of smoothly varying density contours with the density falling off as $\rho \propto r^{-n}$, where $n=3-3.5$ ¹. If, however, the halo was formed by the accretion of small satellite galaxies, as considerable observational evidence suggests², then this bland picture of the halo should be replaced by one of greater complexity arising from streams of stars that were tidally torn from now extinct satellite galaxies as they were accreted (see Johnston, this volume). A firm, theoretical prediction of the cold dark matter scenario of hierarchical galaxy formation is the existence of these streams, particularly in the outer regions of the halo (Bullock, this volume).

Because the halo is very extended and is predicted to have a low density even in the streams, their discovery has become possible only recently with the advent of large format CCD cameras that can image large regions of the sky to the requisite faint magnitudes. Several halo surveys are underway using different types of halo stars as tracers. Our own uses RR Lyrae variables, which are easily detected by their characteristic variability. While they are rarer objects than other tracers, such as red giants, they are better standard candles and are expected to provide exceptionally good three dimensional views of the streams and any other features of the halo.

We are using the QUEST camera³ mounted on the 1m Schmidt telescope

at the Llano del Hato Observatory (Venezuela) to survey for RR Lyrae stars in 700 sq. degrees of the sky to a distance of ~ 60 kpc. The QUEST camera is a mosaic of 16 chips designed to work in drift-scan mode. Thus, we observe long strips of the sky that are 2.3° wide. The very long shape of our survey has a greater chance of crossing a stream than the typical pencil beam survey. Here, we present results for an area of 200 sq. degrees which has recently been completed. We refer the reader to Vivas et al. (2001)⁴ for further details of the instrument and the observational and selection technique of the survey.

2 Results

We have repeated observations of a strip of the sky centered at declination -1° and covering from 10 to 16 hours in right ascension (200 sq. degrees)^a. We were able to find 302 RR Lyrae stars to a magnitude of $V = 19.7$. This sample of stars is much more complete than the search done by Ivezić et al. (2000)⁵ using data from the Sloan Digital Sky Survey in a region which partially overlaps with ours. Our greater completeness ($\sim 78 - 100\%$ vs 42% of Sloan) is due to our large number of epochs (20-30) compared with only 2 epochs in the survey by Ivezić et al. Our light curves provide identification of true RR Lyrae stars with virtually no contamination from other kinds of variables. The mean magnitudes (hence the distances) are well determined from the light curves.

As shown in Vivas et al (2001)⁴ there is a large concentration of stars with magnitudes between $V=18.5-19.5$ and extending as much as ~ 82 sq. degrees on the sky, from $\alpha= 13$ to 15.5 hours. This clump consists of 84 stars located at a mean distance of 50 kpc (using $M_V(RR) = +0.55$ and the extinction corrections of Schlegel et al. (1998)⁶). It has minimum dimensions in α and δ of 30 and 3 kpc respectively. The depth along the line of sight is very small, only 5 kpc. The location and size of this feature is consistent with it being a stream of tidal debris from the Sagittarius dwarf spheroidal galaxy^{7,8,9}.

In order to quantify if a clump like this one is indeed a special feature of the halo we divided our region in 16 equal zones in right ascension and calculated the number density profile in each one, as a function of galactocentric distance. The results can be seen in Figure 1. In all panels, the number density of RR Lyrae stars tends to decrease with distance with a slope close to -3 . However, there are clear deviations from these lines. In particular, there are big over-densities after ~ 35 kpc in the 7 panels that go from $\alpha = 13$ h to 15.6h. This is the feature related with the Sagittarius stream. In some places there is as much as 10 times the expected density for a “normal” halo.

^aResults for half of this region (from 13 to 16 hours) are discussed in Vivas et al. (2001).

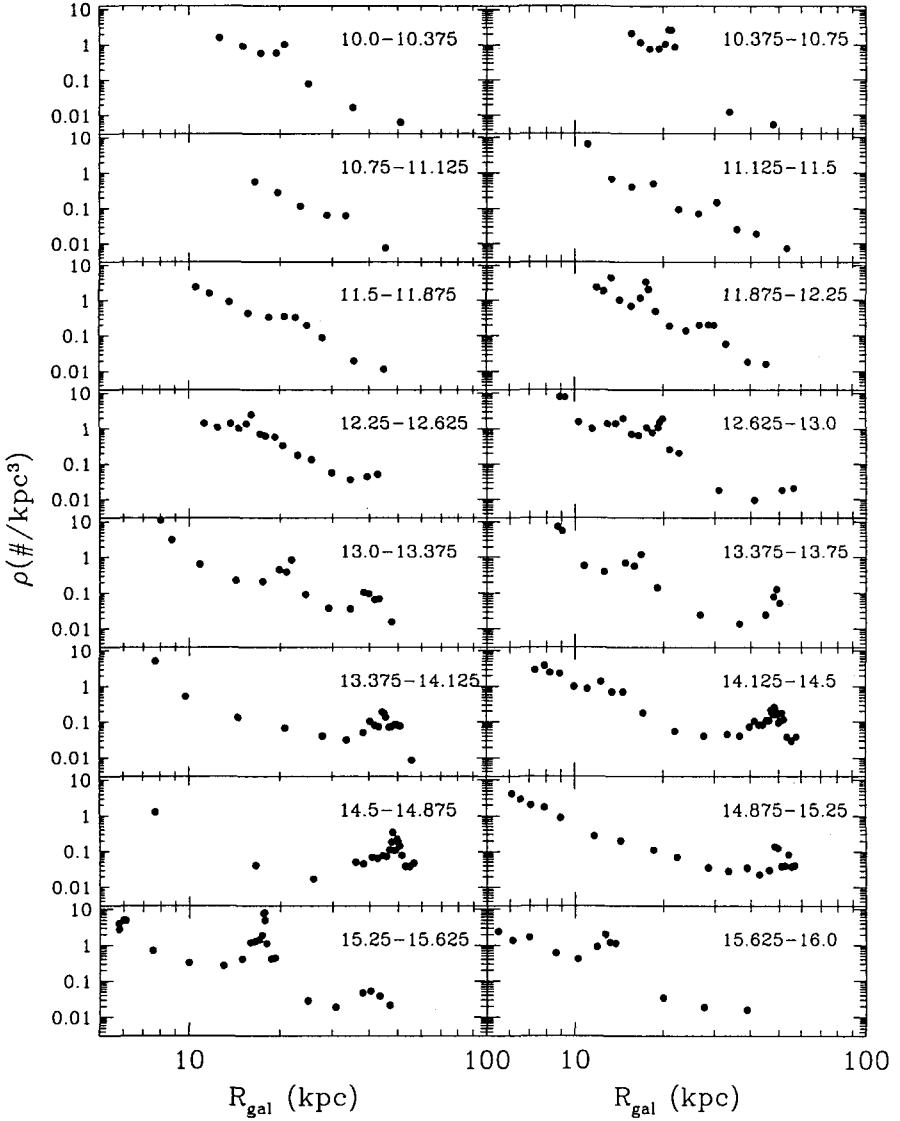


Figure 1: Number of the RR Lyrae stars per unit volume as a function of galactocentric distance. Each panel corresponds to a different range in right ascension (indicated in the upper right corners).

Not as obvious, but equally interesting, is the fact that we find several over-densities over the entire region, though none of them is as big as the clump associated with Sgr. The over-density at $\alpha \sim 15.4h$ and 17 kpc from the galactic center is likely related to the globular cluster Pal 5; this cluster seems to be under the process of disruption¹⁰ and the stars we detected here could be its tidal debris. The rest of the “mini-clumps” have no obvious association with any known structure. All of them are located between 15 and 25 kpc from the galactic center and contain just a few stars. Spectroscopic observations are underway to confirm that the members of each group are really physically associated.

3 Discussion

Our survey has shown that the outer halo of the Milky Way does not have a smooth distribution of stars far from the galactic center. At least one of the structures that we find is related with an accretion event, Sagittarius. It still remains unknown if there are other streams of tidal debris from destroyed satellites, besides Sagittarius, in the halo. We have found several smaller groups of stars in the sky but it is necessary to study their velocity and metallicity distribution before interpreting such groups as true remains of ancient galaxies or just disrupted star clusters.

We would like to give special thanks to all members of the QUEST collaboration for their enormous contributions to this work. This research was partially supported by the National Science Foundation under grant AST 00-98428. The Llano del Hato Observatory is operated by CIDA for the Consejo Nacional de Investigaciones Científicas and the Ministerio de Ciencia y Tecnología (Venezuela).

References

1. C. Wetterer & J. McGraw, *AJ* **112**, 1046 (1996).
2. J. Bland-Hawthorn & K. Freeman, *Science* **287**, 79 (2000).
3. J. Snyder, *Proc. SPIE* **3355**, 635 (1998).
4. A. K. Vivas *et al.*, *ApJL* **554**, L33 (2001).
5. Z. Ivezić *et al.*, *AJ* **120**, 963 (2000).
6. D. Schelegel, D. Finkbeiner & M. Davis, *ApJ* **500**, 525 (1998).
7. R. Ibata, M. Irwin, G. Lewis & A. Stolte, *ApJL* **547**, L133 (2001).
8. A. Helmi & S. White, *MNRAS* **323**, 529 (2001).
9. D. Martinez-Delgado *et al.*, *ApJL* **549**, L199 (2001).
10. M. Odenkinchen *et al.*, *ApJL* **548**, L165 (2001).

THE EXTENDED SHAPES OF GALACTIC SATELLITES

S. R. Majewski, A. D. Forestell, J. C. Ostheimer, C. Palma, M. H. Siegel, S. Sohn,
K. B. Westfall, R. J. Patterson, P. M. Frinchaboy, R. Link

Dept. of Astronomy, University of Virginia

P.O. Box 3818, Charlottesville, VA 22903-0818, USA

E-mail: srm4n,adf2e,jco9w,cp4v,mhs4p,ssf5b,kbw7d,ricky,pmf8b,rl8z@virginia.edu

W. E. Kunkel

Las Campanas Observatory, Carnegie Observatories

Casilla 601, La Serena, Chile

E-mail: kunkel@jeito.lco.cl

K. V. Johnston

Wesleyan University, Department of Astronomy

Middletown, CT 06459-0123, USA

E-mail: kvj@urania.astro.wesleyan.edu

We are exploring the extended stellar distributions of Galactic satellite galaxies and globular clusters. For seven objects studied thus far, the observed profile departs from a King function at large r , revealing a “break population” of stars. In our sample, the relative density of the “break” correlates to the inferred M/L of these objects. We discuss opposing hypotheses for this trend: (1) Higher M/L objects harbor more extended dark matter halos that support secondary, bound, stellar “halos”. (2) The extended populations around dwarf spheroidals (and some clusters) consist of unbound, extratidal debris from their parent objects, which are undergoing various degrees of tidal disruption. In this scenario, higher M/L ratios reflect higher degrees of virial *non*-equilibrium in the parent objects, thus invalidating a precept underlying the use of core radial velocities to obtain masses.

1 Introduction

One of the more remarkable aspects of galactic dark matter (DM) is that the smallest galactic systems, the dwarf spheroidal galaxies (dSph), appear to have the largest mass-to-light ratios (M/L) – approaching 100 in some Milky Way dSphs. Even among the dSph galaxies it appears that intrinsic brightness is anticorrelated with M/L , which has prompted the suggestion that all dSph galaxies have about the same mass, they just vary in luminosity²⁷. Globular clusters, the next smallest stellar systems, seem not to have DM. It has long been recognized² that a primary difference between dSphs and globular clusters lies in the concentrations of their radial profiles. Thus, it is reasonable to consider the *structure* of a stellar system somehow to be connected to the inferred M/L 's, although what the causal relationship may be is unclear: Could

the typical, fluffy profile of dSphs be a response to large DM contents, perhaps in the form of extended cold DM halos? Or do more extended *stellar* systems somehow produce *the appearance* of large M/L 's, even if artificially?

Deep HST imaging to derive the luminosity function of the Ursa Minor dSph has shown⁶ no difference with the luminosity function of the globular cluster M92 down to $0.45 M_{\odot}$, which establishes that the apparent *stellar* M/L is the same for both low and high M/L systems. Thus, it is not surprising that many attempts to eradicate the “high M/L problem” have focused on potential problems with the methodology for dynamically inferring masses. Despite general differences in concentrations, and even shapes, between most globular clusters and dSphs, it is still commonplace to adopt King’s^{16,38} dynamical formalism derived for globular clusters to describe dSph galaxies. The assumptions implicit in this methodology are that the stellar system has an isotropic velocity distribution and a well-defined, flat core in its light profile (i.e., that King profiles fit the light), that M/L is independent of radius, and that the system is in virial equilibrium. Concerns have been raised not only regarding the applicability of each of these assumptions to dSph systems, but also to whether the dynamics of dSphs are simply more complex than accounted for by King’s model. For example, several groups have studied the possibility that the central velocity dispersions, $\sigma_{v,c}$, are inflated due to superposed orbital motions from binary stars, but each concludes that binaries alone cannot account for the large inferred M/L 's^{1,10,33}. Improperly assuming velocity isotropy can also alter inferred M/L 's, although apparently by only factors of two or three, not by factors of 10^{2-3} needed to “solve” the dSph M/L “problem”^{38,28}.

Perhaps the most controversial assumption has been that of virial equilibrium. Hodge & Michie¹¹ long ago proposed that Galactic tides may act to inflate $\sigma_{v,c}$. Later analyses³⁷ found that perhaps some, but not all high M/L measures for dSphs can be accounted for by tides, and that, rather than inflating $\sigma_{v,c}$, tides should produce ordered, shearing-like motions¹⁰. Kuhn & Miller²⁰ suggested the possibility that incited resonances between internal stellar orbits and the bulk Galactic orbit of a stellar system could also inflate $\sigma_{v,c}$, but Sellwood & Pryor⁴⁰ counter that such oscillatory motions are not excited by motion in a logarithmic potential. The discovery of potential “extra-tidal” stars around some dSphs^{42,39,8} raises the specter that tidal disruption processes, long expected to be acting on some globular clusters, also affect the supposedly DM-dominated dSphs. Prodigious disruption, of course, would be inconsistent with an assumption of equilibrium. The Sagittarius (Sgr) galaxy provides an obvious demonstration that Galactic dwarf satellites can face substantial tidal disruption, and its derived¹² M/L , in the range of 20–100, might be considered a convenient illustration of potential problems with dynamical

masses. However, Sgr may be a red herring in the dSph DM argument because its *present* morphology is atypical of Galactic satellites, and it is not obvious that the Sgr progenitor *would have been* similar to “normal” dSphs (though it is likely that Sgr merely represents an extremely disturbed form of dSph). On the other hand, studies of the light profiles of “normal” dSphs also reveal signs of possible tidal effects in the form of radial profile “breaks”^{5,14,22}, which are predicted as a manifestation of stripped stars in models of the tidal disruption of dSph galaxies in a Galactic potential¹⁵

The existence of these profile breaks puts interesting twists on the DM debate. If the break populations are truly unbound, the degree of dynamical equilibrium in dSphs is questionable. Note that Piatek & Pryor³⁷ show that one pericentric passage of a satellite is insufficient to perturb a satellite enough to raise the derived M/L . Nor does the presence of unbound stars inflate the measured σ_v of their parent systems³². However, Kroupa¹⁹ has commented that earlier disruption models utilized N-body codes too small to follow the evolution of a satellite to complete dissolution, and that larger N-body simulations of *large* satellites show that late stages of disruption can produce tidal debris that in places may converge into 1% stable remnants that resemble dSphs, but which contain no DM¹⁷. Such a scenario echos an earlier suggestion²¹ that “large M/L dSphs” are simply coherent, unbound groups of stars on similar orbits, the remnants of tidal disruption. The notion of dSphs and some globular clusters being remnant nuggets floating in, and *as*, the debris of the disruption of larger progenitors was first postulated by Kunkel²³ and Lynden-Bell²⁴ and more recent analyses discuss the possibility of at least some “dynamical families” of daughter objects in the outer Galactic halo³⁵. But while Mayer et al.²⁹ confirm that inflated M/L *can* occur along preferred lines of sight to a disrupting system, apparently this might only account for a small number of the dSphs currently inferred to have high M/L .

However, if the break populations are *bound*, it suggests, in the least, that the structure of dSphs is more complicated than that of typical globular clusters. One prosaic explanation for the existence of bound break populations might be that they are a cloud of still bound retrograde rotating stars, the product of the dynamical imbalance in normal evaporative processes to preferentially strip prograde orbiting stars¹³; such a model should lend itself to an easily recognizable observable kinematical signature at the tidal radius, r_t . Alternatively, the break populations may represent an extended, secondary “halo” component, still embedded in deep dSph DM halos. According to Burkert³, dSphs need these large DM halos, since the cut-off radii of King profile fits to dSph are *too small* to be the true r_t if the inferred M/L are correct.

Searching for and following these break populations to extremely large radii

is therefore critical, in order to (1) check on their ubiquity, particularly among the large M/L systems, (2) look for correlations in the properties of these break populations as a function of the characteristics of the core of the system, and (3) see if the break populations organize themselves, eventually, into the expected tidal streamers. The existence of tidal tails and their association to the break populations is a key discriminant to the various high M/L models discussed, since “even modest amounts of dark matter will be very effective at containing visible stars and halting production of tidal tails”³⁰. We have set out to explore the extended profiles of Galactic satellites (dSphs and clusters), with these, and a number of other, rationale in mind.

2 Extended Profiles of Galactic Satellites

Our survey strategy is intended to go beyond merely obtaining a more accurate rendering of the light profiles of satellites: We aim to identify stars widely separated and dispersed from the cores of their parent systems, and from which we may gather dynamical constraints. The technique we employ to work in the low density, “needle in the haystack” regime of the outer profiles of stellar systems is based on multifilter imaging, including use of the *DDO51* filter centered on the gravity-sensitive Mg b triplet and MgH lines at 5150 Å. The Washington $M - T_2$ color provides a temperature index against which to compare $M - DDO51$ colors, which gauge surface gravity (primarily) and [Fe/H] (secondarily) in late G through early M stars^{7,25}. Thus, by imaging a stellar system to magnitudes not much fainter than the red giant branch (RGB), we can discriminate, with a high degree of confidence and relative ease, between giants associated with that system and foreground disk dwarf stars. The latter are a primary contaminating nuisance and the limiting factor in the effective use of simple starcounting techniques to trace the extended structures of resolved stellar systems. The number of field giant contaminants (i.e., giants that just happen to be at the same color and magnitude as the RGB of the parent system) is relatively small (but is subtracted off from the derived density profiles in Fig. 1 below). Removing virtually all field star “noise” enables us to map these stellar systems to well past their King limiting radii, which is often adopted as the tidal radius for a stellar system.

Hunting for individual far-flung stars that can be associated with a parent stellar system allows one to explore the system to extraordinarily low effective surface brightnesses (some ten or more magnitudes below sky brightness). We have demonstrated this technique in our study of the Carina²⁶ and Ursa Minor³⁴ dSphs. The reality of our identified “candidate extratidal stars” has been investigated in a variety of ways. An *a posteriori* analysis of the poten-

tial contamination of the isolated RGB sample by photometric errors yields at most an 18% expected false detection rate within our Carina sample³⁶. This is much lower than the contamination rate implied by the analysis of our Carina data by Morrison et al.³¹; however, we³⁶ have enumerated a number of assumptions and other problems (foremost among them, utilization of a greatly inflated error distribution for our sample) with the Morrison et al. analysis that invalidates their conclusions. Our estimated *low* false detection rates are upheld by spectroscopy: (1) Of 50 spectroscopically studied candidate RGB giants in the Carina sample we find a false detection rate exactly as predicted above (18%), and we find nine members beyond the King cut-off radius. (2) For 155 stars in the Ursa Minor field with published spectroscopy, we are 100% accurate in classifying dwarfs and giants. The identified extended RGB population is mimicked by the distribution of Ursa Minor’s blue horizontal branch stars³⁴. (3) In similar studies of the And I and III dSphs, Keck spectroscopy of 54 of our giant candidates reveals a 100% identification accuracy⁹.

We have now made “associated star” maps of a number of dwarf galaxy and globular cluster satellites of the Milky Way and M31 systems. Fig. 1 shows preliminary results on five other satellites with published M/L : the Sculptor, Leo I and Leo II dSph galaxies, and the globulars NGC 288 and Palomar 13. For Sculptor, Leo I and NGC 288 we have employed the techniques discussed above. For Pal 13, we use a proper motion membership analysis to identify extratidal candidates⁴¹, while to obtain the density profile of Leo II we have used the classical method of starcounts¹⁴ on very deep UBV imaging.

3 Trend of Departure Density with M/L

All seven systems in Fig. 1 show, with varying amplitudes, a break from their central King profile density distributions that heralds the onset of a second structural population with a shallower, more or less power law, fall-off. We define the “departure density” as the density, normalized to the core, at which the observed profile departs from the best fit King profile to the central parts. Among the ensemble in Fig. 1 one sees a trend of higher departure density for higher M/L objects (Fig. 2). Interpretations at both extremes of the dSph DM debate can be postulated to account for this apparent trend: (1) dSph galaxies (and clusters) with DM can support secondary, but bound, “halo” populations of stars. Fig. 2 implies that objects with larger M/L have larger DM halos that can support more substantial stellar halos. (2) The extended populations around dSph galaxies (and some globular clusters) are not bound, but, rather, consist of extratidal debris from their parent objects, which are undergoing various degrees of tidal disruption. In the satellite disruption models of John-

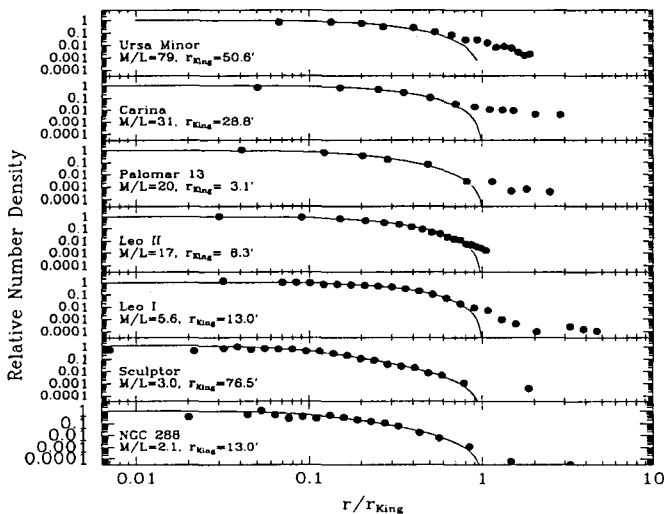


Figure 1: Radial profiles (normalized to the King limiting radius, often adopted as r_t) of the core-normalized density of associated star candidates (minus the mean field background) (filled circles) for seven objects, shown in M/L order. Solid lines show King profiles fit to the centers (all fits are similar to, or taken from, previously published fits). Typical values²⁸ of M/L and r_t are given. Poissonian error bars are typically of order the size of the points.

ston et al.¹⁵, the departure density reflects the tidal mass loss rate. Thus, the apparent correlation suggests that higher inferred M/L 's correspond to higher mass loss rates, and this, in turn, suggests that the high M/L 's are *not* a reflection of the DM contents, but, rather, higher degrees of virial *non*-equilibrium in the parent objects.

That Pal 13 partakes in the Fig. 2 trend lends some support to the second scenario. An M/L of 20 has just been reported for this very small globular cluster⁴, while we report elsewhere a number of reasons why this cluster must be undergoing severe tidal disruption (e.g., Pal 13 has large blue straggler fraction, a double subgiant branch, a break in its density profile, and a highly destructive orbit). In the context of the interpretations for the M/L -departure density trend given above, one must either accept that globular clusters, including very small ones (with only several thousand M_\odot in stars), can have substantial dark matter contents along with their dSph counterparts, or that the masses inferred from $\sigma_{v,c}$ are being substantially inflated due to the effects of tidal disruption. Fortunately, the extreme interpretations discussed here can be discriminated by measuring radial velocity trends with radius: DM halos should produce¹⁸ declining σ_v with r while models of tidally disrupting systems show¹⁹ flat or rising $\sigma_v(r)$. Our survey, which identifies the very

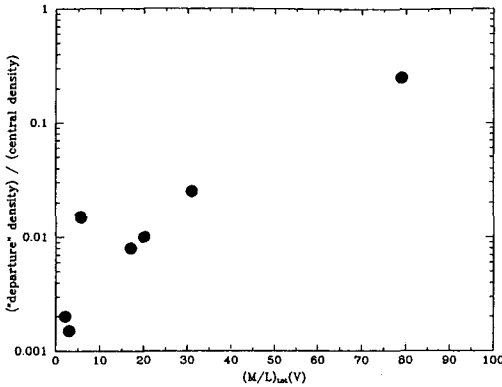


Figure 2: Correlation of departure density to total M/L for Fig. 2 objects. The point falling off the otherwise smooth trend represents Leo I; our preliminary Leo I analysis may be somewhat compromised by the proximity of the star Regulus to Leo I’s core.

“needle-in-the-haystack” targets one needs to do this experiment, has already allowed us to obtain confirmatory ($\sim 15 \text{ km s}^{-1}$ resolution) velocities to significantly larger r (to beyond the King cut-off radii) than previous surveys (which have been limited to the high density dSph cores). Our next challenge is to obtain velocities at a higher resolution capable of testing the physics. Models by Kleyana et al.¹⁸ predict that ≤ 20 quality spectra at $\sim 0.75r_t$ are needed to discriminate between models. These future data will hopefully bring us closer to understanding the mysteriously large M/L ’s of dSph galaxies.

We thank Andi Burkert and Ben Moore for useful discussions and support from the David and Lucile Packard Foundation, The Research Corporation in the form of a Cottrell Scholar Award, and NSF grant AST-9702521.

References

1. Armandroff, T. E., Olszewski, E. W. & Pryor, C. 1995, AJ, 110, 2131
2. Baade, W. 1944, ApJ, 100, 147
3. Burkert, A. 1997, ApJ, 474, L99
4. Côté, P. & Meylan, G. 2001, *in prep.*
5. Eskridge, P. B. 1988, AJ, 95, 1706
6. Feltzing, S., Gilmore, G. & Wyse, R. F. G. 1999, ApJ, 516, L17
7. Geisler, D. 1984, PASP, 96, 723
8. Gould, A., Guhathakurta, P., Richstone, D. & Flynn, C. 1992, ApJ, 388, 345
9. Guhathakurta, P., Grebel, E. K., Pittroff, L. C., Reitzel, D. B., Phillips, A. C., Vogt, S. S., Ostheimer, J. C. & Majewski, S. R. 2001, *in prep.*
10. Hargreaves, J., Gilmore, G., Irwin, M. & Carter, D. 1994, MNRAS, 271,

693

11. Hodge, P. W. & Michie, R. W. 1969, AJ, 74, 587
12. Ibata, R. A., Wyse, R. F. G., Gilmore, G., Irwin, M. J. & Suntzeff, N. B. 1997, AJ, 113, 634
13. Innanen, K. A. & Papp, K. A. 1979, AJ, 84, 601
14. Irwin, M. & Hatzidimitriou, D. 1995, MNRAS, 227, 1354
15. Johnston, K. V., Sigurdsson, S., & Hernquist, L. 1999, MNRAS, 302, 771
16. King, I. R. 1966, AJ, 71, 64
17. Klessen, R. S. & Kroupa, P. 1998, ApJ, 498, 143
18. Kleyna, J., Geller, M., Kenyon, S. & Kurtz, M. 1999, AJ, 117, 1275
19. Kroupa, P. 1997, New Astronomy, 2, 139
20. Kuhn, J. R. & Miller, R. H. 1989, ApJ, 341, L41
21. Kuhn, J. R. 1993, ApJ, 409, L13
22. Kuhn, J. R., Smith, H. A. & Hawley, S. L. 1996, ApJ, 469, L93
23. Kunkel, W. E. 1979, ApJ, 228, 718
24. Lynden-Bell, D. 1982, The Observatory, 102, 202
25. Majewski, S. R., Ostheimer, J. C., Kunkel, W. E. & Patterson, R. J. 2000a, AJ, 120, 2550
26. Majewski, S. R., Ostheimer, J. C., Patterson, R. J., Kunkel, W. E., Johnston, K. V. & Geisler, D. 2000b, AJ, 119, 760
27. Mateo, M., Olszewski, E., Vogt, S. & Keane, M. 1998, AJ, 116, 2315
28. Mateo, M. 1998, ARA&A, 36, 435
29. Mayor, L., Governato, F., Colpi, M., Moore, B., Quinn, T., Wadsley, J., Stadel, J. & Lake, G. 2001, ApJ, *submitted*
30. Moore, B. 1996, ApJ, 461, L13
31. Morrison, H. L., Olszewski, E. W., Mateo, M., Norris, J. E., Harding, P., Dohm-Palmer, R. C., & Freeman, K. C. 2001, AJ, 121, 283
32. Oh, K. S., Lin, D. N. C. & Aarseth, S. J. 1995, ApJ, 442, 142
33. Olszewski, E. W., Pryor, C. & Armandroff, T. E. 1996, AJ, 111, 750
34. Palma, C. 2001, Ph.D. Thesis, University of Virginia
35. Palma, C., Majewski, S. R., & Johnston, K. V. 2001a, AJ, *submitted*
36. Palma, C., Ostheimer, J., Majewski, S., Link, R., Frinchaboy, P., Patterson, R., Kunkel, W., Johnston, K. & Geisler, D. 2001b, *in prep.*
37. Piatek, S. & Pryor, C. 1995, AJ, 109, 1071
38. Richstone, D. O. & Tremaine, S. 1986, AJ, 92, 72
39. Saha, A, Monet, D. G. & Seitzer, P. 1986, AJ, 92, 302
40. Sellwood, J. A. & Pryor, C. 1998, in Highlights of Astronomy, 11A, 638
41. Siegel, M., Majewski, S., Cudworth, K. & Takimaya, M. 2001, AJ, 121, 935
42. van Agt, S. L. T. J. 1978, Publ. David Dunlop Obs. 3, 205

THE IMPACT OF TIDAL INTERACTIONS ON SATELLITE GALAXIES: A Study of the M31 Satellites, M32 & NGC 205

P. I. Choi, P. Guhathakurta

UCO/Lick Observatory, University of California, Santa Cruz, CA 95064

E-mail: pchoi@ucolick.org, raja@ucolick.org

K. V. Johnston

Van Vleck Observatory, Wesleyan University, Middletown, CT 06459

E-mail: kvj@astro.wesleyan.edu

Surface photometry of the M31 satellites M32 and NGC 205 is compared to numerical simulations of satellite destruction to constrain orbital parameters and the interaction history of the M31 subgroup. Our analysis reveals the following preliminary results: (1) Generic features of tidal disruption in the simulations include an extended “extra-tidal” excess region and an inner depletion zone, both of which are observed in M32 and NGC 205; (2) M32 is likely to be on a highly eccentric orbit well away from pericenter; (3) Surface brightness and luminosity evolution estimates for M32, the prototypical compact elliptical galaxy, imply that it is not simply the residual core of a tidally-stripped normal elliptical galaxy, but was instead formed in a truncated state.

1 Introduction

Recent evidence for tidal streams in the halos of the Milky Way⁶ and M31⁴, along with studies investigating extra-tidal material around Local Group globular clusters³ and dwarf spheroidals⁷, indicate that the tidal disruption and accretion of satellites are ongoing processes in the present epoch. In this paper, preliminary results are presented from a study comparing integrated surface photometry of M32 and NGC 205 to satellite simulations^{2, 5}. Spectroscopic observations to determine the internal kinematics in the tidal region of M32 and more finely tuned numerical models will be incorporated in later studies.

2 Observations / Simulations

The observational component of this study is based on $1.7^\circ \times 5^\circ$ *B*- and *I*-band CCD mosaic images centered on M31 and covering both satellites. Standard ellipse fitting techniques are used to model and remove M31 disk light and to perform surface photometry on the satellites to limiting isophotes of $[\mu_B, \mu_I] = [27, 25]$ mag arcsec⁻², corresponding to semi-major axis lengths $\tau_{\text{lim}}^{\text{M32}} = 420''$ (1.6 kpc) and $\tau_{\text{lim}}^{\text{NGC 205}} = 720''$ (2.7 kpc)². In Fig. 1, *B*-band images of M32, before and after M31 subtraction, illustrate the importance

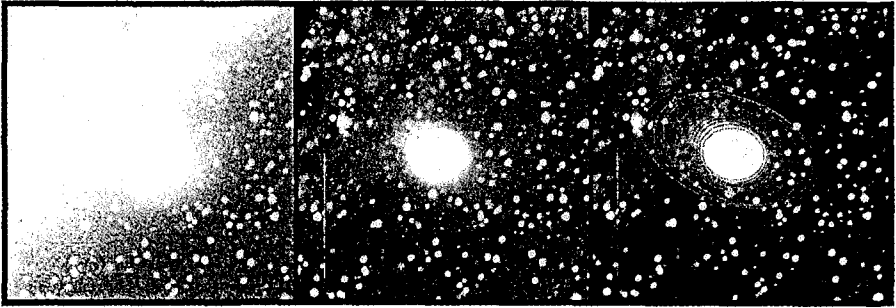


Figure 1: Grayscale representations of B -band images ($17' \times 17'$) centered on M32 with (left) and without (middle) M31's disk light contribution. Note the steep gradient in the background across M32 caused by the inclined disk of M31 (left) and M31's residual fine-scale structure [dust lanes, spiral arms, etc. (middle)] even after subtraction. Best-fit elliptical isophotes of M32 (right) in the semi-major axis range of $100'' < r < 300''$ highlight the low surface brightness region in which signatures of tidal interactions are observed.

of careful background subtraction. For the numerical simulations, single-component, spherical satellites are followed through a fixed three-component potential representative of the disk, bulge and halo of a parent galaxy. The models explore a range of orbital eccentricities and initial mass profiles for the satellite. To facilitate comparison, the ellipse fitting technique used for the observations is also adopted for the simulated satellites.

3 Interpretation of Observations in Light of Numerical Simulations

Generic Features of Tidal Interaction: Breaks in the surface brightness, ellipticity and position angle profiles are common features of the numerical simulations (Fig. 2: right). The presence of an extended region of excess material and an inner depletion zone are other generic features. The excess region corresponds loosely to what is conventionally described as an “extra-tidal” region; however, we find that in many cases they are associated with tidally heated, yet bound material. Similar features are observed in M32 (Fig. 2: left) and NGC 205 suggestive of tidal interaction with and stripping by M31⁵.

Discriminating Orbital Parameters for M32: In the case of M32, three of its profile features are suggestive of a highly eccentric orbit:

- There is a triple break in the position angle ϕ profile, with two of the breaks coincident with breaks in the surface brightness and ellipticity profiles. This is an atypical feature of the simulations, seen only in satellites approaching apocenter on highly eccentric orbits. In Fig. 2, the profiles of one such simulated satellite show striking similarities to those of M32.

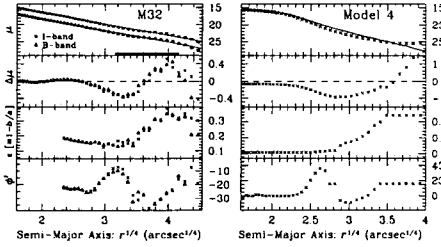


Figure 2: Surface brightness μ , de Vaucouleurs residual $\Delta\mu$, ellipticity ϵ and position angle ϕ profiles plotted in de Vaucouleurs coordinates for a simulation snapshot (*right*) and M32 (*left*) in *B* (*triangles*) and *I* (*crosses*) bands. The surface brightness profile of M32 is well fit by a de Vaucouleurs profile (*top left*) over the radius range $10'' < r < 65''$ with $r_I^{\text{eff}} \sim r_B^{\text{eff}} \sim 30''$ and $[\mu_I^{\text{eff}}, \mu_B^{\text{eff}}] = [18.0, 19.9]$ mag arcsec $^{-2}$. The residual profile shows a deficiency below the extrapolated de Vaucouleurs fit from $50'' - 150''$ and an excess beyond $150''$. These features, coincident with breaks in the ellipticity and position angle profiles, are comparable to those found in Model 4 (*right*) in which a satellite with orbital eccentricity $e = 0.88$ is approaching apocenter. The bold line covering the range $100'' < r < 300''$ in the M32 μ plot (*top left*) shows the region marked by contours in Fig. 1 (*right*).

- The second piece of evidence is the relationship between the classically defined, theoretical King tidal radius r_{tide} and the observed break in the surface brightness profile r_{break} ⁵. The ratio $r_{\text{break}}/r_{\text{tide}}$ typically has values of unity or greater for near-circular orbits and only drops below unity for certain phases of highly eccentric orbits (Fig. 3: *top*). For M32, the measured upper limit of $r_{\text{break}}/r_{\text{tide}} \sim 0.5$ suggests that it is on a highly eccentric orbit away from pericenter.
- Finally, $r_{\text{distort}}^{\text{M32}}$, the radius of the onset of isophotal elongation is coincident with $r_{\text{break}}^{\text{M32}} \sim 150''$. This ratio, $r_{\text{break}}/r_{\text{distort}}$ is typically ≥ 2.0 for near-circular orbits and approaches unity only for the most eccentric orbits (Fig. 3: *bottom*), suggesting that M32 is in this latter category. Since both radii are directly observable, unlike $r_{\text{break}}/r_{\text{tide}}$, this deduction is less model dependent and more robust than the previous one.

Implications on Compact Elliptical Galaxy Formation: M32 stands apart from normal ellipticals—its combination of high central surface brightness and low

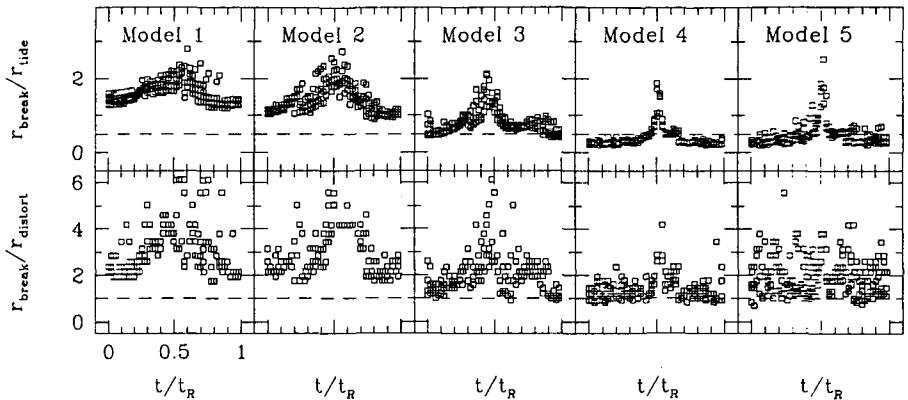


Figure 3: Ratio of $r_{\text{break}}/r_{\text{tidal}}$ (*top*) and $r_{\text{break}}/r_{\text{distort}}$ (*bottom*) as a function of orbital phase. In Models 1–4, satellite orbits range in eccentricity from nearly circular (Model 1) to highly elongated (Model 4) with eccentricities of $e = 0.10/0.29/0.67/0.88$, respectively. Model 5 follows the same orbit as Model 4, but adopts a shallower initial density profile than Models 1–4. The dashed line in each panel represents the measured ratio for M32 and indicates that it is likely to be on an eccentric orbit ($e_{\text{M32}} \geq 0.5$).

luminosity make it the prototype of a rare class of galaxies known as compact ellipticals (cEs). cEs tend to reside in close proximity to massive companion galaxies, and it is commonly believed that cEs are the tidally truncated remnant cores of normal ellipticals. Guided by numerical simulations, we estimate the luminosity L^{orig} and central surface brightness μ_0^{orig} M32 might have had *prior to* tidal stripping by M31. These estimates are compared to the observed (i.e. present-day) values of L and μ_0 for M32 in order to infer the changes ΔL and $\Delta\mu_0$. While the changes are in the right direction they are far too small to explain M32’s position in the L - μ_0 plane. This suggests that the true impact of environment may be in the formation, rather than in the subsequent evolution, of cEs¹.

References

1. A. Burkert, MNRAS **266**, 877 (1993)
2. P.I. Choi, P. Guhathakurta & K.V. Johnston, AJ in preparation (2001)
3. C.J. Grillmair *et al.*, AJ **109**, 2553 (1995)
4. R. Ibata *et al.*, Nature **412**, 49 (2001)
5. K.V. Johnston, P.I. Choi & P. Guhathakurta, AJ in preparation (2001)
6. S. Leon, G. Meylan & F. Combes, A&A **359**, 907 (2000)
7. S. Majewski *et al.*, AJ **119**, 760 (2000)

CONSEQUENCES OF SATELLITE DECAY FOR GALAXY HALO SHAPES

Eelco van Kampen

*Institute for Astronomy, University of Edinburgh,
ROE, Blackford Hill, Edinburgh EH9 3HJ, U.K.*

E-mail: evk@roe.ac.uk

High resolution N-body simulations show a high abundance of galaxy satellites, which is not seen observationally. It appears that too many subhalos survive in simulated galaxy halos. One likely cause for this is that dynamical friction is not properly simulated yet, not even for the highest resolution simulations to date, resulting in an 'undermerging' problem. Another issue that can be resolved by properly simulating dynamical friction is the cuspsiness of N-body halos. The orbital energy loss suffered by satellites causes their parent halo to heat up. This heating up can transform a central cusp into a core, especially if this heating is actually most efficient in the center. The orbital decay of a sufficient number of galaxy satellites can therefore, when properly simulated, resolve both issues.

1 The 'missing satellites' and 'core' problems

Hierarchical structure formation scenarios predict galaxy halo properties that do not seem to match observations on two accounts: the abundance of substructure, i.e. satellites, and the slope of the central density profile, or the 'cuspsiness' of the galaxy halo.

With regards to the first, 'missing satellites' problem, high-resolution simulations^{7,10} show many more galaxy subhalos, i.e. dwarf subhalos, than observed. Our Galaxy contains just two subhalos with a significant mass (the Magellanic Clouds, with a mass of $\approx 10^{10} M_{\odot}$ for the LMC), while the remaining subhalos surviving to the present day found are much less massive⁹. Clearly, galaxy subhalos are either destroyed by a physical mechanism, are much darker (i.e. have a much larger mass-to-light ratio) than cluster galaxies, or were never formed in large numbers in the first place, for example if the power spectrum of density fluctuations turns over below or near the galaxy mass-scale.

The second problem, dubbed the 'core catastrophe' by some¹¹, is a disagreement between the relatively steep inner slope found in numerical simulated dark matter halos, and the constant density cores found observationally¹³. Note that there is also disagreement on the interpretation of the observational results^{2,3}, and the actual slope found in N-body halos^{8,11,12}. Once both disagreements have been resolved, the core problem might be solved automatically as well. However, this is by no means certain, so we take the problem

to be still standing.

The physical mechanism of dynamical friction leads to the complete destruction of subhalos by bringing them to the center of their embedding halo, where they merge with the core region. This process is well-known and extensively discussed in the literature^{1,14}. Besides removing galaxy satellites, the orbital energy lost by galaxy satellites due to dynamical friction will heat up the galaxy halo. If this happens preferentially in the core, any cusps present will likely be dissolved.

Thus, dynamical friction alone can provide a solution to both problems. So why is this not seen to happen in N-body simulations? In the comparison between theory and observations, the reliability of the N-body result is usually taken for granted. But is this warranted?

2 Numerical limitations: undermerging

The results of test simulations presented elsewhere⁶ suggest that the N-body simulation method cannot properly model the gravitational wake that drives dynamical friction, indicating that numerical shortcomings provide one solution to the 'missing satellite' problem. The consequence of this 'undermerging' is that subhalos are not destroyed in sufficient numbers, thus producing an artificially high abundance of subhalos. The numerical problems are most bothersome during the early stages of hierarchical structure formation, where both halos and subhalos are modeled by relatively few particles. Galaxy halos are relatively old, with little ongoing secondary infall. Subhalos that are destroyed are not all replaced; in this picture, the Magellanic Clouds are relatively new to our Galaxy, and will be destroyed within a few Gyr¹⁵.

In order to assess how well dynamical friction is modeled in N-body simulations, we need to establish the volume and shape of the *effective* gravitational wake that generates the drag force, and thus the actual number of N-body particles that are available to model this wake. A rough estimate for the volume from which *half* the drag force originates is $(2r_s)^3$, where r_s is the half-mass radius of the subhalo. This is a fair estimate for a range of subhalo profiles. The number of halo particles within this volume that are to make up the wake is roughly $N_h(r_s/r_h)^3$ (where the subscript h is used to denote a halo property), so for a $r_s \approx 0.01r_h$ subhalo in a halo modeled with $N_h = 10^6$ particles there is just a single particle in the 'half-force volume'.

Because subhalos are usually tidally truncated, their half-mass radii are relatively small, so that the contribution to the drag force acting on a subhalo comes mostly from a small region just trailing the subhalo. It is therefore quite hard to form a compact wake within an N-body simulation, as few particles

are actually available to form the wake.

3 Dynamical friction during hierarchical structure formation

An important factor in the efficiency of dynamical friction is the mass ratio of the embedding halo to its subhalo, m_h/m_s . Taken at face value, this means that a $10^9 M_\odot$ dwarf within a $10^{12} M_\odot$ isothermal galaxy decays on a time-scale of the order of 40 Gyr. However, such a dwarf is likely first spend some time in a smaller galaxy, before ending up in the $10^{12} M_\odot$ galaxy.

For example, assume that through hierarchical merging it spends 1 Gyr in a $10^{10} M_\odot$ galaxy, then 2 Gyr in a $10^{11} M_\odot$ galaxy, and finally 6 Gyr in a $10^{12} M_\odot$ galaxy. The dynamical friction times are then, respectively 0.4, 4, and 40 Gyr. Thus, this example subhalo will already be destroyed by the $10^{10} M_\odot$ galaxy before the latter grows to a $10^{11} M_\odot$ galaxy. Here, we have not taken into account that the crossing time of the $10^{10} M_\odot$ galaxy at look-back time $t_1 = 9$ Gyr is typically smaller than for the final $10^{12} M_\odot$ galaxy, and that its mean density is larger than for a $10^{10} M_\odot$ galaxy that formed recently, which will speed up dynamical friction.

This example, which is not necessarily typical, illustrates that the very nature of hierarchical clustering within an expanding Universe implies that any numerical problem with dynamical friction is most important at the early stages of hierarchical structure formation.

4 Flattening the cusp by frictional heating

Besides destroying satellites, the effect of dynamical friction is to transfer orbital energy from the satellites to the kinetic energy of their parent halo, thus heating up the latter. It is not clear at first which part of the parent halo will be heated most, as this should depend on the density profile and the orbit of the satellite, but the puffing up of the halo in one form or another could be sufficient to transform a cuspy inner region into a core. If the energy transfer mostly happens in the inner regions, this transformation should be almost certain if a sufficient number of satellites of sufficient mass are involved. This has already been suggested and tested for orbiting gas lumps⁵, but should be more efficient for the more massive dark matter subhalos.

A quantitative study is currently under way, but the test simulations used to study the undermerging problem discussed above⁶ already show indications that 'frictional heating' is quite efficient for multiple subhalos falling in at random intervals. The test simulations were for Plummer halos, which already have a core, so simulations with cusps are now being performed. Still, the core was seen to grow under the influence of dynamical friction, and it was

mainly the central regions of the halo heat up. The heat will be transferred to the outer regions, eventually, and a new cusp could form, if frictional heating stops. If satellites continue to be accreted, it might be impossible for a new cusp to form.

These simulations also showed that heating is hardly noticeable for a single subhalo (with a mass equal to one percent of the mass of its parent halo), while it is very clear, even visually when inspecting the particle distribution, in a simulation with 20 such subhalos orbiting on random, eccentric orbits (the total mass in subhalos is thus 20 percent of the parent halo). Note that the subhalos will not make it intact to the center of the halo; the effect of the heating is more important than the sinking of extra material (the satellite remnants) towards the center. An important effect is the stripping of most of the subhalo before it reaches the center; the stripped material is ending up in the core, and not adding to or forming a new cusp.

References

1. Binney J., Tremaine S., 1987, *Galactic Dynamics*, Princeton
2. van den Bosch F.C., Robertson B.E., Dalcanton J.J., de Blok W.J.G., 2000, *AJ*, 119, 1579
3. van den Bosch F.C., Swaters R.A., 2000, *MNRAS*, 299, 728
4. Danby J.M.A., Bray T.A., 1967, *AJ*, 72, 219
5. El-Zant A., Shlosman I., Hoffman Y., 2001, submitted to *ApJL*, astro-ph/0103386
6. van Kampen E., 2000, submitted to *MNRAS*, astro-ph/0008453
7. Klypin A.A., Kravtsov A.V., Valenzuela O., Prada F., 1999, *ApJ*, 522, 82
8. Klypin A.A., Kravtsov A.V., Bullock J.S., Primack J.P., 2000,
9. Mateo M., 1998, *ARA&A*, 36, 435
10. Moore B., Ghigna S., Governato F., Lake G., Quinn T., Stadel J., Tozzi P., 1999, *ApJ*, 524, L19
11. Moore B., Quinn T., Governato F., Stadel J., Lake G., 1999, *MNRAS*, 310, 1147
12. Navarro J.F., Frenk C.S., White S.D.M., 1997, *ApJ*, 490, 493
13. Salucci P., Burkert A., 2000, *ApJ*, 537, L9
14. Saslaw W.C., 1985, *Gravitational Physics of Stellar and Galactic Systems*, Cambridge
15. Tremaine S., 1976, *ApJ*, 203, 72

EXPLORING GROUP HALOS USING GALAXY DYNAMICS

Alan B. Whiting

*Physics Department, U. S. Naval Academy, Annapolis, MD 21402
USA*

E-mail: whiting@usna.edu

I investigate some characteristics of dark matter in the Local Group and the nearby Sculptor Group. I find that there is no evidence for an extended dark matter halo around the Local Group. In addition, the angular momentum of the visible matter in the Sculptor Group is consistent with having been produced by tidal interaction among the galaxies, which indicates that the dark matter and luminous matter angular momenta are aligned.

1 Dark Matter in Galaxy Groups

Observationally, dark matter is found within individual galaxies and also in rich clusters of galaxies. To get more insight into this mysterious stuff it is worth looking for it in other places, for example in small groups of galaxies. Two of these conveniently close enough for examination are our own Local Group and its nearest neighbor, the Sculptor Group.

2 The Dark Halo of the Local Group

There are something like three dozen galaxies in the Local Group. However, most of the Group's mass resides in just two: the Milky Way and Andromeda. This led Kahn and Woltjer⁴ to treat the motion of these two as a linear two-body problem. Given the present separation and radial velocity, a combination of the age of the Group and its mass can be calculated. Lynden-Bell⁸ extended the analysis to dwarf galaxies in the group. The following is a revised version of a calculation following Lynden-Bell's suggestion¹⁵ with updated data.

Taking only those galaxies which are more distant from the center of the Local Group and from each of the big galaxies than 500 kpc, and which have well-determined distances and radial velocities, we are left with six data points. Assuming their observed radial velocities to be the projection of their actual radial velocities along the line of sight we arrive at the effective radial velocities. We plot the values of distance and velocity for each galaxy along with theoretical curves for the assumed type of motion. For a given age and mass of the Group all the r, \dot{r} pairs should fall upon a single curve^a. If there is

^aThe age can be varied to get the best fit of the data to a curve.

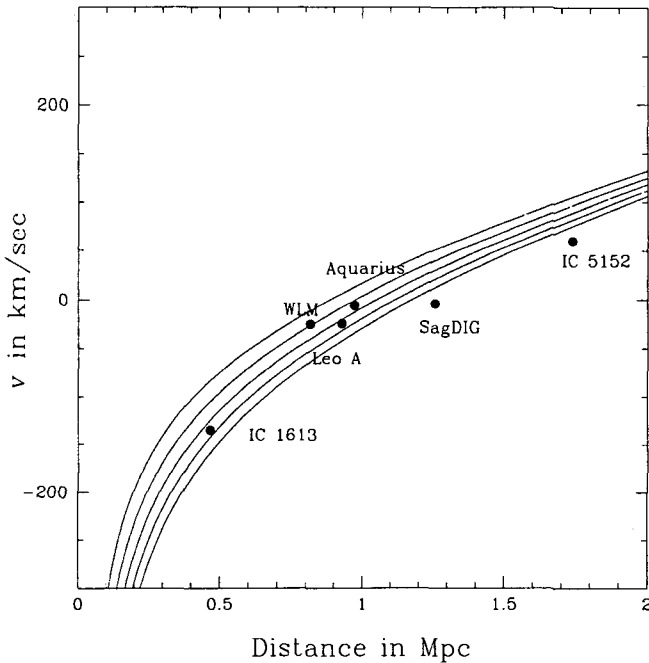


Figure 1: Plot of distance versus radial velocity for the more distant dwarf galaxies in the Local Group, referred to the center of mass. The curves are (from left to right) for 1.3 , 1.8 , 2.2 , 2.7 and 3.1×10^{12} Solar masses.

a significant halo, more distant galaxies will feel a greater effective mass and thus fall on a different (lower) curve.

The best fit to our present data^b, with an age of 14 Gyr, gives a mass of 2.1×10^{12} Solar masses and no trace of a halo. If 12 Gyr is assumed as an age there is a mass amounting to $4.2 \times 10^{12} M_{\odot}$ at IC 5152 (1.7 Mpc) compared with about half that at IC 1613 (500 kpc). This situation is plotted in Fig. 1.

This result cannot be trusted very far. With uncertainties in distance of 10% (an optimistic estimate) the systematic trend can be made to vanish and an average mass of 2.8×10^{12} is obtained for the Group. A systematic trend larger than the uncertainty requires an implausibly low age for the Local Group. Between the probable age of the Group from other sources, the best fit, and the correspondence with the Milky Way mass of Kochanek⁵, it is hard to find an extended dark halo for the Local Group.

^bData are taken from the literature^{1 3 6 7 9 11 12 13}.

3 Angular Momentum in the Sculptor Group

As a contribution to the discussion of alternatives to the tidal-torque theory of galaxy angular momentum, I present here an analysis done on the Sculptor Group¹⁴, extending that performed on the Local Group by Gott and Thuan².

The major galaxies in the Sculptor Group are all spirals and therefore have well-defined angular momentum vectors. They appear in two pairs: NGC 55 and NGC 300; NGC 247 and NGC 253; and one more distant singleton, NGC 7793, with NGC 45 beyond and probably not a bound member.

If the tidal-torque theory is correct, the spin vectors of an isolated pair of galaxies must each be perpendicular to the separation vector between them at the time they spin each other up. This vector is conveniently found by taking the cross product of the spin vectors. If there is no orbital motion the spin-cross and the separation vectors must remain aligned.

Applying this calculation to the three pairs of galaxies, we find that the misalignment angle for NGC 45 and 7793 is 21° ; NGC 55 and 300, 38° or 39° ; for NGC 247 and 253, 48° or 66° (the angular momentum vectors for NGC 55 and 247 are ambiguous through reflection in the plane of the sky, so two cases for each were calculated). The spins of NGC 45 and 7793 are thus consistent with tidal-torque theory for an isolated pair, random vectors having only about a 7% chance of aligning within 21° . The other two pairs do not show this consistency. Either their angular momentum was not generated by tidal torques, or they have not been dynamically isolated.

Suppose that the misalignment calculated above is a consequence of orbital motion since the spin was imparted. Then the spin-cross vector and the present separation vector define the plane of the orbit and, normal to that plane, the orbital angular momentum vector. We may perform a calculation exactly analogous to the first, treating each pair as an object receiving its (orbital) angular momentum from the tidal torque of the other pair. The misalignment between the pair-pair separation vector and the orbital spin-cross vector is, in all cases, about 15° . This close an alignment has less than a 4% probability of happening by chance.

4 Summary and Implications

From some simple calculations on two galaxy groups, I conclude

- There is probably no general dark matter halo for the Local Group, that is, no significant mass beyond 500 kpc from the center of the Group.
- The angular momenta of the luminous matter in the Sculptor Group are consistent with having been produced by tidal interactions within

the Group. There is thus no significant misalignment between dark and luminous matter momenta, and no sign of much angular momentum being produced by accretion of smaller galaxies.

Acknowledgements

I would like to thank Donald Lynden-Bell for drawing my attention to both the timing argument and the original spin-cross calculation, and for pointing out the possibilities inherent in the Sculptor Group. Prasenjit Saha was of invaluable help in preparing the presentation.

References

1. N. Caldwell *et al.*, *Bulletin of the American Astronomical Society* **20**, 1084 (1988)
2. J. R. Gott III and T. X. Thuan, *Astrophysical Journal* **223**, 426 (1978)
3. D. Huterer, D. D. Sasselov and P. L. Schechter, *Astronomical Journal* **110**, 2705 (1995)
4. F. D. Kahn and L. Woltjer, *Astrophysical Journal* **130**, 705 (1959)
5. C. S. Kochanek, *Astrophysical Journal* **457**, 228 (1996)
6. G. Lake and E. D. Skillman, *Astronomical Journal* **98**, 1274 (1989)
7. M. G. Lee in *The Stellar Content of Local Group Galaxies*, eds. P. Whitelock and R. Cannon (Astronomical Society of the Pacific, Provo, UT, 1999), p. 268
8. D. Lynden-Bell, *Observatory* **101**, 111 (1981)
9. D. Minniti and A. A. Zijlstra, *Astrophysical Journal Letters* **467**, 13 (1996)
10. D. Puche and C. Carignan, *Astronomical Journal* **95**, 1025 (1988)
11. A. Sandage and G. Carlson, *Astronomical Journal* **90**, 1464 (1985)
12. E. Tolstoy *et al.*, *Astronomical Journal* **116**, 1244 (1998)
13. S. Van den Bergh, *Astronomical Journal* **107**, 132 (1994)
14. A. B. Whiting, *Astronomical Journal* **117**, 202 (1999)
15. A. B. Whiting in *The Stellar Content of Local Group Galaxies*, eds. P. Whitelock and R. Cannon (Astronomical Society of the Pacific, Provo, UT, 1999), p. 420.

THE SHAPES OF GALAXIES AND CLUSTERS: AN X-RAY VIEW

David A. Buote

*Department of Physics and Astronomy, University of California, Irvine
4129 Frederick Reines Hall, Irvine, CA 92697-4575, USA
E-mail: buote@uci.edu*

Claude R. Canizares

*Department of Physics and Center for Space Research 37-241,
Massachusetts Institute of Technology, 77 Massachusetts Avenue,
Cambridge, MA 02139, USA
E-mail: crc@space.mit.edu*

We present preliminary constraints on the shape of the dark matter halo in the elliptical galaxy NGC 720 obtained from new Chandra imaging data. We also review X-ray constraints on dark matter shapes in galaxy clusters obtained with ROSAT and present some preliminary Chandra results.

1 Introduction

In massive galaxies, groups, and clusters we see X-ray emission from large quantities of hot gas with $T \sim 10^7\text{--}8$ K. This hot gas fills the 3D gravitational potential and extends out to large radii in both galaxies and clusters. When combined with the fact that the gas has an isotropic pressure tensor and that hydrostatic equilibrium is a good approximation in many cases, it is clear that X-ray observations offer a powerful probe of the gravitational potentials in these systems.

Previously in Buote & Canizares (1998a) we have discussed the virtues of using X-ray techniques to probe the shape of the dark matter halos in galaxies. We also reviewed our work on analysis of the ROSAT data of three galaxies. This review will present new Chandra results for NGC 720 and also discuss ROSAT and Chandra constraints on the shapes of clusters.

2 Chandra Observation of NGC 720

Just recently we have begun to analyze a 40 ks Chandra ACIS-S observation of NGC 720 (PI Canizares). Chandra is quite superior to ROSAT – it has $\sim 1''$ spatial resolution and larger bandpass (0.3-10 keV) and greater sensitivity ($\sim 5/3$ of ROSAT PSPC). With such a large improvement in resolution it might be hoped the Chandra would offer some surprises. In fact, our preliminary analysis

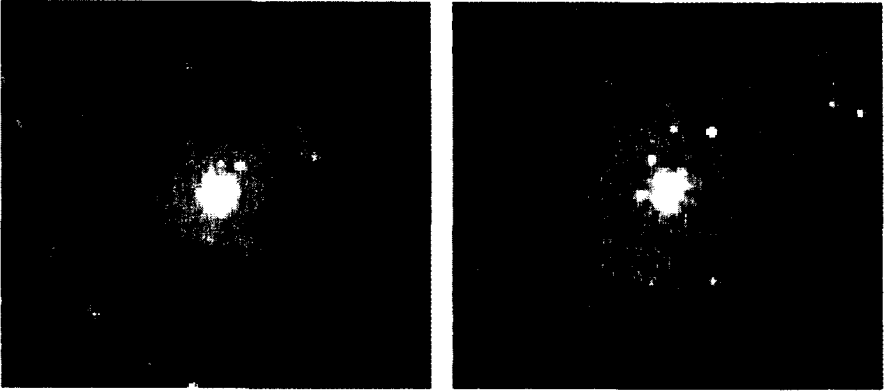


Figure 1: (Left) 0.3-2 keV Chandra ACIS-S image of NGC 720 binned into $2''$ pixels and smoothed 1 pixel width. This shows a $\sim 3'$ radius about the galaxy center. (Right) The same image binned into $1''$ pixels and smoothed with 1 pixel. This is a close-up image showing only $\sim 80''$ radius about the galaxy center.

of the Chandra data does offer some unexpected and interesting results. (For NGC 720 $1' \sim 6h_{75}^{-1}$ kpc.)

The most striking difference between the Chandra and ROSAT images (e.g., Buote & Canizares 1998a) is the large number of point sources clearly detected by Chandra. These sources are mostly concentrated within the inner $\sim 30''$ but there are several farther out as well. In particular, there is a group of four prominent sources to the NW about $70''$ from the galaxy center which must have affected the ellipticities and position angles computed from the ROSAT images. The key question to investigate is, “how much”?

To answer this question we must remove the sources and replace them with a faithful representation of the local diffuse galaxy X-ray emission. This is a relatively simple task for sources at large radii that are well above the galaxy background and also well separated from each other. But for sources near the center extraction and replacement is much trickier. Our preliminary attempts to remove sources within $\sim 30''$ have been largely unsuccessful since the derived ellipticities and position angles in these regions appear to be quite sensitive to the method and parameters used to remove the sources. We are currently exploring techniques to obtain a more reliable source-free image in the central regions.

Despite these difficulties we have removed the sources as best we can and have computed ellipticities and position angles which are shown in Fig. 2. Let us concentrate first on the region interior to $\sim 2'$ where ROSAT was

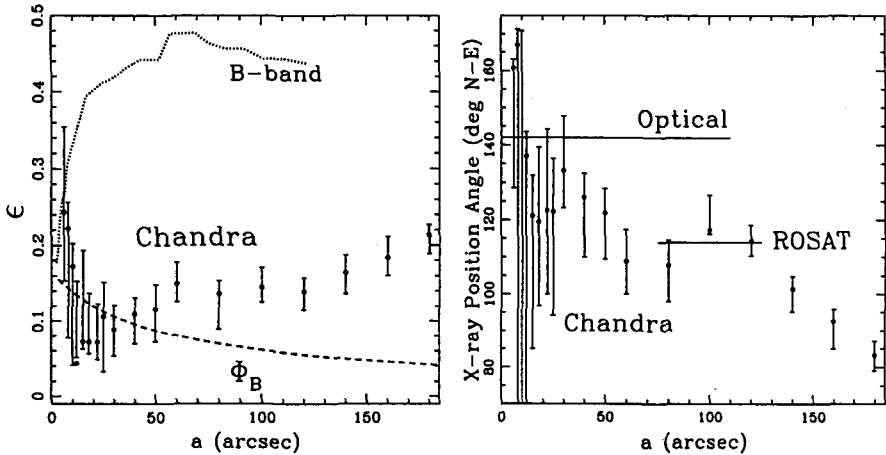


Figure 2: Preliminary results for the ellipticities (Left) and position angles (Right) obtained from the Chandra image of NGC 720. Error bars are 1σ Monte Carlo estimates.

able to provide interesting constraints. Although we just emphasized that the innermost regions need to be treated with caution because of systematics with regards to source extraction, there are some discernible trends that appear to be robust within $r \lesssim 30''$. The ellipticity appears to rise towards the center to take a value between 0.2-0.3. Similarly, the PA rises slowly to a value that is consistent with the optical value. Although not terribly clear from Fig. 2 the error bars are quite small in a region between $5''$ and $10''$.

At larger radii, between $\sim 1' - 2'$, the ellipticity has a value near 0.14. This should be compared to values 0.20-0.25 obtained with ROSAT. The smaller ellipticities measured with Chandra in this region are clearly the result of contamination of the ROSAT image by the group of sources to the NW noted above. The position angle twist seen in the ROSAT data is confirmed by Chandra. However, the precise radial variation is different (see Buote & Canizares 1996b) with most of the twisting within $r \sim 2'$ now occurring only within $\sim 50''$ of the galaxy center.

Finally, Chandra has for the first time provided accurate determinations of the ellipticity and PA from radii $\sim 2' - 3'$. Rather than holding constant or slowly varying, the ellipticity increases significantly to a value of ~ 0.2 and the PA twists rapidly another 30-40 degrees. These variations appear to be highly statistically significant, but since they occur near the edge of the CCD additional checks are required. (These checks are work-in-progress.)

2.1 Implications of Preliminary Results

We emphasize that the results presented above are preliminary, although we do not expect the basic findings to change qualitatively. Consequently, in this section we discuss some of their implications.

Although the ellipticities measured from the Chandra data in the region $a \sim 100'' - 120''$ (a is semi-major axis) are smaller than obtained from ROSAT they are still significantly larger than expected if mass follows the optical light. That is, in Fig. 2 we show the ellipticity profile labelled by Φ_B representing the ellipticities of the gravitational potential generated by mass distributed as the optical B -band light. Recall that such potential ellipticities are equal to those of the volume X-ray emissivity independent of the gas temperature profile according to the ‘‘X-Ray Shape Theorem’’ (e.g., Buote & Canizares 1998a). Hence, like ROSAT the ellipticities of the Chandra data of NGC 720 provide geometric evidence for flattened and extended dark matter.

As with ROSAT this geometric evidence for dark matter cannot be explained by MOND for two reasons (Buote & Canizares 1994). First, the transition between the Newtonian and MOND regimes is $r \sim 12h_{75}^{-1}$ kpc whereas the X-ray isophotes are already flattened within this radius; i.e., the X-ray isophotes are already too flat in the Newtonian domain. Second, if $\mu\tilde{g}_M = \tilde{g}_N$, which is the fundamental MOND equation, then potential shapes in MOND are the same as potential shapes in Newtonian theory; i.e., MOND, which was really designed to address radial manifestations of dark matter, cannot say anything about elliptical signatures of dark matter.

This evidence for flattened dark matter also appears to be in conflict with the self-interacting dark matter model (SIDM) of Spergel & Steinhardt (1999). The SIDM model predicts that DM halos should be spherical at small radius. Using the collisional radius defined by Miralda-Escudé (2000) the SIDM model would predict spherical halos within a radius of ~ 15 kpc for NGC 720 in clear conflict with the Chandra data.

The smaller ellipticities measured from the Chandra data in the region $a \sim 100'' - 120''$ do translate to a smaller estimate of the ellipticity of the dark matter halo. Whereas ROSAT indicated $\epsilon \approx 0.5 - 0.6$ for the dark matter halo apparently exceeding the ellipticity of the optical light ($\sim 0.4 - 0.5$), the small Chandra ellipticities translate to an ellipticity of the dark halo similar to the stars.

Although Chandra has confirmed the large-scale PA twist seen with ROSAT the details of the twist are quite different. In the ROSAT data the PA stays approximately aligned with the stars all the way to $\sim 60''$ before it makes an abrupt turn to a value $\sim 20^\circ$ away. The Chandra PA twist is much more

gradual and does its twisting within $\sim 40''$. This is a potentially crucial finding as Romanowsky & Kochanek (1998) showed that triaxial models could not reproduce the abrupt twist in the ROSAT data occurring at such large radii. The Chandra twist seems to be consistent with their models. Hence, within $a \sim 2'$ the our preliminary analysis of the Chandra data provide novel evidence for a triaxial dark matter halo.

Finally, at the largest radii probed ($2' - 3'$) the ellipticity and PA each set off in new directions. It is natural to wonder whether there is some tidal or ram pressure effects here. But it should be emphasized that NGC 720 is quite isolated from other large galaxies (Dressler et al. 1986). Aside from the PA twist there are no indications of external influences (e.g., centroid shifts) in the X-ray emission. NGC 720 is also a “core galaxy” indicating that it has not been dynamically disturbed in a long time (see B. Ryden, these proceedings). If the X-ray emission is indeed following the potential at these large radii then we are probably seeing the influence of a large-scale massive group potential. The possibility of large quantities of large-scale dark matter in NGC 720 has already been suggested from analysis of its dwarf satellites by Dressler et al. (1986).

3 Galaxy Clusters

Galaxy clusters have some advantages over individual galaxies for studies of their shapes with X-ray observations. Massive nearby clusters ($z \lesssim 0.1$) are typically 10-100 times brighter than NGC 720 in X-rays and have detectable emission extended to much larger radii. Another advantage is that the X-ray emission from stellar sources is quite negligible in clusters. Perhaps the key disadvantage is that since clusters are dynamically younger systems the assumption of hydrostatic equilibrium needs to be more carefully considered. Consequently, one should select clusters that are approximately circular and have little evidence for substructure. It has been shown previously with N-body gas-dynamical simulations that the assumption of hydrostatic equilibrium is quite good for such clusters, even if they do display some irregularities in their isophotal shapes and some small-scale substructure (Buote & Tsai 1995).

We have previously analyzed a small sample of clusters that are mostly regular in appearance, especially outside of their cores (Buote & Canizares 1996a). In Fig. 3 we show a ROSAT PSPC contour image of the massive nearby cluster A2029. The ellipticity profile of this cluster is quite steep and falls from a value of ~ 0.25 at 300 kpc to ~ 0.1 at 1.3 Mpc ($H_0 = 80$ km/s/Mpc). Such ellipticity gradients are found in 4 out of the 5 clusters studied. The values of the ellipticities imply flattened dark matter distributions with ellipticities

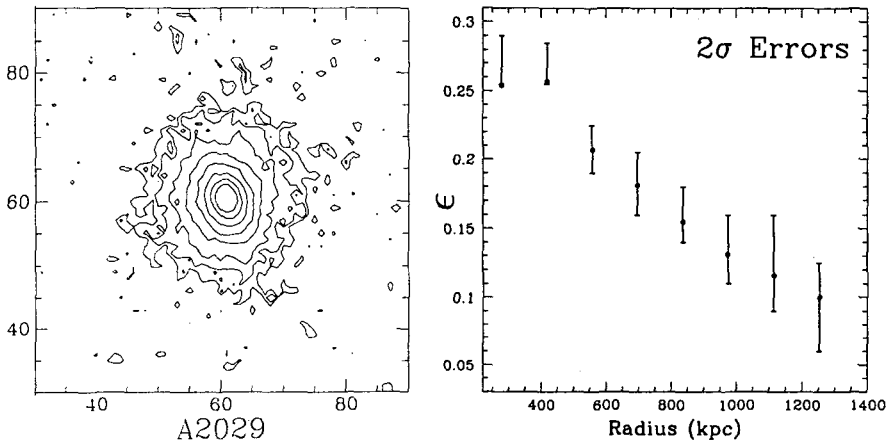


Figure 3: (Left) Contour plot of ROSAT PSPC image of A2029 from Buote & Canizares (1996a) approximately 3 Mpc on each side. (Right) Ellipticity profile computed from the ROSAT image of A2029.

0.4-0.6 (2σ) that are consistent both with the shapes of the galaxy isopleths and simulated CDM halos (see B. Moore and J. Bullock, these proceedings).

However, the steep ϵ_x gradients imply very concentrated mass distributions. Recall again that the X-ray Shape Theorem says that the shapes of isopotential surfaces and iso-volume-X-ray-emissivity surfaces are the same. For any centrally concentrated matter distribution the higher order multipoles rapidly give way to the spherical monopole terms with increasing distance from the center of mass. Our models indicate that the density of the dark matter $\rho \sim r^{-4}$ which is steeper than the NFW profile produced in CDM simulations.

The precise slope of ρ deduced from the ϵ_x profile depends to some extent on the radial temperature profile, though not nearly so much as in the conventional spherical analysis (e.g., see Buote & Canizares 1998a). The small temperature dependence arises because the X-ray isophotes are projections of the volume X-ray emissivity which depends on temperature but has the same shape as the gravitational potential independent of the temperature profile. In fact, recent results from ASCA and SAX (White 2000; Irwin & Bregman 2000) show that clusters like A2029 and A2199 have nearly isothermal temperature profiles as assumed in our analysis. Hence, the steep ϵ_x gradients imply either that $\rho \sim r^{-4}$ which is steeper than the NFW and therefore inconsistent with CDM, or that the ellipticity of the dark matter itself decreases with distance. The latter is also inconsistent with average simulated CDM halos (J. Bullock,

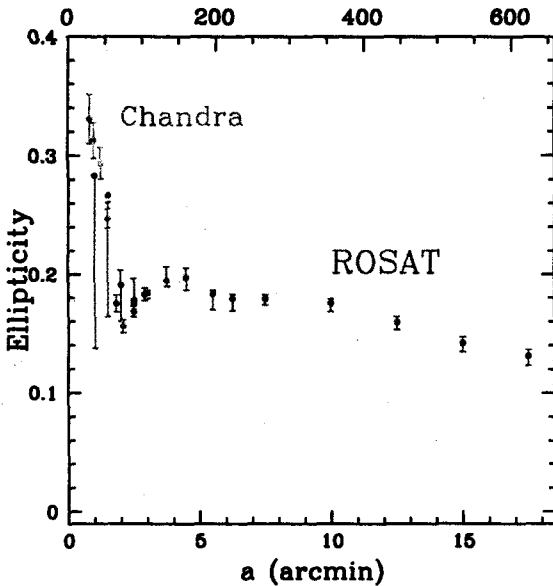


Figure 4: ROSAT (blue) and Chandra (red) ellipticities of A2199.

these proceedings). These ROSAT results for 5 clusters need to be confirmed and extended to a larger sample and with new Chandra and XMM data to determine whether they imply a new crisis with CDM halos at large radius.

We have recently begun to analyze the Chandra data of A2199. Our initial analysis finds no irregularities in the X-ray surface brightness except within the central ~ 50 kpc where there is interaction of the X-ray plasma with the radio emission from the central source similar to that seen in many other clusters. The combined ROSAT and Chandra ellipticity profiles are shown in Fig. 4.

The ellipticities of ROSAT and Chandra agree quite well, though the Chandra values are a little larger at small radius presumably due to the better spatial resolution. Hence, the basic conclusions from ROSAT appear to be confirmed by Chandra. The significantly large ellipticities observed at the center (i.e., within 100 kpc) show that the dark matter must be flattened in the core which is in conflict with the SIDM model (e.g., Miralda-Escudé 2000). The statistically significant ellipticities of ~ 0.1 in clusters at large radius cannot be explained by alternative gravity theories like MOND. At such large radii the collisional X-ray gas is the dominant luminous matter component, and since it is not rotating it should be spherical in a MOND model.

Acknowledgments

DAB thanks P. Natarajan and the SOC for the invitation to provide this review.

References

1. Buote, D. A., & Canizares, C. R., 1994, *ApJ*, 427, 86
2. Buote, D. A., & Canizares, C. R. 1996a, *ApJ*, 457, 565
3. Buote, D. A., & Canizares, C. R. 1996b, *ApJ*, 468, 184
4. Buote, D. A., & Canizares, C. R., 1998a, in *ASP Conf. Ser. vol 136, Galactic Halos: A UC Santa Cruz Workshop*, ed D. Zaritzky (*ASP: San Francisco*), p289 (*astro-ph/9710001*)
5. Buote, D. A., & Canizares, C. R. 1998b, *MNRAS*, 298, 811
6. Buote D. A., & Tsai J. C., 1995, *ApJ*, 439, 29
7. Dressler, A., Schechter, P. L., & Rose, J. A. 1986, *AJ*, 91, 1058
8. Irwin, J. A., & Bregman, J. N. 2000, *ApJ*, 538, 543
9. Miralda-Escudé, J., 2000, *ApJ*, submitted (*astro-ph/0002050*)
10. Romanowsky A. J., & Kochanek C. S., 1998, *ApJ*, 493, 641
11. Spergel, D. N., & Steinhardt, P. J., 1999, *Phys. Rev. Let.*, 84, 3760 (*astro-ph/9909386*)
12. White, D. A., 2000, *MNRAS*, 312, 663

NEW FEATURES IN ELLIPTICAL GALAXIES FROM CHANDRA IMAGES

C. Jones

Center for Astrophysics, 60 Garden St., Cambridge MA 02138 USA

E-mail: cjf@cfa.harvard.edu

Chandra's high angular resolution allows the detailed study of X-ray emission from elliptical galaxies. Chandra images show the interactions of radio plasmas with the hot interstellar medium, populations of galactic sources, structure in X-ray jets and the presence of AGN. Chandra spectroscopy allows the various emission mechanisms to be determined. This paper discusses the ellipticals Cen A and M84 as well as fossil groups.

1 Hot Gas, Jets, and X-ray Binaries in Ellipticals

The X-ray emission mechanisms from elliptical galaxies include central AGN (occasionally accompanied by a one-sided jet), galactic X-ray sources, and a hot gaseous corona. Chandra's high angular resolution and broad energy coverage allows each of these phenomena to be investigated with far greater detail than previously. This paper describes Chandra observations of Centaurus A, M84, and the class of relatively isolated ellipticals at the centers of fossil groups.



Figure 1: Chandra ACIS image of Cen A.

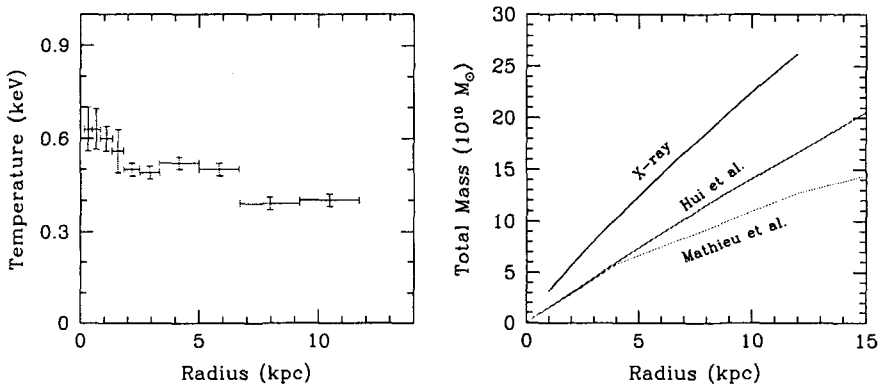


Figure 2: The left panel shows the temperature distribution of the interstellar medium in Cen A, while the right panel shows mass determinations from the X-ray as well as from two studies that used the same sample of planetary nebulae.

As the nearest active elliptical galaxy, Centaurus A (NGC5128) has been extensively studied at all wavelengths. Cen A was observed with the Chandra HRC¹ and with ACIS. The Chandra ACIS image of Cen A in Figure 1 shows X-ray emission from an AGN, a jet and radio lobe, galactic sources and a hot interstellar medium.^{2,3} Chandra's angular resolution allows the detected galactic sources to be excluded from the spectroscopy of the interstellar medium. Figure 2 (left) shows the temperature distribution of the interstellar medium that is used in the right panel to obtain the galaxy's mass distribution, under the assumption that the gas is in hydrostatic equilibrium. Also shown are two determinations of the galaxy mass using the same sample of planetary nebulae.^{4,5} The X-ray jet extends 4 kpc from the nucleus into the NE radio lobe. The jet is composed of a low surface brightness diffuse component and ~ 30 knots of emission, most of which are resolved. Aligned with the SW radio lobe is a region of enhanced X-ray emission, brightest in a partial ring directly opposite the jet. This emission likely was produced as the lobe expanded and compressed the hot ISM into a bubble or shell.

An example of the influence of radio plasma on the X-ray emitting gas in a more typical early-type galaxy is M84 (NGC4374), an E1 galaxy, within, but not at the center, of the core of the Virgo cluster. Figure 3 (left) shows the complex nature of M84 as seen in a deep Chandra ACIS observation.⁶ The structure seen in the soft X-ray emission is defined by two radio bubbles.

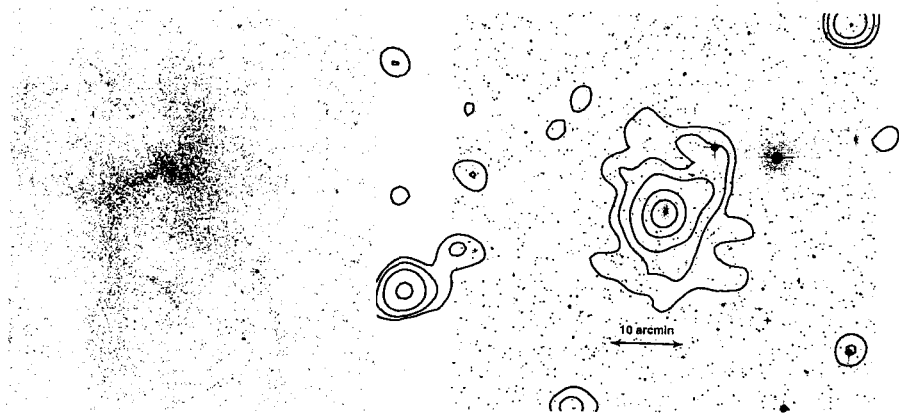


Figure 3: The left panel shows Chandra ACIS image of the soft X-ray emission from M84, while the right panel shows the X-ray contours superposed on a DSS image for the fossil group centered on ESO3060170.

Similar to Cen A (Figure 1) and Hydra A ⁷, the brightest X-ray emission is in regions surrounding the radio lobes. These bright filaments, defining the \mathcal{H} -shaped emission, have gas temperatures comparable to the gas in the central and outer regions of the galaxy and hence argue against any strong shock heating of the galaxy atmosphere by the radio plasma. By modeling the X-ray emission as arising from an outer shell surrounding the radio lobes, we determined the gas density. We combined the determination of the gas density with the radio observations of the Faraday rotation to measure a line of sight magnetic field of 0.8μ Gauss, well below the equipartition value of 20μ Gauss. At the nucleus of M84 is a modest X-ray source ($L_X = 4 \times 10^{39}$ ergs sec⁻¹) surrounded by and possibly heating a hard diffuse component that extends to 10 kpc radius. Finally in M84, as in Cen A and other ellipticals (e.g. NGC4697⁸), we find a population of galactic X-ray sources. These show a steepening in their luminosity function above 5×10^{38} ergs sec⁻¹, in agreement with that seen in NGC4697. The lower luminosity sources are likely binaries with neutron stars, while those above the Eddington limit for a neutron star probably contain a black hole.

Historically, optical galaxies have been used to identify and study a remarkably broad range of mass and size scales ranging from galaxy pairs and triplets to superclusters and filaments extending for hundreds of Mpc. Recent X-ray surveys have complemented these studies and identified a new class of col-

lapsed system – fossil groups or Over-Luminous Elliptical Galaxies (OLEG's). Fossil groups represent the extreme end point of the merging process where all the bright group member galaxies have merged into a single, central, optically bright galaxy. OLEG's cannot be selected optically since they appear as normal, bright, (relatively) isolated elliptical galaxies. However, their X-ray emission shows these apparently unremarkable systems to be surrounded by extended dark matter and hot gas halos typical of groups or poor clusters with spatial extents of 500–1000 kpc, thereby having unusually large mass-to-light ratios that are higher than typical clusters or groups.

The first “fossil” group, *RXJ1340 + 4017*, was found by Ponman and collaborators.⁹ In a search for distant X-ray clusters using ROSAT pointed observations, four fossil groups were identified at high redshifts.¹⁰ Each has an X-ray luminosity exceeding 2×10^{43} ergs sec⁻¹ with a luminous ($M_R < -22.5$), isolated elliptical galaxy centered in the extended X-ray emission. Vikhlinin et al. estimated the space density of such groups to be comparable to the density of all galaxies brighter than $M_R < -22.5$. This suggests that many of the brightest field ellipticals are the remaining members of fossil groups.

Figure 3 (right) shows an example of this class of virialized system with a bright elliptical surrounded by faint dwarf galaxies and X-ray emission extending to several hundred kpc, typical of a group or poor cluster. This example is from a sample of local fossil groups identified using primarily ROSAT X-ray observations and the DSS to determine the local galaxy environment.¹¹

Acknowledgments

The author is grateful for support from the Smithsonian Institution and thanks the Chandra team for making these results possible.

References

1. R. Kraft *et al* ApJ (Lett) 531, 9, 2000.
2. J. Kregenow *et al* ApJ in press 2001.
3. R. Kraft *et al* ApJ submitted.
4. X. Hui, H. Ford, K. Freeman, & M. Dopita, ApJ, 449, 592, 1995.
5. A. Mathiew, H. Dejonghe, & X. Hue, A&A 309, 30, 1996.
6. A. Finoguenov & C. Jones, ApJ (Lett) 547, 107, 2001.
7. B. McNamara *et al* ApJ (Lett) 534, 135, 2000.
8. C. Sarazin, J. Irwin, & J. Bregman, ApJ (Lett) 544, 101, 2000.
9. T. Ponman *et al* Nature 369, 462, 1994.
10. A. Vikhlinin *et al* ApJ (Lett) 520, 1, 1999.
11. C. Jones *et al* in preparation.

THE DETECTION OF LYMAN α ABSORPTION FROM NINE NEARBY GALAXIES

David V. Bowen

Princeton University Observatory, Princeton, NJ 08544

E-mail: dvb@astro.princeton.edu

Max Pettini

Institute of Astronomy, Madingley Rd., Cambridge CB3 0EZ, UK

J. Chris Blades

Space Telescope Science Institute, 3700 San Martin Drive, Baltimore, MD 21218

We have used STIS aboard HST to search for Ly α absorption in the outer regions of nine nearby ($cz < 6000 \text{ km s}^{-1}$) galaxies using background QSOs and AGN as probes. The foreground galaxies are intercepted between 26 and $199 h^{-1}$ kpc from their centers, and in all cases we detect Ly α within $\pm 500 \text{ km s}^{-1}$ of the galaxies' systemic velocities. The intervening galaxies have a wide range of luminosities, from $M_B = -17.1$ to -20.0 , and reside in various environments: half the galaxies are relatively isolated, the remainder form parts of groups or clusters of varying richness. The equivalent widths of the Ly α lines range from $0.08 - 0.68 \text{ \AA}$ and, with the notable exception of absorption from one pair, correlate with sightline separation in a way consistent with previously published data, though the column densities derived from the lines do not. The lack of correlation between line strength and galaxy luminosity or, in particular, the environment of the galaxy suggests that the absorption is not related to any individual galaxy, but arises in gas which follows the same dark-matter structures that the galaxies inhabit.

1 Introduction

The detection of $z \ll 1$ Ly α -forest absorption lines in the spectra of QSOs observed by HST shortly after its launch^{1,2,3} not only demonstrated the existence and evolution of these tenuous neutral hydrogen (H I) clouds over a significant fraction of the age of the universe, but quickly sparked an interest as to whether it might be possible to establish the origin of the clouds themselves. Although generally thought to be intergalactic at high redshift (because of their high rate of incidence along a sightline, and their weak clustering⁴) the remarkable success at detecting galaxies responsible for the higher H I column density Mg II systems at low redshift^{5,6,7} supported the case for investigating whether Ly α absorption lines might also arise in the halos of individual galaxies.

Mapping the galaxies around the sightline towards 3C 273^{8,9} produced little evidence for a direct association between individual galaxies and Ly α -

absorbers. Morris et al.⁹ concluded that Ly α clouds were not distributed at random with respect to galaxies, nor did they cluster as strongly as galaxies cluster with each other, and could only be associated with galaxies on scales of $\sim 0.5 - 1$ Mpc. However, in a study of six different fields, Lanzetta et al.¹⁰ found that *a*) the majority of normal, luminous galaxies possess extended Ly α -absorbing halos or disks of radii $\sim 160 h^{-1}$ kpc, and *b*) between one and two thirds of all Ly α lines arise in such galaxies. Combined with other similar studies^{11,12} it appeared that these disparate results might be reconciled if strong Ly α lines were associated with galaxies, while weak ones arose mainly in the intergalactic medium.

These initial results were soon re-evaluated in light of the rapid development in hydrodynamical and semi-analytic simulations of how gas behaves in hierarchical cold dark-matter structure formation. These simulations showed that gas should follow the same density fluctuations that are gravitationally induced by the dark matter distributions, resulting in a ‘web’ of intersecting filaments and sheets of gas. Analysis of artificial spectra, generated by shooting random sightlines through the simulations, were extremely successful in reproducing the observed properties of the high-redshift Ly α -forest^{13,14,15,16,17}. In particular, they showed that low column density lines are produced predominantly in the filaments, while the higher column density lines arise from denser gas in a virialized halo, i.e., the same regions in which a high galaxy density might be expected.

As the theoretical work continues, Chen et al. (hereafter CLWB)¹⁸ have now extended the original work of Lanzetta et al. and continue to find evidence for direct galaxy-absorber association. They also find that the strength of the absorption depends not only on impact parameter but also on galaxy luminosity, suggesting a stronger link between galaxy and absorber. Ortiz-Gil et al.¹⁹ have associated *individual* components within a complex Ly α system with *individual* galaxies from a group towards Q1545+2101, instead of an intragroup medium (although the Ly α lines are at the same redshift as the QSO, so are not drawn from the same population as the lines normally analyzed). The simulators have also advanced their models to $z \sim 0$, and have again been able to reproduce many features of the observed Ly α -forest^{?,21}. Davé et al.²² have used an algorithm designed to identify clumps of gas and stars in their simulations which are likely to correspond to galaxies, and impressively, have been able to reproduce the correlation of line strength and impact parameter.

In a previous paper²³ we used Archival HST FOS data to search for Ly α lines from present-day galaxies in order to better understand whether Ly α absorption arises in the halos of individual galaxies. We found that, for lines stronger than 0.3 \AA , *a*) nearby galaxies do not possess Ly α -absorbing

Table 1: Probes observed by HST to search for Ly α absorption from foreground galaxies.

Probe	Intervening Galaxy	v_{gal} (km s $^{-1}$)	sep (h^{-1} kpc)	$M_B -$ $5 \log h$	W (\AA)
Mrk 1048	NGC 988	1504	158	-20.0	0.11 ± 0.01
PKS 1004+130	UGC 5454	2792	84	-17.9	0.68 ± 0.05
ESO 438-G009	UGCA 226	1507	110	-17.1	0.36 ± 0.06
MCG+10-16-111	NGC 3613	1987	26	-19.8	0.54 ± 0.02
	NGC 3619	1542	85	-18.5	0.59 ± 0.02
PG 1149-110	NGC 3942	3696	92	-19.1	0.40 ± 0.06
Q1341+258	G1341+2555	5802	31	-18.0	0.08 ± 0.02
Q1831+731	NGC 6654	1821	143	-18.9	0.11 ± 0.02
	NGC 6654A	1558	199	-18.5	0.10 ± 0.01

halos beyond $300 h^{-1}$ kpc in radius, and *b*) the covering factor of galaxies between 50 and $300 h^{-1}$ kpc is $\sim 40\%$. However, we found no correlation of Ly α equivalent width with impact parameter or with galaxy luminosity, and questioned whether the galaxies were indeed responsible for the absorption lines. We instead concluded that our results supported the picture emerging at the time that Ly α lines arise in the sheets and filaments discussed above.

Our analysis suffered from two major deficiencies, namely that we probed few galaxies within the canonical $160 h^{-1}$ kpc, and that we were restricted to looking only for strong lines in the low resolution FOS data. We sought to remedy these deficiencies by obtaining more data with the STIS aboard HST, aiming to search for *weak* lines *within* $160 h^{-1}$ kpc of a nearby galaxy using the G140M grating. In this contribution, we outline some of the results obtained from that program. The experiment is not designed to address the origin of *all* Ly α absorbers, since we start by identifying a suitable galaxy and then search for absorption from that galaxy. We do not seek to establish what fraction of Ly α absorbers arise in galaxy halos.

2 HST Observations

In order to produce a sample of QSO-galaxy pairs which could be observed with HST, we cross-correlated the Third Reference Catalogue of Bright Galaxies²⁴ with version 7 of the QSO/AGN catalog of Véron-Cetty & Véron (1996). We chose galaxies with velocities > 1300 km s $^{-1}$, since absorption below these values would likely be lost in the damped Ly α absorption profile from the Milky Way. The final group of QSO-galaxy pairs successfully observed by HST is listed in Table 1. Half of the galaxies are relatively isolated, while the

other half are found in groups of various richness. In Figures 1 & 2 we show two examples of the fields studied, the poor group towards PKS 1004+130 and the rich group towards MCG+10-16-111. In Figure 3 we show three representative spectra: two are of the QSOs shown in the first two figures, while the third is of Q1341+258 which probes the halo of G1341+2555 at the small separation of $31 h^{-1}$ kpc.

We detect Ly α lines within a few hundred km s^{-1} from all nine galaxies. This suggests that galaxies in the local universe are indeed surrounded by low column density H I with $\log N(\text{H I}) \sim 13 - 15$ at radii of $26 - 200 h^{-1}$ kpc. The ubiquity of the detections suggests a high covering factor — $\sim 100\%$ at these column densities and radii. A plot of equivalent width versus impact parameter shows a weak correlation (not shown herein), consistent with CLWB's results, although column density vs. impact parameter is uncorrelated. There also appears to be no dependency of line strength with any other parameters such as galaxy magnitude or morphology.

The question remains, therefore, whether the neutral hydrogen detected has anything to do with the galaxy itself. In light of the success that the hydrodynamical simulations have had embedding galaxies in sheets of H I (§1), does the detection of gas near a galaxy reflect anything more than the fact that gas and galaxy share the same gravitational potential? Our data show little evidence for individual galaxies producing or influencing the halos around themselves: for example, the detection of at least five individual Ly α components towards PKS 1004+130 at the velocity of UGC 5454 and a companion Low Surface Brightness galaxy LSBC D637-18 (Fig. 1), spanning 740 km s^{-1} , is hard to understand as arising in two overlapping halos 84 and $138 h^{-1}$ kpc from the QSO sightline. On the other hand, intragroup gas could be expected to show a broad velocity spread due to the velocity dispersion of the group. Further, the detection of weak absorption from the isolated galaxy G1341+2555 towards Q1341+258 (Fig. 3, bottom panel) when the impact parameter is only $31 h^{-1}$ kpc is very rare—there are no such cases of such small values of equivalent width for such a small impact parameter in CLWB's sample. Finally, the strong Ly α lines detected towards MCG+10-16-111 (Fig. 2) are coincident in velocity with a strong over-density of galaxies within $2 h^{-1}$ Mpc of the sightline, again suggesting that intragroup gas is probably responsible for the absorption. It seems likely therefore that the H I we detect—and indeed, the galaxies we chose to probe—both reflect the underlying gravitational fluctuations, as the simulations predict.

Support for this work was provided through grant GO-08316.01 from the Space Telescope Science Institute, which is operated by the Association of Universities for Research in Astronomy, Inc., under NASA contract NAS5-26555.

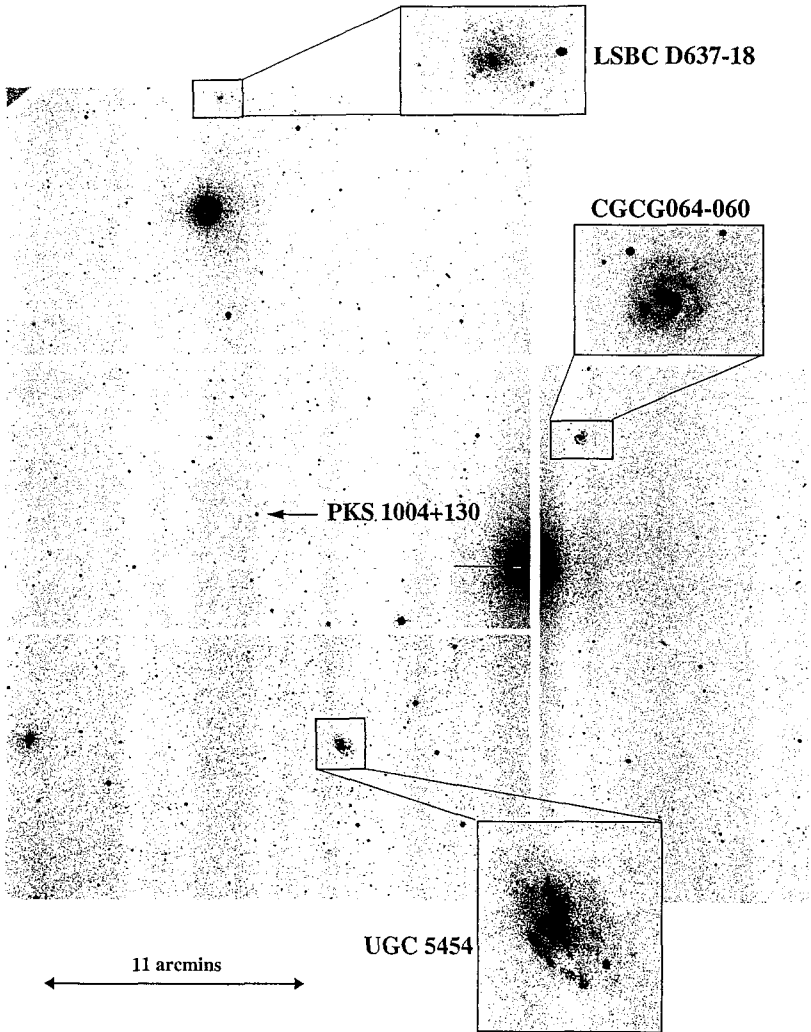


Figure 1: Reproduction of an Isaac Newton Telescope *Wide Field Camera* image of the field around the QSO PKS 1004+130 ($z = 0.240$). The field contains the dwarf galaxy UGC 5454 and an LSB galaxy LSBC D637-18. Below each designation, the galaxy's velocity and separation from the QSO sightline is given. For scale, the separation between the QSO and UGC 5454 is 10.5 arcmins. Ly α absorption is found to arise at the velocity of UGC 5454 & LSBC D637-18 (Fig. 3). The absorption is complex, consisting of at least five individual components, spanning a velocity interval of 740 km s^{-1} . Such strong & complex absorption is unlikely to arise from the halo of UGC 5454 & LSBC D637-18 alone, but probably from intragroup gas.

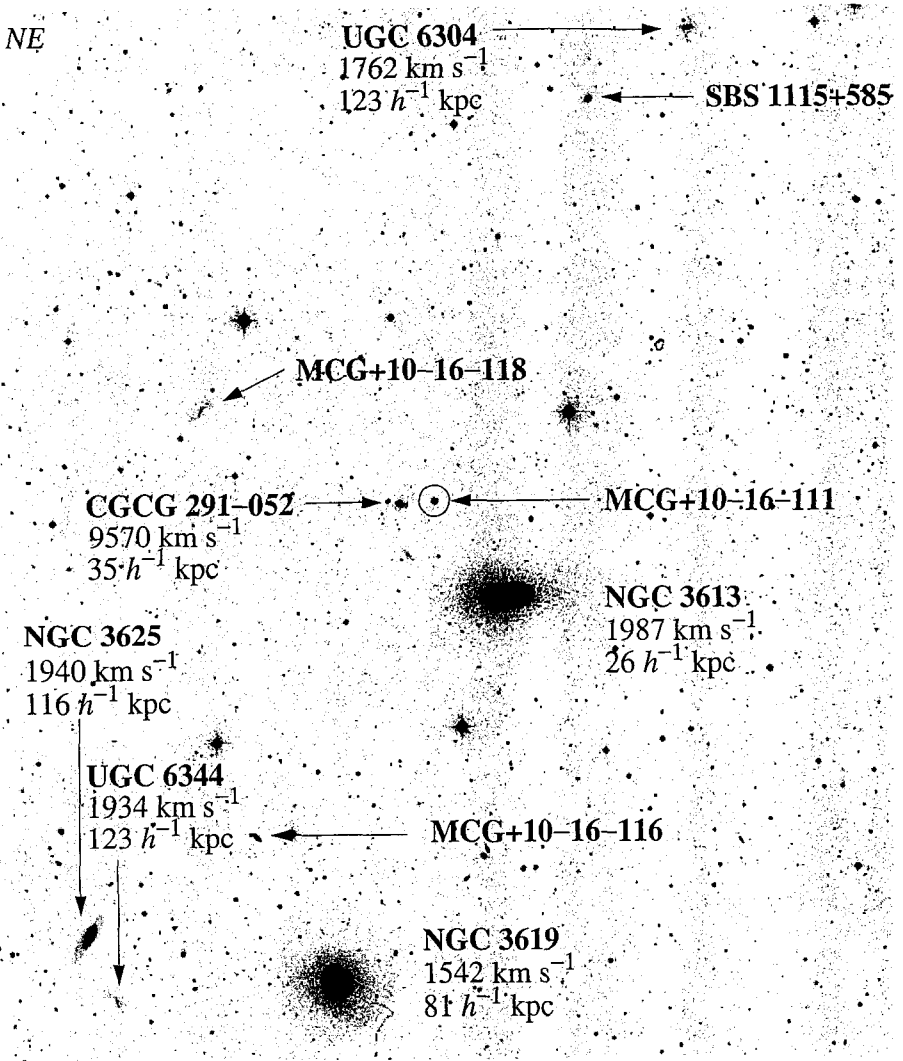


Figure 2: Reproduction of the STScI Digitized Sky Survey centered around MCG+10-16-111 ($z = 0.027$). The field is dominated by two bright galaxies, NGC 3613 & NGC 3619, although many fainter galaxies lie within radii of less than $150 h^{-1}$ kpc. Below each designation, the galaxy's velocity and separation from the probe's sightline is again given, although redshifts are not available for all galaxies identified. For scale, the separation between the MCG+10-16-111 (circled) and NGC 3619 is 18.2 arcmins. Strong Ly α absorption is detected at velocities of many of these galaxies (Fig. 3), although whether a single galaxy gives rise to the absorption is unclear.

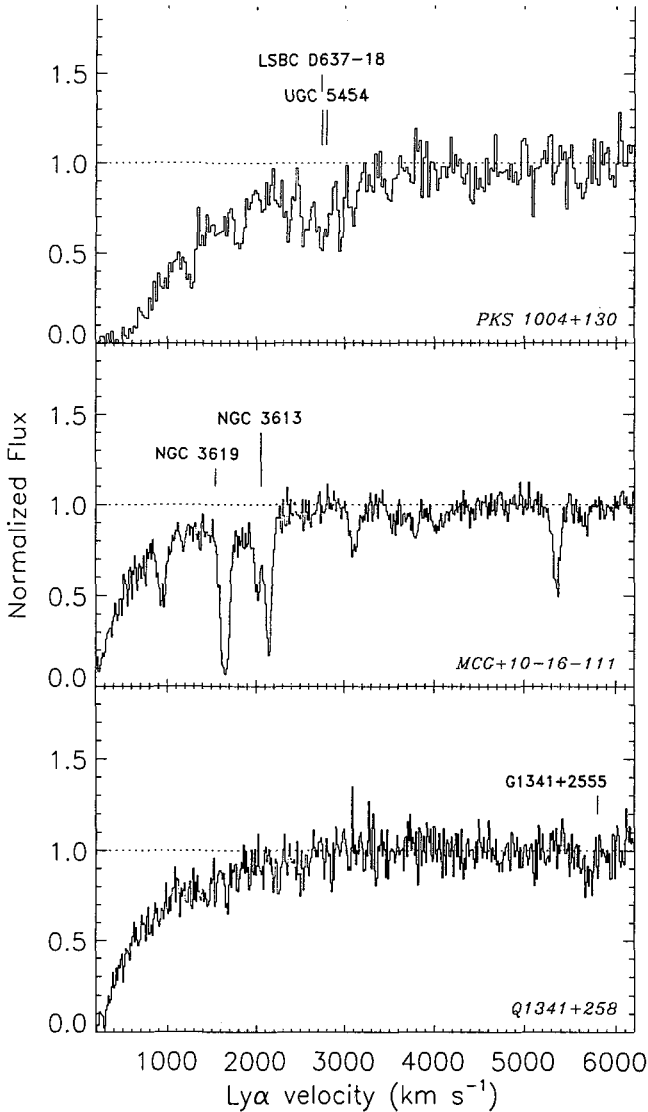


Figure 3: Three HST spectra from our survey. The strong decrease in flux at $v < 1000 \text{ km s}^{-1}$ is due to the damped Ly α profile arising from absorption by Milky Way H I. Velocities of the galaxies close to the probe sightline are labeled. The first two spectra show the absorption from galaxies in the fields presented in Figs. 1 & 2. The spectrum of PKS 1004+130 is binned 2x that of the other spectra due to its low S/N. The third spectrum shows extremely weak absorption towards Q1341+258 from a foreground galaxy only $31 h^{-1} \text{ kpc}$ from the sightline. Such weak absorption so close to a galaxy is extremely unusual compared to the equivalent widths found for galaxies at similar separations by CLWB.

References

1. Bahcall, J. N., Jannuzi, B. T., Schneider, D. P., Hartig, G. F., Bohlin, R. & Junkkarinen, V., *ApJ* **377**, L5 (1991)
2. Morris, S. L., Weymann, R. J., Savage, B. D. & Gilliland, R. L., *ApJ* **377**, L21 (1991)
3. Bahcall, J. N. et al., *ApJS* **87**, 1 (1993)
4. Sargent, W. L. W., Young, P. J., Boksenberg, A., & Tytler, D., *ApJS* **42**, 41 (1980)
5. Bergeron, J., *A&A* **155**, L8 (1986)
6. Bergeron, J. & Boissé, P., *A&A* **243**, 344 (1991)
7. Steidel, C. C., Dickinson, M. & Persson, S. E., *ApJ* **437**, L75 (1994)
8. Salzer, J. J., *AJ* **103**, 385 (1992)
9. Morris, S. L., et al., *ApJ* **419**, 524 (1993)
10. Lanzetta, K. M., Bowen, D. V., Tytler, D. & Webb, J. K., *ApJ* **442**, 538 (1995)
11. Stocke, J. T., Shull, J. M., Penton, S., Donahue, M. & Carilli, C., *ApJ* **451**, 24 (1995)
12. Le Brun, V., Bergeron, J. & Boisse, P., *A&A* **306**, 691 (1996)
13. Cen, R., Miralda-Escude, J., Ostriker, J. P. & Rauch, M., *ApJ* **437**, L9 (1994)
14. Zhang, Y., Anninos, P. & Norman, M. L., *ApJ* **453**, L57 (1995)
15. Hernquist, L., Katz, N., Weinberg, D. H. & Jordi, M., *ApJ* **457**, L51 (1996)
16. Miralda-Escude, J., Cen, R., Ostriker, J. P. & Rauch, M., *ApJ* **471**, 582 (1996)
17. Bryan, G. L., Machacek, M., Anninos, P. & Norman, M. L., *ApJ* **517**, 13 (1999)
18. Chen, H.-W., Lanzetta, K. M., Webb, J. K. & Barcons, X., *ApJ* **498**, 77 (1998)
19. Ortiz-Gil, A., Lanzetta, K. M., Webb, J. K., Barcons, X. & Fernández-Soto, A., *ApJ* **523**, 72 (1999)
20. Theuns, T., Leonard, A. & Efstathiou, G., *MNRAS* **297**, L49 (1998)
21. Davé, R. & Tripp, T. M., *ApJ* **553**, 528 (2001)
22. Davé, R., Hernquist, L., Katz, N. & Weinberg, D. H., *ApJ* **511**, 521 (1999)
23. Bowen, D. V., Blades, J. C. & Pettini, M., *ApJ* **464**, 141 (1996)
24. de Vaucouleurs, G., de Vaucouleurs, A., Corwin, J. R., Buta, R. J., Paturel, G. & Fouque, P., Third reference catalogue of bright galaxies, 1991, (New York, Springer-Verlag)

CONCLUDING REMARKS

Richard S. Ellis

*Astronomy 105-24, Caltech, Pasadena,
CA 91125, USA*

E-mail: rse@astro.caltech.edu

1 Disclaimer

I'm not sure why I was chosen to attempt a summary of this very interesting meeting. I have a suspicion such obligations come only as a result of age. I was making some comparisons during the conference dinner^a and was depressed to see how well-qualified I was on that score. Regardless of the selection criteria, I'm happy to give my thoughts on what I think has been an unusual and successful conference with no pretence at expertise in any of the topics discussed.

At first sight, the conference program covered a very wide list of issues but, in retrospect, one can now see the guiding intelligence of the Local Organizing Committee, and particularly Priya Natarajan. A number of sessions concerning the role that dark matter and stellar halos play in Galactic and extragalactic astrophysics have been cleverly interlocked to great advantage in a single workshop. The meeting has been refreshing because of this diversity which has involved a wider group of experts than in normal run-of-the-mill conferences. However, some of the issues we have discussed are pretty tough ones, requiring considerable progress in physical understanding rather than the purely quantitative gains, e.g. observational or numerical advances routinely discussed in more conventional meetings.

I think this kind of meeting is very much the direction in which our subject needs to move. We can thus feel pleased with where in we are heading even if progress is somewhat incremental in some areas and starting from a low base level.

^aNB: appropriately held in the hall of dinosaurs at the Peabody Museum

2 Statistics of Galaxy Shapes: Weak Lensing & Intrinsic Alignments

The first morning of the meeting was concerned with the statistics of observed galaxy shapes both as tracers of foreground dark matter through the phenomenon of weak gravitational lensing, and in exploring the tidal origin of angular momentum through intrinsic correlations. One might deduce from the recent literature that the latter issue is only of interest in quantifying a troublesome contaminant in the more interesting question of dark matter mapping. Although Ue-Li Pen and many speakers at this meeting reminded us of the astrophysical importance of studying intrinsic galaxy shapes as a topic in their own right, I think it fair to say that our understanding of intrinsic alignments is at such a primitive stage that most workers are indeed content to currently explore the order of magnitude of the effect and its relative amplitude c.f. that of weak lensing. As the data improves no doubt the rightful motivation for studying these correlations will take over.

Starting with the weak lensing results, David Bacon ably summarized the recent progress in this field. In a very short time interval several groups have moved from 3-4 σ detections of lensing by large scale structure on arcminute scales (the so-called “cosmic shear”) to valuable quantitative measures of the amplitude σ_8 of the mass power spectrum and the mean mass density Ω_M . One is struck by the similarity of the shear variance plots David showed to early plots of angular correlations in the microwave background fluctuations^b. A key question is how quickly we can progress to yet more precise measures, genuine dark matter “maps” and constraints on structure growth in various redshift slices. The latter goal would be a wonderful verification of gravitational instability, a goal that is turning out to be a very complex problem to address using biased galaxy data.

While improved statistics provided via dedicated telescopes and large imaging detectors will give us immediate gains, I suspect we will soon hit limits associated with a number of systematic effects, including the technique used to convert measured ellipticities into the wanted shear signal (noting instrumental and other distortions), the redshift distribution of the background sources and, as discussed, intrinsic alignment effects.

Intrinsic shape correlations are expected to arise because of the generation of angular momentum via tidal torques, through mergers and other gravity-driven aspects of galaxy assembly. There are clearly non-linear aspects to the problem and just as we find it hard to predict in detail how galaxies evolve because of our inability to understand star formation, so it should come as

^bat which some of us may have foolishly scoffed at the time

no surprise we might have a hard time predicting shape distributions. Alan Heavens, Robert Crittenden and Jonathon Mackey reviewed numerical, analytical and semi-analytical attempts to predict the correlations. They conclude intrinsic effects are likely to have only a modest effect ($<10\%$) for faint lensing surveys where the median redshift is typically $\simeq 1$, but could be an important contaminant in interpreting local ($z \simeq 0.1$) surveys such as those discussed using SDSS (Tim MacKay) and SuperCOSMOS data (Brown et al 2001 discussed by Alan).

Jonathon Mackey reminded us that weak shear has no handedness and thus can only produce E -modes whereas intrinsic correlations can produce both E and B modes. Although the detection of B modes would seem to be the entry point for estimating the importance of alignments, as the E/B mode ratio is likely to be scale-dependent, we will have to be quite careful. To what extent can we believe theoretical predictions of what we should see? Even if independent approaches agree, remember many of the assumptions adopted are similar.

I suspect what is really needed to make progress here is much better data! Specifically we seek a suitably large catalog of galaxies with reliable shapes based on CCD images *and spectroscopic redshifts in order to overcome projection effects*. Fortunately, we can soon expect to have such samples from the SDSS and 2dF surveys. The existing datasets used to test for intrinsic correlations (e.g. Lambas et al 1992, Brown et al 2001) give us an indication of the trends but, whilst pioneering in many respects, they are reliant on 2-D photographic data.

There was also a healthy discussion of new techniques in analyzing weak gravitational lensing signals and measuring faint galaxy shapes and morphologies by Alexandre Refregier, Tzu-Ching Chang, Sarah Bridle and David Goldberg. Simulations have shown that the well-used Kaiser, Squires and Broadhurst (1995) technique for deducing the shear from measured galaxy ellipticities suffers from a number of well-documented limitations and biases. Alexandre urged that, with the superior resolved imaging data we can expect from future instruments such as HST's ACS and the proposed SNAP satellite, we are not maximally extracting shape information from simple low order image moments. Convincing though these talks were in taking the subject forward, what is missing is a clear statement of the *numerical gain* we can expect via these new techniques. Given the simulations are being used to show the limitations of existing codes, why can they not be used to show the quantitative advantages of new methods?

3 Individual Halo Shapes: Galaxy-Galaxy Lensing Studies

As many authors have indicated, the *shape* of a dark matter halo contains valuable information on those dissipative processes thought to govern galaxy formation, and maybe also on the nature of the dark matter itself. Priya Natarajan showed how we can improve our chances of measuring halo shapes via lensing by analyzing restricted samples and co-adding the 2-D shear signal aligned according to the orientation of the luminous component of the lens. Tereasa Brainerd estimates that if $\epsilon_{halo} \simeq 0.3$, at least 30 deg² worth of data is required to detect the effect at 4σ significance. SDSS should provide an ideal dataset for this experiment. It would seem sensible to commence with a restricted sample, e.g. spheroidal galaxies which display some uniformity in their mean dynamical properties and their stellar populations.

A highlight of the meeting, which represents a first step towards realizing Priya's idea, was Tim McKay's remarkable results on the galaxy-mass correlation function. These were inferred using galaxy-galaxy lensing signals from the SDSS dataset, characterized by class, color and luminosity.^c The g-g lensing signal is well-behaved as a function of visible luminosity in the r, i filters, irrespective of morphology, indicating a remarkably close association of galactic assembly with the dark matter distribution. This is sound observational evidence that dark matter plays the governing role in the formation of galaxies; a result reinforced by the detailed analysis of 21 lenses in the CASTLES survey discussed by Chris Kochanek.

An interesting feature of the SDSS results is the weak correlation with light seen in u . I suspect the signal to noise here must be weaker, but if this holds up, the implication is quite important: the u luminosity of even local galaxies bears little relation to the underlying mass. This disconnect between mass and young stars is likely to be increasingly the case for optically-selected galaxies in faint redshifted surveys with important ramifications for evolutionary studies.

An important question, unlikely to be addressed by the SDSS dataset in the future, is that of *evolution* in the halo M/L ratio. By coadding the g-g lensing signal for early type cluster galaxies, Gillian Wilson examined this issue using cluster galaxies in 3 broad redshift shells to $z \simeq 0.9$ and found little evidence for evolution. Eventually the combination of ACS-based lensing studies of this kind and evolution in the intercept of the fundamental plane, will be a very effective probe of both evolution and environmental effects such as halo stripping.

^cIf ever one needs to find justification for conducting large comprehensive surveys, one can point to this remarkable application which was not originally foreseen as a motivation for undertaking the SDSS survey.

4 The Structure of Halos: Theoretical Expectations

Why do we bother to try and measure the shape of dark matter halos given it is observationally so difficult? Cold dark matter halos form via hierarchical assembly and their final structural form relies on how they relax. Julio Navarro and his colleagues showed us that numerical simulations based on cold, non-interacting dark matter, predicts a single functional form $\rho_{DM}(r)$, irrespective of mass from dwarf galaxies right up to the most massive galaxy clusters. We were inevitably drawn into the apparent crisis that whilst the merging hierarchy is clearly visible in clusters like Coma whereas, on galactic scales, either the halos are not there or something has suppressed star formation within them.

Concerning their shape, Ben Moore emphasized how hard it is to predict what we should see theoretically (though this did not apparently prevent several speakers from doing just that!) Halos can be truncated or rendered rounder by their environment, their shape will depend on the encounter history and could end up as triaxial with complex radial dependences $\epsilon(r)$. This is of course why their observed shape distribution is interesting. For example, James Bullock predicts we can expect to find mass-dependent and time-dependent trends with low mass halos being rounder and high redshift ones being flatter.

I get the impression that there is a lot of uncertainty. As with intrinsic alignments, the theorists tend to have something of a free reign. We desperately need a sound body of data.

5 Baryonic Tracers of Halo Structure in Luminous Galaxies

Let's try something easier then. Can we expect the baryon angular momentum to be aligned with that of the dark matter? SPH simulations by Tom Abel indicated that this is a reasonable assumption. Stellar and gaseous tracers of the outer halo in nearby galaxies offers us a good opportunity to make progress. The peripheral regions of galaxies are more dominated by the dark matter with longer dynamical timescales and thus enable us to glimpse early phases of galactic assembly.

We discussed a number of impressive observational programs in this session made possible via wide-field multi-object spectrographs. Raja Guhathakurta and Claire Halliday discussed the unique opportunities with the stellar halo in nearby M31 using red giants and planetaries respectively. Steve Zepf reviewed what we have learnt about both the inner and outer halos in the closest galaxies. Within $r \simeq R_e = 5$ kpc, the density of dark matter is closely equivalent to that in baryons and thus precise constraints on the mass distribution are hard to infer. It is suggested by inversion techniques that halos are triaxial. From

$r \simeq 5$ to 100 kpc, the dynamical distribution of globular clusters and planetary nebulae can be used to probe mass profiles, halo rotation and perhaps even verify triaxiality. Globulars appear to be the tracer of choice as their number density at large radii makes up for the emission line advantage of the planetary spectra. Moreover, globulars offer metallicity as an added observable. As with the dynamics of galaxies in clusters though, it is hard to get unique solutions on the orbital arrangements, and hence the mass profiles or halo shapes, without appealing to some assumptions or additional data. Surprisingly few of the ellipticals Steve discussed show convincing signs of halo rotation.

Neutral hydrogen was, of course, the first useful observational tracer of extensive halos and Mike Merrifield urged us to pursue this probe further with a view to securing halo shapes. Unfortunately, a number of (controversial?) assumptions about the dynamical distribution and state of the gas are needed to extract the halo shape. Gravity may not be the only force governing the gaseous distribution. Moreover, for “easy” cases such as the polar ring galaxies studied by Linda Sparke, one is examining recent mergers which could be unrepresentative. Unlike the stellar tracers discussed above however, the advantage of using HI is there is data for lots of galaxies! Mike gave us a balanced synthesis of the observational methods and challenges and produced the first “credible”^d distribution $N(c/a)$ of vertically-flattened halo shapes for nearby systems which peaks at $c/a=0.5$.

The distribution of stellar debris, identified in various ways after a tidal encounter, delineates an orbit which is sensitive to the halo potential. Kathryn Johnson illustrated the power of the technique via her delightful movie of the precession of a great circle stream of debris in a non-spherical potential. She also demonstrated the sensitivity to non-uniformities in the dark matter distribution.

Debris has arisen from recently captured satellites such as the Sagittarius dwarf and through the tidal pull on the Large Magellanic Cloud. Can we trace this debris sufficiently accurately? RR Lyrae variables can be found using wide-field imaging surveys on modest telescopes such as in the QUEST program discussed by Kathy Vivas. She showed associations at 50 kpc can be found and connected to streams associated with the Sagittarius dwarf. In the case of the LMC, Roeland van der Marel showed us a remarkable non-circularity ($\epsilon=0.2$) deduced for the stellar distribution of the inclined LMC disk from infrared data. Remarkably, the disk stretches in a direction that points to the Galactic center. As the tidally-induced elongation seems somewhat more pronounced than expected in previous modeling, clearly we have much to learn concerning the interpretation of halo structure from tidal effects.

^dThis was his adjective!

Finally, on large scales, David Buote and Christine Jones showed us the benefits (and complications) arising from the use of Chandra data in constraining the shapes of halos in elliptical galaxies. As we observe only the projected distribution, measuring the temperature profile is critical for a reliable inversion; early work based on ROSAT already showed that the halo is most likely flattened and more extended than the gaseous component. However, the exquisite resolution of Chandra highlights a problem concerned with unresolved sources in the earlier ROSAT data and, in at least one well-studied case, David demonstrated that the Chandra analysis leads to ellipticities which are noticeably rounder. Should we be concerned about the earlier results following this development?

6 Low Surface Brightness Galaxies: Cusps or No Cusps?

Whilst baryons are useful tracers on large scales in normal galaxies, the inference that low surface brightness (LSB) galaxies are dark matter dominated means they can be used to infer the mass structure on scales < 1 kpc. Numerical simulations of structure formation can now resolve down to these fine scales and thus direct comparisons are, in principle, possible.

Stacey McGaugh issued a healthy challenge against the universal dark matter profile introduced earlier. Improved high spatial resolution $H\alpha$ -based measures of the rotation of DM-dominated LSB galaxies reveals inner mass profiles with $\rho \propto r^\alpha$; $\alpha \simeq 0$ as opposed to the cuspy profiles with $0.75 > \alpha > 1.5$ in CDM. Of course, even in LSB galaxies there must be some baryonic contribution from the stellar and gaseous components but unless the mass/light ratio is unreasonably high, the dynamics is always DM-dominated on kpc scales. McGaugh argues that even in the best case for retaining the cuspy CDM profile (where the stellar component is ignored), a strong discrepancy is evident, $\alpha \simeq -0.2$. Until recently, some NFW advocates dismissed the HI observations on grounds of their poor spatial resolution and beam smearing, but with both $H\alpha$ and HI probes it is getting harder to ignore the conflict. We were unable to resolve this problem and clearly it is an important issue.

I'm something of a rogue and always enjoy supporting a challenger when it means possibly demolishing an established paradigm like CDM! However, I worry first whether CDM is actually a fixed target? For me, one of the most puzzling aspects of the debate here was the dispersion in the profiles predicted numerically. If CDM theorists are arguing about whether they are comfortable with $\alpha \simeq -0.75$ rather than -1.5 , under what circumstances would slopes of $\alpha \simeq -0.5$ or -0.3 be permitted?

The implications of Stacey's results are sufficiently important, that given

how little we know about the origin and dynamical state of LSBs, we must find alternative ways to probe the mass distribution on small scales. A number of groups have begun to consider probing the mass distribution elsewhere, e.g. in the cores of rich cluster data where profiles inferred from X-ray data and stellar velocity dispersions can be combined with absolute constraints inferred from strong gravitational lensing. In those cases, the fraction of studies supporting a NFW-like profile is somewhat higher (although by no means unanimous).

7 The Shape of Things to Come

A number of speakers made reference to Penny Sackett's excellent 1998 review on halo shapes at the Rutgers meeting (Sackett 1999). It's interesting to re-read that article and consider where we have got to since in three years.

Penny comprehensively reviewed the literature at that time and quoted only marginal equatorial flattenings of $b/a > 0.7$. However, she seemed firmly convinced of vertical flattenings of $c/a \simeq 0.5 \pm 0.2$. At this meeting, we have largely concentrated on the latter issue. The Milky Way constraints formed a substantial part of the 1998 evidence (c.f. her Table 3). Concerning the Milky Way, although great progress is being made on physical origin of the *stellar* halo and the star formation history of constituent stellar populations of our galaxy, I sense this audience believes c/a could still be anywhere in the range 0.5-1. Sackett likewise emphasized the role of X-ray isophotes but we have seen how improved Chandra data can, at least in some cases, lead to corrections that lead to rounder halos.

The greatest observational progress since 1998 lies in the areas of gravitational lensing and baryonic tracers at large radii using wide-field techniques. Although mentioned in passing by Penny, both have played a very significant part of this week's conference. These observations have advanced significantly our views of the extent and dark matter content of halos on large scales, but I think few would disagree that we are not quite there yet in terms of either inferring detailed mass profiles or shapes. The encouraging thing is how quickly both of these techniques have developed.

We can be optimistic of rapid progress however not least because of the wide range of observational options (lensing, baryonic tracers, tidal processes) but also because of the ingenuity and admirable "flexibility" of the theorists working in this area!


Acknowledgments

As the last speaker standing it only remains for me to thank the Local Organising Committee here at Yale, and Priya Natarajan in particular, for putting

so much thought into the program and arranging all the hospitality that made the meeting so successful!

References

1. Brown, M.L, Taylor, A.N., Hambly, N.C. & Dye, S. 2001 Mon. Not. R. astr. Soc. (submitted, astro-ph/0009499)
2. Lambas, D.G., Maddox, S.J. & Loveday, J. 1992 Mon. Not. R. astr. Soc., **258**, 404.
3. Kaiser, N., Squires, G. & Broadhurst, T. 1995 Ap. J. **449**, 460.
4. P. Sackett 1999 in *Galaxy Dynamics*, ed. D. Merritt et al, ASP Conf Series, 182, p 393.



The cover image is a color (BVR) image of the Virgo Cluster spiral galaxy NGC 4522 observed from the WIYN 3.5m telescope, originally published by **Kenney & Koopmann** (1999, AJ, 117, 181). The WIYN Observatory is a joint facility of the **University of Wisconsin-Madison, Indiana University, Yale**

The Shapes of Galaxies and their Dark Halos

University, and the National Optical Astronomy Observatories. National Optical Astronomy Observatory is operated by the Association of Universities for Research in Astronomy, Inc. (AURA) under cooperative agreement with the National Science Foundation.